Dissertation
submitted to the
Combined Faculties for the Natural Sciences and for Mathematics
of the Ruperto-Carola University of Heidelberg, Germany
for the degree of
Doctor of Natural Sciences

Put forward by
Christoph Johannes Elsässer
Born in Aschaffenburg
Oral examination: 23.01.2013

Exploration of ^{10}Be ice core records using a climatological model approach: Cosmogenic production versus climate variability

Referees:
Dr. Ingeborg Levin
Prof. Dr. Norbert Frank

Abstract

Ice core records of ^{10}Be basically offer a wide range of applications in climate research. However, atmospheric transport and deposition processes still hamper their straightforward interpretation. This work aims at establishing a climatological, data-based model attempt which allows for the first quantitative simulation of ^{10}Be ice concentration on a time scale of several 10kyr. To this end, a global atmospheric multi-box model is configured for the simulation of aerosol-borne radionuclides using extensive observations of natural and artificial nuclides. Validation with short-lived ^{7}Be reveals that the model is capable to simulate its spatio-temporal distribution in the global atmosphere, thereby providing insight into the respective circulation of ^{10}Be. To simulate ^{10}Be ice core records, the model is coupled to a basic air-firn-transfer module based on spatial ^{10}Be variations in polar ice. The model results, driven by precipitation/accumulation rate changes as well as solar and geomagnetic activity, closely reproduce the main features of observations on the Holocene and 75kyr timescale. Regarding the latter, climate-related accumulation rate changes dominate the ice concentration imposing variations of up to 300%. In contrast, incomplete atmospheric mixing of ^{10}Be dampens the geomagnetic modulation of ^{10}Be at polar sites by up to 50% compared to the global atmospheric ^{10}Be inventory. These findings basically challenge the use of ice core ^{10}Be as proxy for past geomagnetic activity.

Zusammenfassung

^{10}Be-Eiskernmessungen finden prinzipiell vielfältige Anwendungen in der Klimaforschung. Noch immer erschweren jedoch atmosphärische Transport- und Depositionsprozesse deren Interpretation. Ziel dieser Arbeit war die erstmalige Etablierung eines klimatologischen, datenbasierten Modellansatzes zur quantitativen Simulation von ^{10}Be-Eiskonzentration auf einer Zeitskala von mehreren zehntausend Jahren. Zu diesem Zweck wurde - unter Verwendung umfangreicher Messdaten natürlicher und künstlicher Radioisotope - ein Multi-Box-Modell der globalen Atmosphäre für die Modellierung aerosolgetragener Radionuklide konfiguriert. Durch Validierung mit Messdaten des kurzlebigen Isotops ^{7}Be konnte gezeigt werden, dass sich das Modell zur Simulation der räumlich-zeitlichen Verteilung von ^{7}Be in der globalen Atmosphäre eignet. Hieraus konnten entsprechende Erkenntnisse bezüglich der ^{10}Be-Verteilung abgeleitet werden. Zur Simulation von ^{10}Be-Eiskernzeitreihen wurde das Modell an ein elementares Luft-Firn-Transfer Modell gekoppelt, welches auf räumlichen Trends der polaren ^{10}Be-Eiskonzentration basiert. Angetrieben durch Änderungen der Niederschlags-/Akkumulationsrate sowie durch solare und geomagnetische Aktivität geben die Modellergebnisse die wesentlichen Merkmale der Eiskerndaten im Holozän sowie auf der 75ka Zeitskala wieder. Bezüglich letzterer wird die ^{10}Be-Eiskonzentration durch klimabedingte Akkumulationsratenänderungen dominiert, die Variationen bis zu 300% hervorrufen. Andererseits dämpft die unvollständige atmosphärische Mischung von ^{10}Be dessen geomagnetische Modulation in polaren Breiten um bis zu 50% (verglichen mit dem globalen atmosphärischen ^{10}Be-Inventar). Beide Effekte erschweren den Einsatz von ^{10}Be-Eiskerndaten zur Rekonstruktion geomagnetischer Aktivität.

Contents

Abbrevations

AAO	Antarctic Oscillation Index
AMAD	Activity Median Aerodynamic Diameter
AMS	Accelerator Mass Spectrometry
asl	above sea level
AWI	Alfred Wegener Institut Bremerhaven
b2k	before the year 2000
BL	Boundary Layer
BP	Before Present (before the year 1950)
CTBTO	Comprehensive Nuclear Test Ban Treaty Organization
EDML	European Dronning Maud Land ice core drilling project
EML	U.S. Environmental Measurements Laboratory
ϕ	Solar Modulation potential
FT	Free Troposphere
FWHM	Full Width Half Maximum
GCM	General Circulation Model
GIS	Greenland Ice Sheet
GISP2	Greenland Ice Sheet Project 2
GRACE	Global Radiocarbon Exploration Model
GRIP	Greenland Ice Core Project
HASP	EML High Altitude Sampling Program
HS	High Stratosphere
IUP	Institut für Umweltphysik Heidelberg
kyr	kilo years
LS	Low Stratosphere
mBq	milli Bequerel
MeV	Mega electron Volt
MS	Mid Stratosphere
Mt	Mega tons
NGRIP	North Greenland Ice Core Project
NH	Northern Hemisphere
ppm	parts per million
SAM	Southern Annular Mode
SASP	EML Surface Air Sampling Program
SCM	Standard Cubic Meter
SEP	Solar Energetic Particles
SH	Southern Hemisphere
SOI	Southern Oscillation Index
SSA	Singular Spectrum Analysis
STE	Stratosphere Troposphere Exchange
UNSCEAR	United Nations Scientific Committee on the Effects of Atomic Radiation
VADM	Virtual Axis Dipole Moment

1. Introduction

Facing future challenges of anthropogenic climate change requires a thorough understanding of the earth's climate system which calls for the investigation of past climate variability. Looking back in time, the earth's climate underwent major variations on very different timescales. During the last several hundred million years, the polar areas of the earth were commonly ice-free making the Quaternary (i.e. the last 2.5 million years) an extraordinary cold period. Moreover, climate archive records reveal that the Quaternary itself comprises periodic alternations of glacial and interglacial periods with cycles of 41kyr (early Pleistocene) and 100kyr (approx. last one million years), respectively. However, while the main driving mechanisms of these Quaternary glacial-interglacial changes are related to variations in the earth orbital parameters (Milancovitch theory), the detailed processes remain unclear. Surprisingly, even the last major natural climate change - the transition from the Last Glacial Maximum to the Holocene period (approx. 11 kyr ago) - is not well understood. Particularly the processes of the global rise of atmospheric CO_2 concentration from a glacial value of approx. 180 ppm to a preindustrial level of 280 ppm lack clear explanation. This increase may be investigated by using the natural carbon isotope ^{14}C as a tracer for changes in the global carbon cycle. More precisely, the different signature of ^{14}C in diverse carbon reservoirs - like the ocean being the largest one - may help to reconstruct past carbon fluxes and thus to identify the processes of the CO_2 rise. However, the knowledge of past changes in the atmospheric production of cosmogenic ^{14}C is a crucial requirement for the application of radiocarbon as a carbon cycle tracer. Both, changes in the magnetic fields of the earth and the sun modulate this production of cosmogenic radionuclides on different timescales. So far, their proper reconstruction remains unsolved. The investigation of paleoclimate conditions like temperature or precipitation changes, but also of climate and geophysical parameters as solar activity or the geomagnetic field relies on measurements of suitable proxys in various archives. Among tree-rings, sediments or stalagmites, polar ice cores stand out as an unique archive: Besides offering high-resolution informations on past accumulation rates, isotope temperatures, the composition of air and the atmospheric aerosol load, ice cores sample the long-lived cosmogenic radionuclide ^{10}Be.

In the last decades, ^{10}Be has become a common component in ice core studies due to routine Accelerator Mass Spectrometry (AMS) techniques. First and foremost, ^{10}Be may be used as a proxy for past changes in cosmic ray intensity and related variations in the magnetic fields of the earth and the sun. While the atmospheric production of ^{10}Be is comparable to the (cosmogenic) one of ^{14}C, their geochemical cycles differ: On the one hand ^{14}C is oxidized to ^{14}CO (and finally to ^{14}CO$_2$) and enters the global carbon cycle, on the other, ^{10}Be quickly attaches to aerosol particles which govern its atmospheric cycle. Having a tropospheric lifetime of several weeks only, ^{10}Be deposition fluxes reflect the cosmogenic production signal more directly than ^{14}C concentrations and are independent from changes in the global carbon cycle. Indeed, during the last decades, several studies focused on the reconstruction of the solar activity [Usoskin *et al.*, 2003; Vonmoos *et al.*, 2006; Muscheler *et al.*, 2007], the geomagnetic field [Wagner *et al.*, 2000; Muscheler *et al.*, 2005] and carbon cycle changes [Muscheler *et al.*, 2004; Köhler *et al.*, 2006] based on variations of ^{10}Be ice concentration. However, the short timescales inherent to the atmospheric aerosol cycle may significantly imprint transport and deposition effects on the local ^{10}Be ice concentration. Moreover, the hand-over from air-borne ^{10}Be to the ice complicates the application of ice core ^{10}Be. Studies on ^{10}Be-based cosmogenic production rate reconstructions oversimplify this matter by e.g. equating calculations of the global mean production rate with relative deviations of local measurements. As a consequence, improving the application of ice core ^{10}Be is associated with a better understanding of its geochemical behaviour.

Unsolved issues regarding the interpretation of ice core ^{10}Be are highlighted by three major topics:

- **Atmospheric transport**
  The production of cosmogenic nuclides in the atmosphere shows a significant spatio-temporal variability. Given major differences between polar areas and low-latitudes, the degree of atmospheric mixing affects the production signal recorded in ice cores. Several studies investigated this effect using different methods ranging from data-based to modelling attempts [Mazaud *et al.*, 1994; Steig *et al.*, 1996; Bard *et al.*, 1997; McCracken, 2004; Vonmoos *et al.*, 2006; Field *et al.*, 2006; Heikkilä *et al.*, 2009]. However, respective results remained inconclusive as ranging from a "small [...] contribution from the low-to-mid latitude stratosphere" [Steig *et al.*, 1996] to Antarctic ^{10}Be to well-mixed atmospheric ^{10}Be [Heikkilä *et al.*, 2009]. Interestingly, even both attempts applying GCMs give different results [Field *et al.*, 2006; Heikkilä *et al.*, 2009]. Studies reporting ^{10}Be-based reconstructions of solar or geomagnetic activity assume either a globally well-mixed ^{10}Be signal [Wagner *et al.*, 2000; Muscheler *et al.*, 2005], or a polar enhancement of solar-activity related production variability [Bard *et al.*, 1997]. So far, the question to what extent the local polar ^{10}Be air concentration reflects changes in the global inventory remains unsolved.

- **Aerosol deposition**
  Ice sheets basically sample ^{10}Be from the boundary layer air mass which governs the respective deposition flux. The radionuclide supply of this air mass is thus the

primary reference for the global inventory (as well as for cosmogenic production rates and related parameters). However, the relation between concentrations in air and ice is not straightforward due to complex aerosol deposition processes involved. In brief, the ratio of dry to wet deposition determines if the ^{10}Be ice concentration (sampling sites with dominating wet deposition) or the derived ^{10}Be deposition flux (sampling sites with dominating dry deposition) more closely reflects atmospheric changes (i.e. less influence by accumulation rate variability). However, both measures reflect unrealistic limiting cases (zero dry or zero wet deposition) and do not capture the correct dependency on varying accumulation rates. Finally, the type of dominating deposition process depends on the mean accumulation rate which varies in time.

- **Climate modulation**
  Climate modulation of both, atmospheric transport patterns as well as deposition processes may significantly influence the local ^{10}Be ice concentration. In this regard, two GCM-based modelling attempts report on somewhat different results: While Heikkilä *et al.* [2008a] point out that "climate changes do influence the ^{10}Be deposition fluxes, but not enough to significantly disturb the production signal", Field *et al.* [2006] conclude that "over the Holocene [...] the ^{10}Be response to climate change should not be neglected when inferring production changes".

To investigate these issues and enhance the understanding of ice core ^{10}Be, the present work envisages an innovative measurements-based model approach: Different to previous global-circulation model attempts [Field *et al.*, 2006; Heikkilä *et al.*, 2008b, 2009], the study focuses on climatological features of the atmospheric ^{10}Be cycle. To this end, a global box-model enables to (i) investigate transport and deposition processes more directly, (ii) significantly expand the timescale under investigation and, (iii) accomplish a large number of model runs under various conditions (as well as sensitivity studies). However the gain of handiness and clearness is at the cost of expense in data analysis. Extensive measurement data of (polar and global) short-lived aerosol-bound (natural and artificial) radionuclides are applied to configurate a well-established box-model of the global atmosphere for the simulation of ^{10}Be. In doing so, model calibration of (sub-micron) aerosol-related parameters is based on the extensive history of research on aerosol-bound radioactivity which emerged from 60 years of nuclear test radionuclide fallout monitoring programs. The focus on ice core ^{10}Be requires a detailed analysis of atmospheric transport and deposition in polar areas. Thus, backed-up with own measurements, the polar spatio-temporal distribution of ^{10}Be as well as short-lived ^{7}Be and ^{210}Pb is investigated. These polar investigations allow for parameter-estimation of a basic air-firn-transfer model. The coupling of this model to the atmospheric box-model - for the first time - enables a direct comparison of ^{10}Be model results to measured ice core time series.

The overarching goal of this work is to establish a measurements-based model setup for the quantitative simulation and interpretation of ice core ^{10}Be. This main objective may be broken down into three main tasks reflecting the basic structure of the thesis:

1. The first part of this work encompasses a detailed investigation of the main polar climatology of aerosol-bound ^{10}Be, ^{7}Be and ^{210}Pb (chapter 3). To do so, existing data is compiled, supplemented with own measurements and analysed with comprehensive time series analysis. The investigation of the radionuclides' spatio-temporal variation as well as transport and deposition processes sets the stage for the envisaged modelling attempt.

2. In the second part of this work (chapter 4), a global atmospheric box-model is used to investigate climatological features of aerosol-borne radionuclides on the global scale. Bomb-fission products (^{90}Sr and ^{137}Cs) as well as terrigenic (^{222}Rn and ^{210}Pb) and cosmogenic radionuclides (^{10}Be and ^{7}Be) are implemented in the model setup. The calibration and validation of the model aerosol parameters is based on global datasets of atmospheric concentrations and deposition fluxes which emerged from 60 years of nuclear test radionuclide fallout monitoring.

3. Finally, the results of part one and two are compiled to simulate ice core ^{10}Be on the long timescale up to 75kyr (chapter 5). Here, a main focus is the discussion of model input parameters on the long timescale: precipitation changes, solar activity and variations of the geomagnetic field. Model-measurement comparison of ice core ^{10}Be gives implications for ^{10}Be-based cosmogenic production rate reconstructions.

All parts of the presented work require dedicated tools of statistics, time series analysis and numerics. To allow for readability, details of these techniques applied as well as on well-established measurement methods are given in the appendix.

2. Basics on the cosmogenic radionuclides ^{10}Be and ^{7}Be

2.1. Production of cosmogenic radionuclides in the atmosphere

Naturally occurring radioactive nuclides can be classified in those which stem from earth formation (primordial radionuclides) and others which are continuously produced in the earth system. The latter ones split in terrestric nuclides (emerging from the decay of primordial radionuclides) and cosmogenic nuclides which are produced from interaction between cosmic radiation and the earth matter. While cosmogenic radionuclides comprise a large number of different nuclides, the following section focuses on the production of ^{7}Be (half life 53 days) and ^{10}Be (half life 1.39 x 10^{6} years) being the focal point of this work. Even though the detailed production processes differ due to different production cross sections involved, most of the features may be transferred to other nuclides. This does also hold for ^{14}C (half life 5730 years) although it is produced in thermal neutron caption reactions. The cosmogenic radionuclides ^{7}Be and ^{10}Be are mainly produced from spallation reactions of oxygen and nitrogen with the secondary component of the cosmic radiation in the atmosphere (e.g. Masarik & Beer [1999]).

$$^{14}\mathrm{N} + n(p) \rightarrow {}^{10}\mathrm{Be} + 3p + 2n(+4p + n) \quad ^{1}$$

$$^{16}\mathrm{O} + n(p) \rightarrow {}^{10}\mathrm{Be} + 4p + 3n(+5p + 2n)$$

The production rate is neither constant in time, nor in atmospheric space. Basically, the production rate at a given atmospheric location x depends on the intensity of primary cosmic rays impinging on the earth atmosphere, the evolution of secondary particles in the atmosphere and the number of target atoms. The dependence on these parameters leads to a complex shape of the atmospheric production distribution which varies in time. In order to describe the parameters involved it is meaningful to separate two different processes: (i) The modulation of primary cosmic ray particles which impinge the atmosphere by geomagnetic and solar activity and (ii) the production process in the atmosphere.

---

[1] Muscheler [2000]

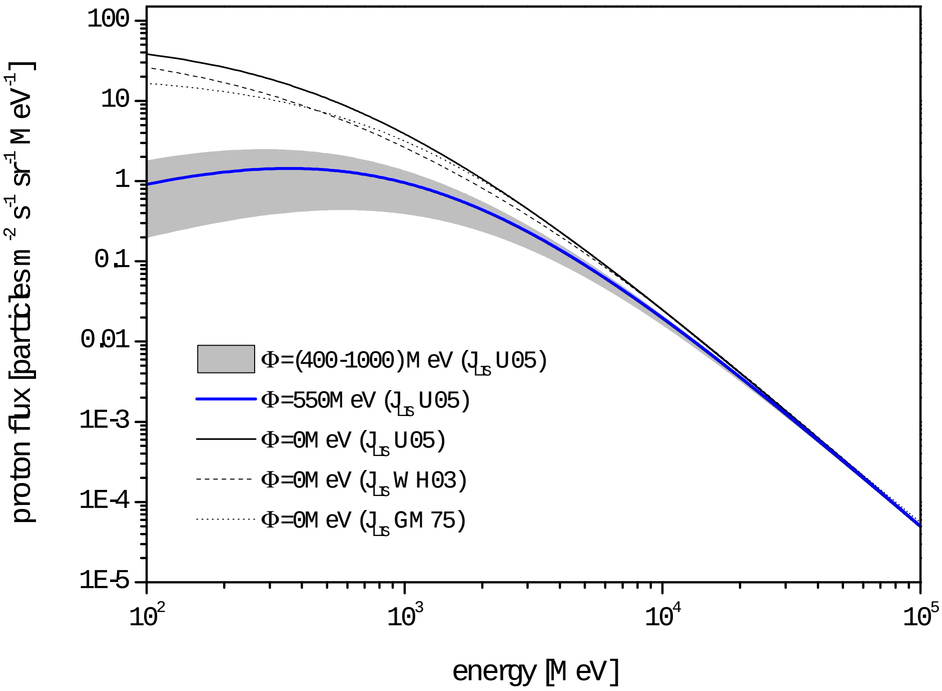

Figure 2.1.: Differential spectrum of galactic cosmic protons at the earth orbit without any modulation from the geomagnetic field. Different values of Φ denote different levels of solar activity: The value of 550MeV is a longterm mean [Masarik & Beer, 1999] and the grey shaded area depicts average solar cycle variations during 1950-2000 [Usoskin *et al.*, 2011]. Note that a value of Φ=0 represents the local interstellar spectrum (LIS) without any solar modulation. Different assessments of this local interstellar spectrum are given as U05 [Usoskin *et al.*, 2005], GM75 [Garcia-Munoz *et al.*, 1975] and WH03 [Webber & Higbie, 2003] (see Herbst *et al.* [2010] for a review and parameterizations).

Primary cosmic ray particles

Initially, the spectrum of primary cosmic ray particles which impinge on the earth atmosphere (87% protons, 12% alpha particles and 1% heavier nuclides - see Simpson [1983] for a review) is modulated by variations in the open solar magnetic field. While the transport equation of cosmic ray particles in the heliosphere (the Fokker-Planck equation) lacks an analytical solution, it is possible to parametrize their spectra by using the so-called force-field approximation [Gleeson & Axford, 1968; Caballero-Lopez & Moraal, 2004]. In doing so, the modulation of the galactic cosmic rays by the open solar magnetic field which interpenetrates the heliosphere can be described by a single parameter: The solar modulation parameter Φ. Gleeson & Axford [1968] note, that this parameter "has been identified tentatively with the mean energy loss experienced by cosmic-ray particles in penetrating into the interplanetary region from the interstellar region". When taking into account other cosmic ray particles than protons, it is advisable to refer to the modulation potential ϕ [MV] which is related to the solar modulation parameter following $\Phi = \frac{Z_i}{A_i} e\phi$ (with $\frac{Z_i}{A_i}$ being the respective charge to mass ratio of particle i [Usoskin, 2008]). In addition to the solar magnetic field, the geomagnetic field shields the earth from cosmic rays. Being a first order dipole field, the deflection is not uniform across the globe but impresses a shape upon the production rate which is a function of geomagnetic latitude (see figure 2.2). More precisely, the deflection of a single particle depends on its ratio of momentum to charge - the rigidity. Particles are deflected if this value undershoots a cutoff rigidity which is a function of latitude. The conversion from latitudes to this geomagnetical cut off rigidities depends on the geomagnetic field strength with higher dipole moments resulting in a stronger gradient between polar and mid-latitudinal production [Masarik & Beer, 2009]:

$$P_{cutoff} = 14.9 \cdot \frac{M(t)}{M_0} \cdot cos^4(\lambda) \tag{2.1}$$

$\mathrm{P_{cutoff}}$: cutoff rigidity
M(t): geomagnetic dipole moment
$\mathrm{M_0}$: current geomagnetic dipole moment
λ: geomagnetic latitude

The dependence of this relation on the relative geomagnetic dipole strength $\frac{M(t)}{M_0}$ finally accounts for a nonlinear dependence of the global mean production rate of cosmogenic radionuclides from the geomagnetic field.

Production of ^{7}Be and ^{10}Be in the atmosphere

Finally, the production rate at a given atmospheric point depends on the number of atmospheric target atoms and the evolution of cosmic ray showers in the atmosphere. In short, rising from sea level to higher atmospheric layers initially increases the local production rate due to enhanced intensity of secondary cosmic ray particles. However, from a certain atmospheric layer the decline in the density of target atoms drags the production rate down. This dependence on the atmospheric depth results in a production peak in the lower stratosphere. Figure 2.3 shows the latitudinal cut assuming a homogeneous geomagnetic dipole field (equation 2.1) and a mean solar activity of ϕ=550MV. It is important to note, that every combination of solar and geomagnetic activity produces a different distribution of production rates in the atmosphere. Production rates can be calculated by using the following function [Masarik & Beer, 1999]

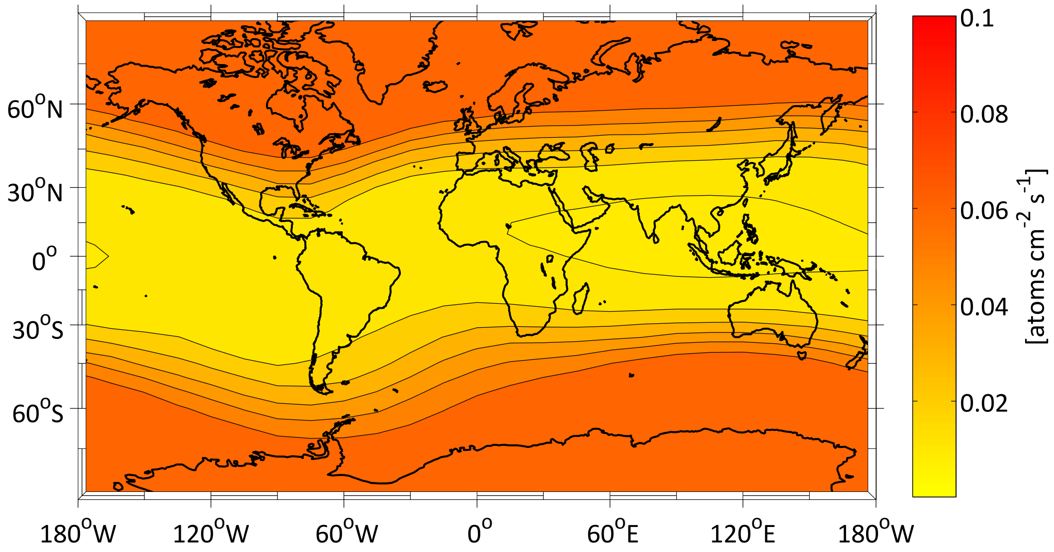

Figure 2.2.: Geomagnetic influence on the vertically integrated ^{10}Be production rate. Production rate calculations are based on [Kovaltsov & Usoskin, 2010] for a mean solar activity of ϕ=550MV. Geomagnetic cutoff rigidities are obtained from Smart & Shea [2008] for the Epoch 1995. Note that in general the cutoff rigidities (and though the production rates) vary along different latitudes. This effect is due to non-dipole moments of the geomagnetic field and results in 8-9% higher production in the southern hemisphere mean.

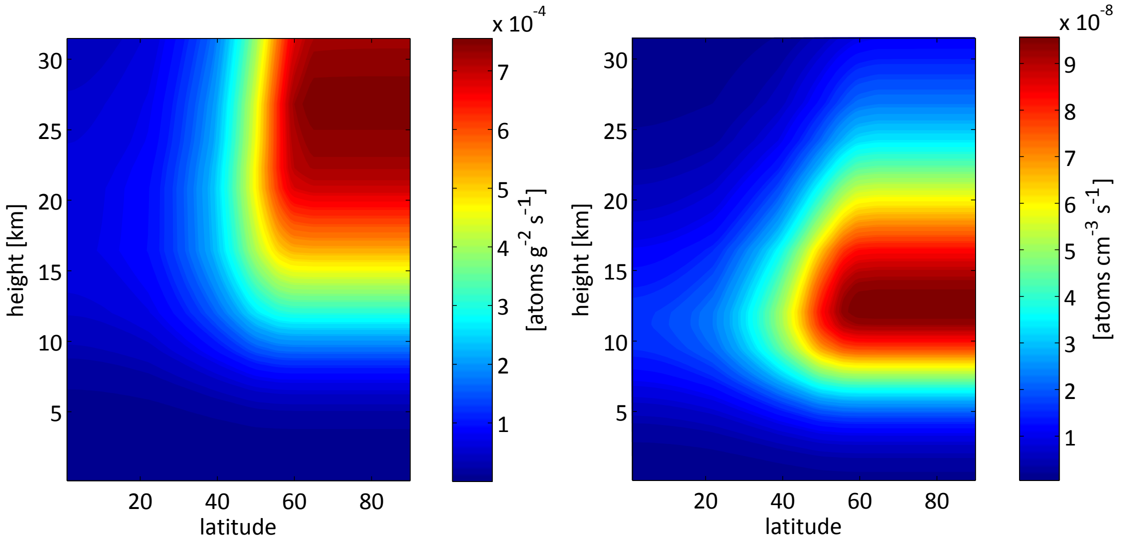

Figure 2.3.: Distribution of ^{7}Be production in the atmosphere for a mean solar activity ($\phi = 550MV$) and the current geomagnetic dipole field strength. Left: Production rates given as ratio to airmass. Right: Production rates given as volume ratio. Calculations are done with production rates of [Usoskin & Kovaltsov, 2008] using the U.S. Standard Atmosphere 1976 (NOAA [1976], MATLAB implementation of Lewis [2007]).

$$P_k(x, M, \phi) = \sum_i N_i \sum_j \int_0^\infty \sigma_{kij}(E_j) J_j(E_j, x, M, \phi) dE_j \tag{2.2}$$

N_i: Number of target atoms of the element i

$\sigma_{kij}(E_j)$: Cross section of the production of nuclide k from target i and particle j

$J_j(E_j, x, M, \phi)$: Flux of secondary cosmic ray particles j (Energy E_j) at the atmospheric point x depending on the current solar activity ϕ and the geomagnetic field M.

Production rate calculations

Within the last decades, several attempts have been made to quantify the means of production rates and their variation in time and space. While the trailblazing work of Lal & Peters [1967] is based on an empirical approach, subsequent investigations range from application of semi empirical [Nagai *et al.*, 2000] to analytical [OBrien, 1979] models (see the reviews in Usoskin & Kovaltsov [2008] and Kovaltsov & Usoskin [2010]). Although modern production rate calculations are predicated on elaborate numerical Monte-Carlo simulations of the atmospheric particle cascades [Masarik & Beer, 1999; Usoskin & Kovaltsov, 2008; Kovaltsov & Usoskin, 2010], their results are still matter of debate mainly

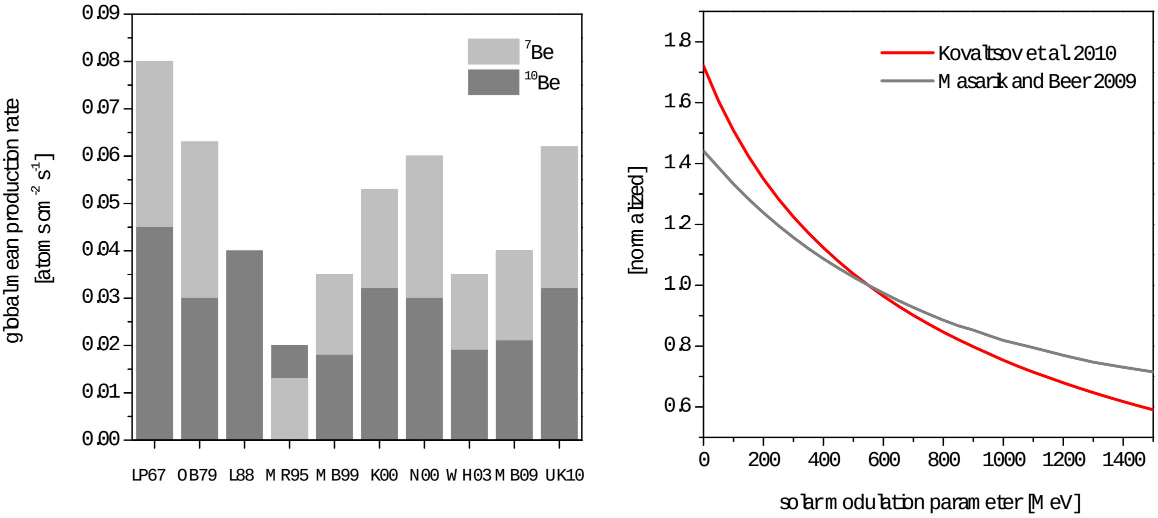

Figure 2.4.: Left: Global mean (depth-integrated) production rates of ^{7}Be and ^{10}Be compiled by Kovaltsov & Usoskin [2010] and averaged over a solar cycle. Different studies are: LP76 - Lal & Peters [1967]; OB79 - OBrien [1979]; OBrien *et al.* [1991]; L88 - Lal [1988]; MR95 - Masarik & Reedy [1995]; MB99 - Masarik & Beer [1999]; K00 - Kollár *et al.* [2000]; N00 - Nagai *et al.* [2000]; WH03/07 - Webber & Higbie [2003]; Webber *et al.* [2007]; MB09 - Masarik & Beer [2009]; UK - Usoskin & Kovaltsov [2008]; Kovaltsov & Usoskin [2010] (see Kovaltsov & Usoskin [2010] for details). Right: Differences of solar activity dependence of the global mean ^{10}Be production rate between calculations of Masarik & Beer [2009] and Kovaltsov & Usoskin [2010]. Note that the production rates are normalized to the respective value at ϕ=550MV.

due to sketchy known cross sections of the involved spallation reactions and different estimations of the local interstellar cosmic ray spectrum (see figure 2.1). Figure 2.4 (left) based on the data compiled by Kovaltsov & Usoskin [2010] (table 1 in respective publication) gives a review on the means of global ^{7}Be and ^{10}Be production. Absolute global mean production rates differ up to a factor 5 in case of ^{7}Be and still a factor 2.5 in case of ^{10}Be. For ^{7}Be the standard deviation from an overall mean value of different calculations is 61% and around 67% in case of ^{10}Be. Eventually, production rate calculations differ also in case of the dependence on solar and geomagnetic activity, respectively. Figure 2.4 (right) shows the difference between the production rate calculations of Masarik & Beer [2009] and Kovaltsov & Usoskin [2010] with respect to solar activity dependence (constant geomagnetic field strength). These differences make the production of cosmogenic radionuclides in the atmosphere an unresolved topic which needs further investigations. However, open questions related to the geochemical cycles of aerosol and related aerosol-borne radionuclides are much more substantial making cosmogenic radionuclides suitable tracers for the sub-micron aerosol cycle.

2.2. The geochemical cycle of aerosol-borne radionuclides

After production, the radionuclides ^{10}Be and ^{7}Be quickly get attached to aerosol particles (e.g. Junge [1963]). Thence, the atmospheric transport and deposition processes are governed by the respective aerosol cycle. A critical parameter governing the processes involved is the diameter of the carrier aerosol. Small aerosol particles (with diameters $< 0.1\mu$m) which emerge from homogeneous nucleation of supersaturated gases are by far the most numerous particles in the atmosphere (e.g. Papastefanou [2008] and references therein). Indeed, processes which control the adsorption of radionuclides to aerosol particles are sensitive to aerosol surface which shows a trimodal distribution in the atmosphere (following Papastefanou [2008]):

- Aitken mode: Particles with diameter $< 0.1\mu$m
- Accumulation mode: Particles with diameter $> 0.1\mu$m and $< 2\mu$m
- Coarse mode: Particles with diameter $> 2\mu$m

Measurements of radionuclide air concentration using impactors show, that ^{7}Be is generally attached to accumulation mode aerosol (Papastefanou [2008] and references therein). Papastefanou [2008] as well as Sykora & Fröhlich [2010] and Dorrian [1997] give a review on Activity Median Aerodynamic Diameter (AMAD) measurements for ^{7}Be and find a comparatively wide range of AMADs (0.29 - 2.06 μm). Different studies report on dependencies on altitude and latitude as well as on the sampling season and meteorological conditions (see Papastefanou [2008] for details). Size specific deposition processes like rain as well as aerosol coagulation and respective aerosol/airmass age are supposed to alter the activity size spectrum. These effects could explain different AMADs for different types of radionuclides (with respect to source region and radioactive lifetime). However, while very short-lived terrigenic radionuclides (decay products of ^{222}Rn) clearly have a different size spectrum with significant portions in the aitken mode [Papastefanou, 2008], the AMADs of ^{210}Pb (half life 22.3 years) (e.g. Winkler *et al.* [1998]) as well as long-lived bomb fission products (e.g. Junge [1963] and references therein) have comparable activity size distributions (see section 2.3 for details). This finding indicates, that atmospheric transport and deposition processes of ^{10}Be may be investigated using measurements of ^{7}Be (and further terrigenic and bomb fission nuclides, see section 2.3).

In the following some details on the two fundamental processes which govern the ^{10}Be and ^{7}Be distribution in the atmosphere are outlined: Atmospheric transport and aerosol deposition.

Atmospheric transport

The shape of the atmospheric production rate distribution does not directly transform into an identical distribution of mean atmospheric concentration of ^{10}Be and ^{7}Be. In fact, atmospheric airmass transport regimes lead to very different airmass ages in the atmosphere and atmospheric lifetimes of aerosol-borne radionuclides, respectively. This effect is mostly pronounced in the difference between stratospheric and tropospheric levels of the atmosphere. As a consequence of stable layering, stratospheric lifetimes of aerosol-borne radionuclides are in the order of one to two years [Feely *et al.*, 1966]. On the other hand, turbulent mixing of the troposphere quickly transports sub-micron aerosols to the boundary layer sink regions and limits their (tropospheric) lifetime to several weeks. This leads to a steep gradient between stratospheric and tropospheric concentrations up to 2-3 orders of magnitude (in case of ^{7}Be [EML-SASP, 2010]) which is considerable larger than differences based on the production process (see figure 2.3). This vertical gradient of mean atmospheric concentration is responsible for a sensitivity of aerosol-borne radionuclides to transport effects which influence boundary layer air concentration on different timescales. Basically, the stratosphere-to-troposphere exchange (STE) but also vertical and partly latitudinal mixing contribute to an obvious seasonal cycle seen at most measurement sites [Feely *et al.*, 1989]. A model attempt which intends to reproduce measurements of ^{7}Be and ^{10}Be needs a proper representation of the Stratosphere-Troposphere-Exchange.

Deposition processes

Deposition processes can be divided into wet and dry deposition processes. Following relevant literature [Junge, 1963; Davidson *et al.*, 1996; Roedel, 2000], the mechanisms of wet deposition may be divided in processes occurring within clouds (rain out) and below clouds (wash-out). According to Roedel [2000] there are three processes contributing to rain-out: At first aerosol serves as condensation nucleus (nucleation scavenging), second aerosol particles get attached to existing droplets (or ice crystals) by diffusion or third by phoretic effects (related to the electric forces and Stefan flow). However, the latter two mechanisms (also referred to as in-cloud scavenging (e.g. Davidson *et al.* [1996]) contribute only in case of small aerosol radius (considerably smaller than 0.1 μm). On the other hand, wash-out is the effect of rain-drops (or snow) catching aerosol on their way from a cloud to the surface. Here, impaction (radius > 1 μm) and diffusion (small particles) are contributing mechanisms and moreover evaporation of raindrops results in an increase of rainwater concentration [Junge, 1975]. According to calculations in Junge [1975] (see Roedel [2000] for respective chart), condensation is the dominating effect for aerosol radii in the range of 0.1 to 1 μm. Indeed, the contribution of wash-out depends on the altitude profile of the trace element: The wash-out fraction increases for air concentrations increasing from cloud base to ground [Roedel, 2000]. The term dry deposition comprises all mechanisms which contribute to aerosol deposition in the absence of precipitation events. Roedel [2000] gives diffusion (r $<$ 0.1 μm), segregation due to inertia (0.1 μm $<$ r $<$ 1 μm) and sedimentation (r $>$ 1 μm) as being the relevant processes. Davidson *et al.* [1996] classify three main processes: aerodynamic transport (from the free atmosphere to the viscous sublayer), boundary layer transport (across the sublayer to the surface), and interactions with the surface.

In summary, deposition processes are complex and depend on the local meteorology as well as on aerosol size distribution. Although an important field of research, the investigation of the detailed processes is clearly beyond the scope of this work. This is even more true as there is no hope to assess the determining factors on the global scale. A reasonable approach is to investigate and parametrize the deposition effects of cosmogenic radionuclides using measurements of bomb fission and terrigenic radionuclides.

2.3. Applications of terrigenic radionuclides and bomb fission products for the investigation of ^{10}Be

Terrigenic and bomb fission radiounclides which underly similar transport and deposition processes but emerge from different sources may support the investigate of the geochemical behaviour of aerosol-borne radionuclides. Certainly, source distributions and production rates have to be known properly to serve as adequate tracers. In the following main features and state-of-the-art knowledge on these isotopes are shortly summarized.

The terrigenic nuclide ^{210}Pb

Having a very different source distribution, measurements of the terrigenic radionuclide ^{210}Pb (which is a decay product of ^{222}Rn) may help to investigate the atmospheric behaviour of ^{10}Be. ^{222}Rn is produced within the radioactive series of ^{238}U (also known as radium series) from its precursor ^{226}Ra which is part of the soil/rock matrix. As the nuclide ^{226}Ra emits an alpha particle, the recoil suffices to displace its decay product (^{222}Rn) by a few tens of a nanometer [Sykora & Fröhlich, 2010]. Thus, ^{222}Rn atoms contiguous to the pore space of the soil break loose from the soil matrix, and, being a noble gas, diffuse to the atmosphere. Having a radioactive lifetime of 5.5 days, ^{222}Rn decays further to a series of short-lived heavy metals and eventually to ^{210}Pb (radioactive lifetime 32 years). Radon decay products rapidly form clusters by oxidation and reaction with trace gases and air vapours and eventually attach to existing aerosol particles by diffusion [Schery, 2001; Papastefanou, 2008].

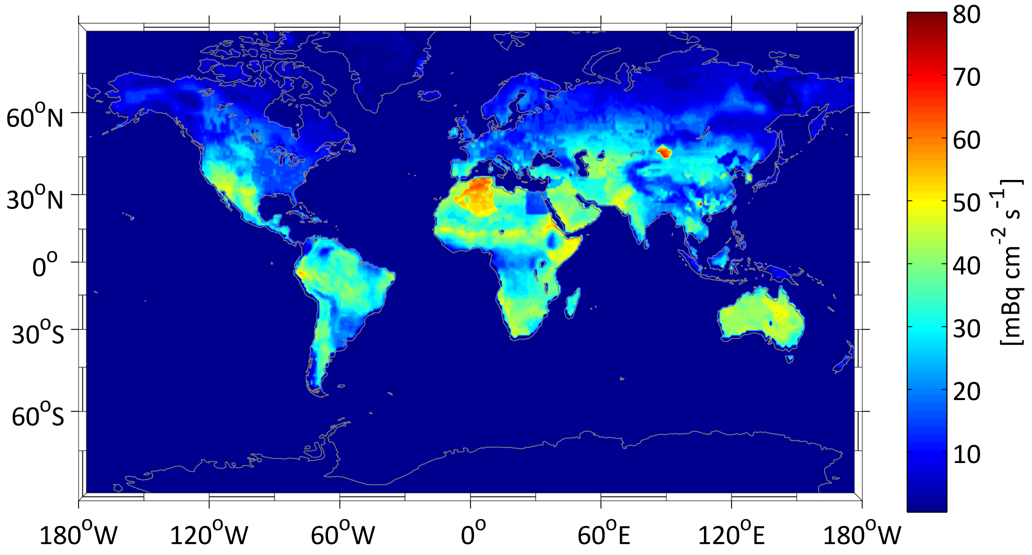

Figure 2.5.: ^{222}Rn flux model results from Hirao *et al.* [2010] (S. Hirao, pers. comm.). Note that the fluxes from the ocean and the ice-covered areas are actually not equal. While ice-sheets inhibit any ^{222}Rn flux from underlying soil, an oceanic ^{222}Rn source might indeed contribute to the ^{222}Rn air concentration at remote areas. Admittedly, the flux from ocean water to the atmosphere is about two orders of magnitude less than the flux from soil to air [Wilkening & Clements, 1975; Peng *et al.*, 1979]. Schery & Huang [2004] report on large spatial variations in the oceanic ^{222}Rn flux up to a factor ten.

Since measurements of atmospheric ^{222}Rn concentrations are sparse and restricted to boundary layer air, ^{210}Pb model attempts have to rely on estimations of the ^{222}Rn flux from soil to atmosphere. This flux basically depends on the concentration of ^{226}Ra in the soil, the soil type (porosity, grain size distribution) and the respective diffusion parameter. The latter is primarily a function of soil moisture and might impose a seasonal modulation on the ^{222}Rn flux [Dörr & Münnich, 1990]. Moreover, ice coverage represses the ^{222}Rn flux (see figure 2.5). During the last decades several studies investigated the means of ^{222}Rn fluxes and their spatial and temporal variability. Approaches cover direct measurements [Wilkening & Clements, 1975; Turekian *et al.*, 1977] as well as indirect measurements based on ^{210}Pb (see review in Conen & Robertson [2002]). While a constant land ^{222}Rn flux of 1 at cm^{-2} s^{-1} was presumed in early atmospheric model studies of ^{222}Rn or/and ^{210}Pb [Heimann *et al.*, 1990; Balkanski *et al.*, 1993; Rehfeld & Heimann, 1995; Liu *et al.*, 2001], Lee & Feichter [1995] came up with an idea of a latitudinal dependent flux. Conen & Robertson [2002] re-assess published data and find a linearly decreasing radon flux from 1 at cm^{-2} s^{-1} at 30°N to 0.2 at cm^{-2} s^{-1} at 70°N. Recently, developments with respect to ^{222}Rn flux modelling produced more sophisticated ^{222}Rn maps on the continent-wide [Szegvary *et al.*, 2009; Zhuo *et al.*, 2008; Griffiths *et al.*, 2010] or global [Schery & Wasiolek, 1998; Hirao *et al.*, 2010] scale (see figure 2.5). Still there is considerable uncertainty in the total budget of ^{222}Rn in the atmosphere related to different source estimations and consequential the ^{210}Pb source is not satisfactorily known.

The bomb fission products ^{90}Sr and ^{137}Cs

In addition to natural radionuclides, anthropogenic radioactive isotopes emerged from extensive atmospheric nuclear bomb tests during the last century (e.g. Junge [1963]; Schery [2001]). From 1945 to 1980 five countries performed several hundred atmospheric tests at roughly 21 test sites widely spread over the earth [UNSCEAR, 2000]. While the number of different radionuclides which are produced in a nuclear burst exceed 200 [Mazarik, 2010], most of the nuclides have a short radioactive lifetime and are thus not dispersed globally. Within a fireball of an atmospheric nuclear test, temperatures breed the vaporization of radioactive matter (and ambient material). As the temperatures cool down, refractory elements condense first to large aerosols whereas volatile elements and those having gaseous precursors (like ^{90}Sr and ^{137}Cs) condense later which results in a smaller aerosol particle size (e.g. Junge [1963]). Since the atmospheric lifetime of aerosol particles strongly depends on the size distribution, refractory elements are likely deposited in the vicinity of the nuclear test and less spread globally. On the other hand, the fireball transports long-lived isotopes associated with smaller aerosols, like ^{90}Sr (radioactive lifetime 41.5 years) and ^{137}Cs (radioactive lifetime 43.5 years), to upper tropospheric and stratospheric levels. These nuclides are thereby spread globally and, having a large stratospheric inventory,

atmospheric transport and deposition are supposed to coincide with cosmogenic nuclides. Indeed, the production of bomb fission products follows a different time behaviour since the largest part of bomb fission products was produced during two periods of most frequent nuclear tests (1954-1958 and 1961-1962 [Bennett, 2002]).
Although more and more specifics on nuclear test programs were published in recent decades, the detailed number and timing of different tests is still a matter of debate (see e.g. Naegler [2005]). The amount of radionuclides produced in a single test (the fission yield) basically depends on the energy released which is commonly reported in terms of its total explosive force (units: Mt TNT). Different compilations give the following summary of all tests (performed during 1945 and 1980): 380 tests / 512 Mt [Enting, 1982], 440 tests / 598 Mt [Rath, 1988], 1433 tests / 405 Mt [Yang *et al.*, 2000b] and 543 tests / 440Mt [UNSCEAR, 2000] (taken from a summary in Naegler [2005], UNSCEAR data revised). The assessment of the bomb fission source is even more complicated since a major determining factor of every contribution from a single nuclear test is the type of the bomb. While early nuclear explosions were based on fission reactions only, subsequent tests applied fission to initiate fusion reactions. Hence, an assessment of the fission radionuclides produced in a certain bomb test requires the knowledge of the total yield separated in the amount of fission and fusion yield. Even though during the last years different countries provided informations like location, type and the total explosive force on their atmospheric nuclear bomb tests, the different fission (resp. fusion) yields are largely unknown and have to be estimated [UNSCEAR, 2000]. Figure 2.6 shows some basic features of the production of bomb fission nuclides in atmospheric nuclear weapon tests as reported in UNSCEAR [2000]. Figure 2.6b gives a simple assessment of fission yields as a function of total yields. Using these estimates, the contribution of every bomb test to the global fission radionuclide source can be obtained by means of a constant value of 1.45 x 10^{26} fissions per Mt and a nuclide-specific production fission yield of 3.5% for ^{90}Sr and 5.57% in case of ^{137}Cs [UNSCEAR, 2000].

In addition to the fission yield of a single test, an assessment of the atmospheric fission product source requires the dispersal of radionuclides into different atmospheric layers. This is especially important, since a significant amount of matter remains at the local or regional vicinity of the test site and hence does not contribute to the global source. At first the vertical distribution of atmospheric input is again a function of the total explosive yield with higher values supplying energy to rise material to higher atmospheric levels. According to Junge [1963] (and references therein), the minimal energy of an atmospheric test which penetrates the tropopause sufficiently is 0.2 Mt. Moreover, the vertical atmospheric distribution depends on the geographic location and the type of test (land surface, tower, balloon, air drop, etc.) [UNSCEAR, 2000]. Following [UNSCEAR, 2000] (and references therein) bomb test events may be separated into two basic classifications: In case of surface

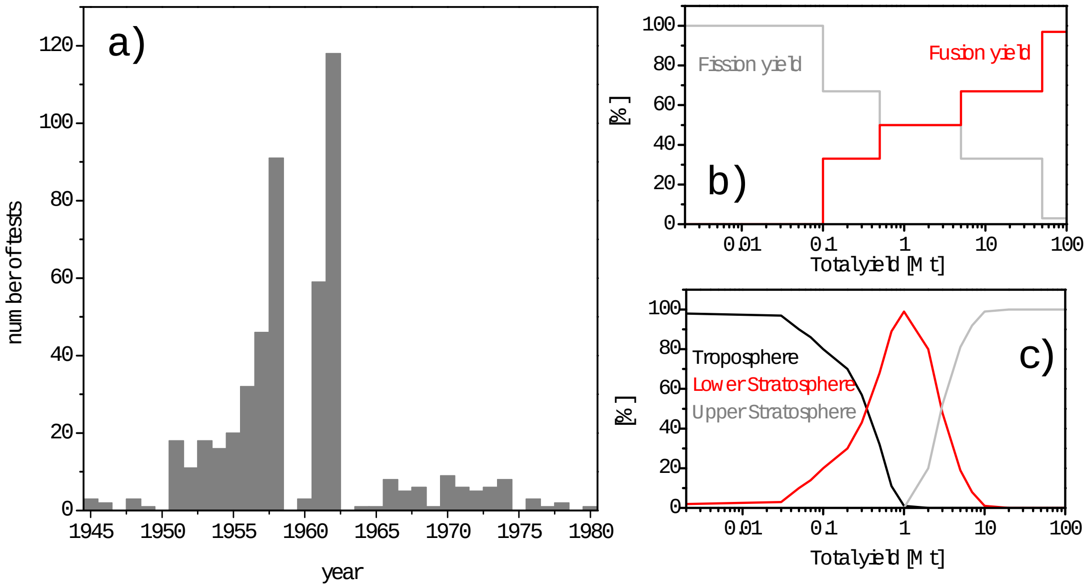

Figure 2.6.: Basic features of the production of anthropogenic fission radionuclides from atmospheric nuclear tests based on UNSCEAR [2000]. Left: Time series of the total number of atmospheric nuclear tests. Upper right: Partitioning of fission and fusion yield as a function of total energy released from a single test. Lower right: Empirical breakdown of fission nuclides produced in a single test into different atmospheric compartments as a function of total energy released (UNSCEAR [2000] referring to [Peterson, 1970]).

tests (land, tower, barge, water surface, or underwater) half of the volatile bomb fission radionuclides (such as ^{90}Sr and ^{137}Cs) are deposited locally and regionally and thus are not part of the global bomb fission source. For airbust tests (balloon, air drop, rocket and tests conducted at a certain height (depending on its explosive force)) all radionuclides are dispersed to the global atmosphere. The latter portion is subject to further classification into a tropospheric and two stratospheric (lower and upper) fractions (see figure 2.6c). On the basis of these estimations, the total production of ^{90}Sr and ^{137}Cs from atmospheric bomb tests is 733 PBq (3.0x10^{19} atoms) and 1115 PBq (4.8x10^{19} atoms), respectively. 84.8% of these nuclides are released globally (76.5% in the stratosphere and 8.2% in the troposphere) and 15.2% remain on the local/regional scale [UNSCEAR, 2000].

2.4. General survey on global measurements and modelling attempts

2.4.1. Atmospheric monitoring and modelling

Long before evolution of accelerator mass spectrometry (AMS) enabled measurements of long-lived isotopes like ^{10}Be, radionuclides with short half-lifes like ^{7}Be were routinely measured by using decay-based methods. From a historical perspective, the era of atmospheric nuclear testings has initiated extensive monitoring of artificial and natural radionuclides all over the world. In 1956 the U.S. Naval Research Laboratory (NRL) initiated a global measurement program on 'fission product radioactivity in air along the 80th meridian west' monitoring ground level air for the presence of fission product activity at 13 sites [Lockhart *et al.*, 1963]. From 1962 on the Environmental Measurements Laboratory (since 2009 National Urban Science Technology Laboratory (NUSTL)) continued the program with its Surface Air Sampling Program (SASP) which was conducted until 1999 (before 1977 Health and Safety Laboratory (HASL)). Through the years, the data base of radionuclides in ground-level air extended to 84 different sites [EML-SASP, 2010], by expanding the network and including other programs (like the EML's Remote Atmospheric Measurements Program (RAMP)) and networks (like from the United Kingdom's Atomic Energy Authority (UKAEA)), but was terminated in 1999 [EML-SASP, 2010]. With diplomatic efforts to ban (atmospheric) nuclear tests (Partial Test Ban Treaty, 1963; Nuclear Non-proliferation Treaty, 1968; Comprehensive Nuclear Test Ban Treaty, ongoing) global atmospheric radionuclide monitoring continued within the Comprehensive Nuclear Test Ban Treaty Organization (CTBTO) International Monitoring System. Being under construction for more than a decade, 62 of the total 80 stations are currently operating [CTBTO, 2012]. These data sets are augmented by plenty of scientific time series (Ioannidou *et al.* [2005]; Kulan *et al.* [2006]; Dibb [2007]; Leppänen *et al.* [2012] to give just a small excerpt) investigating

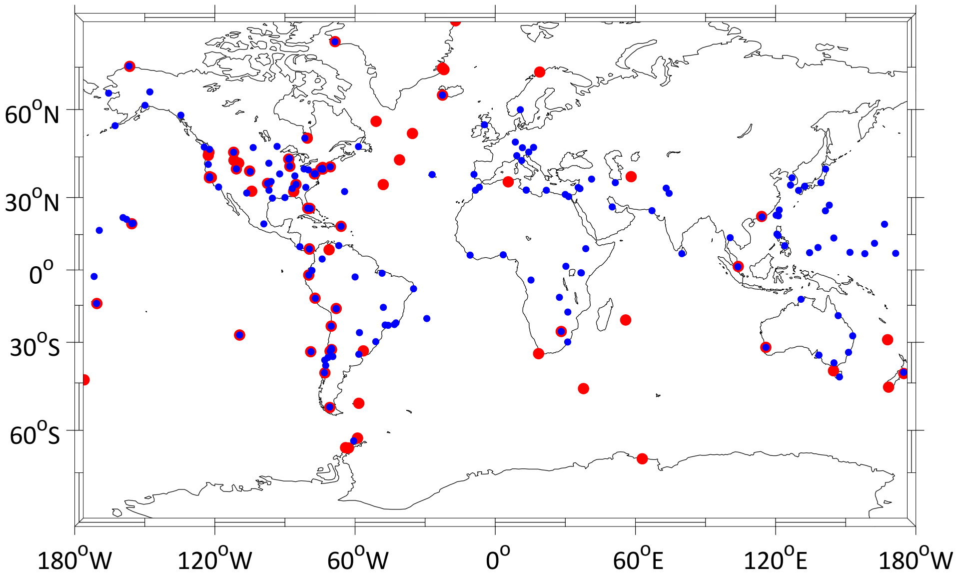

Figure 2.7.: Sampling sites of the U.S. Environmental Measurements Laboratory (EML). Red dots denote air concentration sampling and blue dots are locations of ^{90}Sr fallout measurements [EML-SASP, 2010; EML-Fallout, 2010].

different subjects like airmass transport or aerosol deposition.

Providing extensive global data sets which cover up to several decades and comparatively well-known sources, short-lived aerosol-bound radionuclides have been subject to several model attempts. In particular, ^{7}Be and ^{210}Pb as well as ^{222}Rn were used to investigate or parameterize aerosol transport or deposition parameters [Brost *et al.*, 1991; Balkanski *et al.*, 1993; Lee & Feichter, 1995; Rehfeld & Heimann, 1995; Koch *et al.*, 1996; Guelle *et al.*, 1998; Liu *et al.*, 2001; Considine *et al.*, 2005]. In case of ice core related ^{10}Be, investigations of two different teams using the ECHAM-HAM5 and GISS ModelE Global Circulation Model (GCM), respectively, are of special interest [Vedder, 2009; Heikkilä, 2007]. These studies extensively contributed to the knowledge on the atmospheric distribution and deposition patterns of ^{10}Be on the global scale. To take a case in point: Usoskin *et al.* [2009] applied the latter model attempt to investigate short-term, synoptical influences on extra-polar boundary layer air concentrations of ^{7}Be during January and February 2005. The authors report on model results that capture ”a great deal of the synoptic variability at timescales of 4 days and longer” [Usoskin *et al.*, 2009]. Despite these progresses in modelling and related understanding of the model targets under investigation, several inconsistencies remained. Basically, three problems lack a proper solution

1. Some model studies report on contradictory results. At first, Field *et al.* [2006] and Heikkilä *et al.* [2009] do not agree in the degree of global mixing of ^{10}Be in the atmosphere. On the one hand Heikkilä *et al.* [2009] find no latitudinal differences in the cosmogenic production signal and conclude that "^{10}Be is well mixed in the atmosphere before its deposition". On the other, Field *et al.* [2006] report on a significant polar enhancement of solar activity-driven production changes in high latitudes indicating a less-mixed ^{10}Be concentration. Further, while Heikkilä *et al.* [2009] state that climate change influences on the ^{10}Be deposition fluxes do "not [...] significantly disturb the production signal", Field *et al.* [2006] argue that “the ^{10}Be response to climate change should not be neglected when inferring production changes”.

2. The GCM model results using the ECHAM5 model [Heikkilä *et al.*, 2008b, 2009] significantly underestimate polar air concentrations of ^{7}Be for unknown reasons (U. Heikkilä, pers. comm.). Heikkilä & Smith [2012] report on mean Antarctic ^{7}Be air concentrations which undershoot polar measurements up to a factor 10.

3. High-resolution model attempts consume large amounts of computational power and are thus restricted to the decennial timescales excluding investigations of long-term effects of climate change, like glacial-interglacial transitions. Admittedly, the long time scale is especially interesting in case of interpretations of ^{10}Be ice core records

2.4.2. Measurements of ^{10}Be in ice cores

First measurements of the isotopes ^{10}Be in environmental samples were accomplished by Arnold [1956] who used deep-sea sediments. By means of counting methods he measured ^{10}Be activities in the order of (0.06 - 0.13) mBq per cm^{3} of clay which is equivalent to (4 - 8) x 10^{9} atoms of ^{10}Be per cm^{3} of clay. Given a mean global production rate of 1x10^{6} atoms cm^{-2} yr^{-1} it is quite obvious, that high-resolution ice core measurements were unfeasible until the evolution of accelerator mass spectrometry in the early 1980s. Using AMS techniques Raisbeck *et al.* [1981a] reported on ^{10}Be concentrations of an Antarctic ice core from Dome C station covering 30kyr. In the following, subsequent studies measured ^{10}Be concentrations in different ice-cores from Greenland and Antarctica focusing on different timescales and respective time resolution (see figure 2.8): Vostok [Yiou *et al.*, 1985], Milcent [Beer *et al.*, 1985], Byrd [Beer *et al.*, 1987], Camp Century [Beer *et al.*, 1988], South Pole [Raisbeck *et al.*, 1990], Dye3 [Beer *et al.*, 1990], Taylor Dome [Steig *et al.*, 1996], Renland and DML [Aldahan *et al.*, 1998]. A 'quantum leap' in the evolution of ^{10}Be ice core

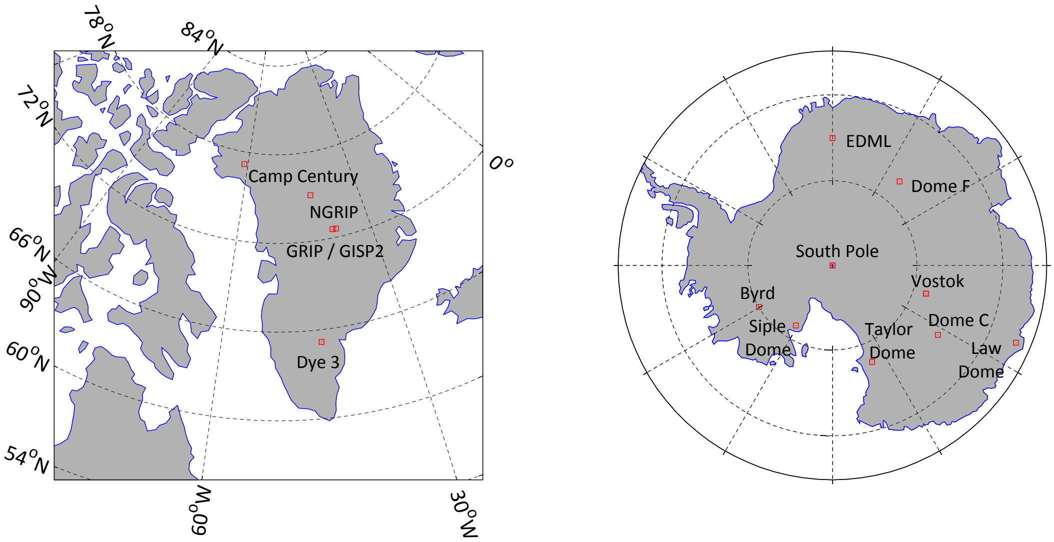

Figure 2.8.: Ice coring sites in Greenland (left) and Antarctica (right) with ^{10}Be measurements performed.

research were the measurements at Greenland Summit: GRIP [Yiou *et al.*, 1997; Vonmoos *et al.*, 2006] and GISP [Finkel & Nishiizumi, 1997]. Being the first high-resolution, long-term time series, the combination of these data sets was extensively used to investigate the polar paleoaccumulation rate [Wagner *et al.*, 2001b], the earth geomagnetic field [Wagner *et al.*, 2000; Muscheler *et al.*, 2005], changes in the carbon cycle [Muscheler *et al.*, 2004] and the solar activity [Vonmoos *et al.*, 2006]. In recent years, high-resolution measurements from Law Dome, [Smith *et al.*, 2000; Pedro *et al.*, 2011], NGRIP [Berggren *et al.*, 2009], Siple Dome [Nishiizumi *et al.*, 2007], Dome F [Horiuchi *et al.*, 2008], EDML [Steinhilber *et al.*, 2012], Dome C and Vostok [Baroni *et al.*, 2011] augmented the ^{10}Be ice core studies.

2.5. A note on absolute calibration of ^{10}Be measurements

Ice core studies on ^{10}Be typically compare relative deviations from an overall mean ^{10}Be concentration (e.g. Steinhilber *et al.* [2012]) and attach less importance to quantitative comparison of different series of measurements. On the contrary, a model attempt which aims to quantitatively simulate ^{10}Be requires consideration of different calibration procedures accomplished by various laboratories. Since AMS systems measure the ^{10}Be/^{9}Be ratio of a specific sample relative to the ratio of a standard material, the absolute ^{10}Be results depend on the calibration standard and its nominal ^{10}Be/^{9}Be ratio used in the measurement. In principle, two types of ^{10}Be standards have been used in the past: (i)

Standards with a ^{10}Be/^{9}Be ratio determined by β-counting of ^{10}Be (using a known amount of ^{9}Be) and (ii) those with a ^{10}Be/^{9}Be ratio measured by mass spectrometry (see Nishiizumi *et al.* [2007] for a review). While the first method requires the conversion from ^{10}Be activities to atom numbers, the latter method is independent from the ^{10}Be radioactive lifetime. Several studies report on different ^{10}Be half-lives broadly ranging between 1.3 x 10^6yr and 1.7 x 10^6yr [Nishiizumi *et al.*, 2007]. Recently, Korschinek *et al.* [2010] and Chmeleff *et al.* [2010] found a ^{10}Be half-life of (1.388 ± 0.018) x 10^6yr and (1.386 ± 0.012) x 10^6yr using Heavy-Ion Elastic Recoil Detection and multicollector ICP mass spectrometry / liquid scintillation counting, respectively. These new results would cause a revision of some ^{10}Be measurements which have used an activity-based AMS standard and a different ^{10}Be life-time (M. Christl, pers. comm.). On the other hand, standards based on mass spectrometric methods are not influenced. In view of ^{10}Be ice-core studies, most measurements are related to the standard material of the National Institute of Standards and Technology (NIST SRM4325), the ICN Chemical and Radioisotope Division [Nishiizumi *et al.*, 2007] or an internal ETH Zurich standard material (BEST433 and S555, Kubik & Christl [2010]). However, in addition to the standard material used for the ^{10}Be measurement a comparison between different measurements requires also the specification of its assumed ^{10}Be/^{9}Be ratio. An obvious discrepancy between different AMS measurements appear to be the ^{10}Be measurements at the adjacent ice-cores GRIP and GISP2. While GISP2 measurements refer to an activity-based ICN standard, GRIP measurements are related to the NIST SRM4325 standard which leads to an overall discrepancy of approx. 10-20%. In this thesis, the study of Nishiizumi *et al.* [2007] as well as Kubik & Christl [2010] is used as reference for a recalibration of all ^{10}Be measurements considered and table 2.1 summarizes the respective recalibration factors.

Table 2.1.: Absolute calibration of ^{10}Be measurements according to Nishiizumi *et al.* [2007] and Kubik & Christl [2010]. For the alignment of different laboratory measurements, the standard material as well as its nominal ratio or the used ^{10}Be half-life have to be known.

Standard material	NIST SRM4325	ICN	BEST433 / S555
Nominal ^{10}Be/^{9}Be ratio	2.68 ±0.14 x 10^{-11}		9.55 x10^{-11}
Nominal ^{10}Be half life		1.5x10^7yr	
recalibration factor	1.041	0.904	0.912

3. A polar view on ^{10}Be, ^{7}Be and ^{210}Pb: Spatio-temporal variability in boundary layer air and ice

3.1. Introduction

As given in section 2.4 vast global measurement programs, mostly related to nuclear monitoring, led to a deeper understanding of atmospheric behavior of aerosol-borne radionuclides (e.g. Feely *et al.* [1989]). However, most of the measurements are restricted to mid-latitudinal sites while remote areas - like polar latitudes - obviously lack sufficient data coverage. This deficiency in knowledge is especially precarious, since on the other hand, ice-core based reconstructions of the past atmospheric ^{10}Be inventory (as well as other paleoclimatic parameters and conditions) are exclusively restricted to the polar areas at present. A detailed interpretation of these radionuclide ice-core measurements requires profound knowledge of the spatio-temporal variability of aerosol-borne radionuclides in polar air and the processes which govern the air-firn transfer of respective particles. The following chapter gives a résumé on measurements of natural radionuclides in polar areas. Intending to augment the few literature data, the IUP Heidelberg Ice and Climate group has accomplished several surveys on the natural radionuclides ^{7}Be, ^{10}Be and ^{210}Pb in polar areas during the last decades [Stanzick, 1996; Auer, 1997; Stanzick, 2001; Wegner, 2003; Rohlfs, 2004; Offermann, 2006; Elsässer, 2008; Klose, 2010]. Besides measurements in shallow firn cores and snow pits along several traverses, these data sets also include a 25 years time series of ^{7}Be, ^{210}Pb and ^{10}Be measurements in boundary layer air at coastal Antarctica as well as several observation (e.g. the first year-round observation of ^{210}Pb) at Antarctic inland deep-coring sites. Backed-up with further measurements presented in this thesis, these data sets are contrasted and placed in a comprehensive context for the first time. In the following, findings from Antarctica and the Arctic are discussed detachedly. These two sections are followed by a sketch of an air-firn transfer model and finally an overall summary to set the stage for modelling aerosol-borne radionuclides.

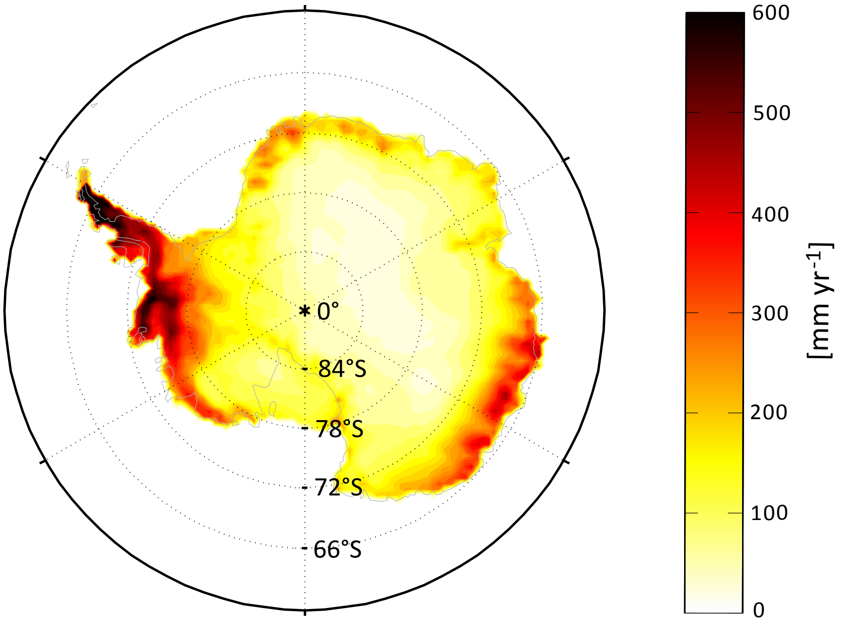

Figure 3.1.: Mean snow accumulation rate at the Antarctic continent. Data is taken from Arthern *et al.* [2006]. Note that black shaded areas depict accumulations rates $\geq$ 600 mm yr^{-1}.

3.2. The radionuclides ^{7}Be, ^{210}Pb and ^{10}Be in Antarctica

3.2.1. Glacio-meteorological situation

Remoteness of the Antarctic continent results not only from geographical distance to the next continent (distance between Tierra del Fuego and South Pole approx. 4000km) but also from climatological/meteorological conditions. Containing 90% of the world's fresh water, the Antarctic ice shelf rises closely to the coast, extents up to 4km and thus governs the local climate conditions [Shaw, 1979]. Surface cooling and the gently slopes of the Antarctic plateau result in a katabatic wind system which drains air mass from the interior to the coastal areas (e.g. King & Turner [1997]). The influence of these air masses diminishes northwards of the coast, where a circumpolar trough prevails. This "'wall of storms' constitutes an effective barrier mitigating against distant particles reaching Antarctica" [Shaw, 1979].Although mean annual temperatures stay below the freezing point in the entire Antarctic area (only 0.35% of Antarctica is ice-free [Barry & Gan, 2011]) the Antatctic climate is anything but homogeneous. Temperature is correlated to elevation which makes the Antarctic plateau one of the coldest places on earth (lowest measurement of natural temperature on earth at Vostok station -89.2°C [Warren, 2007]) while temperatures at coastal stations have summer values higher than -5°C [König-Langlo *et al.*, 1998].

Even more distinct are differences in the local mean accumulation rate [Arthern *et al.*, 2006]. Katabatic outflow in the interior boundary layer entails major subsidence of air mass and associated adiabatic warming which results in high-frequency of clear weather on the high Antarctic plateau [Shaw, 1979; King & Turner, 1997]. On the other hand circumpolar storm tracks may supply momentum to rise moist oceanic air masses to the plateau near the coast which results in adiabatic cooling and comparatively high precipitation rates. Thus, the range of mean accumulation rates ranges between < 50 mm/year (water equivalent) in the interior and > 1000 mm/year at some coastal sites [King & Turner, 1997], see figure 3.1. Moreover the type of precipitation differs significantly. While coastal precipitation is in form of snow, precipitation on the high Antarctic plateau usually is in form of ice crystals which fall from the clear sky ('diamond dust') [King & Turner [1997], and references therein]. Another important feature of the Antarctic meteorology (more precisely atmospheric circulation) is a strong boundary layer inversion which results from continuous surface cooling [King & Turner, 1997]. This inversion has a seasonal cycle following the seasonality in short-wave radiation and is especially distinct on the high plateau during austral winter. Although boundary layer inversions are a persistent feature of the interior of the Antarctic continent [Phillpot & Zillman, 1970], König-Langlo *et al.* [1998] show that the effect is also inherent to the coastal atmosphere. However, coastal areas are influenced by synoptical meteorology due to the influence of oceanic air masses and boundary layer inversions "are no persistent barrier against vertical air mass exchange, even during wintertime" [König-Langlo *et al.*, 1998]. The Antarctic Peninsula differs from eastern and western Antarctic by its extension to northern latitudes and a resulting climate which is more moderate than these of eastern and western Antarctica (e.g. Simmonds [2003]). The peninsula consists of a mountain range (mean height 1500m) which is an effective barrier on atmospheric circulation leading to "different climate conditions over the Bellingshausen and the Weddell Seas" [King & Turner, 1997]. On the western side of the Antarctic Peninsula, summer temperatures exceed freezing which results in rain precipitation.

In summary, though very different to mid-latitudinal climate regimes, the Antarctic climate system is in itself very inhomogeneous. For the sake of interpretations of radionuclide measurements on the Antarctic continent, a rough classification of different Antarctic climate regimes seems reasonable. However, since the number of measurement sites is limited (see following sections), there is no way around a simplistic approach. Given the features listed above, the Antarctic climate may be roughly separated into the three different parts: (i) the high plateau, (ii) the coastal areas of eastern and western Antarctica and (iii) the Antarctic Peninsula. It is meaningful to compile measurements of radionuclides into these basic classes and investigate deviations due to climatic differences.

3.2.2. Radionuclides in boundary layer air: Long-term measurements at Neumayer Station and comparison to other sampling sites

Ice sheets basically sample radionuclides from the ambient air. Accordingly, long-term air concentration monitoring enables a more direct investigation of the radionuclide source term than ice core measurements. Moreover, besides omitting elaborative dating of ice samples, measurements of air concentration allow for high-resolution time series which are infeasible in case of ice core or snow pit studies. Finally, contemporaneous measurements of ice and air concentration offers the opportunity to study the processes of air-to-firn-transfer.

The IUP Heidelberg ice and climate group (nearly-) continuously measures the air concentration of the radionuclides ^{7}Be, ^{210}Pb and ^{10}Be at the coastal Antarctic Neumayer Station (70°39'S, 8°15'W, 39m a.s.l.) since 1983 [Wagenbach, 1996; Wagenbach *et al.*, 1998]. For this purpose, 20000m^3 of air on an average are pumped through a high-volume air filter system having a sampling time of approx. 14 days. Air filters are shipped to the Heidelberg laboratory once a year where the short-living radionuclides ^{7}Be and ^{210}Pb are measured by using low-level gamma spectroscopy (see appendix for details on the methods). The overall measurement uncertainty (consisting of air volume determination, counting statistics and detector efficiency calibration) is in the order of 5%-10%, but may be significantly higher (up to 30%) for ^{7}Be in case of the oldest samples. Measurements are composited to monthly means which results in the time series given in figure 3.2. Measurements of ^{10}Be are mostly less resolved since the measurement procedure is more extensive. To this end, filters are composited up to yearly means and spiked with a ^{9}Be carrier solution. After leaching and chemical concentration (following Stone *et al.* [2004]) the samples are pressed into AMS-targets and measured using accelerator mass spectroscopy (see appendix for details). Typical uncertainty of the AMS measurements is around 4%. Figure 3.2 shows the resulting time series from 25 years of measurements which stand out as the only high-quality, long-term measurement of all three radionuclides in (coastal) Antarctica.

The Neumayer data is augmented by ^{7}Be and ^{210}Pb measurements within the framework of EML nuclear monitoring [EML-SASP, 2010] at Marsh Station (62°11'S, 58°59'W, 5m a.s.l.), Palmer Station (64°46'S, 64°4'W, 30m a.s.l.), Base President Frei (64°49'S, 62°52'W, 10m a.s.l.), Mawson Station (67°36'S, 62°53'E, 30m a.s.l.) and South Pole Station (90°0'S, 0°0'W, 2800m a.s.l.). However, most of these time-series are short and show substantial unsteadiness like ambiguous changes, frequent data gaps or extraordinary errors (up to several 100%). Moreover, longterm measurements of ^{7}Be and ^{210}Pb are available from coastal station Dumont D'Urville (66°40'S, 140°01'E) [Sanak *et al.*, 1985; Lambert *et al.*, 1990], but restricted to earlier periods of the 20th century. In recent years, first radionuclide measurements have been obtained at the Antarctic deep-coring sites Kohnen station

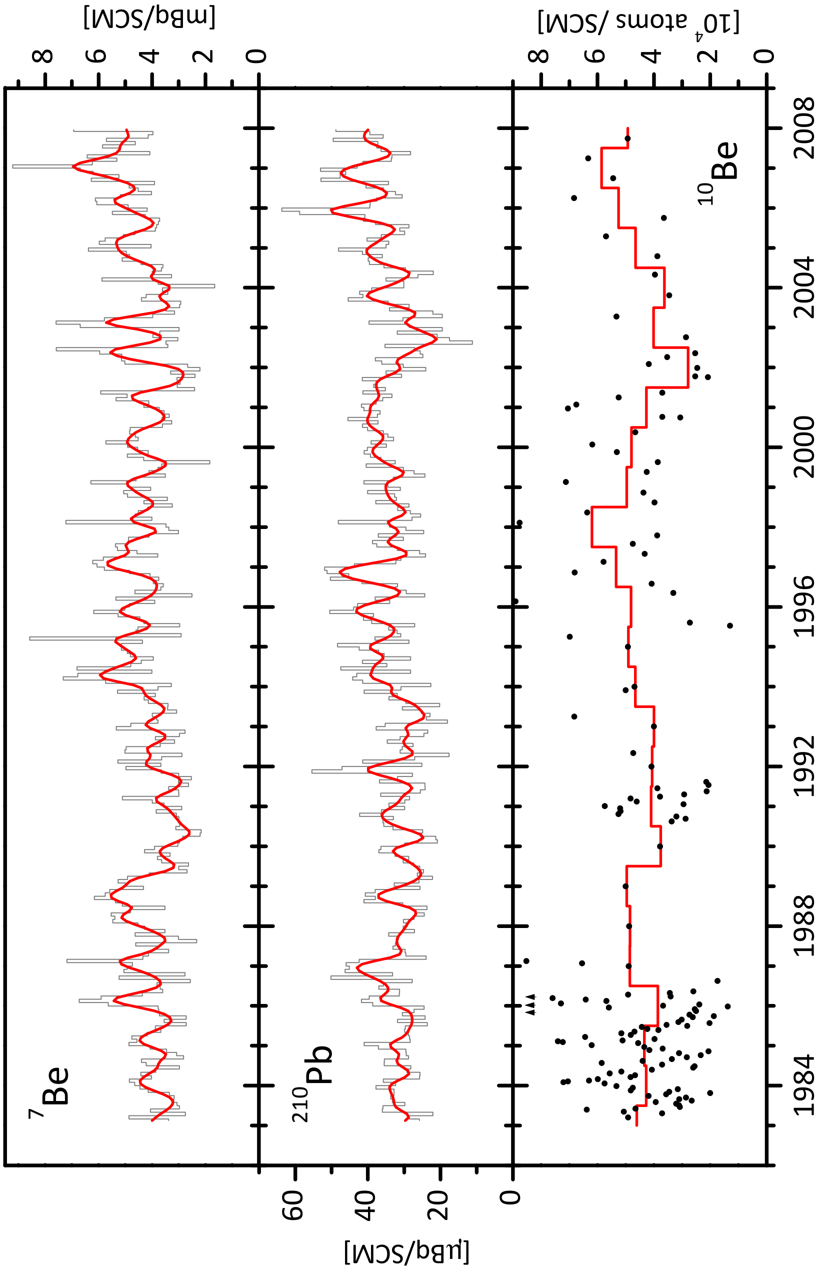

Figure 3.2.: Radionuclide time series from Neumayer station in coastal Antarctica. Red curves denote Gaussian smoothing in case of (equidistant) monthly mean values of ^{7}Be and ^{210}Pb. Note that the Gaussian filter dampens a seasonal cycle amplitude by approx. 27%. In case of ^{10}Be red lines depict yearly means calculated from (time-weighted) single measurements.

and Dome C though these data sets are short covering several months or years at most (D. Wagenbach, pers. comm.). For the Dome C station, Klose [2010] reports on first year-round measurements of ^{210}Pb. In the following, the spatial variability of mean radionuclide air concentrations derived from the different sampling stations is shown. Afterwards, the variability in time is investigated by using the Neumayer time series.

Spatial variability

Figure 3.3 gives the overall statistics for the different sampling sites as a box plot. With respect to the EML-SASP [2010] data, values with errors >60% as well as measurements which exceed or undershoot the respective median by a factor 5 were disregarded. Since full-year sampling of aerosols requires either an automatic sampling station or an overwintering crew, some polar measurements are restricted to the summer months. Taking this into account the plot contains the summer mean values of Dec-Feb (red dots). Following section 3.2.1 the available measurements can be separated into the three basic classes of the Antarctic climate:

- *Coastal Antarctica:* Neumayer station, Mawson station, DDU
- *Antarctic Plateau:* South Pole station, Kohnen Station, Dome C
- *Antarctic Peninsula:* Marsh Station, Palmer Station

As can be seen in figure 3.3, mean values at the Antarctic Peninsula are clearly lower than the values at the Antarctic continent by a factor 2-3. Otherwise, mean coastal Antarctic radionuclide air concentrations do not significantly differ from the high plateau area. Slightly higher summer values at the plateau sites may be assigned to a more pronounced seasonal cycle which is in line with the lower values during austral winter. Mean concentrations at coastal Mawson station and DDU somewhat exceed respective Neumayer measurements (see figure 3.3). This may be due to a higher katabatic influence at these too stations and related influence of inland airmass (e.g. König-Langlo *et al.* [1998]).

At first, the lower radionuclide air concentrations at the Antarctic Peninsula are in line with the different climate conditions which may result in a higher aerosol sink in this region. Extending to the north, "the Peninsula lies within the circumpolar pressure trough throughout the year and [...] is situated at the eastern end of a region of very frequent, intense cyclones"' [Simmonds, 2003]. Moreover, the aerosol sink at the region of westerlies in the southern mid-latitudes is expected to be even more pronounced due to the renowned stormy weather ('roaring forties', 'furious fifties', 'screaming sixties'). Being the most northern region of the Antarctic, the Antarctic Peninsula might be most influenced by aerosol-depleted mid-latitude airmasses. On the other hand, climate differences between the coastal Antarctic region and the high Antarctic plateau are very different (see

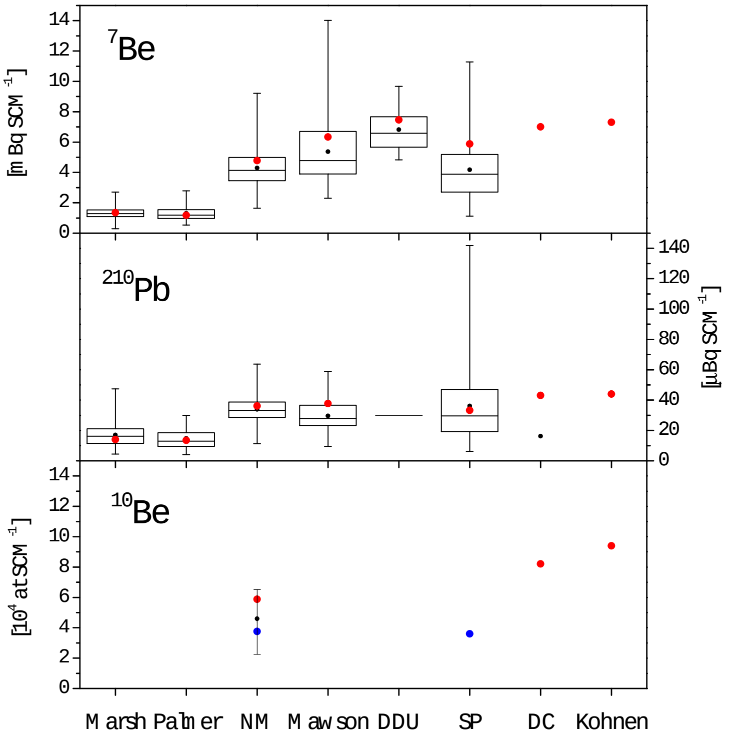

Figure 3.3.: Air concentration of radionuclides at several Antarctic sites. Red dots denote summer mean values (December - February), blue dots display July-December means. The boxes depict 25% and 75% percentiles and whiskers (vertical bars) are the respective maximum and minimum value of the monthly mean data. In case of missing boxes the data basis was too low for statistics or values refer to literature. Data: Mawson, Palmer, Marsh and South Pole (SP) - EML SASP archive [EML-SASP, 2010]; Neumayer (NM) - this work; Dumont D'Urville (DDU) - [Sanak *et al.*, 1985; Lambert *et al.*, 1990]. ^{10}Be measurements at South Pole station are from Field *et al.* [2006] (referring to S. Harder). Kohnen Station, Dome C (DC) (D. Wagenbach, pers. comm., Klose [2010])

section 3.2), too, and the overall similarity of radionuclide air concentration is unexpected. A possible explanation could be the ice sheet specific katabatic flow draining air masses from the plateau to the coastal areas. However, meteorological conditions at the coastal Neumayer site indicate, that air masses are not predominantly influenced by southern flow [König-Langlo *et al.*, 1998]. Hence, the conclusion remains that transport and deposition processes are comparable over large parts of the Antarctic boundary layer.

Time series analysis of Neumayer measurements

Time variability of the radionuclide boundary layer air concentration is investigated by essentially using the Neumayer monthly resolution ^{7}Be and ^{210}Pb data. Time series at the other stations are mainly short or interrupted by frequent data gaps which hamper time series analysis. Nevertheless, these measurements are used for completing the picture, where feasible.
Time series analysis methods encompass Monte-Carlo Singular Spectrum Analysis (MC-SSA) and Wavelet Analysis which are proven to be ideal tools for the present task (see appendix for details on the methods). Major findings are shown in figure 3.4 and comprise (i) a seasonal cycle being the most significant signal in both time series, (ii) a decadal signal in the ^{7}Be data set, (iii) a 2-3 years oscillation inherent to the ^{7}Be measurements which is not formally significant and (iv) a 4-5 years oscillation in case of the ^{210}Pb time series (see also previous results of Elsässer [2008] based on filter methods and SSA without Monte-Carlo analysis). Wavelet analysis reveals that all signals are not stationary in time, and, interestingly, both radionuclides do not coincide in the periods of distinct seasonal or multi-annual variability: ^{7}Be seasonality is especially pronounced during 1985-1987 and 2000-2002, while the ^{210}Pb shows a distinct seasonal variation during 1995-1997 and 2004-2007. To investigate the multi-annual trends, the respective seasonal cycle is eliminated by dividing each monthly value with the respective overall mean. Amplitudes of the so-derived multi-annual oscillations vary but generally do not exceed 20% of the overall mean value. In case of ^{7}Be the first minimum of the decadal variation around 1991 shows the highest amplitude but a quantitative investigation remains difficult since depending on the parameters of the method applied. In detail, the variation of the SSA parameter results in a trade off between the amplitude modulation and a clear seperation of the signal from underlying noise. The relative amplitude of the ^{210}Pb 4-6 years signal is comparable to the ^{7}Be decadal but is more distinct during the second half of the record. Main driving mechanisms are discussed in the following.

Seasonal cycles

The most significant signal of the radionuclide time series is their seasonal cycle inherent to

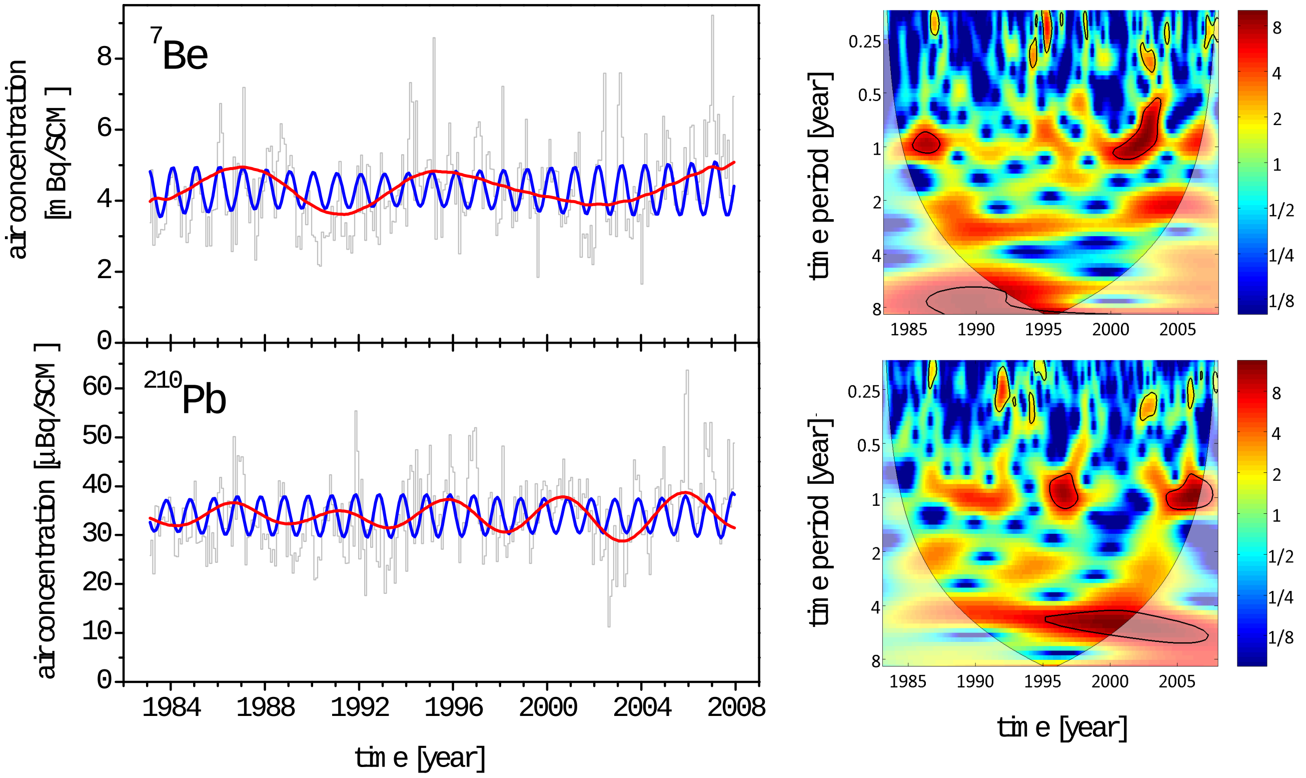

Figure 3.4.: Time series analysis of the Neumayer ^{7}Be (above) and ^{210}Pb (below) records applying two different methods (left: MC-SSA; right: Wavelet Analysis). The left side shows significant results of the Monte-Carlo Singular Spectrum Analysis (MC-SSA) method based on window length of 90 months. The grey curves depict the original data. Blue curves display the significant first plus second EOF components which comprise the seasonal variability. The red curves show the significant third plus forth EOF (multi-annual variability). On the right side, results from a Wavelet Analysis are shown. Wavelet Analysis is based on a Morlet-6 wavelet and the code offered by Grinsted *et al.* [2004]. The black lines border areas of 5% significance (tested against red noise), the light areas denote area where edge effects might distort the analysis. Details on the methods are given in the appendix.

all three types of radionuclides. While ^{210}Pb generally peaks in the austral spring/summer months, there is a clear delay in the cosmogenic radionuclides cycles which peak in austral summer/autumn. Figure 3.5 shows the stacked seasonal cycles of ^{7}Be, ^{210}Pb and ^{10}Be at NM station. Although the data basis of monthly mean ^{10}Be measurements is sparse, it is obvious that the amplitude of the ^{10}Be seasonal cycle (approx. 50%) exceeds those of the short-living radionuclides (22% in case of ^{7}Be and 18% for ^{210}Pb). Measurements at other Antarctic sampling stations confirm that finding although the amplitude and significance of the respectice seasonal cycles vary (see appendix, figure A.1). In general, seasonality is more pronounced in case of inland sites while the amplitude diminishes at coastal stations and vanishs in case of the Antarctic Peninsula region (see figure A.1).

For the interpretation of the seasonal cycles, first and foremost local as well as large-scale transport and deposition processes have to be considered: On the one hand neutron monitor data confirm that there is no seasonality in the cosmogenic production rate (see figure 3.6 in the next section). On the other hand a minor contribution of the ^{222}Rn source to the ^{210}Pb seasonality may be neglected since there is no local source term and southern polar areas 'receive' a mixed signal. Radionuclide-ratios are an important tool for the analysis of the processes driving the seasonal cycles. Assuming comparable local transport and deposition processes, the ratios should be less effected by the local meteorology. Indeed, a relative variability of the monthly time series of ^{7}Be/^{210}Pb is by approx. 40% lower than the value expected from formal error propagation. Having nearly identical sources, the ^{10}Be/^{7}Be ratio allows for a straightforward interpretation: Due to different radioactive lifetimes, the ratio is a proxy of atmospheric residence time (e.g. Raisbeck *et al.* [1981b]). In this regard, a high ^{10}Be/^{7}Be ratio during late austral summer/autumn indicates a stronger influence of stratospheric air masses (see figure 3.5). In contrast, the stratospheric source term of ^{210}Pb is thought to be of minor importance. Even if some measurements as well as atmospheric model calculations point to a significant amount of ^{210}Pb in the lower stratosphere [Moore *et al.*, 1973; Heikkilä *et al.*, 2008b], the contrast between statospheric and tropospheric concentrations is too low to contribute to a annual cycle (even in case of remote areas like the Antarctic). Hence, other processes contribute to the ^{210}Pb seasonality. In fact the boundary layer inversion strength inherent to the structure of the Antarctic atmosphere shows a pronounced seasonal variation closely following the seasonality of sunlight (see appendix, figure A.2). During Antarctic winter, the layering of the atmosphere is stable and boundary layer inversion is well pronounced. Hence, vertical transport of free tropospheric airmass is weaker than during austral summer. This effect might account for the contrast of seasonal cycle amplitude at different sampling sites. A larger influence of synoptic meteorology (as in case of coastal stations) should weaken this transport effect which is in line with the finding of large seasonal cylce amplitudes at inland sites.

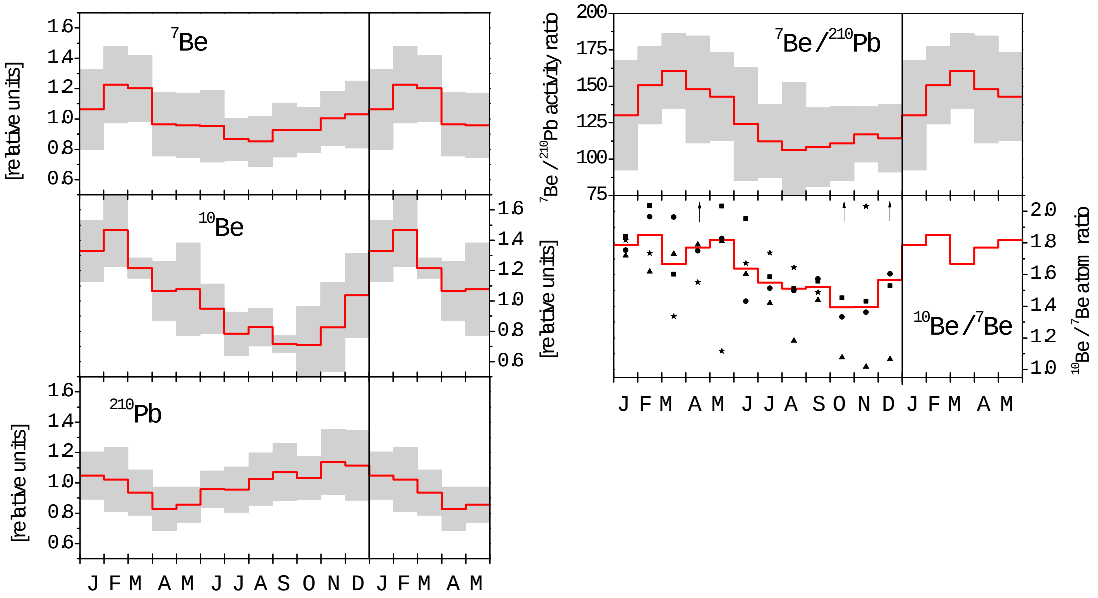

Figure 3.5.: Mean seasonal cycles of the Neumayer radionuclide air concentration measurements. Data refers to stacked monthly means with eliminated multi-annual variability. The grey band denotes the 1σ standard deviation. In case of the ^{10}Be, monthly data relies on four years of measurements: (squares) 1983/1984, (dots) 1984/1985, (triangles) 1985/1986 and (stars) 1990/1991 [Wagenbach *et al.*, 1988; Auer, 1997]. Arrows indicate out of picture data up to 2.8.

Multi-annual variability

Processes which influence the radionuclide air concentration may basically vary on a multi-annual timescale, too. Furthermore, different to the sub-annual variations, production effects have to be taken into account. The decadal signal of ^{7}Be from Singular Spectrum Analysis (together with annual mean values of ^{10}Be and ^{7}Be) is shown in figure 3.6. It is obvious, that the decadal oscillation clearly reflects the production signal driven by the 11years solar cycle (‘Schwabe cycle´). However, the shape of this production signal somewhat differs between the ^{7}Be and ^{10}Be time series. Excluding artefacts of measurements, this divergence may be explained by differences in the source term or transport effects based on the different radioactive lifetimes of both isotopes. Regarding the production of cosmogenic radionuclides, solar energetic particles (SEP) may contribute to the polar production of ^{7}Be while the SEP based production of ^{10}Be is significantly smaller [Webber *et al.*, 2007; Masarik & Beer, 2009]. Indeed, Koch & Mann [1996] interpreted an ambiguous phase-shift of the 11-years signal in the ^{7}Be South Pole measurements as an effect of excess production by solar energetic particles. This SEP flux is restricted to polar areas (due to the low geomagnetic cutoff rigidity) and peaks phase-shifted to the solar cycle. Webber *et al.* [2007] calculated the production of excess ^{7}Be due to outstanding SEP events during the last decades. Years with possible contribution are shown in figure 3.6. Obviously, these single years of enhanced SEP events do not correlate with distinct yearly means of ^{7}Be and a possible contribution of SEP-based ^{7}Be to the Antarctic air concentration can be excluded. This is in accordance to Usoskin *et al.* [2009] who modelled short-term effects of SEP events on the atmospheric concentration of ^{7}Be and find a significant enhancement only in the polar stratosphere. The remaining explanation for the difference in the shape of the ^{7}Be and ^{10}Be decadal oscillation is a transport effect due to the different radioactive half-lifes of both radionuclides.

The 4-6 years oscillation in the ^{210}Pb time series remains unexplained. Time series analysis of several direct meteorological parameters at Neumayer station (R. Weller and G. König-Langlo, pers. comm.) reveals a common variability on the same time scale inherent to the local meteorology (e.g. snow event frequency, de-seasonalized temperature or boundary layer inversion strength, see appendix figure C.1 and). In addition, other studies on different Antarctic measurements report on variability in this frequency range [Jacobs & Mitchell, 1996; Weller *et al.*, 2011]. However, correlation analysis does not reveal a significant covariation of any meteorological parameter with ^{210}Pb. The most obvious correlation exist between ^{210}Pb and the Antarctic oscillation index (AAO or Southern Annular Mode - SAM), see figures A.3 and C.2 (appendix). This relation suggests a climate/meteorological induced modulation of the ^{210}Pb signal. Eventually, it remains ambiguous if this modulation occurs on the local or global scale.

3.2.3. Temporal and spatial variability in firn and snow: ^{10}Be measurements in Antarctic traverses and shallow firn cores

In recent decades ^{10}Be has emerged to be routinely measured in deep ice-core studies (see section 2.4.2). Nonetheless, deep ice-core drilling sites remain being scarce and therefore sample only a minor part of polar climate regimes. Following Stanzick [2001] who demonstrated the usefulness of ^{10}Be measurements within traverses on the Greenland ice shelf (see section 3.3.2) some pilot surveys in the Antarctic were accomplished by the IUP Heidelberg ice and climate group in cooperation with the Alfred-Wegener Institute (AWI) during the last decade (see figure 3.7, EPICA traverses). Finally, in 2006, the AWI performed a 280km long traverse upstream from Kohnen Station (EDML drilling site) ranging in altitude from 2890m to 3300m a.s.l. (see figure 3.7). In 2007/2008 a Japanese-Swedish expedition (JASE) augmented this survey up to Dome F station. Within the present work, a total of 24 snow pit samples of both traverses could be analyzed for mean ^{10}Be concentration. In the following, the results are presented and compared with firn-core measurements of the IUP Heidelberg ice and climate group and the existing literature data of mean ^{10}Be

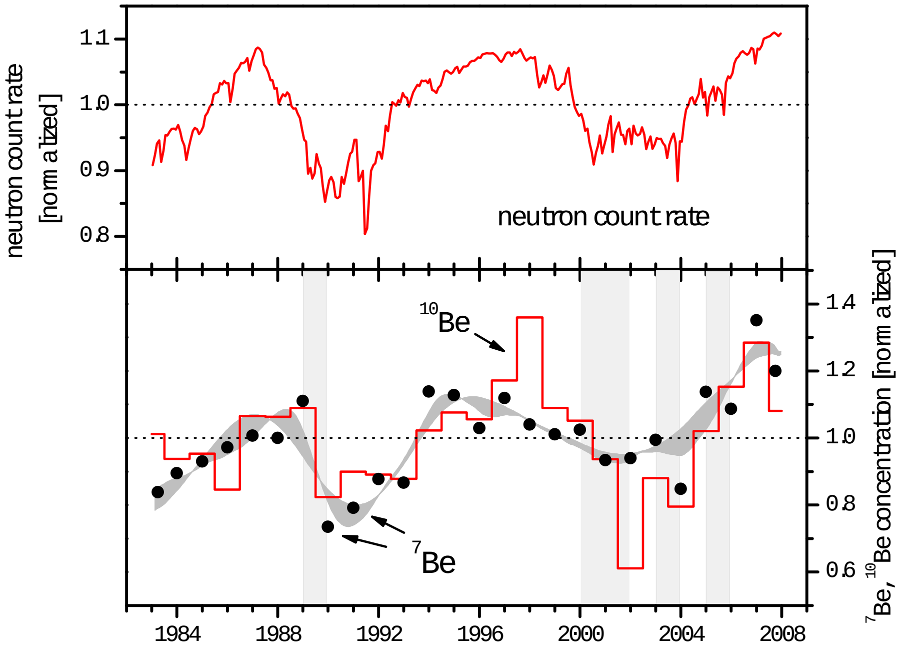

Figure 3.6.: Long-term signal in the ^{7}Be and ^{10}Be air concentration at Neumayer station (lower layer) compared to the neutron count rate from Antarctic McMurdo station [Bartol-Research-Institute, 2010] (upper layer). Dots illustrate the ^{7}Be yearly mean concentration and the grey shaded curve denotes the results from time series analysis (SSA using different parameters, see appendix). The red curve are yearly mean values of the ^{10}Be concentration. Grey shaded bars give years where solar energetic particles might have contributed to a ^{7}Be production rate according to Webber *et al.* [2007].

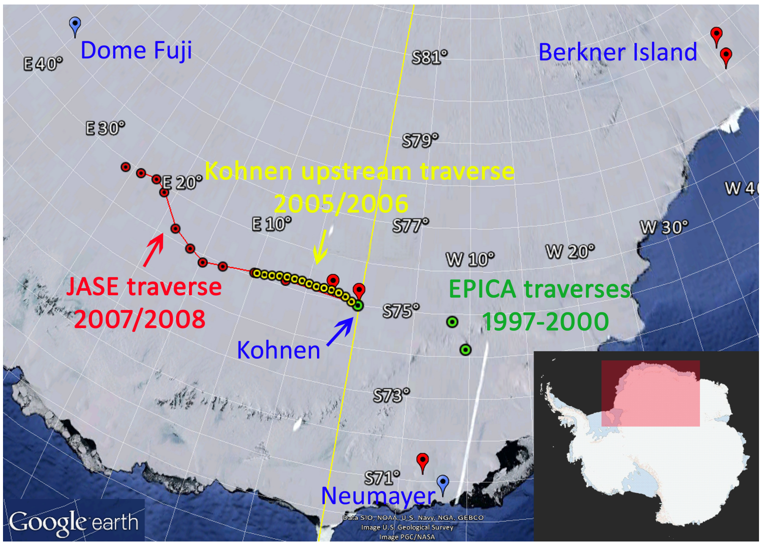

Figure 3.7.: Map of firn and ice sampling sites for IUP ^{10}Be measurements in Antarctica. Colours show different sampling surveys, red drops denote firn coring sites.

ice concentration. In doing so, a comprehensive picture of spatial ^{10}Be variability in the Antarctic firn is given.

The Kohnen upstream and JASE traverses

In the framework of the Kohnen upstream traverse, 15 snow pits of approximately 2 m depth were sampled by the Alfred-Wegener Institut and sent to the IUP Heidelberg laboratory for ^{10}Be measurements. Dating of the cores and analysis of mean accumulation rates was performed by H. Oerter (AWI) using δ^{18}O measurements [Oerter *et al.*, 2008]. It was found, that the oldest snowpits cover a time period of 1991-2006 (higher elevation, less accumulation sites), while younger ones represent 1994-2006 (lower elevation, enhanced accumulation sites). Measurements of ^{10}Be were performed on an integral sample of each site covering the upper part (ranging from (0-1.3) m to (0-2.1) m) of each snow pit (see appendix for details on the measurement procedure). Taking into account a decreasing snow accumulation rate along the traverse, the length of the integral snow pit sample was reduced from 210cm at Kohnen station to 130cm at the endpoint of the traverse. However, it was not accomplished that all integral snow pit samples cover the same period of time but differ between 1991-2006 and 1995-2006. In case of the highest sampling sites, additional measurements on the lower part of the snow pit (1.3m-1.7m and 1.4m-1.8m, respectively) have been performed.

The Japanese-Swedish expedition (JASE) in 2007/2008 performed a traverse from coastal Wasa Station to Dome Fuji (3810m a.s.l.) and Syowa Station, subsequently. It was pos-

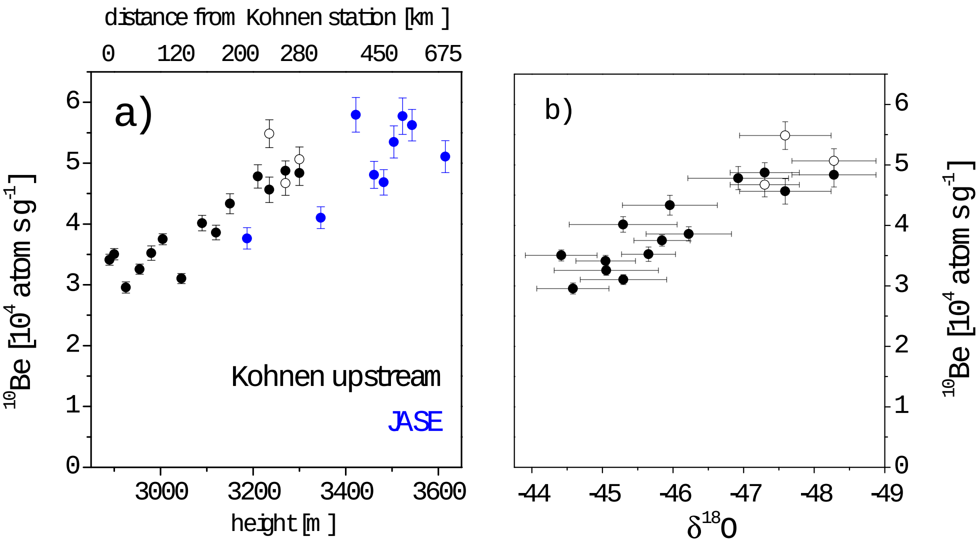

Figure 3.8.: ^{10}Be firn concentration measurements of samples from the Antarctic Kohnen station upstream traverse and JASE traverse and correlation to respective δ^{18}O measurements. Open circles denote measurements in a lower part of the respective snow pit (see text for details). Mean δ^{18}O values are based on yearly means of Oerter *et al.* [2008].

sible to receive integral snow samples from nine different sites which extend the Kohnen upstream samples towards the plateau (300m higher than the last sampling site of the Kohnen upstream traverse, M. Hansson pers. comm.). The samples were manually mixed and an aliquot was taken for ^{10}Be analysis. A detailed information on the time coverage of the sample could not be obtained. However, given a crude estimation of the accumulation rate and the fact, that the snow pits depths are about 2 m, time coverage is broadly comparable to the Kohnen upstream samples. Figure 3.8 gives the results from the ^{10}Be measurements as a function of sampling altitude (a) as well as the correlation with mean δ^{18}O values (b). The results reveal a clear upstream effect with mean ^{10}Be concentration increasing with height. Correlation with δ^{18}O values or accumulation rates (derived from annual layer thickness, [Oerter *et al.*, 2008]) indicates, that changes in the mean accumulation rate are the main driver of this effect. The measurements as a function of accumulation rate is given in figure 3.9 together with literature data and firn-core measurements performed at the IUP in previous studies.

Firn core measurements

IUP high-resolution measurements of ^{10}Be in shallow firn cores comprise seven different Antarctic cores from different polar climate regimes ranging from high-accumulation sites (Neumayer Hinterland) to the dry Antarctic plateau (Kohnen Station) (M. Huke, unpublished,Wegner [2003]; Rohlfs [2004]; Offermann [2006]; Elsässer [2008]). Four of these cores have a time-resolution higher than 2.5 years and cover the observations period and two cover several hundred years (with a lower resolution). In summary, in case of high resolution measurements, variations of the ^{10}Be concentration basically lie within the 30% range. It is obvious, that the ^{10}Be variations do not consistently covariate with the solar activity production signal. On the other hand, lower-resolution measurements which cover periods of obvious low solar activity (like the Maunder Minimum) clearly show a long-term trend similiar to the production signal. Eventually, the ^{10}Be amplitudes of the overall production signal during periods of exceptional low solar activity do not exceed 40% and are thus slightly lower than the atmospheric seasonal cycle of ^{10}Be.

Ice core measurements

In comparing mean ^{10}Be concentrations from different studies one has to take into account that measurements cover different periods of time and are normalized to different AMS standards. For a quantification of the former, ^{14}C-based solar activity reconstructions (see section 5.3.3) as well as the production rate calculations of Kovaltsov & Usoskin [2010] can be used to assess the effect of time-varying production rates. In doing so, all ^{10}Be time series are corrected to a reference period (1950-2000) which results in correction factors ranging from -4% to 7%. Aiming to correct the effect of different AMS standards used by various laboratories all ^{10}Be measurements are recalibrated using the study of Nishiizumi *et al.* [2007] and Kubik & Christl [2010] (see section 2.5). This correction imposes a further factor of -11% - 4%. In some cases, it is not possible to reconstruct the used standard. These values are disregarded in the final comparison.

Figure 3.9 shows the compilation of literature data together with the IUP firn core results and the results of traverse measurements presented within this thesis. At first, mean Antarctic ice/firn concentration of ^{10}Be ranges over a factor >8 with lowest levels in case of high-accumulation areas and highest values on the dry plateau. Mean ^{10}Be ice-concentrations show a remarkable inverse relation to the accumulation rate. The results of section 3.2.1 indicate that differences in the ^{10}Be air concentrations do not explain this finding since these values are broadly similar over the Antarctic continent. In fact different mechanisms of aerosol air-firn transfer hold for the huge deviation and will be investigated in section 3.3 in context of a simple model approach.

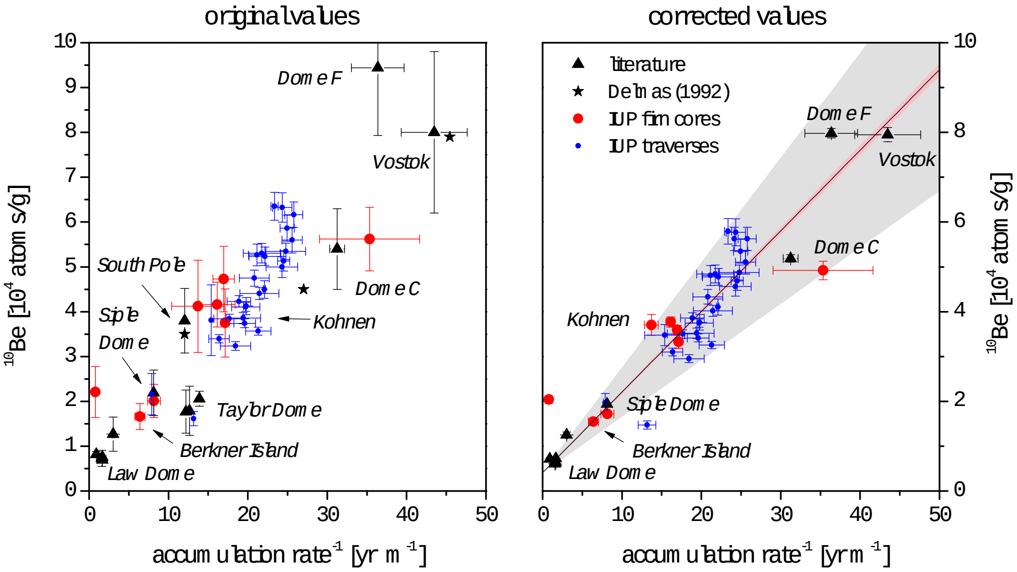

Figure 3.9.: Comparison of mean ^{10}Be ice concentrations in Antarctica and the relation to the respective accumulation rate. In the right picture, the straight line denotes a linear fit to the data and the red shaded area depicts the formal fitting error. Grey shaded area is based on 30% higher and lower slope and covers all data points (except some outliers: 4.5%; 11.4% disregarding error bars). Left picture shows original measurement values uncorrected for different AMS standards and covered time periods. Error bars in the left picture denote 1σ standard deviations of respective time series. Data: Raisbeck *et al.* [1990]; Delmas [1992]; Steig [1996]; Steig *et al.* [1998]; Aldahan *et al.* [1998]; Steig *et al.* [2000]; Smith *et al.* [2000]; Wegner [2003]; Rohlfs [2004]; Offermann [2006]; Nishiizumi & Finkel [2007]; Horiuchi *et al.* [2008]; Elsässer [2008]; Baroni *et al.* [2011]; Pedro [2012]; Wagenbach [2012]. Further accumulation rate data:Taylor *et al.* [2004]; Rotschky *et al.* [2007]; Oerter *et al.* [2008, 2011].

3.3. The radionuclides ^{7}Be, ^{210}Pb and ^{10}Be in Greenland

3.3.1. Glacio-meteorological situation in the Arctic

The Arctic and Antarctic show lots of analogies and remarkable differences. For the interpretation of ice coring sites, first and foremost the glacio-meteorological setting of the Greenland Ice Sheet is a matter of concern. However, different to the Antarctic, the Ice Sheet covers a lesser part of the polar area. Thus, consideration of residual polar zones is necessary for a discussion on meteorology and related atmospheric transport. Classifying different Arctic climate regimes, Serreze & Barry [2005] give (i) the Greenland Ice Sheet, (ii) polar desert, (iii) maritime arctic and (iv) the central Arctic ocean. Atmospheric transport is dominated by a polar vortex in the stratosphere and troposphere and three "centers of action" in the wintertime surface circulation: "(1) the Siberian High over east-central Asia; (2) the Icelandic Low off the southeast coast of Greenland; (3) the Aleutian Low in the North Pacific basin" [Serreze & Barry, 2005]. Precipitation is generally low in the Arctic compared to mid-latitudes (see figure 4.7 in section 4.4). However spatial variability is large with annual precipitation rates broadly ranging from 200mm per year over the Canadian Arctic Archipelago and Beauford Sea to more than 1000mm over the Atlantic southeast of Greenland [Serreze & Barry, 2005]. For Greenland main features are "very low accumulation (100m) over the northern portions of the island with highest values along the southeast coast" [Serreze & Barry [2005] and references therein]. In the latter area, (orographic) uplift of moist air can result in precipitation rates >2000 mm per year (see Bromwich *et al.* [1993] for respective map). Low-level temperature inversions which "represent(s) strong vertical stability" are a persistent feature of the Arctic and "are most strongly expressed during the winter season" [Serreze & Barry, 2005]. In comparison to the Antarctic, the ice-sheet is significantly lower having the two elevation maxima: Summit (3208m) and a secondary maximum in the south of the ice sheet (2800m). This results in a lower contrast in different mean accumulation rates which is an important feature in regard to the interpretation of aerosol-bound radionuclides.

3.3.2. Temporal and spatial variability in boundary-layer air

In accordance with the Antarctic data basis, the overwhelming part of ^{7}Be and ^{210}Pb air concentration measurements in the Arctic is restricted to accessible areas in coastal regions. Time series emerging from nuclear monitoring exist in case of coastal Greenland (Thule, Greenland Nord, Constable Point and Kap Topin [EML-SASP, 2010]) and the northern coast of Alaska (Barrow [EML-SASP, 2010]). These data sets are augmented by scientific studies at Spitzbergen [Myslek-Laurikainen *et al.*, 2006; Paatero *et al.*, 2010] and the Greenland Ice Sheet (Dye3 [Dibb & Jaffrezo, 1993] and Summit [Stanzick, 2001;

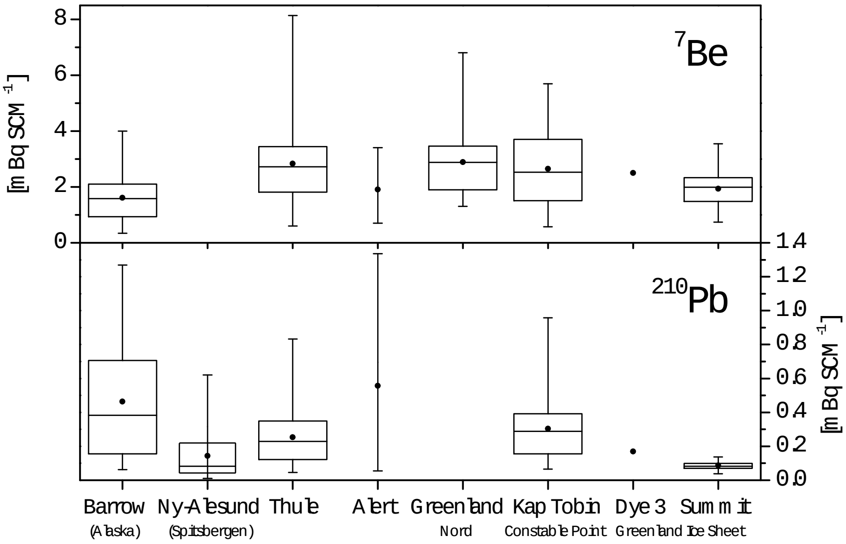

Figure 3.10.: Mean atmospheric activity concentrations of ^{7}Be and ^{210}Pb in Arctic (boundary layer) air. The boxes depict 25% and 75% percentiles and whiskers (vertical bars) are the respective maximum and minimum value of the monthly mean data. Data: Barrow, Thule, Kap Tobin/Constable Point, Greenland Nord - EML-SASP [2010]; Ny-Alesund - Paatero *et al.* [2010]; Alert - Dibb *et al.* [1994]; Dye 3 - Dibb & Jaffrezo [1993]; Summit - Dibb [2007].

Dibb, 2007, 2012]). Figure 3.10 shows the compilation of statistics on these data sets. In short, mean ^{7}Be values differ by up to a factor of 1.8. There is a wider range in ^{210}Pb concentrations with concentrations decreasing with increasing height. Note that the measurements at Ny-Alesund are performed at Mt. Zeppelin (474m a.s.l.), Dye3 and Summit have elevations of 2480m and 3220m, respectively. However, interpretation of yearly mean values should not be overrated, since all time series exhibit strong seasonal cycles with minimum-maximum ratios up to a factor >15 (^{210}Pb at Alert see figure 3.11). While seasonal cycles of both, ^{7}Be and ^{210}Pb generally coincide at single measurement sites, there is a clear difference between seasonal cycles of the Arctic basin (coastal Greenland including Barrow and Spitzbergen) and the Greenland Ice sheet (Summit and Dye 3) with respect of both radionuclides [Dibb & Jaffrezo, 1993; Dibb, 2007]. It is hence reasonable, to separate the following discussion on the different seasonalities.

The Arctic basin

In case of the Arctic basin, radionuclides show a distinct seasonal cycle with a clear minimum in Arctic summer and a broad maximum from autumn to spring (see figure 3.11).

Feely *et al.* [1989] as well as Dibb *et al.* [1994] and Paatero *et al.* [2010] agree that there is an analogy to the Arctic Haze phenomenon, i.e. accumulation of pollutants like sulfate in the wintertime Arctic boundary layer. As discussed in Stohl [2006], the details of the main drivers of this phenomenon remain controversial and two different types of explanations are given: On the one hand, studies propose an enhanced transport of pollutants from the mid-latitudes. For example, Rahn & McCaffrey [1980] report on enhanced concentration of ^{222}Rn and pollution emissions (both having mid-latitudinal origin) and propose a simple transport model based on a shift of the polar front. On the other hand studies give enhanced aerosol lifetime as a main reason for the Arctic Haze phenomenon. In this regard, Shaw [1995] gives a "suppression of the atmosphere‘s removal machinery" composed of a stabilized atmosphere due to temperature inversions, reduced removal caused by low water vapor pressure and general indifferent atmospheric dynamics as the main reasons. This is in line with measurements of ^{210}Pb at Barrow which exceed mid-latitudinal concentrations (e.g. New York) in winter [Rahn & McCaffrey, 1980] despite a suppressed high-latitudinal ^{222}Rn source. Recently, a model study by Stohl [2006] finds that "inefficient removal processes are certainly important" but a more permeable transport barrier between mid-latitudes and the polar dome would alone cause a winter-peak of pollution levels.

The Greenland ice sheet

Seasonal cycles of ^{210}Pb and ^{7}Be on the Greenland ice sheet measured at Summit [Stanzick [2001]; Dibb [2007]; J. Dibb, pers. comm.] and Dye 3 [Dibb & Jaffrezo, 1993] clearly deviate from the Arctic basin time series. Long-standing year-round sampling campaigns show a weaker seasonal cycle with a summer maximum in case of Summit station [Dibb, 2007] and a single-year measurement at Dye3 shows two maxima in spring and late summer /autumn [Dibb *et al.*, 1994]. This led Dibb & Jaffrezo [1993] and Dibb [2007] to the conclusion that the Arctic Haze phenomenon does not influence airmasses over the Greenland ice sheet and that the ice sheet boundary layer seems to be isolated from the Arctic basin. Moreover, the covariance of ^{7}Be and ^{210}Pb concentrations led them suggest that boundary layer dynamics are the "dominant control on activities in air just above the ice sheet". Different to the Arctic basin, the seasonal cycle of the two sites, Dye 3 and Summit differ (in case of both radionuclides). Measurements of ^{10}Be / ^{7}Be ratios at Alert and Summit may give additional information on the differences between basin and ice sheet. While Dibb *et al.* [1994] report on a basically constant ^{10}Be/^{7}Be ratio of 2.2 (with a small July/August peak of 3) at Alert, the ratio at Summit shows a clear seasonal cycle with a lower ^{10}Be/^{7}Be ratio during most of the year and a peak of 2.5 in early summer [Stanzick, 2001] (see also figure 4.17 in section 4.5.3). These differences support the interpretation of different airmass history on the Greenland Ice Sheet and the residuary Arctic basin, since the ^{10}Be/^{7}Be ratio is a

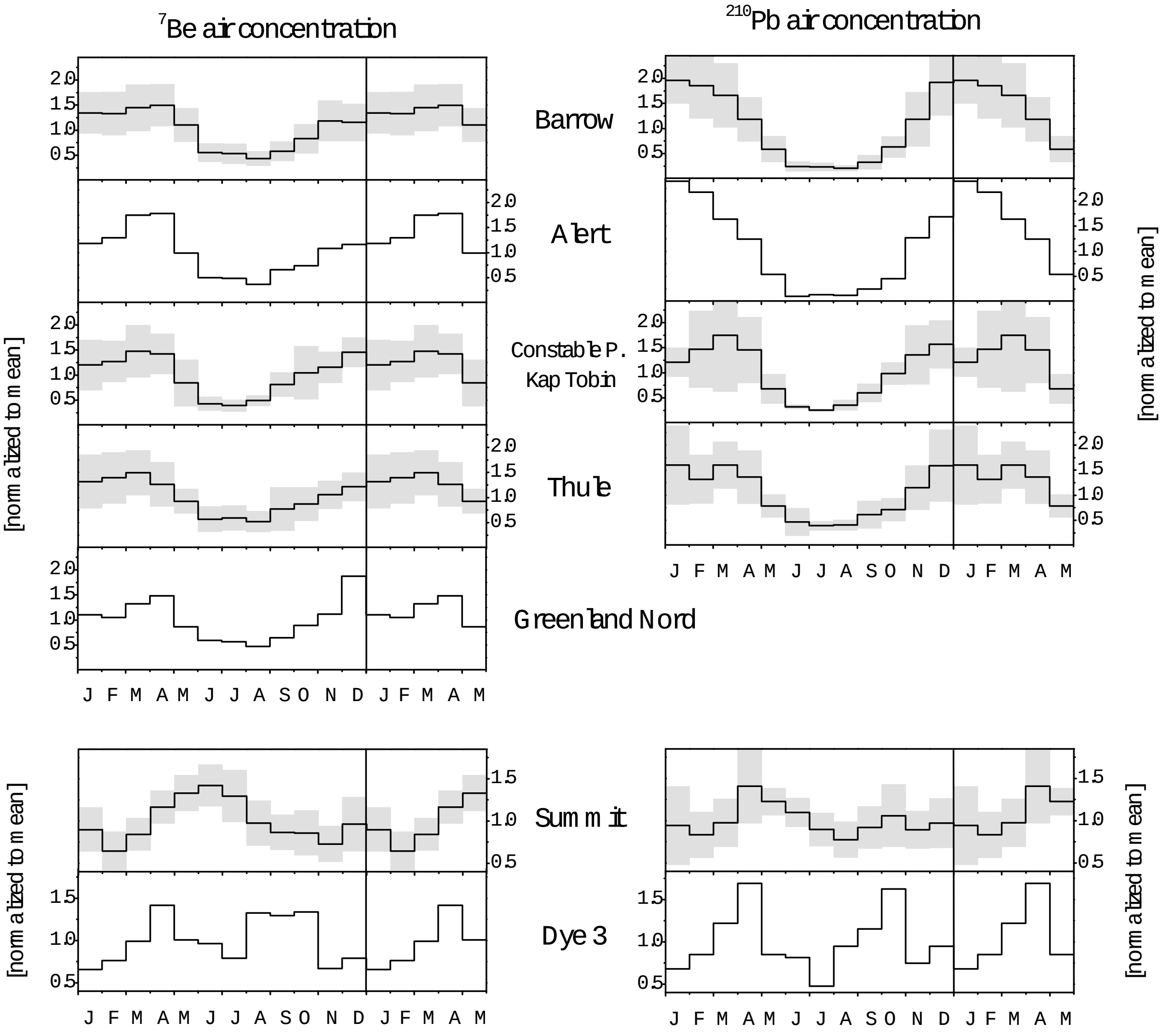

Figure 3.11.: Seasonal cycles of normalized ^{7}Be and ^{210}Pb atmospheric activity concentration in the Arctic basin (Barrow, Alert, Kap Tobin, Thule, Greenland Nord) and on the Greenland Ice Sheet (Summit, Dye 3). Grey areas denote 1σ standard deviation of multi-annual variations. Data without error bars represent measurements from a single year. Note the different scaling in case of basin and ice sheet. Data: [EML-SASP, 2010; Dibb & Jaffrezo, 1993; Dibb *et al.*, 1994; Dibb, 2007].

proxy for atmospheric residence times of the radionuclides.

3.3.3. ^{10}Be measurements in Greenland firn and ice

To complete the picture, measurements of ^{10}Be in Greenland firn and ice are shortly summarized. Here, the most comprehensive data set comprises the measurements by Stanzick [1996, 2001] in the framework of two Greenland traverses including 17 firn and 7 ice cores. Figure 3.12 shows the results o these measurements completed with more recent literature data (corrected for different ^{10}Be calibration standards, see section 3.2.3). Following Stanzick [2001], his measurement results are separated into two different time periods: Pre-industrial (1861-1928) and observational (1950-1995) period. This is reasonable since an obvious trend in the Greenland ^{10}Be time series during the last century is not attributed to a first-order production effect [Stanzick, 2001]. Differences in ^{10}Be measurements which cover different periods of time can thus not be corrected using ^{14}C-based production estimations (as done in case of the Antarctic, see figure 3.9). Note that the Antarctic data was corrected to the reference period 1950-2000 which is actually the time coverage of data shown in figure 3.12 (left). Figure 3.12 shows, that the mean ^{10}Be ice concentrations in Greenland are clearly related to the inverse accumulation rate as in case of the Antarctic measurements. However, the linear function is quite different from the Antarctic results (shown as dashed line in figure 3.12). In case of pre-industrial values, the data-basis is less profound and the difference between Greenland and Antarctic accumulation rate relation is less distinct.

3.4. The basic air-firn-transfer model

The transfer of air-borne aerosol into firn is a complex process which hampers a direct interpretation of ice-core records. While differences in, for example, the composition of aerosol in Arctic snow and air have been found decades ago [Rahn & McCaffrey, 1979], most studies on ice-core ^{10}Be still lack from a proper consideration of air-firn transfer effects. Different processes which deliver the atmospheric ^{10}Be into polar firn result in a complicated dependence on different parameters within wet and dry deposition (see section 2.2 for details). Certainly, a detailed study of the processes involved (see e.g. Slinn [1977]) is clearly beyond the scope of this work. Instead the results of sections 3.2 and 3.3 are used to estimate the parameters of a basic air-firn-transfer model. Related depictions can be found in Fischer [1997] and Stanzick [2001].

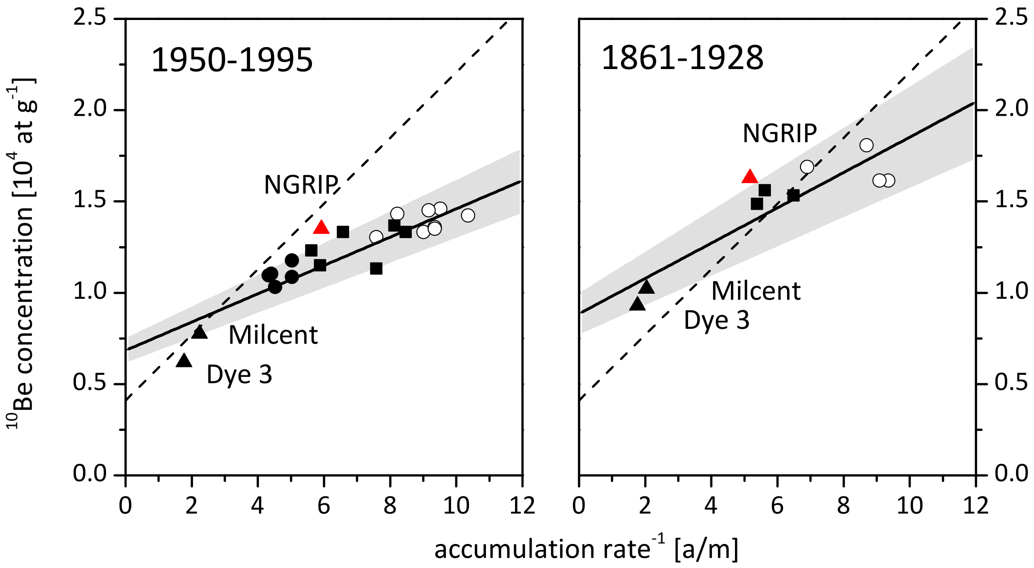

Figure 3.12.: Mean ^{10}Be firn/ice concentrations in Greenland compared to the respective accumulation rate. The data is based on Stanzick [2001] but recalibrated to Nishiizumi *et al.* [2007]. Further literature data is shown in red [Berggren *et al.*, 2009]. The lines indicate (i) the original fit to the Greenland data from Stanzick [2001] (solid line) and, (ii) for comparison, the fit of the Antarctic data shown in figure 3.9 (dashed lined). Values referring to Dye 3 and Milcent sampling sites have been extrapolated by Stanzick [2001] to the period under investigation.

The basic air-firn-transfer model

The most direct way of expressing ^{10}Be ice concentration as a function of air concentration is using deposition fluxes and deposition velocities (e.g. Alley *et al.* [1995]; Fischer [1997]). Following section 2.2 the ^{10}Be deposition flux at a certain sampling site can be separated into a so called wet and a dry fraction:

$$J_{tot} = J_{dry} + J_{wet} = v_{dry} \cdot c_{air} + c_{snow} \cdot P \tag{3.1}$$

J: Deposition flux
c: Concentration in air and firn, respectively
P: Precipitation rate
$\mathrm{v_{dry}}$: Dry deposition velocity

The particle concentration of fresh snow can be substituted by using the scavenging ratio ($\epsilon = c_{snow}/c_{air}$) which indicates the efficiency of aerosol removal by precipitation. Assuming that the air concentration which determines the fluxes is identical in both cases (dry and wet deposition), the total deposition flux may be expressed as a linear function of ^{10}Be air concentration as follows

$$J_{tot} = (v_{dry} + \epsilon \cdot P) \cdot c_{air} \tag{3.2}$$

Since fluxes are not measured directly, the firn concentration is calculated from total flux by using the net accumulation rate ($\mathrm{A_{net}}$) over a defined time interval (Δt) using equation 3.2. Note that the dry deposition velocity may be assumed as being constant in first-order.

$$c_{firn}^{\Delta t} = \frac{\int_{t_0}^{t_0+\Delta t} J_{tot}(t)dt}{\int_{t_0}^{t_0+\Delta t} A_{net}(t)dt} = \frac{\int_{t_0}^{t_0+\Delta t}[(v_{dry} + \epsilon(t) \cdot P(t)) \cdot c_{air}(t)]dt}{\int_{t_0}^{t_0+\Delta t} A_{net}(t)dt} \tag{3.3}$$

There is no hope to quantify the specific time behaviour of all parameters by measurements. In fact, the focus of this study is to identify first-order processes which govern the relation between concentration in firn and air. To this end, all parameters except the well-known radionuclide air concentration may assumed to be constant in a certain time period under investigation. In doing so, the respective parameters become 'climatologically' averaged terms (depicted with a vertical bar). This first-order approximation estimates equation 3.3 to

$$\bar{c}_{firn} \approx \left(\frac{\bar{v}_{dry} + \bar{\epsilon} \cdot \bar{P}}{\bar{A}_{net}} \right) \cdot \bar{c}_{air} \tag{3.4}$$

Results from measurements in air and firn clearly indicate, that ^{10}Be firn concentration shows large variations over different polar climate regimes (up to a factor 8 in Antarctica, see sections 3.2.3 and 3.3.3) while the respective air concentrations are subject to small deviations, if any (see sections 3.2.2 and 3.3.2). Hence, spatial variability of firn concentration may be investigated by using equation 3.4 - denoted as a function of x

$$\bar{c}_{firn}(x) \approx f(x) \cdot \bar{c}_{air} = \left(\frac{\bar{v}_{dry}(x) + \bar{\epsilon}(x) \cdot \bar{A}(x)}{\bar{A}_{net}(x)} \right) \cdot \bar{c}_{air} \tag{3.5}$$

The relation between net and gross accumulation depends on common wind drift and evapo-sublimation. In case of the Greenland Ice Sheet, modelled precipitation maps (gross accumulation) encompass the general features of net accumulation (Serreze & Barry [2005] and references therein) and in case of the Antarctic continental interior, "net snow accumulation closely approximates precipitation" [Bromwich, 1988]. Hence, a linear relation $A_{net}(t) = \alpha(x,t) A_{gross}(t)$ may be a good approximation. The parameter α might show some spatial variations and certainly varies on a seasonal scale. However, following previous assumptions a mean value is assumed. Figures 3.9 and 3.12 indicate, that these assumptions are reasonable, since the ^{10}Be mean firn concentrations at different sites indeed show a remarkable inverse relation to the respective mean net accumulation rate ($\bar{A}_{net}$). This finding indicates, that spatial variations in dry deposition, scavenging or the ratio between net and gross accumulation are less distinct leading to the following approximation

$$\bar{c}_{firn}(x) \approx \left(\frac{\bar{v}_{dry}}{\bar{A}_{net}(x)} + \bar{\alpha} \cdot \epsilon \right) \cdot \bar{c}_{air} \tag{3.6}$$

Indeed the other parameters, especially the scavenging ratio may be correlated to or driven by the net accumulation rate and it can not be excluded that several spatial effects might cancel each other out. Certainly, possible influences do not alter the overall high correlation of mean ^{10}Be concentration with mean (inverse) accumulation rate and are most likely no first-order effects. In this regard, the main parameter which governs spatial variability in mean ^{10}Be firn concentration is the net accumulation rate. Using the linear correlation of the inverse net accumulation rate with the mean ^{10}Be firn concentration shown in figures 3.9 and 3.12 as well as equation 3.6, climatological mean parameters of the model can be

Table 3.1.: Results of air-firn transfer model. Data: Greenland - [Stanzick, 2001], Antarctica - this study. Dry deposition velocity and scavenging ratio rely on the respective mean ^{10}Be air concentration and errors include the seasonal cycle standard deviation. These latter calculations assume a constant air concentration over the entire Ice Sheet. Hence, the results depict an assessment only.

	J_{dry} [10^4 at cm^{-2} yr^{-1}]	c_{snow} [10^4 at g^{-1}]	v_{dry} [cm s^{-1}]	ϵ [10^5]
Greenland 1950-1995	8.5 ± 1.0	0.75 ± 0.07	0.1 ± 0.05	(2.8 ± 1.4)
Greenland 1861-1921	10.6 ± 1.8	0.97 ± 0.12	0.12 ± 0.06	(3.6 ± 1.8)
Antarctica this study	17.98 ± 0.24	0.41 ± 0.01	0.12 ± 0.03	(0.9 ± 0.2)
Antarctica [Delaygue & Bard, 2011]	20.5 ± 1.6			

estimated if mean air concentrations are known. Results are given in table 3.1

In summary, a basic model which quantitatively transfers ^{10}Be air concentration into ice concentration may be based on three main parameters: (i) The net accumulation rate, (ii) the dry deposition velocity and (iii) the scavenging ratio (including differences in net and gross accumulation rates). Using spatial correlation of mean firn concentrations as well as mean accumulation rates and a constant air concentration, climatological average parameters of this model can be estimated.

Consideration of seasonal cycles

Indeed the assumption that the parameters of equation 3.3 are constant in time is a rough oversimplification which is refused by a closer look at the Antarctic meteorology. As a matter of fact seasonality is a prominent feature of the polar areas where the contrast in summer and winter insulation is at maximum. Therefore, a seasonal cycle is often the most significant signal in meteorological parameters superimposing any multi-annual variability (e.g. Weller *et al.* [2011], see also supplementary material of Elsässer *et al.* [2011]). Ice-core records do in most cases not exceed annual resolution and hence seasonal cycles of e.g. the air concentration do not directly influence the ice concentration measurements. Admittedly, different phase lags and amplitudes of the parameters in equation 3.3 may indeed impress an indirect ('interference') effect on the resulting firn concentration. Using their mean values (given in table 3.1) it is possible to give a formal solution of equation 3.3 and to investigate the influence of different seasonal cycles involved.

In fact, the determination of seasonalities of polar precipitation or the scavenging ratio is difficult. Measurements of precipitation rates in polar areas are challenging or even

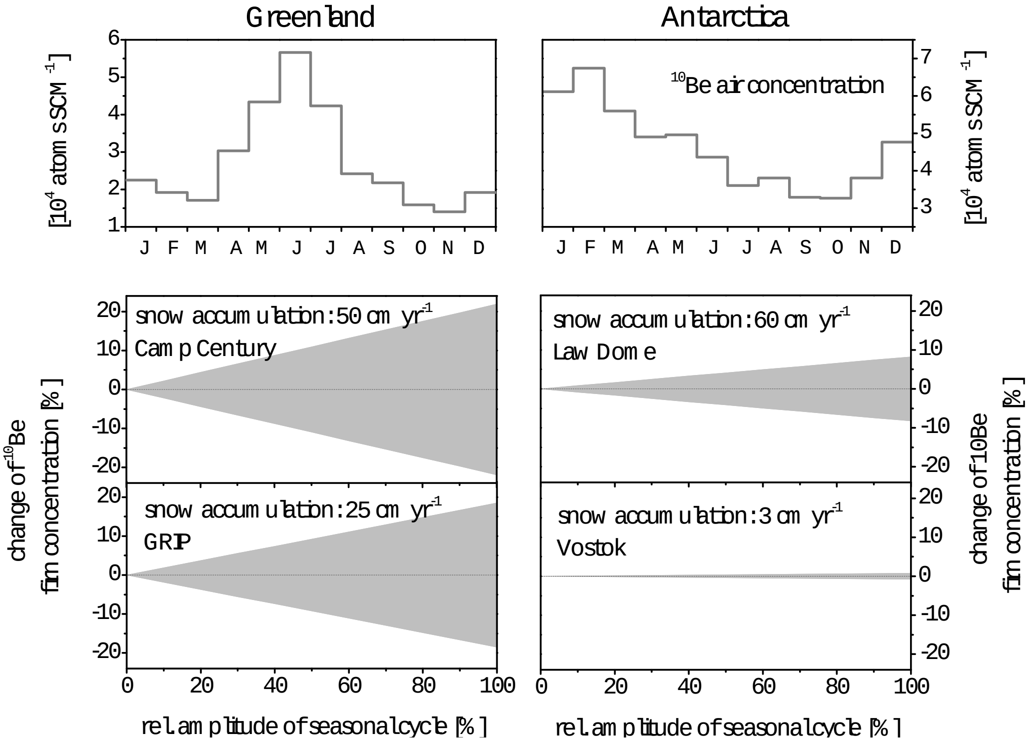

Figure 3.13.: Effect on seasonal variation of air-firn transfer parameters on the (yearly) mean ^{10}Be firn concentration for different ice coring sites (mid and lower layers). Calculations are the numerical solution of equation 3.3 applying measured seasonal variation of the ^{10}Be air concentration (shown in upper layers) as well as sine-type seasonal cycles of the precipitation and scavenging product $P(t) \cdot \epsilon(t)$. Mean values for v_{dry} and ϵ are taken from table 3.1. Mean snow accumulation rates for different sampling sites are denoted in the figure. See text for details.

unfeasible with snow drift precluding the application of snow stakes or collectors. Thus, the estimation mostly relies on (low resolution) snow pit or ice core studies which give the net accumulation rate. The application of automatic weather stations on the Greenland Ice Sheet revealed an obvious annual cycle in wind speed with an amplitude of some 30% [Steffen & Box, 2001] and seasonality of temperature is a persistent feature of the polar boundary layer air [König-Langlo *et al.*, 1998; King & Turner, 1997]. Eventually, while it is likely that ϵ is related to meteorology, a quantitative correlation remains unknown. Thus, different scenarios on the phase and amplitude of the $P(t) \cdot \epsilon(t)$ seasonal cylce are used in the following. Wagenbach *et al.* [2012] estimate the effect of interference between δ^{18}O signals and net accumulation in case of Alpine ice drilling sites (with dominating wet deposition). They applied harmonic cycles for both, variations in the atmospheric signal as well as the accumulation rate which allows for an analytical solution. Here, the atmospheric signal of ^{10}Be air concentration is known from measurements (see figure 3.13 upper layers) and harmonic variations are assumed for the sum of precipitation and the scavenging ratio (see equation 3.3), only:

$$P(t) \cdot \epsilon(t) = P_0 \cdot \epsilon_0(1 + a \cdot sin(t + \psi)) \tag{3.7}$$

P_0: Mean precipitation rate
ϵ_0: Mean scavenging ratio, i.e. mean ratio of ^{10}Be snow and air concentration
a: Relative amplitude
ψ: phase

This practice prohibits an analytical solution and demands for a numerical calculation. Figure 3.13 shows the results of a numerical evaluation of equation 3.3 using the basic parameters of table 3.1 as well as the measured seasonal cycle of atmospheric ^{10}Be (upper layers) and a sine-type seasonality of $P(t)\epsilon(t)$ (as noted in equation 3.7). The mid and lower layers of the figure depict the effect of seasonal cycles on the mean ^{10}Be firn concentration as a function of the relative amplitude (a) of equation 3.7. Maximum effects from different phases ψ (actually the phase difference between c_{air} and $P \cdot \epsilon$ seasonality) applied in the calculation boarder the grey areas. The four mid and lower figures differ in mean accumulation rates representative for different ice core drilling sites and basically border the full range of ice sheet accumulation rates. The results show, that the effect is largest in case of Greenland and diminishes at Antarctic low accumulation sites. In case of the former, the modulation of the firn concentration is restricted to <10% in case of <50% seasonal cycle amplitudes. A major shift to an inversely phased seasonal cycle as well as a major variation of the relative amplitude could basically induce a significant change in the Greenland mean ^{10}Be firn concentration (>10%). However, even in case of major climate change events this worst case scenario is unlikely.

3.5. Summary

The application of ^{10}Be ice core measurements as a proxy for climate parameters or the cosmogenic production rate requires the proper understanding of its geochemical behaviour in polar latitudes. Indeed, model studies of global ^{10}Be using earth system models still do not capture the basic features of polar ^{10}Be. For example, Heikkilä & Smith [2012] report on modeled results using the ECHAM5-HAM global circulation model and give air concentrations which undershoot polar measurements up to a factor 10. Obviously, remote areas like polar latitudes (and especially the ice sheets) are not comparable to moderate latitudes with respect to the data basis of both, meteorological observations and radionuclide measurements. A detailed investigation of the polar radionuclides' climatology can thus significantly support model attempts. In this chapter, measurements of ^{7}Be, ^{210}Pb and ^{10}Be in polar air and ice were compiled to interpret their polar climatology. Basically, findings can be summarized as follows

1. **Air concentrations**
   Results from long-standing monitoring showed that polar air concentrations are representative for a large spatial scale including a wide range of glacio-meteorological settings. Evidence is provided in the Arctic, where seasonal cycles of ^{7}Be and ^{210}Pb show a remarkable resemblance over the whole Arctic basin as well as in the Antarctic, where mean values (and partly seasonal cycles) of coastal areas and the high plateau coincide. On the other hand, there are climatological/meteorological boundaries which separate regions of different radionuclide concentrations as the Antarctic Peninsula from the rest of the Antarctic or the Greenland Ice Sheet from coastal areas where seasonality is quite different. Time-behaviour of radionuclides in polar air is dominated by a significant seasonal cycle which is at maximum in the Arctic basin, distinct in the Antarctic interior sites and less pronounced but clearly observable in coastal Antarctica and the Greenland ice sheet. Several processes contribute to this seasonality. The Antarctic seasonality is clearly dominated by the boundary-layer inversion phenomenon and the stratosphere-troposphere exchange in case of cosmogenic radionuclides. On the other hand, seasonal cycles of measurements in the Arctic basin coincide with the Arctic haze phenomenon which is driven by the strong contrast in summer and winter meteorology. Here, a variable sink strength may be more crucial in addition to seasonal differences in atmospheric mixing. Conditions on the Greenland ice sheet seem to be more comparable to the Antarctic seasonal cycle and influence of BL inversion variability is likely. The overlying seasonal variation demanded a detailed time series analysis to investigate multi-annual variability. While a 4-6 years oscillation in the ^{210}Pb time series resemble the Southern Annular Mode index, the 11-years cosmogenic production signal could be significantly detected in the Neumayer Station ^{7}Be time series. For the first time, measurements show that

this Schwabe-cycle is inherent to polar air concentrations of ^{10}Be, too. Differences in the shape of the ^{7}Be and ^{10}Be decadal variation are attributed to transport effects and significant production of excess ^{7}Be based on SEP can be ruled out.

2. **Firn and ice concentration**
   A complex, climate driven air firn transfer process transmits the atmospheric radionuclide load into firn. Having a higher spatial variability than the air concentration, the accumulation rate turns out to be the dominate parameter governing this process. This is especially demonstrative in the Antarctic, where the ascent from high-accumulation coastal areas to the dry plateau results in a factor >20 accumulation rate changes and a related rise of mean ^{10}Be firn concentration of a factor >8. On the other hand, temporal variability of multi-year firn concentration is restricted to 30% while the cosmogenic production signal may cause variations of 30-40%. Similar to a study of Greenland spatial variations in mean ^{10}Be ice concentration [Stanzick, 2001] the parameters of a basic air-firn transfer model could be estimated from correlation with mean accumulation rates in Antarctica. Consideration of seasonal variations of the air-firn transfer parameters and radionuclide air concentration reveals, that shifts in the annual cycle phase or amplitude can significantly alter the mean Greenland ^{10}Be firn concentration.

In summary, this investigation suggest, that a low-resolution atmospheric model might be suited for reproducing radionuclide polar air concentration climatology if the following basic features are implemented: (i) a well-calibrated (seasonal varying) Stratosphere-Troposphere exchange, (ii) a polar boundary layer separated from the free troposphere and (iii) a boundary layer resolution which separates regions of different climate conditions (like the Antarctic Peninsula from the rest of the Antarctic continent). In case of firn and ice concentration the spatial resolution of a model attempt has to be much higher, basically mapping figure 3.1. Consequently, there is no hope to use a simple box-model to simulate the ^{10}Be ice concentration over the whole Antarctic or Greenland Ice Sheet. In fact, the simple air-firn transfer model presented in section 3.4 is well suited to calculate ^{10}Be ice concentrations at single sampling sites using atmospheric model results as well as local accumulation rates.

4. Modelling aerosol-borne radionuclides using a global multi-box model

4.1. Introduction: The model approach

In recent decades, several studies reported on model attempts dealing with aerosol-bound radionuclides such as ^{10}Be, ^{7}Be, ^{210}Pb and their atmospheric transport and deposition (see section 2.4.1 for a short review). In spite of the overall (modelling) progress, several puzzles and challenges remained, especially related to polar areas. In addition to remaining (model-measurements and model-model) inconsistencies, it is of special interest to largely extend the time scale under investigation to interpret ice core ^{10}Be: Both, changes in the geomagnetic field strength as well as climate variability (like Dansgaard-Oeschger events or the glacial-interglacial transition) occur on the long timescale of several thousand years. So far, complex Global Circulation Models (GCM) can just reproduce small extracts of this variability due to their restriction to the decennial timescale.

Within this thesis, an entirely different model approach is applied to investigate the spatio-temporal variability of aerosol-bound radionuclides: A coarse-grid 2-dimensional box model of the global atmosphere is used to simulate climatological features of their transport and distribution in the atmosphere. While this model is extensively used in studies on atmospheric greenhouse-gases and their isotopic composition (e.g. Levin *et al.* [2010b]), it is not a priori clear if this relatively simple model approach is capable to reproduce climatological features of aerosol-borne radionuclides on the global scale. In this regard a proper calibration of the global radionuclide sink distribution is a major challenge. To tackle this task, extensive global data sets of the bomb fission products ^{137}Cs and ^{90}Sr are used to calibrate the parameters of radionuclide deposition. In the following the model is shortly described and modifications of the setup are explained. Subsequent to a presentation of the radionuclide source terms implementation, the setup and calibration of the radionuclide sink is described. Finally, the model results are validated using measurements of current atmospheric ^{7}Be and ^{210}Pb.

4.2. The GRACE model setup and its modifications with respect to aerosol modelling

4.2.1. Basics and structure of the GRACE model

The Global RAdioCarbon Exploration model (GRACE) is a model of the global carbon cycle originally developed by Hesshaimer [1997] and substantially revised by Naegler [2005] and Levin *et al.* [2010b]. Within several studies on the modern geochemical cycles of CO_2 and CH_4 (including also their isotopes ^{14}C, ^{13}C and ^{2}H), H_2 and anthropogenic SF_6 (Levin *et al.* [2010a]; Hammer [2008], C. Veidt, unpublished) the model was proved to be well suited for applications on the global scale, covering a period of time from the pre-industrial era to date. The GRACE model consists of a two-dimensional representation of the atmosphere which is coupled to a biosphere and an ocean module. The focal point of this study lies on the model atmosphere whereas biosphere and ocean modules were disconnected to save computing power.

The boxes of the atmospheric model represent the main features of the global atmosphere (see figure 4.1): A vertical division into Planetary Boundary Layer (PBL), Free Troposphere (FT) and three stratospheric subdivisions Low Stratosphere (LS), Middle Stratosphere (MS) and High Stratosphere (HS). The horizontal breakdown is 30° in the total atmosphere (except for the boundary layer) which represents the three main atmospheric circulation cells (Hadley, Ferrel and Polar cell). While this structure is identical to the prior version of the model (see supplementary information of Levin *et al.* [2010b]) the horizontal resolution of the boundary layer was increased to 10° within this work. This is basically on account of the global distribution of aerosol sinks (see section 4.3) which mainly correlates with the global distribution of precipitation. The transport of different atmospheric constituents is based on tracer-calibrated airmass transport which comprises different processes (see next section). Hence, the transport of tracers follows

$$F_{ij}^{tracer}(t) = c_i^{tracer}(t) \cdot F_{ij}^{airmass}(t) - c_j^{tracer}(t) \cdot F_{ji}^{airmass}(t) \tag{4.1}$$

F_{ij}: Flux between box i and j
c_i^{tracer}: Tracer concentration in box i

This setup results in a complex system of ordinary differential equations with time-dependent parameters which is solved numerically using a Runge-Kutta method within the MATLAB/Simulink software package.

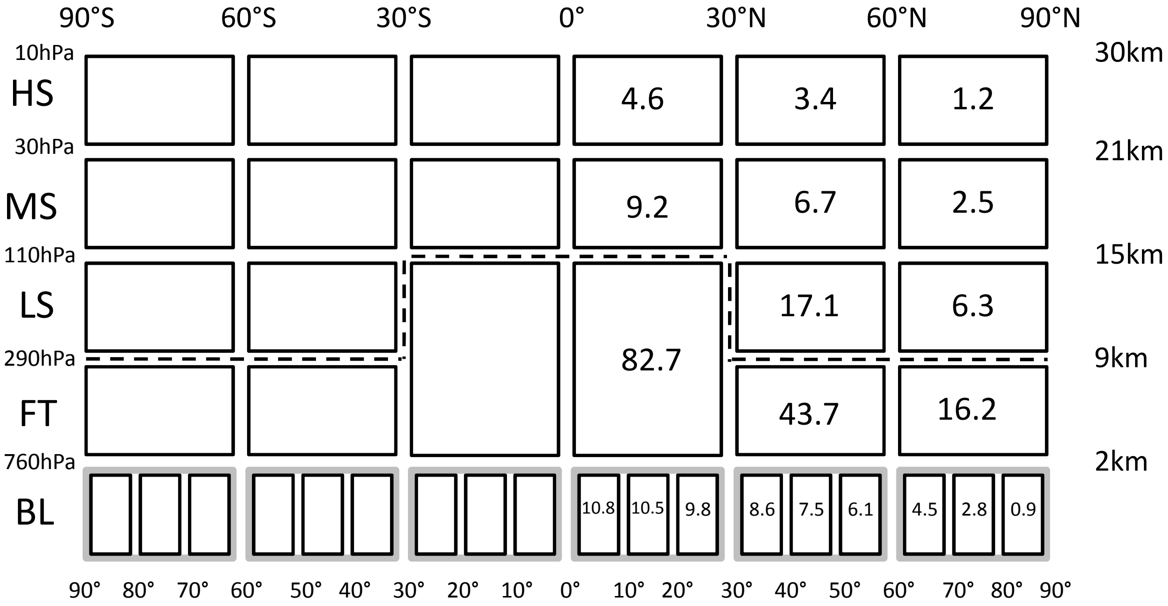

Figure 4.1.: The GRACE atmosphere model setup. Numbers in the different boxes denote the respective box airmass in 10^{16}kg. The airmass of the total atmosphere is 510 x 10^{16} kg. Note that the airmasses are symmetrical in both hemispheres. Grey boxes display the model setup previous to this work. The additional Greenland Ice Sheet box is incorporated in the 70°N - 80°N box and not shown. The Tropopause is depicted as dashed line.

4.2.2. Atmospheric transport processes

There are three basic transport processes involved in the model setup: Brewer-Dobson circulation, diffusive air mass exchange and (seasonal) variability of the tropopause height:

Diffusive (turbulent) air mass exchange

The gross diffusive air mass exchange between two neighbouring boxes is defined by the respective turnover time τ

$$F_{ij}^{airmass}(t) = \frac{m_i^{air}}{\tau_{ij}} \tag{4.2}$$

F_{ij}: Flux from box i to j
m_i^{air}: Airmass of box i
τ_{ij}: Residence time of air in box i with respect to exchange with box j

For all boxes the net diffusive flux is zero, which means that the respective turnover times for diffusive exchange between two adjacent boxes scale with the box airmass. The diffusive air mass exchange is seasonally varying. In the troposphere seasonal variation is approximated by a sine-function whereas the seasonality of the cross-tropopause transport is represented by the function $f(t) = A \cdot tanh(15(sin(2\pi t + \Phi)))$ which "allows a sharper transition between weak and vigorous exchange" (supplement of Levin *et al.* [2010b]). There is no seasonality of exchange fluxes between stratospheric boxes.

Brewer-Dobson circulation

The Brewer-Dobson circulation lifts up air into the tropical stratosphere and transports it to the mid and polar stratosphere where it descents and returns to the mid and tropical free troposphere / boundary layer. Different to the diffusive air mass exchange, the implementation of the Brewer-Dobson circulation indeed results in a net flux of airmass between adjacent boxes. However, the circulation is balanced which means that the Brewer-Dobson process does not change any box airmass. Table 4.1 gives a summary on the Brewer-Dobson parameters of the GRACE model. The models Brewer-Dobson circulation underlies a seasonal cycle with an amplitude of 90% peaking in Feb - May (northern hemisphere) and Aug - Nov (southern hemisphere), respectively.

Seasonal variability of tropopause height

In contrast to the Brewer-Dobson circulation and the diffusive air mass exchange, the seasonal variability of the tropopause height is associated with a net flux of airmass between

Table 4.1.: Parameters of Brewer-Dobson circulation in the GRACE model. Percentage values denote the partitioning of the Brewer-Dobson flux between the two mentioned compartments on the way from the tropics to the polar boundary layer. In total, 4% of the global airmass is lifted upwards each year [Levin *et al.*, 2010b]

Northern Hemisphere - Southern Hemisphere	63.5% - 37.5%
Mid Stratosphere - High Stratosphere	80% - 20%
Mid Latitudes - Polar Latitudes	73% - 27%
Free Troposphere - Boundary Layer	90% - 10%

the free troposphere and the lower stratosphere which results in a variation of box airmass. In the GRACE model, the height of the extra-tropical tropopause underlies a seasonal variation with a 1 km (0.6 km) higher level in the northern hemisphere (southern hemisphere) summer.

The atmospheric transport of the GRACE 28-box version was calibrated by Naegler [2005] using observations of SF_6 and excess radiocarbon. Furthermore the ^{10}Be/^{7}Be ratio at Neumayer Station, which is assumed to be independent from radionuclide production or deposition processes at first order is used to calibrate the STE seasonality in the SH. The details of the calibration strategy are given in the supplementary information to Levin *et al.* [2010b]. The authors state that "the overall good to excellent agreement between simulated and observed excess radiocarbon, SF_6 mixing ratios and ages as well as the ^{10}Be/^{7}Be ratio - both absolute concentrations as well as seasonal variations - suggest that major characteristics of atmospheric transport are well captured by GRACE". See e.g. figure S.6 in the supplementary information of Levin *et al.* [2010b] which shows simulated and observed concentrations of (bomb) radiocarbon in the different model boxes.

4.2.3. Modifications of the original setup

Changing the substance to be simulated from greenhouse gases to sub-micron aerosol particles required several modifications of the original model setup. While the different implementations of radionuclide production rates are shown in section 4.3, modifications of airmass and additional aerosol transport are described in the following.

Boundary layer resolution and free troposphere coupling

Global measurement data of aerosol-bound radionuclides [EML-SASP, 2010] suggest that the resolution of the original model setup is too coarse to capture the spatial variability in boundary layer air. Hence, the resolution of the boundary layer (BL) was enhanced from 6 to 18 boxes (i.e. from 30° to 10° per box, see figure 4.1). Assuming that the BL aerosol sink mainly driven by global meteorological fields is responsible for the (high-resolution) spatial variability of mean radionuclide air concentrations, the horizontal resolution of the free troposphere was kept at 30°. An important difference between the atmospheric transport of aerosol-borne radionuclides and greenhouse gases is its different sensitivity to boundary layer - free troposphere coupling. While the difference between mean air concentrations of CO_2 in the boundary layer and free troposphere is only small, differences in the concentration of ^{7}Be may amount up to an order of magnitude [EML-SASP, 2010; EML-HASP, 2011]. Associated with the enhancement of the boundary layer model resolution, the diffusive coupling of the boundary layer boxes and the free troposphere was re-assessed using ^{90}Sr air concentration and deposition flux measurements (see section 4.3). The parameters of the horizontal transport and of Brewer-Dobson-circulation were adjusted to the new model resolution by maintaining the gross airmass fluxes across box boundaries. In case of some under-determinations (e.g. the partitioning of vertical Brewer-Dobson fluxes between Free Troposphere and new resolution BL), fluxes were scaled with box mass ratios.

The Greenland ice sheet boundary layer

With regard to the focus on ice-core ^{10}Be, the polar areas require special consideration. Chapter 3 revealed, that polar radionuclide air concentrations are representative for wide areas. But, on the other hand, there are different regions of climate conditions which require discriminative representation in the model. In case of the Antarctic, the 10° resolution of the boundary layer broadly represents three different Antarctic climate regions (see section 3.2.1 and 3.2.2):

- The high Antarctic plateau: 90°S - 80°S
- Coastal Antarctica: 80°S - 70°S
- Antarctica Peninsula: 70°S - 60°S

In case of the Arctic, atmospheric radionuclide measurements revealed that the Greenland Ice Sheet differs from the Arctic basin (see section 3.3.2) and requires a different model box. However, the Greenland plateau represents only a minor part of the polar area and is thus not allocated to a 10° boundary layer box. In fact an additional box was inserted in the model which simulates the Greenland ice sheet and is coupled to the free polar troposphere as well as (to a much lesser extent) to the mid polar boundary layer box. Finally, this approach results in a global box number of 41. The area of the new Greenland Ice Sheet box is set to 1.71×10^{6} km^{2} which results in an airmass of 5% of the polar boxes and 0.08% of the global airmass. The Greenland box is incorporated in the northern mid polar box (70°N-80°N) reducing its airmass by 15%.

Gravitational settling

(Sub-micron) Aerosols are subject to gravitational settling. While this effect is of minor importance in the troposphere, it may have a significant influence on the aerosol transport in less turbulent stratospheric layers. The model setup was upgraded with an aerosol gravitational settling module by estimating the (constant) terminal gravitational settling velocity $\mathrm{v_t}$ using the Stokes-Cunningham-friction force and the gravitational force (e.g. Schery [2001]; Lazarev [2003])

$$F_{friction} = \frac{6\pi\nu r_{aerosol} v_t}{C} \tag{4.3}$$

$$C = 1 + Kn(1.142 + 0.558e^{-\frac{0.999}{Kn}}) \tag{4.4}$$

$$Kn = \frac{\lambda}{r_{aerosol}} \tag{4.5}$$

$$F_{grav} = \frac{4\pi}{3} r^3 g \rho_{aerosol} \tag{4.6}$$

ν= viscosity of air
$r_{aerosol}$ = aerosol radius
v_t = terminal velocity resulting from equilibrium between friction and gravitational force
C = Cunningham slip correction factor
Kn = Knudsen number
λ = mean free path length of an air molecule
$\rho_{aerosol}$ = density of aerosol
g = gravitational acceleration

Here, the Knudsen number gives an estimation whether the surrounding air behaves like a continuous medium (larger aerosol radii, Kn<<1) or as individual molecules (small aerosol radii, Kn>>1) [Schery, 2001]. This involves a correction of the Stokes friction formula - the empirical Cunningham slip correction factor C - which is here given following Allen & Raabe [1985]. Using the 1976 U.S. standard atmosphere (NOAA [1976], MATLAB implementation of Lewis [2007]), an estimation for different aerosol densities and sizes are calculated. Figure 4.2 shows the dependence of the gravitational settling velocity on different aerosol radii, different aerosol densities (H_2O and H_2SO_4) and the atmospheric height (i.e. the mean free path length of an air molecule and the viscosity of air). As can be seen in the figure, a critical parameter is the aerosol diameter. Hence, an assessment of radionuclide transport due to aerosol gravitational settling requires the proper knowledge of the respective size of aerosols which carry radionuclides. In case of ^{7}Be, impactor

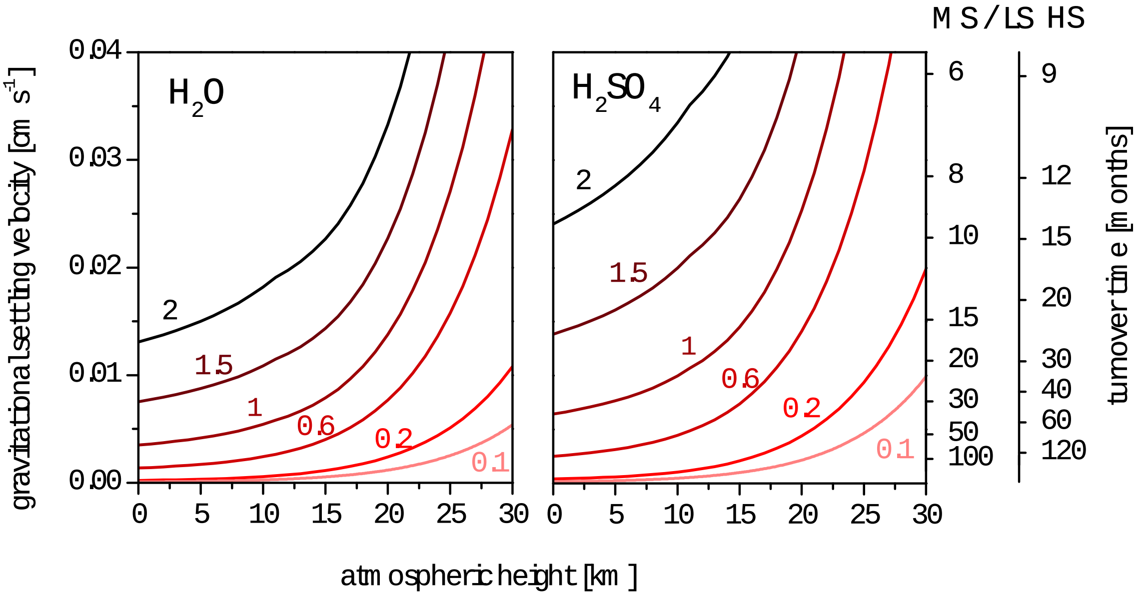

Figure 4.2.: Gravitational settling terminal velocities of small aerosol particles in the atmosphere. The left and right plot differ in the respective aerosol density: water and H_2SO_4. Different curves denote different aerosol diameter in μm. The right axis denote turnover times which correspond to the deposition velocity in the lower and mid stratosphere (MS/LS) and high stratosphere (HS) boxes of the GRACE model.

measurements in boundary layer air reveal Air Activity Median Aerodynamic Diameters (AMAD) ranging from 0.29μm to 2.06μm [Papastefanou, 2008] but likely do not exceed 1μm (see also Dorrian [1997] and Sykora & Fröhlich [2010] for a review). A conservative estimation of gravitational velocities of these aerosol sizes reveals values lower than 0.02 cm s^{-1} in case of H_2O (and lower than 0.037 cm s^{-1} for H_2SO_4) in the troposphere (see figure 4.2). Resulting tropospheric lifetimes associated with gravitational settling only are thus larger than a year and more likely in the order of several years. Since total tropospheric residence times of ^{7}Be aerosols (resulting from all transport processes) broadly range between 10 and 30 days (e.g. Koch *et al.* [1996]) respective total deposition velocities are orders of magnitude larger than the tropospheric gravitational settling velocities. In the model troposphere, gravitational settling can thus be disregarded. However, things are getting complex in case of the stratosphere. On the one hand, gravitational settling velocity is clearly enhanced in higher atmospheric layers (see 4.2). On the other the aerosol diameter is supposed to depend on the atmospheric height and is significantly lower in the stratosphere [Junge, 1963]. Indeed measurements of the size distribution of stratospheric aerosol carrying cosmogenic radionuclides are rare. Junge [1963] estimates, that the maximum of the distribution "is below but still close to 0.1μm radius" (=0.2μm diameter) in case of cosmogenic radionuclides. Martell [1966] reports on artificial radioactivity "associated with particles below 0.02 μ radius above 27 km and with particles very nearly 0.1 μ radius between 21 km and the tropopause". Given that the stratospheric lifetime of aerosol-borne radionuclides is about 1-2 years, figure 4.2 indicates that the gravitational settling of aerosol within this size range indeed may contribute to radionuclide transport in high atmospheric levels. Indeed, Feely *et al.* [1966] impute differences in the stratospheric residence time of gaseous excess (bomb) ^{14}C and particulate bomb-fission radionuclides to the influence of gravitational settling which influences the latter, only. Thus, the model is fitted with an aerosol gravitation settling module which contributes to vertical transport in the model stratosphere. Following Junge [1963] a mean radius of stratospheric aerosol (carrying radionuclides) of 0.1 μm is assumed in the model.

4.3. Implementation of radionuclide sources in the model setup

4.3.1. Cosmogenic radionuclides: ^{10}Be and ^{7}Be

Considerations of the cosmogenic production are given in section 2.1. In spite of the variety of studies reporting on different calculations of its quantity and atmospheric distribution (see figure 2.4), atmospheric ^{10}Be and ^{7}Be modelling attempts basically rely on a small selection of studies: Early models of atmospheric ^{10}Be and ^{7}Be were based on the calcu-

lations of Lal & Peters [1967] (e.g. Brost *et al.* [1991]; Rehfeld & Heimann [1995]; Koch *et al.* [1996]; Liu *et al.* [2001]). Later, studies focused on the work of Masarik & Beer [1999] by the majority [Field *et al.*, 2006; Heikkilä *et al.*, 2008a; Field & Schmidt, 2009] and recent studies used an updated version of these calculations [Masarik & Beer, 2009] [Heikkilä *et al.*, 2009; Heikkilä & Smith, 2012]. Recently, also production rate calculations of Usoskin & Kovaltsov [2008] were employed in the work of Usoskin *et al.* [2009].
Both, the production rate calculations of Usoskin and Kovaltsov [Usoskin & Kovaltsov, 2008; Kovaltsov & Usoskin, 2010] (in the following denoted as UK10) and Masarik & Beer [2009] (in the following MB09) are used in this work. While the data of MB09 was readily available as a function of atmospheric depth and geomagnetic latitudes, the data from UK10 was given as a function of cutoff rigidity (see section 2.1 for details). In the latter case, equation 2.1 (Störmer‘s equation) was used to adopt dependence on the geomagnetic latitude (and geomagnetic dipole field strength). The application of more realistic cutoff rigidity data from Smart & Shea [2008] (see figure 2.2) results in a 8-9% higher production in the southern hemisphere. However, there is no simple relation to the geomagnetic dipole strength in this case which prohibits the use of these calculations for model runs of the past. The model actually covers atmospheric depths from 10 g cm^{-2} to 1023 g cm^{-2}. However, the full range of atmospheric depths (0-1030 g cm^{-2}) is used for production rate calculations in the model to capture the full atmospheric inventory of ^{7}Be and ^{10}Be with the model. In case of the polar boundary layer boxes, the production is adapted to the overall shifted heights. To this end, mean altitudes of 3km (Antarctic plateau), 2km (Greenland Ice Sheet) and 1km (coastal Antarctica) as well as an overall polar boundary layer height of 1km is assumed. This correction results in a factor of 3 higher local production rate on the Antarctic plateau, a factor 2 in case of the Greenland Ice Sheet and 10% higher local production rate at coastal Antarctica. However, the effect on the local air concentration is much lower (final model calibration applied): 6% (12%) enhancement on the Antarctic plateau in case of ^{10}Be (^{7}Be) and 14% (27%) in case of ^{10}Be on the Greenland Ice Sheet.

The production rate calculations from UK10 and MB09 reveal some substantial discrepancies. At fist, comparison of different calculations is hampered by the fact, that different production rate studies use different approximations for the unmodulated galactic cosmic ray spectrum (see figure 2.1). Hence, the quantification of solar activity by using the solar modulation potential depends on the spectrum applied. In other words, means of different production calculations for a specific ϕ are not quantitatively comparable but have to be adapted. Herbst *et al.* [2010] propose a simple linear conversion of ϕ between the individual spectra. In case of the UK10 and MB09 data, the difference is small and a cosmogenic production using data from UK10 and a solar activity parameter of 200MV (1000MV) corresponds to the MB09 data using ϕ=159MV (986MV). Figure 4.3 shows calculations based on both data sets as a function of height and latitude. While the depth-integrated

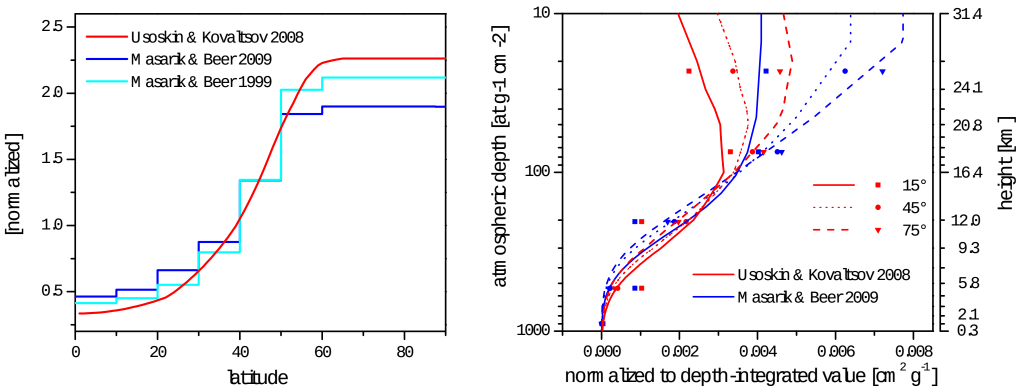

Figure 4.3.: Distribution of ^{7}Be production rates in the atmosphere calculated from Masarik & Beer [1999, 2009] and Usoskin & Kovaltsov [2008] in the atmosphere for mean solar activity (550MV for UK08 and 520.6MV in case of MB09, see text for details). Left: Depth-integrated production rate as a function of latitude. Right: Height dependence at different latitude bands (representing the main GRACE model resolution). The original data is normalized to the respective depth-integrated value. The points denote the adaption of the respective production rates to the GRACE grid so as to every point actually represent a mean over a range of atmospheric depths. Note that the MB09 data actually is not defined for atmospheric depths smaller than 10g cm^{-2} and values are extrapolated. There is no tropical lower stratosphere in the GRACE model setup and thus respective values deviate from original production rate calculations.

production rates of Masarik & Beer [1999] and UK10 show similar latitudinal behaviour, the MB09 update reveals a weaker gradient between low and high latitudes. This effect probably originates in an update of their consideration of alpha particles resulting in a different latitudinal dependence. By contrast, the height gradient of the MB09 data is stronger than the one in the UK10 data which leads to a higher stratosphere/troposphere production ratio (see figure 4.3 right). A conclusive comparison between the two different production rate calculations and their implementation in the GRACE model is obtained from calculating global mean values as a function of solar and geomagnetic activity (see figure 4.4). Comparing the calculations of MB09 with the data from UK10 it is obvious, that the latter data include a stronger modulation due to solar and geomagnetic activity. Taking the present day geomagnetic dipole strength and an average solar cycle variation of ϕ=450-1000 MV the ratio between maximum and minimum global mean ^{10}Be production is 1.31 in case of MB09 and 1.43 for the UK10 data. On the other hand, a drop in the geomagnetic dipole field strength to half of the current value results in an increase by a factor of 1.25 (MB09) and 1.42 (UK10) (with ϕ=550MV). For comparison with older model attempts: The production rate calculations of Masarik & Beer [1999] give values of 1.29 (current solar activity variations) and 1.27 (geomagnetic field drop with ϕ=521MV) and are thus comparable to the MB09 data.

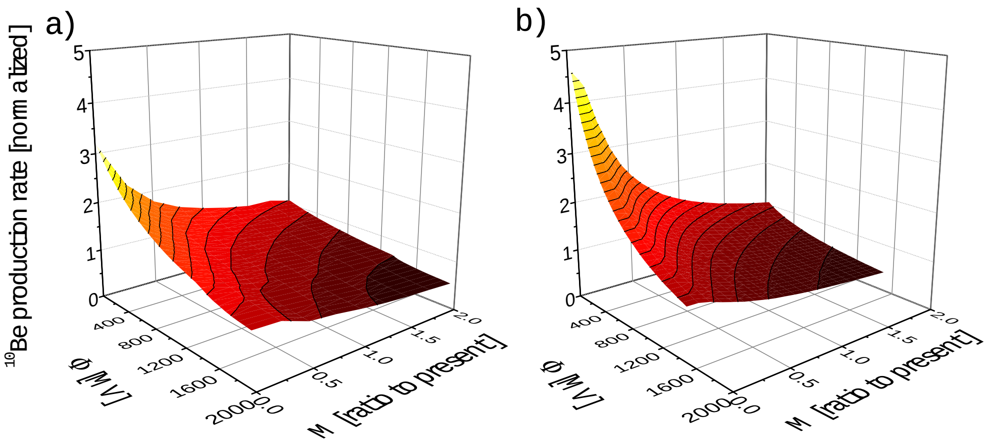

Figure 4.4.: Global mean ^{10}Be production rate based on a) Masarik & Beer [2009] and b) Kovaltsov & Usoskin [2010]. Production rates are normalized to a mean solar activity (ϕ=550MV) and the present geomagnetic field strength. In case of the data from Masarik & Beer [2009], the solar modulation parameter is converted to Kovaltsov & Usoskin [2010] using calculations of Herbst *et al.* [2010].

4.3.2. Bomb fission radionuclides: ^{137}Cs and ^{90}Sr

The time-dependent global production distribution of the bomb fission radionuclides in the GRACE model is based on the composition of single atmospheric tests and their respective characteristics as given in the UNSCEAR [2000] report. Given the assumptions on fission/fusion relations involved (see section 2.3), it is not necessary to include other compilations of nuclear tests. This is especially true, since different to ^{14}C (see Naegler & Levin [2006] for estimations on the bomb radiocarbon production), the atmospheric inventory of aerosol-bound radionuclides is quite variable in time due to the short atmospheric residence times involved. Local and regional production rates are not taken into account since these fission yields are not assumed to spread over the whole latitudinal band (and thus cannot be simulated with a 2-dimensional model approach). Eventually, this assumption is reasonable if the sampling sites are not in the regional vicinity of the test sides. Figure 4.5 gives the spatial characteristics of the source term resulting from assumptions shown in figure 2.6. It is obvious that the major part of the ^{137}Cs and ^{90}Sr yield enters the tropical and polar stratosphere. Moreover, given the short tropospheric lifetimes of aerosol particles and the fact that most of the production occurred within short periods of extensive testings, tropospheric bomb fission radionuclides are considered to be basically of stratospheric origin.

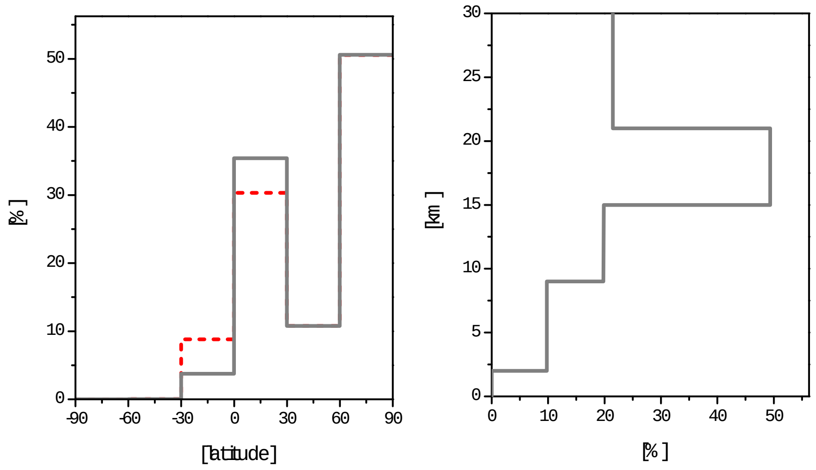

Figure 4.5.: Atmospheric distribution of time-integrated bomb fission sources in GRACE based on UNSCEAR data (see figure 2.6 for assumptions involved). Left: Latitudinal distribution of the given UNSCEAR [2000] data (grey) and the effect of partitioning sources close to box boundaries (<5°) (red). Right: Height distribution.

4.3.3. Terrigenic radionuclides: ^{222}Rn and ^{210}Pb

Oceanic fluxes of ^{222}Rn are two orders of magnitude lower than fluxes from soil. Hence, the ^{222}Rn source shows a huge spatial variability on the global scale and it is therefore not intended to correctly reproduce boundary layer measurements of ^{222}Rn activity concentration with a low-resolution, two-dimensional model. This is even more true, since activity concentrations of short-lived ^{222}Rn (radioactive lifetime 5.5 days) in the atmospheric boundary layer are driven by small-scale atmospheric transport processes making ^{222}Rn to a much-applied tracer for atmospheric mixing (e.g. Levin *et al.* [1999]). However, a realistic simulation of the global atmospheric ^{222}Rn inventory can be used as an online source term for its long-lived decay product ^{210}Pb. Even though this introduces some uncertainty to the ^{210}Pb production as errors in the airmass transport calibration directly translate into ^{210}Pb source errors, a fixed ^{210}Pb source would be even more vague.

Four types of different ^{222}Rn production schemes are implemented into the GRACE model: (i) A constant ^{222}Rn flux of 1 atom cm^{-2} s^{-1} from ice-free land, (ii) a linear reduction of the ^{222}Rn flux from 30°N to 70°N according to Conen & Robertson [2002], (iii) data from a global ^{222}Rn exhalation model based on Schery & Wasiolek [1998] and (iv) global exhalation rates based on Hirao *et al.* [2010] (S. Hirao12, pers. comm., see figure 4.6). The latter studies show that a high spatial (up to a factor of three) and seasonal (up to a factor of two) variability can be expected in the ^{222}Rn soil flux on the global scale. Chances are that a constant ^{222}Rn flux from soil which is a common assumption in atmospheric model attempts (see section 2.3) is a crude oversimplification. Figure 4.6 shows the latitudinal average of the different ^{222}Rn fluxes from soil and the resulting source term in the GRACE model. It is obvious that the data from the ^{222}Rn exhalation models exceed the source obtained from a constant ^{222}Rn soil flux. For the interpretation of seasonal cycles, an estimation of a possible contribution from sub-annual variations in the ^{222}Rn flux are essential. Since the transport of radionuclides to polar areas is a focal point in the GRACE model study, the ocean ^{222}Rn source has to be regarded in detail. Even if this input can be neglected on the global scale, maritime or remote areas might be influenced by the huge ocean surface. This is especially true for the Antarctic which is located far from any continental ^{222}Rn sources and the oceanic contribution to the coastal Antarctic ^{222}Rn was estimated to be 40% on average by Heimann *et al.* [1990]. Schery & Huang [2004] report on large spatial variations in the oceanic ^{222}Rn flux up to a factor of ten having a global mean of 1.8 x 10^{-3} atoms cm^{-2} s^{-1}.

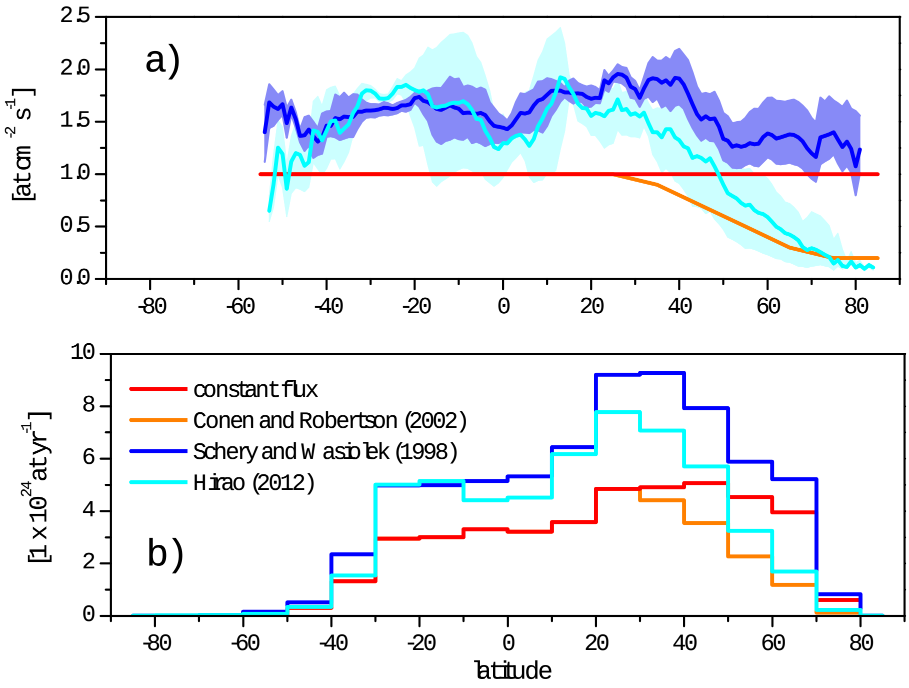

Figure 4.6.: The global ^{222}Rn source term and its implementation in GRACE. a) Latitudinal mean ^{222}Rn flux from soil surfaces as reported from several studies. In case of model results (deep and light blue), the flux is calculated as a latitudinal mean disregarding small fluxes from the ocean or ice-covered land. Coloured bands denote seasonal variations based on average monthly mean data. b) Resulting yearly mean ^{222}Rn source in the model. Note that the latitudinal distribution of land and ocean translates the ^{222}Rn soil flux into the model source.

4.4. Deposition of sub-micron aerosol: Calibration with bomb fission products ^{90}Sr and ^{137}Cs

Following explanations in sections 2.2 and 3.4 the radionuclide sink is implemented in the model as an atmospheric deposition flux depending on (i) the air concentration, (ii) a dry deposition fraction represented by the dry deposition velocity and (iii) a wet deposition fraction governed by the scavenging ratio (related to a scavenging efficiency) as well as the precipitation rate. It is worth mentioning that this implementation is not essentially different from high-resolution global transport models (e.g. Stohl *et al.* [2005]; Sportisse [2007]). Assuming that dry as well as wet deposition fluxes are governed by the same airmass (see section 3.4 for details), the aerosol/radionuclide sink is restricted to the boundary layer boxes and can be formulated as

$$J^i(t) = v^i_{total}(t) \cdot c^i_{air}(t) = (v^i_{dry} + \epsilon^i(t) \cdot P^i(t)) \cdot c^i_{air}(t) \tag{4.7}$$

J^i: Deposition flux in box i
v^i: Deposition velocity in box i
c^i_{air}: Radionuclide air concentration
P^i: Precipitation rate
ϵ^i: Scavenging ratio (i.e. ratio between concentration in precipitation and air)

While $\mathrm{c_{air}}$ is calculated online, the time-dependent and spatially varying parameters P(t), $\mathrm{v_{dry}}$(t) and ϵ(t) are defined within model initialization. To this end, parameters are calibrated using global data sets of ^{90}Sr and ^{137}Cs air concentration as well as ^{90}Sr deposition flux measurements. Calibration data, procedure and results are summarized in the following section (see also appendix D1 for details).

Precipitation

Global precipitation data was obtained from the Global Precipitation Climatology Project (GPCP) [Adler *et al.*, 2003] which is based on satellite data and surface rain gauge observations over the time period 1979-2010. Figure 4.7 shows the latitudinal average of this data as well as seasonal variations and the adaption to the GRACE model grid. It is obvious, that the (2-dimensional) 10° model resolution captures the major part of the variability. Certainly, there are further estimations of the global precipitation rate (like NCEP or ECWMF reanalysis data). However, differences are restricted to the local and regional scale while large-scale features of the global climatology are comparable [Adler *et al.*, 2003; Janowiak *et al.*, 1998]. Note that there is no noticeable increase of the global

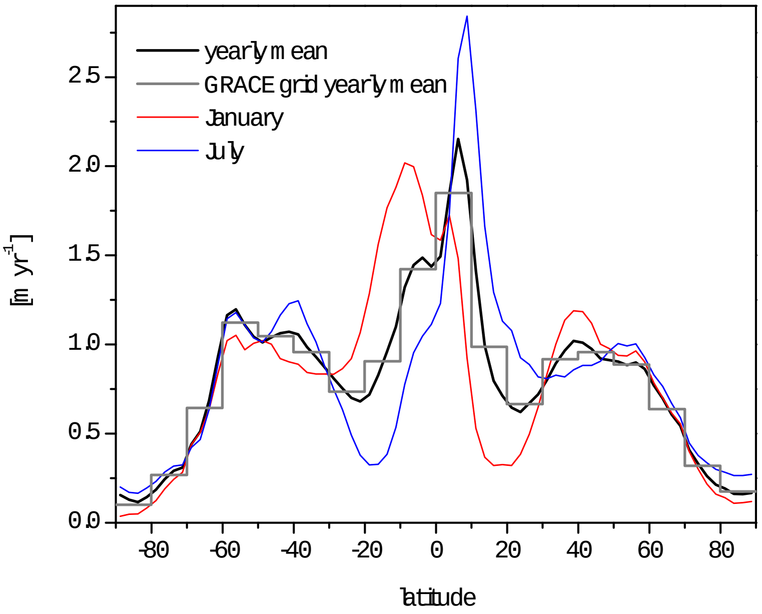

Figure 4.7.: Global distribution of the mean precipitation rate based on GPCP data [Adler *et al.*, 2003] and respective adaption to the GRACE boundary layer grid. Global distributions in January and July indicate the seasonal cycle of precipitation. Model implementation is based on monthly average data.

mean precipitation rate during 1979-1999 [Adler *et al.*, 2003] which allows for deploying long-term (climatological) average monthly data.

Model adjustments to reproduce ^{90}Sr and ^{137}Cs

Time series of aerosol-bound radionuclides are noisy and influenced by synoptic meteorological forcing as well as short-term atmospheric transport processes. Thus, the determination of climatological parameters like the average seasonal cycle usually requires longterm measurement efforts (see e.g. the Neumayer time series in figure 3.2). In case of bomb fission radionuclides, this challenge is even more sophisticated since their source term is highly inconstant in time following the prominent 'spike' of atmospheric nuclear bomb tests. Basically, contemporaneous measurements of air concentration and deposition fluxes at the same sampling site could eliminate this source term and a great deal of temporal variability when calculating deposition velocities (deposition velocity = deposition flux / air concentration). Unfortunately, measurements which come up to these criteria are sparse and hence can provide first-order estimations only. On the other hand, the EML SASP and fallout data bases provide huge amounts of measurements of ^{90}Sr deposition or ^{90}Sr and ^{137}Cs activity concentration at plenty of sites (84 stations of surface air radionuclide measurements and 165 stations providing fallout measurements, see figure 2.7). These data sets are compiled, augmented with further data [Kolb, 1992] and applied within an elaborate calibration strategy to adapt the model to reproduce ^{90}Sr and ^{137}Cs from bomb fission sources (see details in the appendix D). In addition to the calibration of the aerosol scavenging ratio (using GPCP precipitation data), the application of both, air concentrations and deposition fluxes from UNSCEAR [2000] (see figure 4.8) allowed for the calibration of the diffusive boundary layer - free troposphere coupling, too. In case of the polar areas, the UNSCEAR [2000] data provides extrapolated deposition fluxes only. Therefore further data sets are applied to estimate the respective radionuclide deposition [Roos *et al.* [1994]; Pourchet *et al.* [2003]; EML-Fallout [2010]; see appendix figure A.4]. The Greenland ice sheet lacks measurements of bomb fission radionuclide activity concentration or deposition flux measurements. In contrast to the Antarctic, the comparably high accumulation rate hampers measurements of the total ^{90}Sr or ^{137}Cs inventory: To give an example, measurements at a Summit ice-core of the bomb spike total beta activity encompass nearly 20m of ice [Dibb, 1992]. So far, scavenging ratios from the Antarctic coastal box as well as vertical diffusive airmass transport from surrounding Arctic basin are applied. Details, concerning e.g. the calibration of additional seasonal variability are described in the appendix D.

The fitted model (time-integrated) deposition of ^{90}Sr is given in figure 4.8 compared to the reference data (and model results previous to the calibration). It is not possible to perfectly fit the model to the UNSCEAR [2000] data since the model has to match air-concentrations

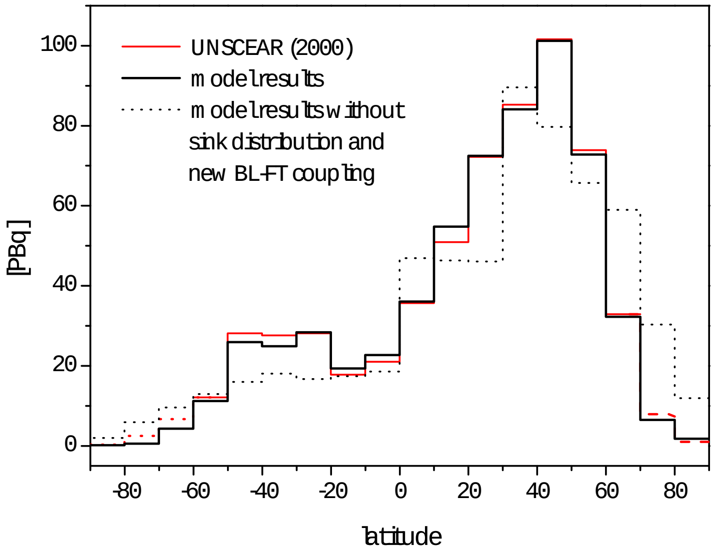

Figure 4.8.: Time-integrated deposition of ^{90}Sr according to UNSCEAR [2000] and respective model adaption. The dotted line denotes model results with applying neither a latitudinal distribution of aerosol sinks nor of diffusive boundary layer - free troposphere fluxes. Note that UNSCEAR [2000] reports on extrapolated polar values (60°S - 90°S and 70°N - 90°N) which are denoted as dashed red lines. Since the model has to match atmospheric activity-concentrations as well, it is not possible to perfectly fit the model to the measured deposition data.

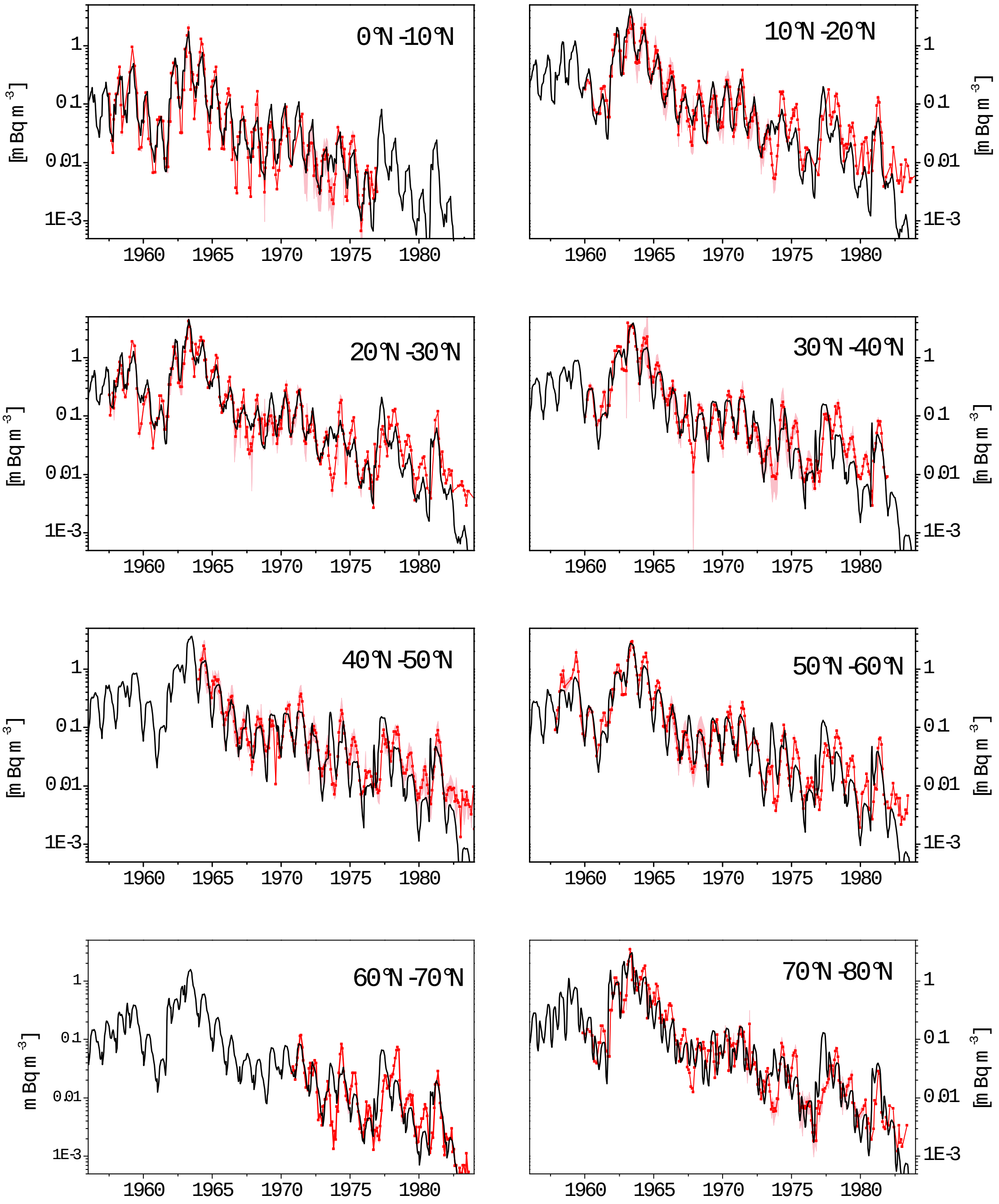

Figure 4.9.: Compilation of northern hemisphere ^{90}Sr atmospheric activity concentration measurements based on EML-SASP [2010] and Kolb [1992] compared with the adapted model results. Red shaded areas denote maximum and minimum values in case of several data sets combined. ^{137}Cs data is used to augment ^{90}Sr measurements by using a fixed ratio of 1.524. Note that records of the most northern BL box (80°- 90°) are not shown due to the low measurements data basis: Observations which were used for calibration comprise 20 months of data (September 1970 - April 1972) only.

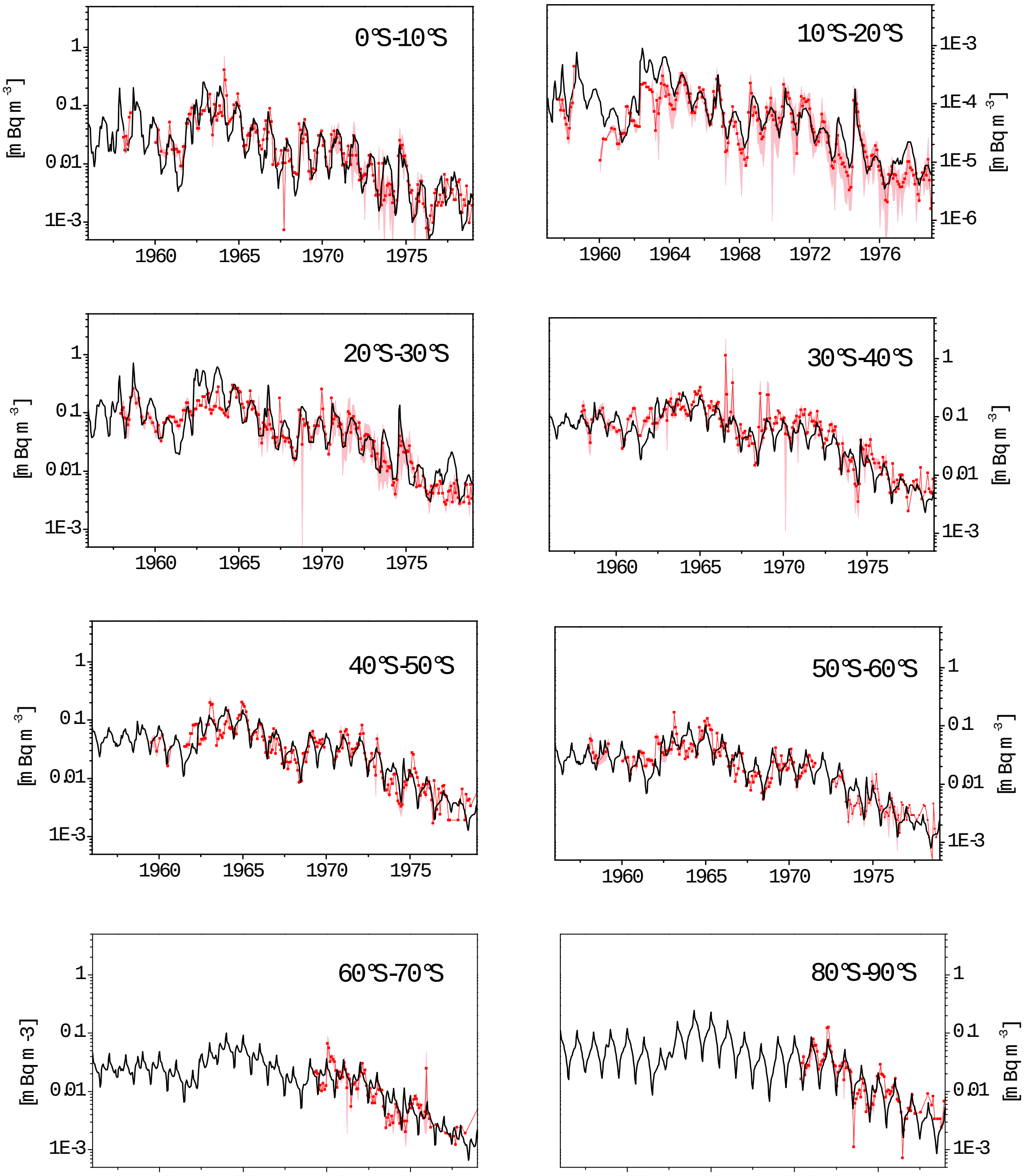

Figure 4.10.: Same as figure 4.9 but for the southern hemisphere. Note that the 70°S to 80° box is not shown since there is no data available. However, results from chapter 3 indicate that radionuclide air concentrations are similar to the Antarctic plateau box (80°S - 90°S).

as well. Anyway, the match is nearly perfect (correlation coefficient: 0.998) which indicates that the model reproduces the overall latitudinal distribution of radionuclide deposition. Fitted model outcomes of the ^{90}Sr air concentrations are shown in figures 4.9 and 4.10 together with the calibration target (compiled measurements of EML-SASP [2010] and Kolb [1992]). It is obvious that the model captures the majority of time variability although all calibrated parameters (aerosol scavenging and diffusive boundary layer free troposphere transport) have no long-term trends in the model. Certainly, the model measurement ratio is time-dependent which hampers an exact calibration. It is obvious that there are large deviations in single monthly (and some yearly) data to some extent. However, applying a Gaussian smoothing filter (FWHM = 3 years) to both, measurements and respective model outcomes reveals that most of the model boxes show deviations lower than 30% in case of multiannual variability (before 1976; after 1976 measurements of ^{90}Sr have quarterly resolution). Certainly, there are deviations close to or larger than 50% in some cases: (i) A pronounced spike in the southern hemisphere tropical boxes (20°S - 30°S) around 1963 has no counterpart in the measurement data; (ii) in case of the northern polar areas (70°N - 80°N) the seasonal cycle of the measurements seems to change with time; (iii) Some sharp peaks in the southern mid-latitudes (40°S - 50°S) are not represented by the model but may be measurement artefacts as well. In summary, it may be concluded that it is possible to calibrate the model with aerosol-bound bomb fission radionuclides.

Figure 4.11 shows the parameters resulting from (aerosol deposition) model calibration. While it is not primarily intended to reproduce realistic physical characteristics of the atmospheric aerosol cycle with this simple model approach, meaningful parameter settings point to a realistic model setup. In this regard parameters resulting from calibration provide reasonable interpretations: A smaller scavenging ratio in the tropics and subtropics may be predicated on predominance of single-event precipitation (in contrast to steady rain) accompanied by lower radionuclides rain concentration. The sharp break at 70° to very small scavenging ratios may rest upon the crossing from stormy regions ('furious fifties' and 'screaming sixties') to dry, polar regions with different meteorological regimes. This crossover is also seen in the ratio of dry to total deposition which shows a huge rise from subpolar to polar boxes. This rise cannot be solely explained by smaller precipitation rates but requires an additional drop in the scavenging ratio in conjunction with a change in precipitation characteristics (e.g. absence of liquid precipitation). The coupling of the boundary layer and the free troposphere is expected to be smaller in polar areas. Moreover, a larger ocean surface (like in the southern hemisphere boxes) may result in a stronger mixing/coupling. Finally, a great deal of spatial variability may result from additional effects, too, which lack a representation in this simple model approach.

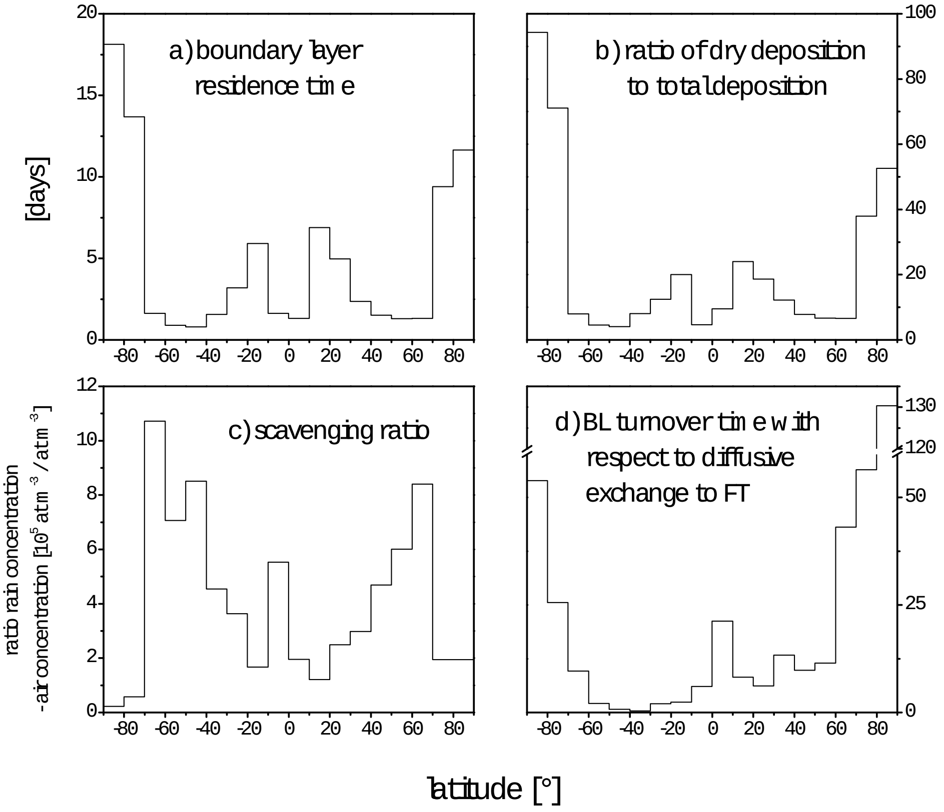

Figure 4.11.: Model-calibration results of the global (sub-micron) aerosol sink using global data sets of bomb fission radionuclides.

4.5. Model performance

4.5.1. Validation with ^{7}Be and ^{10}Be measurements

Having successfully adapted the model for the simulation of anthropogenic radionuclides, the model can be validated using long-term measurements of natural radionuclides. With respect to ice-core ^{10}Be, the models ability to reproduce cosmogenic ^{7}Be is especially important. In contrast to ^{10}Be, the comparably high activity concentration of ^{7}Be in atmospheric aerosol makes it a common measure in atmospheric aerosol monitoring studies. Hence, a model-measurements comparison can be based on large amounts of globally distributed long-term measurement data. Where available, model validation is backed-up by ^{10}Be measurements, too.

Spatial variability

Different to anthropogenic radionuclides, the comparatively small variations in the cosmogenic source strength permits the comparison of overall mean concentrations. Figure 4.12 shows a compilation of mean ^{7}Be concentrations in boundary layer air obtained from various longterm monitoring attempts. The picture shows that the model reproduces the main features of the global ^{7}Be distribution: (i) a strong decrease from subtropical to (high) mid latitudes, (ii) an increased concentration in polar areas and (iii) a small ^{7}Be concentration in the tropics comparable to high (extra-polar) latitudes. It is remarkable that the application of the production rate calculation from Masarik & Beer [2009] clearly underestimate the measurements, while the model results based on the Usoskin & Kovaltsov [2008] production data seems to quantitatively fit the global ^{7}Be distribution very well. The results of chapter three showed a more or less homogeneous polar air concentration, these Antarctic concentrations are underestimated by the model by 24-30%. Note that the difference between model results and measurements shown in figure 4.12 is slightly larger since the model results refers to the 1950-2000 period. On the contrary, mean ^{7}Be air concentration on the Greenland Ice Sheet is overestimated by a factor 2.5 (not shown in figure 4.12). In case of Greenland, this model deviation is not surprising since parameters of the aerosol deposition and BL-FT diffusive coupling had to be adopted from the Arctic basin and the Antarctic boxes, respectively. Greenland ice sheet air concentration measurements of ^{10}Be exist from Stanzick [2001] only and encompass 10 measurements which cover a time period between June 1997 and March 1998 (see figure 4.17 in section 4.5.3). These measurements (linearly interpolated to cover a whole year) suggest a yearly mean value of 2.5 x 10^{4} atoms SCM^{-1} but the data basis is very low due to the strong seasonal cycle inherent to the atomspheric concentrations. Model results are a factor 3.6 larger which is somewhat higher than the difference in case of ^{7}Be.

Vertical gradients of atmospheric ^{7}Be concentration exceed the latitudinal ones by some orders of magnitude. Unfortunately, higher atmospheric layers lack any long-term measurements and analysis relies on punctual observations obtained from aircraft or balloon surveys. Figure 4.13 shows measurements of ^{7}Be carried out in the frame of the EML High Altitude Sampling Program (HASP). As expected from short-term measurements the values show a large variability. Systematic errors may be inherent to the results of the HASP due to partly ambiguous aerosol filter efficiencies [Junge, 1963]. Nevertheless, basic features like (i) a systematic gradient in the mean concentration decreasing from polar to equatorial latitudes inherent to all altitudes and (ii) the major decrease in air concentrations from the mid stratosphere to the boundary layer is depicted in both, the EML data and the model results. The model results show a systematically lower ^{7}Be air concentration in the SH free troposphere than in corresponding NH atmosphere. This

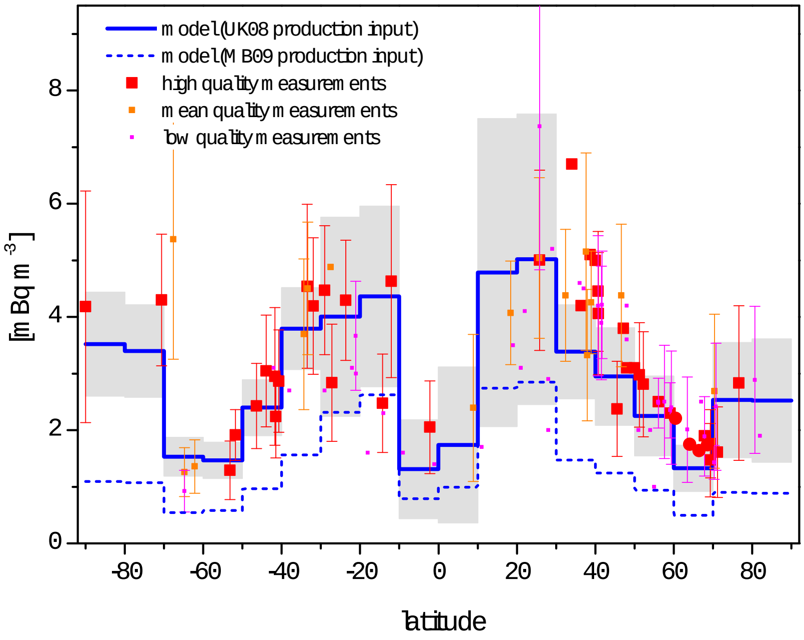

Figure 4.12.: Model-measurements comparison of mean ^{7}Be concentrations in boundary layer air. Different colours of measurements (dots) denote different quality of long-term mean values: High quality (time series longer than 10 years, >10 months of data per year on average), mean quality (time series longer than 3 years, >9 months of data per year on average) and low quality (shorter time series and literature data without details on sampling time). Round dots denote median values, squared dots represent mean values. Note that all elevated sites (>1000m a.s.l.) except South Pole station at -90° are excluded. Model results differ in the production input applied: Production calculation from Usoskin & Kovaltsov [2008] (solid line) and from Masarik & Beer [2009] (dashed line). Grey bars denote the standard deviation of the model results dominated by the seasonal cycle of the atmospheric concentrations. Model results encompass the mean of 1950-2000 whereas measurements represent various periods. Data: EML-SASP [2010]; Kolb [1992]; Durana *et al.* [1996]; Megumi *et al.* [2000]; Ioannidou *et al.* [2005]; Kulan *et al.* [2006]; Kulan [2007]; Chae *et al.* [2011]; Leppänen *et al.* [2012]; Wershofen [2011],Doering [2007] and references therein.

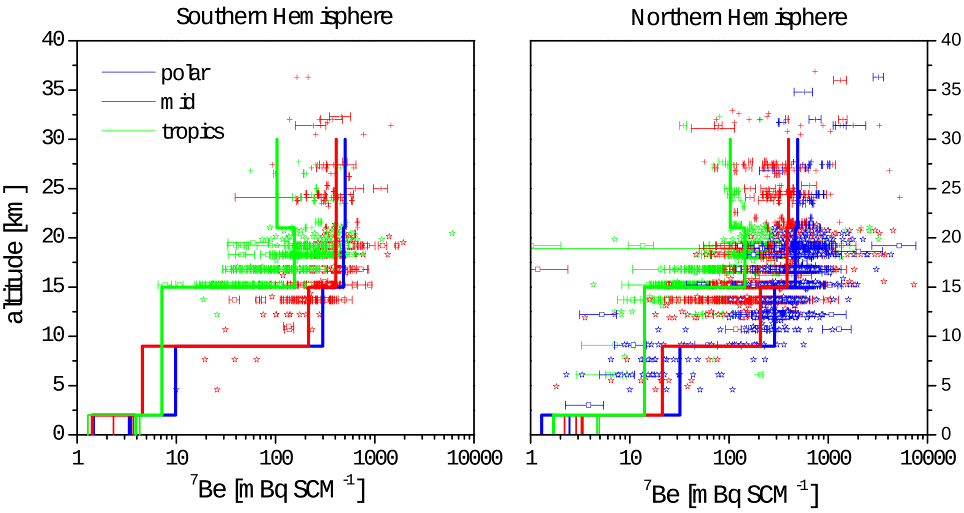

Figure 4.13.: Vertical distribution of ^{7}Be in the atmosphere according to EML-HASP [2011] data and the GRACE model (UK10 production rate calculations). Different colours denote different latitudinal bands according to the model resolution: polar (60° - 90°), mid (30° - 60°) and tropical (0° - 30°). Different symbols represent the three different High Altitude Sampling programs: stars (Star Dust), squares (Airstream) and crosses (Ashcan). Model results comprise mean values of the 1950-2000 period.

finding is probably based on the higher BL-FT coupling in addition to a higher scavenging ratio resulting in slightly higher deposition fluxes (see figure 4.11). With respect to somewhat sketchy known vertical distribution due to the lack of longterm measurements, it is interesting to compare the model outcome to results from other model approaches. Table 4.2 gives some key characteristics of cosmogenic radionuclides simulated with the ECHAM-HAM5 General Circulation Model [Heikkilä & Smith, 2012] and the here presented model approach. Since Heikkilä & Smith [2012] scaled the production data of Masarik & Beer [2009] by a factor of 1.5 in the ECHAM model (U. Heikkilä, pers. communication) this is also done in GRACE for a better comparability of the two models. Table 4.2 reveals that GRACE predicts a longer stratospheric residence time of cosmogenic nuclides than the ECHAM-HAM5 model. This breeds (i) a higher stratospheric ^{10}Be burden in case of GRACE and (ii) lower ^{7}Be deposition fluxes in GRACE since more ^{7}Be decays in the stratosphere as well as (iii) a larger contrast between mean ^{10}Be production and mean ^{10}Be deposition due to the stratospheric damping (time shift). In case of the UK10 production rates, the stratospheric residence time is lower due to a different production distribution (lower fraction of stratospheric production). In addition to the overall higher production, this contributes to the higher deposition flux of ^{7}Be in comparison to the MB09 production data.

Table 4.2.: Key characteristics of ^{10}Be simulated with the global circulation model ECHAM5-HAM [Heikkilä & Smith, 2012] compared to the GRACE results. Both model outcomes represent the five years period 1998-2002. Note that Heikkilä & Smith [2012] scaled the production rate of Masarik & Beer [2009] by a factor 1.5 (U. Heikkilä, pers. communication). The middle column shows GRACE results with comparably scaled production rates, for comparison. In comparison to ECHAM-HAM5, the GRACE model reveals significantly higher stratospheric residence times leading to higher stratospheric (and global) burdens in case of ^{10}Be.

	ECHAM5 (MB09)	GRACE (MB09) scaled	GRACE (UK10)
Global ^{10}Be production [g yr^{-1}]	73.7	73.7	78.2
Stratospheric ^{10}Be production	67%	72%	62%
Global ^{10}Be burden [g]	50.9	118.0	82.8
Stratospheric ^{10}Be burden [g]	46.8 (92%)	112.9 (95.7%)	78 (94.1%)
Tropospheric ^{10}Be burden [g]	4.1	5.1	4.9
Deposition [g yr^{-1}]	74.8	77.8	75.2
Deposition [% of global burden yr^{-1}]	147	66	90.8
Mean global residence time [months]	8.1	18.2	13.2
Mean stratospheric residence time [months]	11.3	23.9	19.4
Mean tropospheric residence time [days]	20	23.9	23.6
Global mean ^{7}Be production [g yr^{-1}]	105.5	100.5	112.3
Stratospheric ^{7}Be production	72%	75.9%	69.3%
Global ^{7}Be burden [g]	14.5	16.2	16.6
Stratospheric ^{7}Be burden [g]	12.6 (87%)	14.5 (89.8%)	14.4 (86.5%)
Tropospheric ^{7}Be burden [g]	1.9	1.6	2.2
Deposition [g yr^{-1}]	36.9	24.7	34.80
Deposition [% of global burden yr^{-1}]	254	153	209

Table 4.3.: Model-measurements comparison of radionuclide deposition fluxes. Model results without indication of a time period refer to the years 1950-2000.
* Range based on yearly data

	reference (time period)	latitude	deposition flux [atoms cm^{-2}yr^{-1}]	model results [atoms cm^{-2}yr^{-1}]
^{10}Be	Stanzick 2001	75°N-85°N	(15-26) x 10^4	40 x 10^4
	Heikkilä et al. 2008 (1998-2005)	47°N	(2.6 ± 0.2) 10^6	1.4 10^6
	Wagenbach (pers. comm.)	71°S	40 x 10^4	16 x 10^4
^{7}Be	Heikkilä et al. 2008 (1998-2005)	47°N	(1.2 ± 0.1) x 10^6	0.8 x 10^6
	Young and Silker 1980	30°S - 60°N	(0.6-1.1) x 10^6	0.3-0.9 x 10^6
	Basrakan et al. 1993 * (1989-1991)	29°N	(0.7-1.8) x 10^6	0.5 x 10^6
	Todd et al. 1989 * (1983-1984)	37°N	(0.9-1.0) x 10^6	0.6 x 10^6
	Akata et al. 2008 * (2001-2005)	41°N	(1.0-1.5) x 10^6	0.8 x 10^6
	Doering 2007 * (2004-2006)	27°S	(0.5-0.6) x 10^6	0.8 x 10^6
	Turekian et al. 1983	41°N	1.7 x 10^6	0.9 x 10^6
	(1977-1978)	36°N	1.3 x 10^6	0.7 x 10^6

Comparing measurements of deposition fluxes or rain concentration with respective model results is difficult since these quantities underlie strong spatial and temporal variability. Notwithstanding, the model outcome is compared to some longterm measurement results. Table 4.3 shows respective model-measurements comparisons and indicates that the model basically reproduces measured fluxes in a range of a factor 2. However, it is obvious that the GRACE model underestimates the fluxes in most cases. In case of ^{10}Be this may be due to a certain amount of recycled ^{10}Be from soil which is not simulated in the model. Due to its short radioactive lifetime this is not the case for ^{7}Be.

Temporal variability

The most dominant signal in all boundary layer ^{7}Be time series is its seasonal cycle. Hence, the reproduction of the respective phase and amplitude is a major goal of any modelling

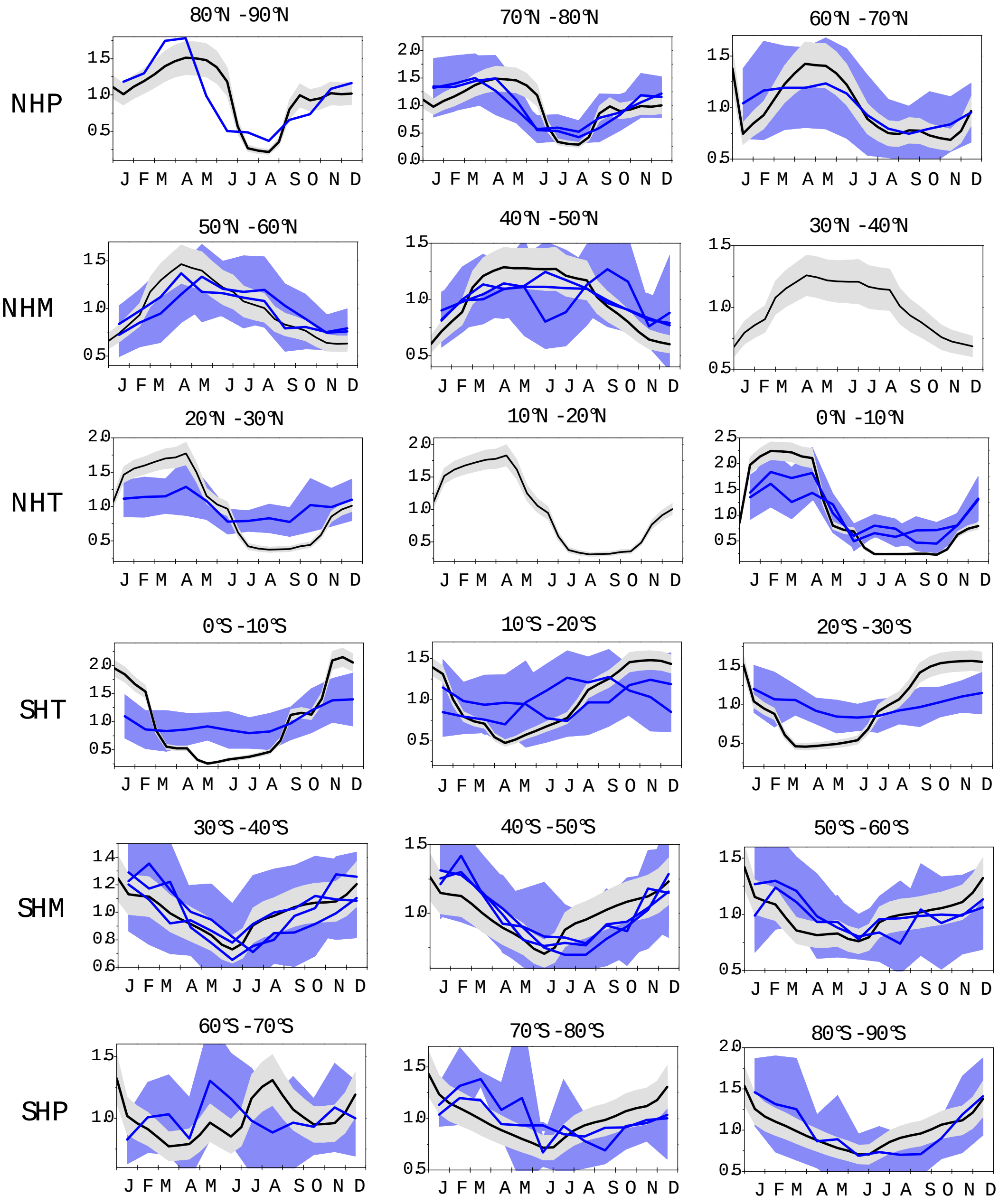

Figure 4.14.: Model-measurement comparison of mean ^{7}Be seasonal cycles in the boundary layer on a global scale. Model results are shown in grey, stacked seasonal cycles from different time series [EML-SASP [2010]; Kolb [1992]; Dibb *et al.* [1994]; Wershofen & Arnold [2005]; H. Wershofen, pers. comm.] are shown in blue. All data sets are normalized to the respective overall mean. Shaded areas denote standard deviations of multi-annual variability. In case of the model results, this variability is based on production rates during the time period 1950-2000.

attempt. Figure 4.14 shows the compilation of boundary layer activity concentration seasonalities normalized to the respective mean value [EML-SASP [2010]; Kolb [1992]; Dibb *et al.* [1994]; Wershofen & Arnold [2005]; H. Wershofen, pers. comm.]. The model closely matches the measurement seasonal cycles in mid-latitudes (of both hemispheres) and on the southern Antarctic plateau with respect to phase and amplitude. In the tropics the model seems to overestimate the seasonal cycle amplitudes. However, tropical measurements may be less representative due to spatial precipitation differences. Measurements of ^{10}Be air concentration are rare but exist from some selected sites. Different to ^{7}Be these measurements cover a short period of time which permits the calculation of mean (climatological) seasonal cycles. However, since the focus of the model attempt is on ^{10}Be, measurements of boundary layer air concentration in Vienna, Summit (Greenland) and Neumayer (Antarctica) are compared to respective model results in figure 4.17 (see section 4.5.3). Due to the single measurements data base, several measurements deviate from (climatological) model results. Nevertheless, the comparison reveals the overall ability of the model to reproduce ^{10}Be seasonality especially in polar areas (in case of Vienna, the measurements data basis is quite low).

With respect to multi-annual variability, the ^{7}Be air concentration is mainly driven by the 11-years production signal. However, due to the overlying seasonal cycle and the overall low signal-to-noise ratio of aerosol-borne radionuclides, the detection of this production signal in long-term measurements is challenging [Koch & Mann, 1996; Aldahan *et al.*, 2008; Elsässer *et al.*, 2011]. To investigate the model's ability to reproduce the production signal, two long-term time series are compared to the model results: Results of long-term monitoring (i) at the Physikalisch Technische Bundesanstalt Braunschweig [Wershofen & Arnold [2005]; H. Wershofen pers. comm.] and (ii) at the coastal Antarctic Neumayer time series presented in section 3.2. Model results clearly match the features of the time series even if the longterm mean values are somewhat lower. In case of the nearly 50 years time series of the PTB Braunschweig, the measurements show an increasing trend which is missing in the model data (see figure 4.15). Possible explanations for this inconsistency comprise (i) a failure in the production module of the model, (ii) long-term climate effects which bias the atmospheric activity concentration and which are not considered in the model. The latter part of the Neumayer measurements may point to a long-term deviation from model results as well. However, the time series is too short to provide conclusive evidence. Finally, it is worth mentioning that the long-term data sets of the EML network mostly show an 11-years production signal (see Koch & Mann [1996] for an evaluation). While the detailed shape of these signals do generally not overlap with the model results only one of the time series shows an obvious increasing measurement-model deviation. However, again it has to be considered, that the low signal-to-noise ratio inherent to short-lived nuclides hampers the detection of a long-term signal. In case of EML, high-quality time series of cosmogenic ^{7}Be were not the primary intention of nuclear monitoring.

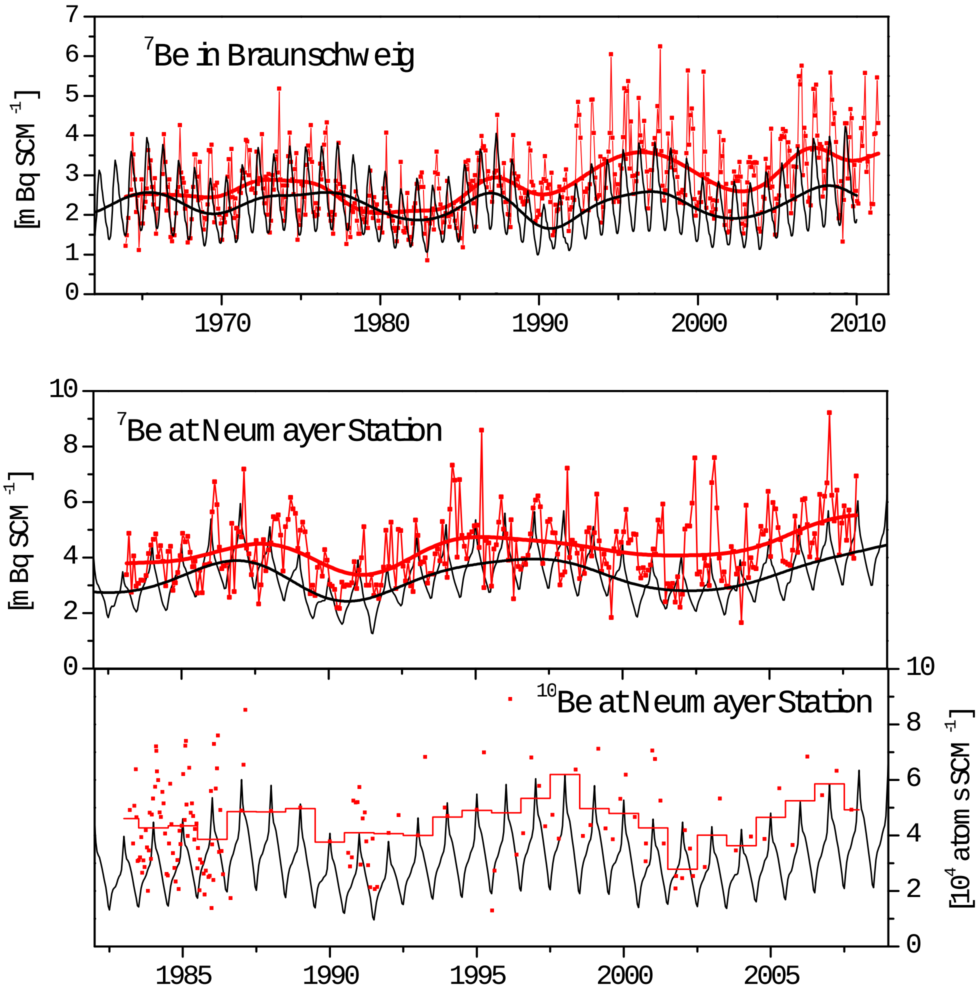

Figure 4.15.: Model-measurements comparison of ^{7}Be and ^{10}Be air concentration in Braunschweig and at Neumayer Station, coastal Antarctica. Long-term model results clearly match the features of the measurement time series. Note that the model underestimates Antarctic long-term mean ^{7}Be values by 24-30% and ^{10}Be values by 49%. The latter model-measurements difference is significantly reduced to 13% when using ^{7}Be measurements for an update of the aerosol sink calibration (see section 4.5.3).

4.5.2. Modelling ^{210}Pb and ^{222}Rn

Model results of terrigenic radionuclides contrast and complement the findings on cosmogenic (and bomb fission) radionuclides since their source term is completely different. As measurements of gaseous ^{222}Rn are challenging and thus restricted to a few sites, the focus is on terrigenic ^{210}Pb.

Figure 4.16 shows the model-measurement comparison of the latitudinal distribution of ^{222}Rn and ^{210}Pb based on different ^{222}Rn source estimations applied. At first the measurements as well as the model results clearly reflect the north south gradient of terrigenic radionuclides which is a result from ^{222}Rn source and corresponding land ocean distribution. Moreover the simulated air concentrations match nearly all measurements (except a few outliers) within a factor of 4-6 which points to an overall correctness of the model's aerosol deposition parameters. However, by contrast with cosmogenic radionuclides (see figure 4.12), model-measurements comparison is more difficult due to a somewhat larger scattering of observations (note the logarithmic scaling in figure 4.16). In fact, different to ^{7}Be a definite source term can not be determined from figure 4.16. Longitudinal difference of the ^{222}Rn source due to the land ocean distribution may hold for an explanation of the larger scatter. Indeed, some of the highest ^{210}Pb activity concentrations in figure 4.16 can be attributed to continental sampling sites (e.g. Munich [Winkler & Rosner, 2000]) while maritime sites (e.g. American Samoa, Easter Islands [EML-SASP, 2010]) show lower values. Despite a missing clear latitudinal distribution in boundary layer air, the model may basically reproduce the free tropospheric and stratospheric concentrations which are supposed to be less influenced by longitudinal differences. However, the model systematically overestimates the ^{210}Pb air concentration (at least in the northern hemisphere, EML-HASP [2011], not shown). Longterm time series of some high-altitude stations indeed corroborate this finding of a model overestimation of the free tropospheric ^{210}Pb concentration (not shown).

Comparison to some time series reveals [EML-SASP, 2010; Wershofen & Arnold, 2005], that the model is not able to reproduce the ^{210}Pb seasonal cycles in most cases (not shown). Again this may be predicated on the two-dimensional setup of the model. In case of continental measurement sites, the boundary layer acts as a source for ^{210}Pb whereas in maritime conditions, the boundary layer is a sink for ^{210}Pb (e.g. Sykora & Fröhlich [2010]). Being a mixture of continental and maritime, the models boundary layer boxes cannot produce the correct gradient between FT and BL and hence fails to simulate the proper seasonality. In fact, this should not be the case for the polar areas which generally lack from ^{222}Rn sources. Hence, the seasonal cycle of ^{210}Pb can be applied to calibrate the boundary layer inversion seasonal variability in these regions (see appendix D.1).

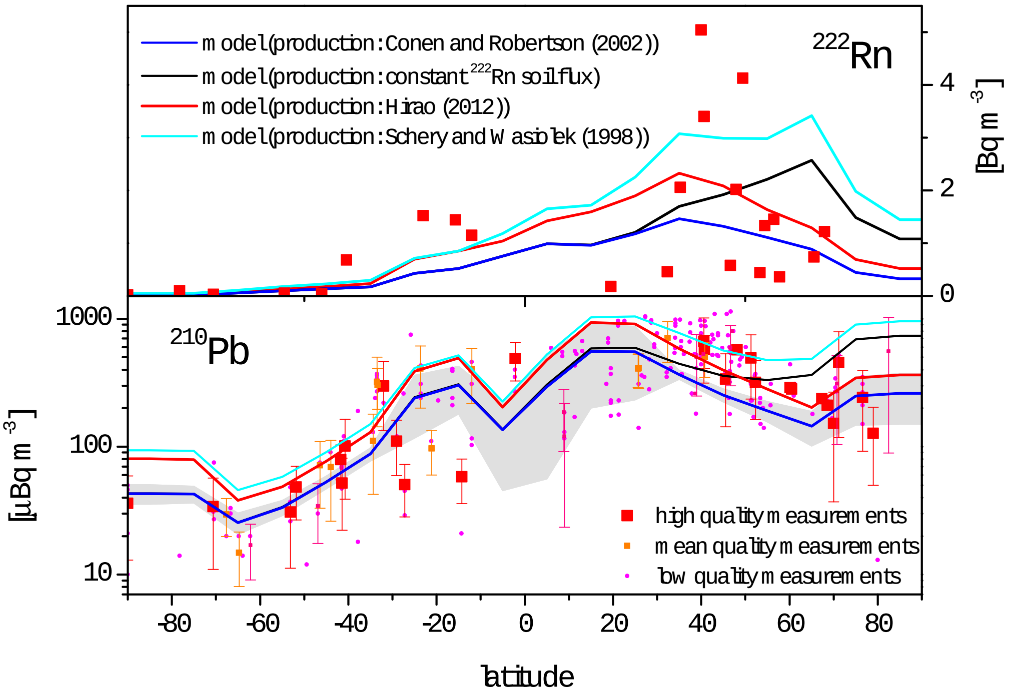

Figure 4.16.: Model-measurements comparison of ^{222}Rn and ^{210}Pb boundary layer air concentration. Note the logarithmic scaling in case of ^{210}Pb for reason of air concentrations ranging over two orders of magnitude. The model results differ in the ^{222}Rn source applied (see section 4.3.3 for details). Measurements are mean values of long-term time series. In case of ^{222}Rn, air concentration measurements refer to the compilation of Robertson *et al.* [2005]. ^{210}Pb measurements are classified in three different types: High quality (time series longer than 10 years, >10 months of data per year on average), mean quality (time series longer than 3 years, >9 months of data per year on average) and low quality (shorter time series and literature data without details on sampling time). The latter class contains the entire compilation of Preiss *et al.* [1996] and thus some points may be identical to other classes. Further references: EML-SASP [2010]; Kolb [1992]; Dibb *et al.* [1994]; Paatero *et al.* [1998]; Winkler & Rosner [2000]; Ioannidou *et al.* [2005]; Hammer *et al.* [2007]; Paatero *et al.* [2010]; Wershofen [2011] and references therein.

4.5.3. Model corrections based on (polar) natural radionuclides

The calibration of BL-FT coupling as well as the scavenging ratios in case of the Antarctic continent (without Antarctic Peninsula) and Greenland ice sheet relies on various measurements of Antarctic ^{90}Sr deposition fluxes [Pourchet *et al.*, 2003] (see figure A.4) but on one short time series of ^{90}Sr (and ^{137}Cs, respectively) atmospheric activity concentration at South Pole station, only. Since the primary intention of the model approach is to simulate ice-core ^{10}Be, some minor corrections of these polar parameters based on the various polar ^{7}Be atmospheric activity measurements (see chapter 3) are meaningful. In doing so, the parameters of the model's polar aerosol deposition (and BL-FT coupling) rely to some extend on informations from cosmogenic ^{7}Be, but still are completely independent from ^{10}Be measurements.

Section 4.5.1 revealed, that the model underestimates ^{7}Be air concentrations on the Antarctic Ice Sheet by 24-30% while it overestimates mean Greenland ^{7}Be air concentration by a factor 2.5, respectively. In case of the Antarctic it is possible to adjust the mean ^{7}Be concentration by enhancing the BL-FT diffusive coupling, reducing the dry deposition velocity (to the minimum value within the error range given in table 3.2) and the scavenging ratio. In doing so the model correctly estimates the mean ^{7}Be air concentration while the resulting ^{90}Sr deposition fluxes remain realistic (see figure A.4). However, the model still underestimates the mean ^{10}Be concentration by 13% (see figure 4.17). In case of the Greenland Ice Sheet the application of ^{7}Be atmospheric activity measurements from Summit station is difficult due to missing measurements of bomb fission (or ^{7}Be) deposition fluxes. Here, a model-measurement comparison of ^{210}Pb can help to enhance the model calibration even if the model is not capable to closely simulate ^{210}Pb: Measurements of ^{210}Pb deposition fluxes vary between 5 Bq m^{-2}yr^{-1} and 12 Bq m^{-2}yr^{-1} [Dibb, 1990; Stanzick, 2001]. With the long-term mean ^{210}Pb air concentration at Summit station of 0.1mBq m^{-3} [Dibb, 2007, 2012] resulting deposition velocities are in the range (5-12)x10^{4} m yr^{-1}. The respective model value is 5x10^{4} m yr^{-1} which is at the lower end of the measurement results. Since the range of ^{210}Pb deposition flux measurements may be partly explained with different snow accumulation rates, the low-end model value is reasonable: Lower (higher) measurements of the ^{210}Pb deposition flux correspond to snow accumulation rates of 10-18 cm yr^{-1} (57 cm yr^{-1}) [Stanzick, 2001] and the mean snow accumulation rate of the Greenland Ice Sheet in the model is 30 cm yr^{-1} (which is in the middle of the measurement conditions). It is thus reasonable to enhance the model's aerosol deposition flux by a factor of roughly 1.5 by adjusting the scavenging ratio. The resulting overestimation of Greenland Ice Sheet ^{7}Be air concentration is corrected by adjusting the BL-FT diffusive airmass coupling. In doing so the models ability to simulated mean ^{10}Be air concentration on the Greenland Ice Sheet is considerable enhanced: The model overestimated the measurements of Stanzick [2001] by 10% (see figure 4.17). As mentioned earlier, this deviation could be based on the very low data basis of Greenland ^{10}Be measurements, too. Finally, it has to be noted that the results of section 4.5 remain valid since the Ice Sheet radionuclide sink (70°S - 90°S and Greenland Ice Sheet) accounts for <0.7% of the global cosmogenic radionuclide sink, only.

4.6. Investigation of ^{10}Be transport and deposition

4.6.1. Atmospheric mixing

The short tropospheric lifetimes of aerosol-borne radionuclides (in the order of several weeks) raise the question of the degree of their atmospheric mixing. Concerning cosmogenic nuclides this is especially important, since their production rate variability depends on latitude (and altitude). In brief, short-term production rate variability due to solar activity is highest in the polar regions where geomagnetic shielding is at minimum. On the contrary, variations in the geomagnetic field strength have the largest effect on cosmogenic production in low latitudes. Hence, the amplitude of production-based air concentration variability depends on the degree of atmospheric mixing to some extent. Studies on this atmospheric transport differ in their findings: While Field *et al.* [2006] indeed find a latitude-dependence of ^{10}Be deposition flux variations based on changes in the geomagnetic field strength or solar activity, Heikkilä *et al.* [2009] report on changes independent from latitude. This latter study indicates "that ^{10}Be is well-mixed in the atmosphere before its deposition" [Heikkilä *et al.*, 2009].

Figure 4.18 shows changes of the ^{10}Be air concentration due to solar and geomagnetic activity simulated by the GRACE model. It is obvious that polar air concentrations show stronger solar and less geomagnetic modulation relative to the global mean (i.e. the global atmospheric inventory). Thus, the GRACE model results reveal that ^{10}Be is not well mixed in the atmosphere. This so-called polar enhancement effect (polar damping in case of geomagnetic variations) is especially important with respect to ^{10}Be-based reconstructions of solar activity or the geomagnetic field. In this regard the GRACE model indicates that the production related variations of polar ^{10}Be are not a linear function of the global mean production rate change. The effect is strongest in case of geomagnetic variations and the production rates of Kovaltsov & Usoskin [2010] where Antarctic (Greenland) variations are up to 51% (48%) lower than the global ^{10}Be inventory. In case of the Masarik & Beer [1999] production rates the effect is somewhat lower with 31% (25%). The polar enhancement effect of solar activity is lower, Greenland and Antarctic values as well as the different production rate calculations are comparable. In case of the Antarctic and Kovaltsov & Usoskin [2010] production rates, the polar enhancement effect varies from 9% (high solar activity) to 17% (low solar activity).

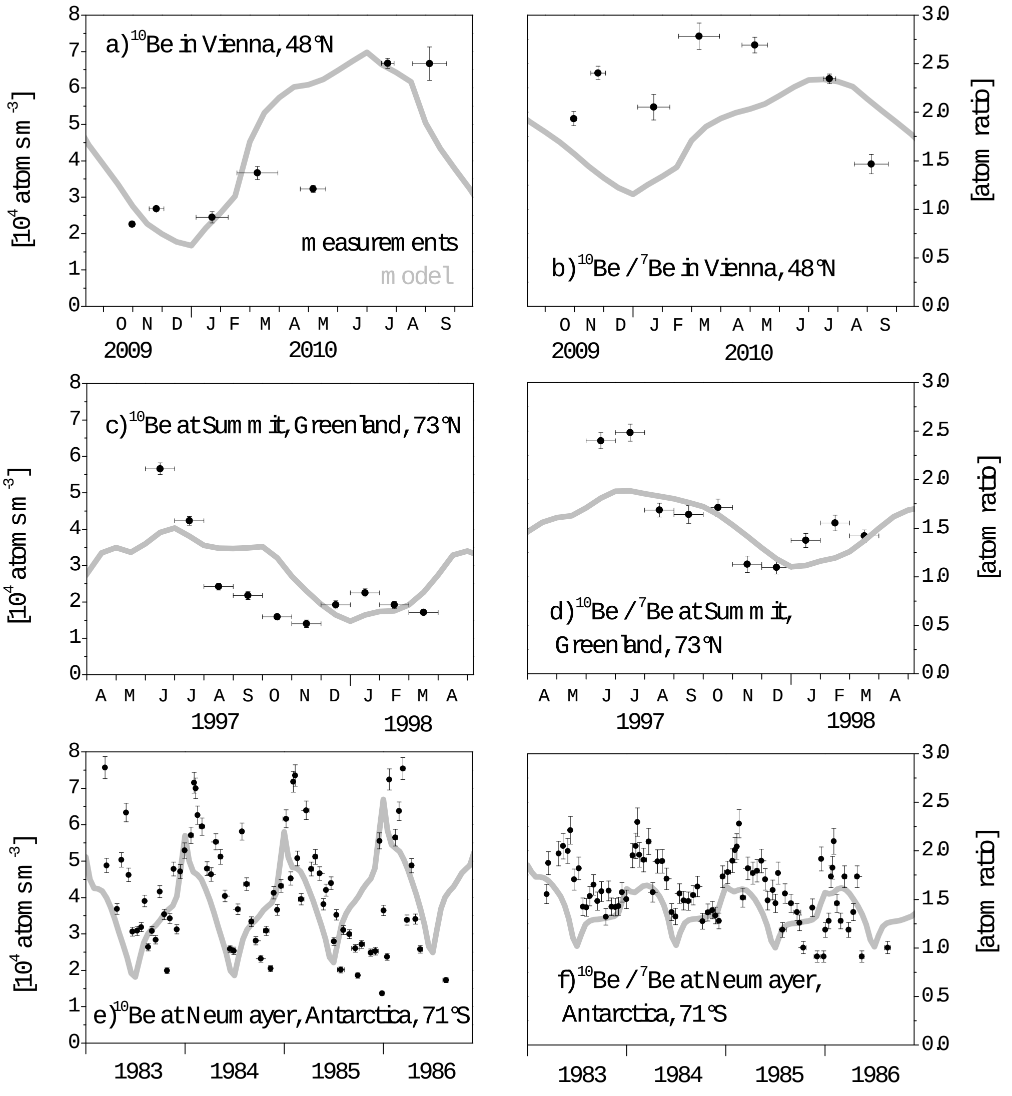

Figure 4.17.: Model measurements comparison of ^{10}Be boundary layer air concentration and the ^{10}Be/^{7}Be atom ratio in Vienna, at Summit (Greenland) and at Neumayer Station (Antarctica). Model values (grey curves) refer to results after ^{7}Be-based corrections of ice sheet aerosol sink parameterization (see text for details). In case of Neumayer measurements, errors denote standard measurement errors of 4% (AMS measurements) and 5% (gamma spectroscopy). Measurements: Bremen [2011], R. Bremen pers. comm., Stanzick [2001], Wagenbach *et al.* [1998].

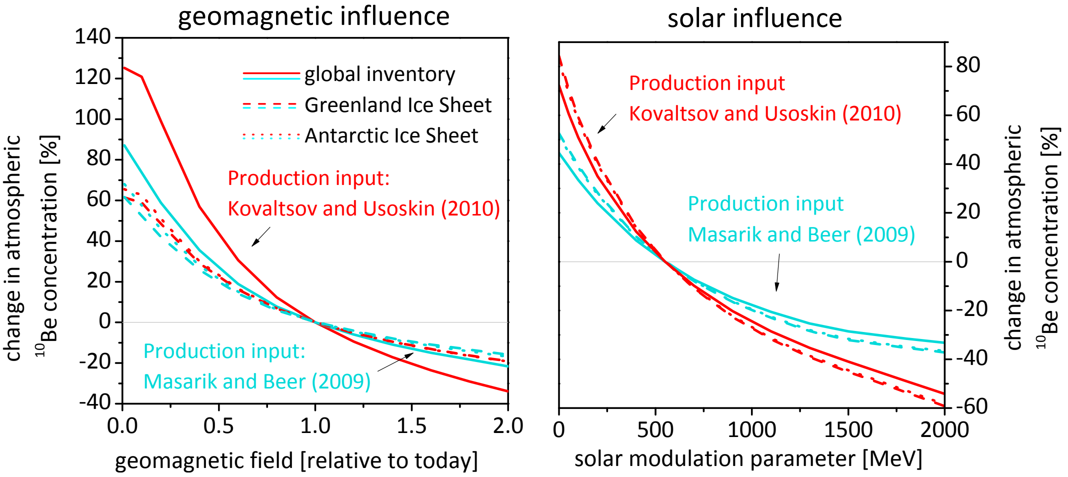

Figure 4.18.: Transport effects on the polar ^{10}Be production rate variability. Left: Relative changes of ^{10}Be as a function of geomagnetic variability. Solid lines represent the global atmospheric inventory of ^{10}Be and dashed (dotted) lines the Greenland (Antarctic) air concentration. Different colours represent different production rate calculations applied in the model. Right: Same figure for solar activity. Polar air concentrations are less (stronger) modulated by geomagnetic (solar) activity than the global mean value.

4.6.2. Sensitivity on transport and deposition parameters

While it is not possible to investigate the response of ^{10}Be on climate condition changes, the basic model approach applied in this work allows for studies on concrete transport and deposition processes. Therefore, different model parameters are varied and the effect on ^{10}Be activity concentration and deposition fluxes is investigated. The first 10 years model results (after parameter shift) are refused to ensure equilibrium conditions. So far, chosen parameter comprise

- the strength of the airmass flux related to the Brewer-Dobson circulation
- the diffusive Stratosphere-Troposphere airmass Exchange
- the airmass flux due to variable tropopause height
- the polar scavenging ratio
- the polar dry deposition
- the polar BL-FT diffusive coupling

In both cases, the Greenland as well as the Antarctic ice sheet, model results are most sensitive to changes in the dry deposition velocity, the scavenging ratio and the BL-FT coupling. On the other hand, shifts in the Brewer-Dobson circulation are less influential followed by variations in the tropopause height and finally the STE diffusive airmass exchange. To give some precise examples, a factor of two drop in the polar BL-FT diffusive flux results in a 33% (24%) lower ^{10}Be air concentration on the Greenland (Antarctic) ice sheet, whereas the same factor of two reduction in the Brewer Dobson (Tropopause height, diffusive STE) airmass flux causes a 4% (2%,1%) reduction of the Greenland ^{10}Be boundary layer air concentration. Again it has to be noted that the model applied in this study is rather basic. However, assuming a more or less realistic setup, these findings indicate that polar boundary layer parameters which govern the supply of radionuclides from the free troposphere have a larger influence on the boundary layer air concentration than changes in the global transport.

4.7. Summary

Modelling attempts can significantly contribute to the interpretation of polar ^{10}Be. The aim of this chapter was to configurate an extensively-used multi-box model of the global atmosphere for the modelling of aerosol-bound radionuclides. Different to high-resolution earth system model attempts the present approach is comparatively basic and intends to focus on climatological features (as long-term mean concentrations and seasonality) of the radionuclides under investigation. However, having short tropospheric lifetimes in the order of days to weeks, it was not a priori clear if the spatial and temporal climatology of aerosol-borne radionuclides can be reproduced with this basic (two-dimensional) box model.

After some adjustments of the model transport and resolution (mainly regarding boundary layer boxes), the GRACE model was fit with components of different (cosmogenic, terrigenic and anthropogenic) radionuclide production. Finally, the model was forced to simulate bomb fission radionuclides (atmospheric activity concentration as well as deposition fluxes) within a calibration of aerosol sink parameters. Here, major challenges were (i) the efficiency of aerosol wash-out by precipitation and (ii) the coupling of the model‘s boundary layer to the free troposphere which needed recalibration to simultaneously match both, atmospheric activity and deposition fluxes. It could be shown that this model setup is capable to quantitatively reproduce basic features of the cosmogenic radionuclides ^{7}Be and ^{10}Be which underly a strong vertical gradient in the atmosphere similar to the bomb-fission radionuclides. On the other hand, the model fails to reproduce terrigenic radionuclides in detail, likely because of a missing breakdown of the boundary layer boxes into continental (source) and maritime (no source) boxes. In polar areas the model (with applying Usoskin & Kovaltsov [2008] and Kovaltsov & Usoskin [2010] production data) underestimates mean Antarctic ^{7}Be and ^{10}Be measurements by 24-30% and 49%, respectively. Since the Greenland Ice Sheet lacks any measurements of bomb fission radionuclides air activity, the calibration was updated by using measurements of natural ^{7}Be and ^{210}Pb. In doing so the model matches mean polar ^{10}Be air concentrations within 13% (Antarctica) and 10% (Greenland Ice Sheet).

For the interpretation of polar records, the following findings on the radionuclides' transport and deposition may be emphasized:

- **Production rate calculations of cosmogenic radionuclides**
  Both, the cosmogenic production rate calculations of Masarik & Beer [2009] and Usoskin & Kovaltsov [2008]/Kovaltsov & Usoskin [2010] were applied within this study. Model-measurement comparisons reveal, that the latter production data quantitatively reproduce atmospheric activity concentrations, while the calculations of Masarik & Beer [2009] underestimate the ^{7}Be (and ^{10}Be) measurements by a factor of roughly 2. Time series of atmospheric observations are too short to clarify if the stronger modulation of the production rate by solar and geomagnetic variability inherent to the Usoskin & Kovaltsov [2008] data is in line with observations.

- **The polar radionuclide sink**
  Polar radionuclide deposition fluxes are significantly lower compared to moderate latitudes. The model results indicate, that the likewise depleted polar precipitation rates cannot solely account for these low deposition fluxes. In fact, a significant reduction of the aerosol scavenging ratio as well as a reduced airmass exchange with the free troposphere are required to reproduce polar radionuclides' deposition fluxes.

- **The 'footprint' of polar radionuclides**
  Regarding the distribution of cosmogenic radionuclide production in the atmosphere the question on the amount of atmospheric mixing has some impact on the production signal (solar and geomagnetic variability) seen at polar latitudes. In short, an enhanced global mixing is accompanied with a higher (long-term) variability due to geomagnetic variations but lower variations based on solar activity. The model results of this study point to latitudinal differences in the amount of production variability related to an incomplete mixing of ^{10}Be in the atmosphere. This is in line with the model results of Field *et al.* [2006] but in contradiction to Heikkilä *et al.* [2009].

Finally, the results of the model validation with ^{7}Be measurements advise the application of the model on the long (ice core) timescale.

5. Looking to the past: Interpretation of ^{10}Be ice core records using a climatological model approach

5.1. Introduction

Having a model which successfully reproduces the atmospheric climatology of aerosol-bound radionuclides consuming moderate computational power, it is possible to quantitatively simulate atmospheric ^{10}Be concentrations on the long (ice core) timescale up to 75kyr. For the first time, model results can thus be quantitatively compared to ice core measurements if the model is coupled to an air-firn transfer model. To do so, results of chapter 3 and 4 are combined and the model timescale under investigation is considerably expanded up to the last 75kyr. A major challenge is the definition of crucial model input parameters. So far, reconstructions of the accumulation rate as well as geomagnetic and solar activity (during the Holocene) are chosen to drive the time variations of the model results. In the following, these model input parameters are presented in detail (section 5.2). Afterwards, the model is applied on two different periods of time:

1. During the Holocene high-resolution data allow for the investigation of decadal to centennial variability. Moderate carbon cycle changes enable the application of ^{14}C-based reconstructions of past solar activity as model input. In doing so, a model-measurement comparison allows for the investigation of shared common production-related variability in ^{14}C and ^{10}Be time series.

2. The Last Glacial Maximum and the subsequent glacial-interglacial transition marks a period of strongest climate variations. On this long timescale, confrontation of model results and ice-core measurements may show if geomagnetic and accumulation rate changes are able to quantitatively explain the ^{10}Be ice core variability. If not, rigorous changes in the ^{10}Be transport and deposition parameters may have to be taken into account

In the following, most figures show different quantities varying in time. Different to the common practice in ice core research, the time axis is chosen to increase from past to present. This is done on account of the model calculations which are naturally evolving forwards in time. The time axis refers to years before present (i.e. the age). Unfortunately, studies on paleoclimate research differ in the reference date: While some authors give years before 1950 AD (commonly denoted as [BP]), recent studies report on years before 2000 AD [b2k]. Following notation of the most recent Greenland ice core timescale, the latter date is used as reference and labelling of plots is [b2k].

5.2. The model approach: Combination of the atmospheric box-model with the air-firn transfer module

Building of the atmospheric ^{10}Be model was extensively presented in chapter 4. The model was proven to be suitable to simulate global atmospheric boundary layer activity of ^{7}Be and the polar air concentration of ^{10}Be. Due to the climatological approach and the comparatively low resolution, the model can be run on timescales of several thousand years. To give the order of magnitude of computational power involved: A multi-processor version of the model (see appendix D) is able to simulate 50kyr (monthly resolution) in about one day. Monthly resolution is necessary to account for interference of different parameters' seasonalities. The atmospheric model outcomes involve radionuclide deposition fluxes which basically are the only atmospheric sink of long-living radionuclides like ^{10}Be. However, different to radionuclide air concentrations, deposition fluxes show strong spatial variability due to the precipitation rate involved. Hence, the respective 10° resolution model results are not supposed to match deposition measurements at a single site but rather balance the atmospheric concentration. Indeed, chapter 3 revealed that mean ^{10}Be concentrations of Antarctic ice vary by a factor of eight, while respective air concentrations are comparable over a wide spatial scale. Hence, to directly simulate ice concentrations at a single drilling site the air-firn transfer model which is presented in section 3.4 is applied. In doing so, the global atmospheric model serves as an online input of polar ^{10}Be air concentration into the air-firn module. Figure 5.1 summarizes the model approach in a simple sketch. The second time-varying input parameter to the air-firn-transfer model is the local accumulation rate derived from the respective ice core. Numerically there is no feedback mechanism from the air-firn module to the atmospheric model involved. More precisely, the air-firn module does not serve as a radionuclide sink to the global atmosphere. This oversimplification is reasonable since this module represents the local conditions at a specific drilling site which are not supposed to influence the global (or even regional) ^{10}Be cycle.

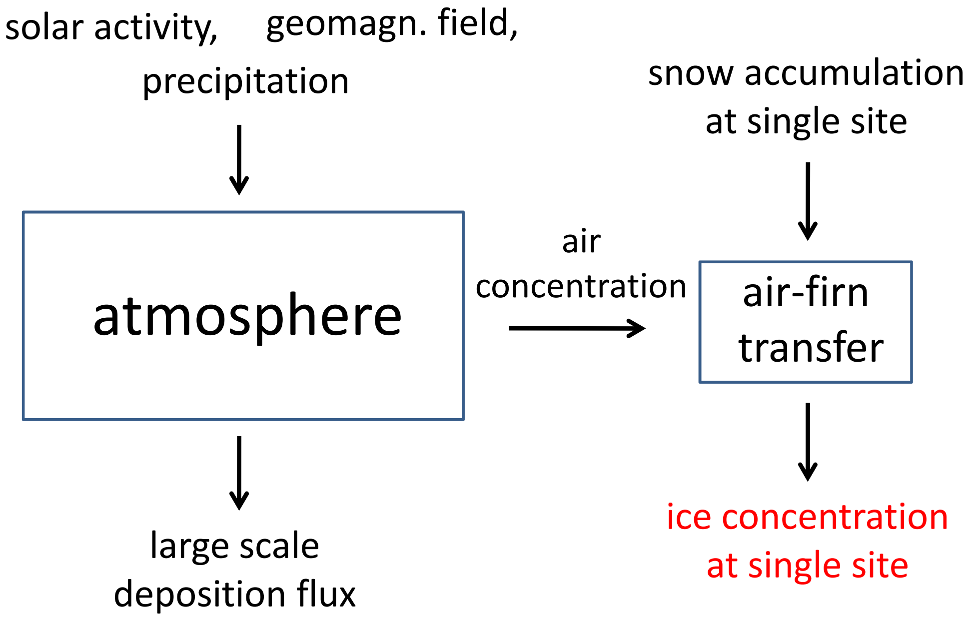

Figure 5.1.: Sketch of the model approach to simulate ^{10}Be ice concentration. The atmosphere represents the global model as presented in chapter 4 while the air firn transfer module is put forward in section 3.4. Note that a variety of parameters actually are input to the model setup of the global atmosphere. However, nearly all of these are constant or underly a constant seasonal cycle whereas the here shown input parameters are time-dependent on different scales.

5.3. Time-dependent model input

Various parameters are input to the model setup defined above. However, due to the climatological approach, nearly as of these are constant or underly a seasonal variation only. This chapter aims at defining the time-dependent input parameters of the model comprising the accumulation/precipitation rate as well as solar and geomagnetic activity. To do so, state-of-the-art knowledge is summarized and supplemented with own calculations (in case of the GRIP accumulation rate and ^{14}C-based solar activity).

5.3.1. Past precipitation rates

Although being a fundamental parameter in the climate system, the reconstruction of past precipitation rates remains a continuous problem in climate science. With respect to the present model study, long-term variations in the precipitation rate concern two major aspects (see figure 5.1): (i) Variations in the global aerosol sink and the radionuclides' atmospheric lifetimes and (ii) the interpretation of ice core signals with respect to the local air-firn transfer, respectively.

Polar accumulation rates

Polar ice cores basically allow the reconstruction of past accumulation rates due to precipitation stored in the glaciers. However, flow-dynamics of the ice and the related thinning of annual layers by reason of vertical strain prevent a direct measurement. In case of moderate/high accumulation sites like the Greenland summit (e.g. the GRIP and GISP2 ice cores), it is possible to directly determine annual layer thickness up to a certain ice depth by using measurements of stable isotopes, soluble ions or dust. However, ice flow models have to be applied to calculate the thinning of these annual layers and to reconstruct changes in the annual snow accumulation rate, respectively. Dahl-Jensen *et al.* [1993] used a simple steady state model to calculate the thinning of the annual layer thicknesses measured in the upper part of the GRIP core. They could thus reconstruct accumulation rates from measured annual layer thickness in parts of the core and found a correlation with δ^{18}O measurements. This correlation permits an estimation of the accumulation rate changes on the basis of the high-resolution stable isotopes measurements (covering the total core) using an exponential relation. Johnsen *et al.* [1995] used this kind of relation and the respective accumulation rates are given in figure 5.2 (lower panel). The picture also shows the results of Cuffey & Clow [1997] who report on accumulation rates obtained from the application of a combined heat- and ice-flow model based on GISP2 ice core measurements. Their results for the snow accumulation history are somewhat lower than the GRIP data and the difference between Greenland interstadial and Greenland stadial periods is less pronounced.

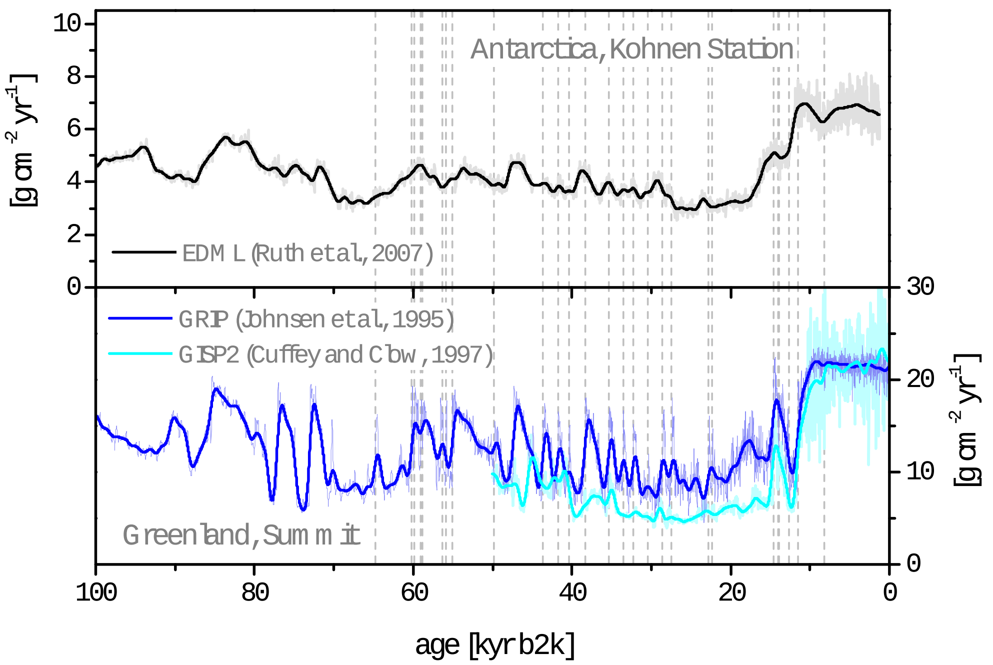

Figure 5.2.: Comparison of accumulation rate reconstructions for the drilling sites EDML (Kohnen, Antarctica, Ruth *et al.* [2007]), GRIP (Summit, Greenland, Johnsen *et al.* [1995], ss09sea timescale) and GISP2 (Summit, Greenland, Cuffey & Clow [1997]). Time axis is given in years before 2000 (b2k) following common practice. Note that GRIP and GISP ice cores have a distance of 30km and should basically record similar climate variations. Vertical lines indicate beginning of Greenland interstadials as given in Southon [2004] (on ss09sea timescale). Shaded areas denote the full data resolution (i.e. 20yr interpolation in case of GISP2).

The authors find a frequency dependent relation between surface temperature and accumulation rate and thus question the application of a constant relation of stable isotopes and accumulation rates. While there is a common correlation on the glacial-interglacial timescale, smoothed data show a negative correlation during the Holocene period. As in the study of Kapsner *et al.* [1995], they give a shift of storm tracks as a major explanation. The comparison of the data from Johnsen *et al.* [1995] and Cuffey & Clow [1997] show the difficulties of accumulation rate reconstruction, even in case of medium accumulation sites. In case of very low accumulation rates, like on the Antarctic plateau, ice cores lack the information on the annual layer thickness and a common approach is to reconstruct accumulation rates from temperature reconstructions based on stable isotope measurements. This is done by using the assumption that "average accumulation on an ice sheet should vary with the temperature-derivative of the saturation pressure at cloud level if dynamical processes in the atmosphere do not change" (Alley *et al.* [1993] and references therein). An example for such a reconstruction is given by Ruth *et al.* [2007] for the EDML drilling site, depicted in figure 5.2 (upper panel). However, this isotopic-temperature based approach implies several assumptions which probably oversimplify polar snow accumulation. Udisti *et al.* [2004] calculated the ratio between Dome C and Vostok accumulation and found a ratio varying from 1.4 during the Holocene to 1.0 during the last glacial period. The authors give "variations in regional atmospheric circulation" as being the most likely reason for this variation. If this is true, "the assumption of accumulation rate depending only on temperature change, as derived from the conventional approach, needs modification" [Udisti *et al.*, 2004]. In any way, the approach fails in case of several ice-coring sites which underwent dramatic changes in ice sheet elevation, for example. Furthermore, in case of small coastal domes (like e.g. Antarctic Siple Dome), the Clausius Clapeyron relation may not completely control synoptic precipitation (E. Waddington, pers. comm.).

In summary, published accumulation rates from both, Antarctica and Greenland are in agreement regarding a major drop from Holocene to the Last Glacial Maximum as well as variability within the last glacial period (e.g. related to Dansgaard-Oeschger events). However, detailed features like the mean Holocene/LGM ratio or the glacial stadial/interstadial amplitudes differ not only between Antarctic and Greenland reconstructions but also in case of different reconstructions for the same site.

In the current model setup the accumulation rate reconstruction from Ruth *et al.* [2007] is applied for the EDML core and the one of Parrenin *et al.* [2004] for the Vostok site. In case of Greenland, accumulation rate reconstructions require an update owing to a refinement of the GRIP ice core chronology based on the recent North Greenland Ice Core Project (NGRIP, some 100km north of the GRIP/GISP2 drilling sites). Glaciological conditions at that drilling site allow for the detection of annual layers down to a larger depth and thus a straightforward dating of the core [NGRIP, 2004]. This enables the construction of a more precise common Greenland Ice Core Chronology 2005 (GICC05) [Vinther *et al.*, 2006; Rasmussen *et al.*, 2006; Andersen *et al.*, 2006; Svensson *et al.*, 2008] by combining three Greenland cores (Dye-3, GRIP and NGRIP). It has to be mentioned, that dating of an ice core is an ongoing process resulting in different timescales for the same core (see e.g. Southon [2004] for a review on the Greenland Summit timescales) and the new GICC05 scale is considered the most precise timescale at the moment. The application of this timescale to the GRIP core significantly alters the reconstruction of respective accumulation rates. However an adaption of GICC05 to the GRIP core beyond 32kyr b2k as well as a recalculation of accumulation rate reconstructions is not published so far. Using (i) the published adaption of the GICC05 scale to the GRIP core from 0 - 32 kyr b2k [Rasmussen *et al.*, 2008], (ii) tie points of Greenland interstadial events as given in Southon [2004] and Wolff *et al.* [2010] from 32 kyr b2k - 60 kyr b2k and (iii) the ss09sea timescale (A. Svensson, pers. comm.) subtracting 705 years (following Wolff *et al.* [2010]) beyond 60kyr b2k, the GICC05 scale was adapted to the GRIP core. Subsequently, snow accumulation rates are calculated from annual layer thickness using ice flow model results of S. Johnsen (A. Svensson, pers. comm.). Figure 5.3 shows a) the results of the timescale adaption as well as b) the vertical strain rate of the GRIP core (i.e. the thinning of the annual layer thickness due to ice flow) modelled by S. Johnsen (A. Svensson, pers. comm.). The resulting recalculated accumulation rates (on the GICC05 timescale) are given in the lower part of the figure (d) together with results from previous studies. It is obvious, that the new GICC05 accumulation rate reconstruction is significantly lower especially in the 15kyr-20kyr b2k period.

Extra-polar accumulation rates

In addition to polar records, reconstructions of mid- or low-latitudinal precipitation are needed to constrain the model's global aerosol sink behaviour. However respective assessments covering the last glacial maximum are even more sparse than polar investigations. Moreover, on the global scale, climate conditions show significant spatial variations which make investigations at a specific sampling site less representative for the global atmospheric aerosol sink. Thus, results from global climate modeling attempts might be a good first-order approach to quantify possible precipitation changes on the global scale. The Paleoclimate Modelling Intercomparison Project (PMIP) concentrates paleoclimate modeling activity and Braconnot *et al.* [2007] summarize large-scale features of model runs from several state-of-the-art climate models with respect to mid-Holocene and Last Glacial Maximum conditions. They give precipitation pattern "characterized by a large-scale drying (up to -1 to -4 mm/d [(-0.37 to -1.46) m yr^{-1}] depending on the regions) resulting from the large-scale cooling and reduced evaporation" [Braconnot *et al.*, 2007]. According to the authors, the "simulations show that in both hemispheres at high latitudes the drying is largest over the ice sheets and sea ice". Hence, the polar recon-

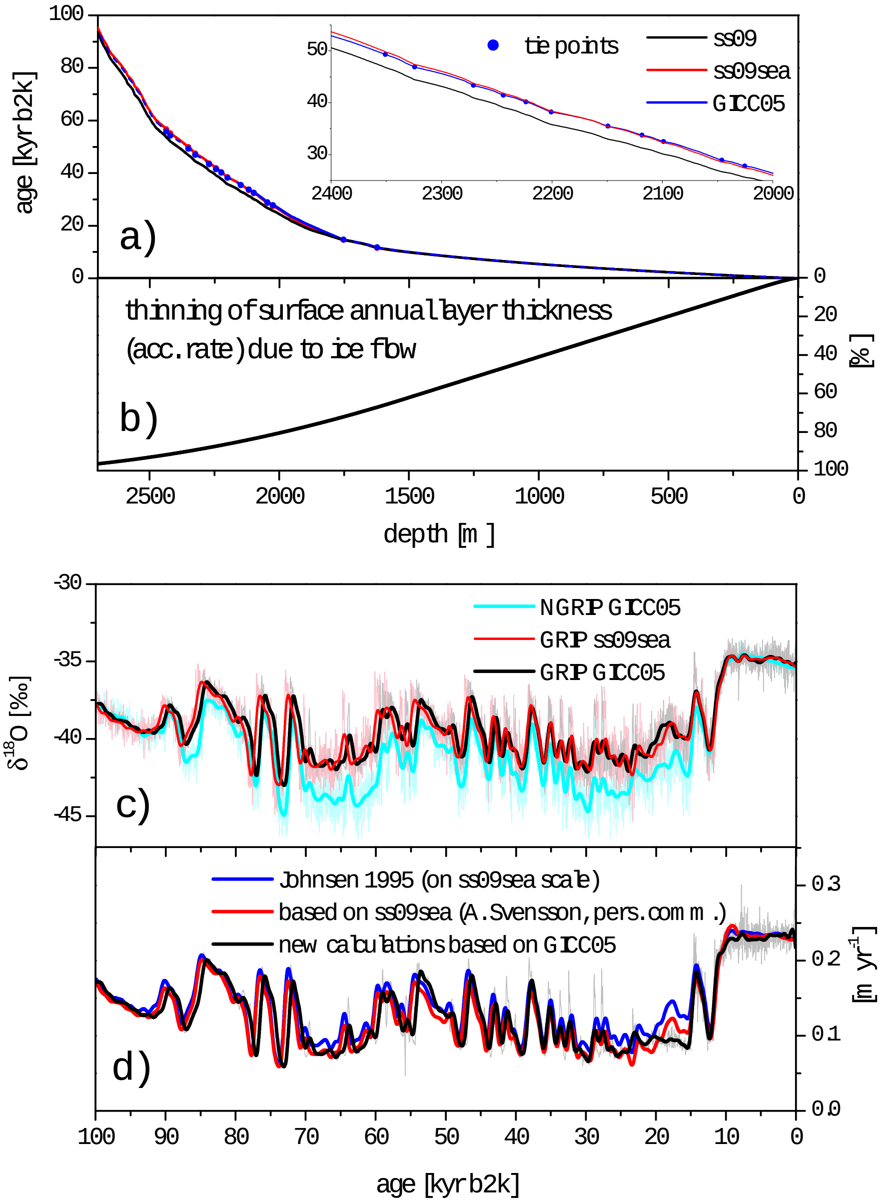

Figure 5.3.: Recalculation of the GRIP ice core accumulation variability. a) Different depth-age scales for the GRIP ice core together with tie points given in Southon [2004] and Wolff *et al.* [2010] which are used to extend the GICC05 scale to ages older than 32kyr. b) Thinning of the annual layer thickness modelled by S. Johnsen (A. Svensson, pers. communication). c) δ^{18}O measurements at the GRIP and NGRIP core. d) Reconstruction of GRIP ice accumulation rates from Johnsen *et al.* [1995] and calculations based on the ss09sea and GICC05 scale. Note that the significant older ages of the ss09sea and GICC05 depth age scales compared to ss09 (see a) result in lower accumulation rates during the Last Glacial Maximum.

structions (shown in previous section, figures 5.2 and 5.3) may give a kind of upper limit to changes in the global precipitation regime. Finally, having a look at single model results (http://www.ncdc.noaa.gov/paleo/modelvis.html, October, 2011), it seems that the overall latitudinal distribution of precipitation rates does not significantly change in the Last Glacial Maximum runs except for an attenuation in polar regions. However, there is significant scatter between different model results which inhibits a clear quantitative estimation: In mid- and low-latitudes, latitudinal average differences between present day and Last Glacial Maximum (21 kyr b2k) precipitation rate broadly lie in the +/- 30% range. Finally, for the here presented model study, the primary scenario is to apply reconstructions from ice cores and restrict precipitation changes to the high-latitudes beyond ±60°. In doing so, precipitation changes are estimated to be equal to net accumulation rate changes, which is a reasonable first-order assumption for the polar areas (see chapter 3).

5.3.2. Reconstructions of the geomagnetic field

On the long timescale of several thousand years, production rate variability of cosmogenic nuclides is supposed to be governed by variations in the geomagnetic field strength (see section 2.1 for details on the effect of geomagnetic shielding). During the last two decades, strenuous efforts were made to reconstruct past variations of the geomagnetic field intensity (see e.g. Valet [2003] for a comprehensive review). Basically, different approaches comprise (i) thermoremanent magnetization of archaeological pottery/material and volcanic rocks, (ii) relative paleointensity derived from (marine) sediments and (iii) records of cosmogenic radionuclides in sediments and ice cores. All three methods considerably differ concerning the manner of recording the geomagnetic field. While on the one hand thermoremanent magnetization offers a direct and quantitative measure of the geomagnetic field at a single site and an explicit date in the past, sedimentary records 'sample' a wide-stretched time-interval of geomagnetic variations. Hence, in the latter case 'fast' oscillating (higher) non-dipole moments of the geomagnetic field are less influential [Valet, 2003]. On the other hand, sedimentary records provide only relative information and the calibration to absolute values is often complicated due to low sedimentation rates in connection with a scrapping of the youngest part of the samples (sediments). Figure 5.4 shows different reconstructions of the geomagnetic field strength based on thermoremanent and sedimentary magnetization. Studies based on ^{10}Be are excluded from this compilation to avoid circular argument in the interpretation of ice core ^{10}Be. To quantify changes in the geomagnetic dipole strength, the Virtual Axis Dipole Moment (VADM) is shown which supposes an axial geocentric dipole. This is a reasonable assumption if "the time period covered by the calculation is long enough (i.e., on the order of at least several millennia [...])" [Valet, 2003]. Indeed geomagnetic and geographic poles are generally not coincident on shorter timescales which may have an influence on the local production of cosmogenic nuclides (see e.g. McCracken [2004] for an assessment).

Laj *et al.* [2004] provide a reconstruction of the geomagnetic field intensity over the last 75 kyr, based on a selection of 24 high-accumulation marine sediment records (GLOPIS-75). They used the results of Laj *et al.* [2000] (NAPIS-75) to correlate the individual records and the reconstruction of the Holocene geomagnetic intensity from Yang *et al.* [2000a] to extrapolate and normalize their results to absolute values. Similar results are reported from Channell *et al.* [2009] who used a different stacking approach (together with a diverse compilation of records). Different to these studies on relative geomagnetic paleointensity, the study of Knudsen *et al.* [2008] focuses on absolute paleointensity samples. The authors used "all absolute paleointensity data published in peer-reviewed journals" to reconstruct the intensity of the geomagnetic field. While they provide a reconstruction over the last 50kyr, their focus is the Holocene period due to the data basis significantly dying in the pre-Holocene period. Third, model studies on the geomagnetic field combine both kind of measurements; figure 5.4 shows results from Korte *et al.* [2011] and Ziegler *et al.* [2011]. The first study applies a spherical harmonic geomagnetic field model based on archaeo- and paleomagnetic data to investigate the Holocene geomagnetic field. In doing so, they take into account higher moments of the field. Ziegler *et al.* [2011] use a "penalized maximum likelihood [...] approach to recover a cubic B-spline representation of axial-dipole field variations".

Summing up the results of paleomagnetic reconstructions shown in figure 5.4, different studies coincide in main features of the past geomagnetic dipole field strength during the last 75kyr. These are (i) an overall increasing trend from the Last Glacial Maximum to current values, (ii) a pronounced minimum around 42kyr attributed to the Laschamp geomagnetic excursion and (iii) a return to the current strength around 50kyr b2k. However, other details like "short-term" oscillations as well as the timing, duration and strength of the Laschamp event (around 42kyr b2k) remain unclear. For the ^{10}Be model study the data of Laj *et al.* [2004] serves as the main input but implications of other records will be discussed.

5.3.3. Reconstruction of the solar activity using ^{14}C measurements

Variations of solar activity modulate the production rate of cosmogenic radionuclides (see details in section 2.1). At first, neutron monitor measurements which are available since the first half of the 20th century clearly show the decadal ('11 years') variation of cosmic rays which hit the earth surface. This Schwabe cycle is clearly seen in high-resolution measurements of cosmogenic radionuclides in air and ice (see e.g. the Neumayer time series shown in section 3.2 for the former). Second, observations of sunspots which go back to the early 17th century point to periods of low solar activity (and correlated higher radionuclide

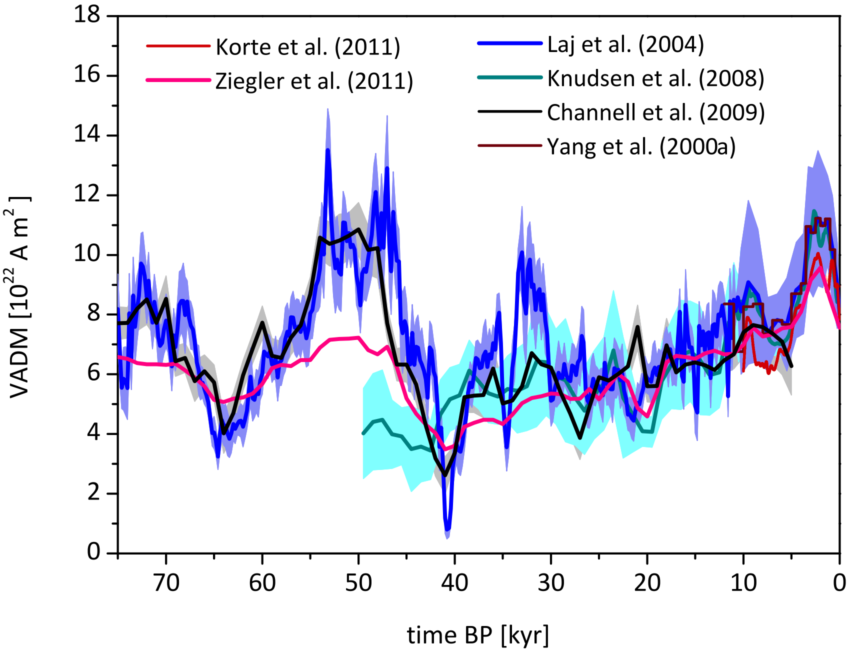

Figure 5.4.: Reconstructions of the virtual axis dipole moment strength (VADM, see text for definition). Absolute paleointensity records [Yang *et al.*, 2000a; Knudsen *et al.*, 2008] compared to relative paleointensity records [Laj *et al.*, 2004; Channell *et al.*, 2009] and model results [Korte *et al.*, 2011; Ziegler *et al.*, 2011]. Shaded areas denote according uncertainty estimates.

production rates) which span several decades. Indeed, records of cosmogenic radionuclides correlate fairly well with sunspot observations (e.g. Berggren *et al.* [2009] and Horiuchi *et al.* [2008]) and indicate solar activity oscillations on the timescale of centuries (Gleissberg cycle, de Vries cycle). Finally, variations on longer timescales of several centuries are discussed but remain ambiguous (see e.g. review in Usoskin [2008]).

So far, the reconstruction of solar activity beyond the observational period is restricted to the application of cosmogenic radionuclides. In addition to ice core ^{10}Be, ^{14}C measurements in climate archives as tree rings allow the investigation of the solar activity parameter ϕ (see section 2.1 for definition). Admittedly, stable climate conditions are required to exclude drastic changes in the carbon cycle which may modulate the atmospheric Δ^{14}C value as well. Indeed the climate of the Holocene period is commonly supposed to be less variable and ^{14}C-based reconstructions of solar activity have been published for the last several thousand years during the last decades (e.g. Solanki *et al.* [2004]). However, ice core based reconstructions of the atmospheric CO_2 concentration reveal a decrease of approx. 7 ppm between 11 kyr b2k and 8 kyr b2k followed by a subsequent increase of 20ppm to a preindustrial CO_2 concentration of 280ppm in the atmosphere [Indermühle *et al.*, 1999]. While these variations are significantly lower than the glacial-interglacial rise of 76ppm [Monnin *et al.*, 2001], they nonetheless indicate changes of carbon cycle fluxes during the last 11kyr. So far, the Holocene carbon cycle changes lack a straightforward explanation. Joos *et al.* [2004] give "a range of mechanisms, including calcite compensation in response to earlier terrestrial uptake, terrestrial carbon uptake and release, SST changes, and coral reef buildup" as contributions to the last 8kyr CO_2 rise. In terms of ^{14}C, especially carbon fluxes from "old" (^{14}C depleted) carbon reservoirs may pretend production signals. Recently, measurements of the stable isotope δ^{13}C in ice-core CO_2 point to oceanic "carbonate compensation of earlier land-biosphere uptake and coral reef formation" [Elsig *et al.*, 2009] as being the main reason for the 20ppm Holocene CO_2 rise. Dedicated carbon-cycle studies are necessary to investigate a possible influence on the atmospheric Δ^{14}C. However, very briefly, the process of ocean compensation of the terrestrial carbon uptake results from a shift in the marine carbonate chemistry equilibration. The resulting increase of the CO_2 partial pressure leading to a higher air-sea CO_2 exchange [Joos *et al.*, 2004] should have minor effects on Δ^{14}C at first glance (see e.g. Siegenthaler *et al.* [1980]).

Assuming only minor effects of the Holocene carbon cycle on Δ^{14}C, the well established ^{14}C calibration record (INTCAL09, Reimer *et al.* [2009]) can be used to reconstruct solar activity changes during the Holocene period. However, despite excluding minor climate effects during the Holocene, carbon cycle dynamics require the usage of a carbon cycle model to infer ^{14}C production rate variability from tree ring records (see appendix E for details on the methods). Figure 5.5 shows the ^{14}C data used to reconstruct the solar activity (lower part) together with the resulting solar modulation parameter (upper part). A main caveat of this reconstruction is the unknown carbon cycle during the last glacial

- more precisely, the unknown ^{14}C production rate during the last glacial. Changes of atmospheric Δ^{14}C due to carbon cycle changes, which have most likely occurred during the glacial-interglacial transition, quickly reach new equilibrium conditions (e.g. Muscheler [2000]; Asgeirsson [2012]). The early Holocene Δ^{14}C can thus be assumed to be independent from past carbon cycle dynamics. On the other hand, it is important to consider, that a step function in the ^{14}C production causes an atmospheric decay/rise to a new equilibrium state in the order of several thousand years. Since the ^{14}C production rate at the end of the last glacial period is not known (i.e. masked by unknown carbon cycle fluxes), this indefiniteness bears on several thousand years of the early Holocene.

Taking this effect into account, two different scenarios are used to reconstruct the solar modulation parameter from the INTCAL09 ^{14}C data set: Scenario 1 estimates pre-Holocene ^{14}C production rates from INTCAL09 and thus neglects major changes in the relation between ^{14}C production and atmospheric Δ^{14}C (i.e. no carbon cycle changes assumed). In scenario 2 pre-Holocene ^{14}C production is estimated from a reconstruction of the geomagnetic dipole strength (GLOPIS75). Hence, in the latter scenario the difference between the INTCAL Δ^{14}C data and Δ^{14}C calculated from the geomagnetic field strength is accredited to carbon cycle changes (see appendix for details). The reconstructed solar modulation parameter is given in figure 5.5 (upper panel). Both scenarios significantly differ in the first millennia of the Holocene and resemble during the mid and late Holocene. Previous publications of solar activity reconstructions show results which are similar to scenario 1 [Solanki *et al.*, 2004; Vonmoos *et al.*, 2006].

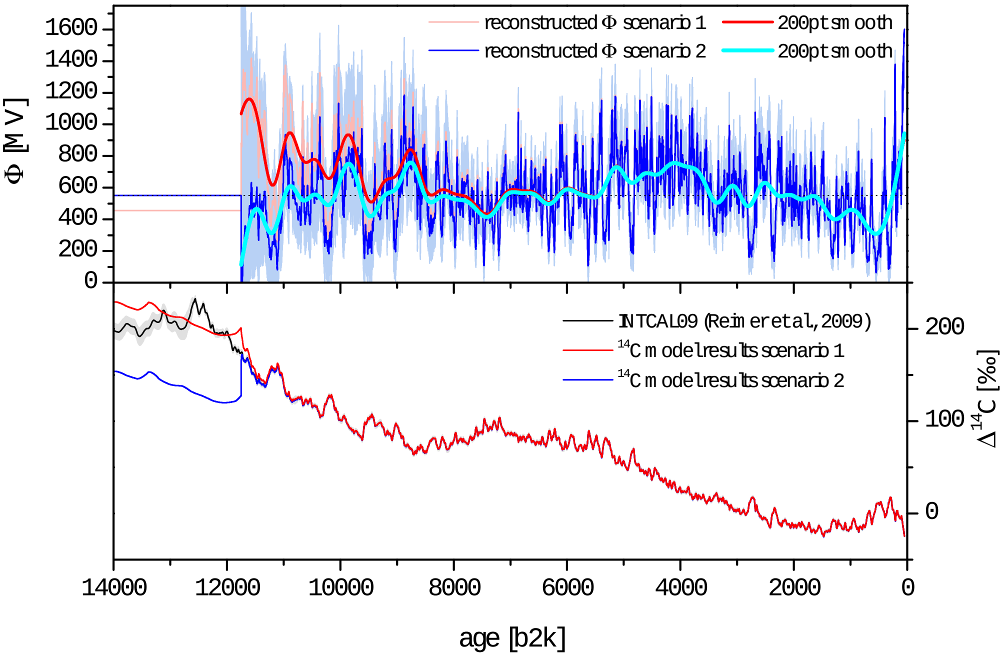

Figure 5.5.: Solar modulation parameter reconstructed from ^{14}C measurements using a carbon cycle model as well as reconstructions of the geomagnetic dipole strength. Upper picture: Solar modulation parameter resulting from two different scenarios of pre-Holocene conditions (see text and appendix for details). The error range shown for the scenario2 data only (shaded area) is based on the error of the geomagnetic field reconstruction (which exceeds the INTCAL 1σ error). Lower picture: Compilation of ^{14}C measurements (INTCAL09, Reimer *et al.* [2009]) used for the reconstruction together with ^{14}C carbon cycle model result using ϕ (shown in upper picture) again as an input parameter for quality control.

5.4. Model results: The Holocene

Using the input data given in section 5.3 the model is run on different timescales to simulate ice core ^{10}Be. At first, model runs are restricted to the Holocene period. The Holocene encompasses the current interglacial period persisting since the Younger Dryas cold event 11.7 kyr ago. Although generally regarded as a period of stable climate conditions, paleoclimate studies based on multi-proxy records as well as modelling attempts point to significant climate variability during the Holocene [Mayewski *et al.*, 2004; Schmidt *et al.*, 2004]. An overall summary of these variations is given in the current IPCC report [Jansen *et al.*, 2007] and changes in the Earth‘s orbit as well as volcanic and solar forcing are given as main forcings among others. According to the latter report, both, "long-term and abrupt changes in temperature, precipitation, monsoon dynamics and El Nino-Southern

Oscillation" are induced by climate forcings during the Holocene. Mayewski *et al.* [2004] report on periods of rapid climate change which mostly are "characterized by polar cooling, tropical aridity, and major atmospheric circulation changes". Due to its short atmospheric lifetime ^{10}Be may be sensitive to high-frequency variations of atmospheric circulation or deposition related to climate variability. Indeed, Pedro *et al.* [2006] find climate modulation of ^{10}Be in an Antarctic snowpit study.

For the investigation of Holocene ^{10}Be two measured ice core records are simulated which have been subject to studies on solar activity: The recent EDML ice core from Antarctic Kohnen station (75°0'S, 0°4'E, 2892 m a.s.l.) [Steinhilber *et al.*, 2012] as well as a much applied combination of GRIP and GISP ^{10}Be data from the vicinity of Greenland Summit (72°32'N, 37°29'W, 3216m a.s.l.) [Yiou *et al.*, 1997; Finkel & Nishiizumi, 1997; Vonmoos *et al.*, 2006; Muscheler *et al.*, 2007; Steinhilber *et al.*, 2012]. As discussed in section 5.3, the model input data comprises accumulation rate variability (as well as precipitation changes), geomagnetic changes from magnetization studies and ^{14}C-based solar activity (for the Holocene period). For the GRIP and GISP data, the 'GICC05' timescale is applied which is extended in time and adapted to the two ice cores. In case of the EDML core, the 'EDML1' timescale [Ruth *et al.*, 2007] is used.

Model results

Figure 5.6 shows the ^{10}Be model results of EDML (Antarctica) ice concentration compared to respective measurements (Steinhilber *et al.* [2012], J.Beer, pers. comm.). It is obvious that the model underestimates the absolute ^{10}Be ice concentrations for Kohnen station. Both, errors in the atmospheric air concentration as well as the air firn transfer contribute to this mean deviation of approx. 42% (Kovaltsov & Usoskin [2010] production calculations applied in the model study). For this reason, data normalized to the respective overall mean are given in figure 5.6, too. Despite the underestimation of the mean concentration, the model reproduces well the main features of the measurements: (i) A longterm trend with higher values around 6-9kyr before present and lower ^{10}Be concentrations between 2kyr and 5kyr before present and (ii) a variety of short-term spikes with broadly 100-300 years duration. Model-measurements deviations (figure 5.6c) show an interquartile range of 15% and reveal that several short-term spikes are over- or underestimated. Correlation between EDML model and measurements (normalized) amounts 0.69 and indicates that a good deal of measurements variability is simulated by the model. Published high-resolution data of the GRIP ice core [Muscheler *et al.*, 2004; Vonmoos *et al.*, 2006] could not be obtained from authors in charge of the data, but a comparison of model results to previously published low-resolution data (R. Muscheler, pers. comm.) reveals that the model underestimates the GRIP measurements by 28% (using production rate calculations of Kovaltsov & Usoskin [2010] for the model run). The nearby GISP2 ice core

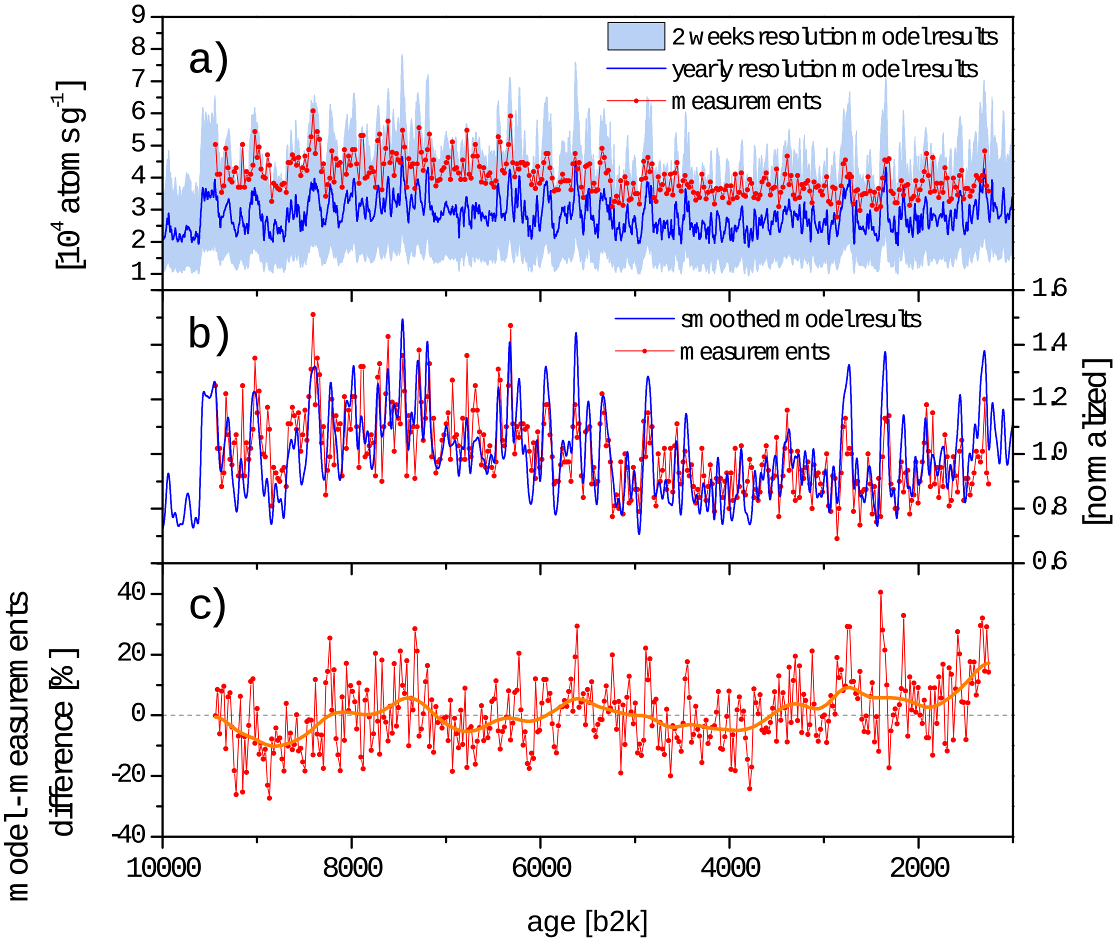

Figure 5.6.: Model results of EDML ^{10}Be ice concentration compared to respective measurements. a) Comparison of absolute ice concentration. Blue shaded band denotes the full (sub-monthly) model resolution. The model underestimates the overall mean by 42%. b) Comparison of normalized data. The model results are smoothed (cutoff frequency: 0.5 x 1/22 years^{-1}, Nyquist frequency for respective measurements resolution) to approximate the measurements resolution of 22 years. c) Model-measurements difference of normalized data. The orange line denotes smoothed data using a Gaussian filter which dampens the amplitude of a 250 year period to 0.1%. Measurements: J. Beer, pers. comm.

allows for model-measurements comparison of parts of the Holocene period (figure 5.8) and supports findings from EDML core. Moreover a comparison of the GRIP (high-resolution) ice core record with EDML shown in Steinhilber *et al.* [2012] (figure 2A) indicates, that both records show a large amount of similarities.

For the first time the model simulates a monthly ice core resolution which enables a comparison of longterm variability with the simulated seasonal cycle amplitude. The seasonal cycle of the ice concentration model results is driven by the respective seasonality of atmospheric radionuclide concentrations model results. Further contributions to an annual cycle from air-firn transfer are neglected, so far. Figure 5.6a shows the full (sub-monthly) model resolution as a blue shaded band together with yearly data (blue line). In case of these EDML model results, the seasonal variability shows an amplitude of roughly 50-70% whereas multidecadel variability (22 years resolution) shows slightly lower amplitudes of max. 50% (which is somewhat higher than in case of the measurements). In case of the GRIP/GISP model results, seasonal variability generally does not exceed 50% and the difference to the models multidecadel amplitudes is less. Regarding the dominating annual cycle, it becomes clear that high-resolution ice-core measurements (e.g. 1 or 2 years resolution) result in noisy time series.

Share of production and accumulation variability

Intending to investigate different contributions to the ^{10}Be decadal/centennial variability, the model is run with different parameters kept constant. The comparison of a constant snow accumulation rate run with results from a full forcing model run (figure 5.7) reveals that production rate variability exceeds variations due to Holocene accumulation rate changes by far. Assuming realistic accumulation rate changes applied, ^{10}Be variations due to accumulation changes only (yearly resolution) are lower than 15% (one outlier) in case of GRIP and lower than 20% (one outlier) in case of EDML during the last 10kyr. Certainly, variability is significantly lower regarding multi-decadal/centennial variability. However, the EDML model results driven by accumulation forcing only show a longterm oscillation of roughly 5% amplitude (minimum: 4kyr b2k, maximum 8.5 kyr b2k) and the GRIP model results reveal a rise from 10kyr b2k to 11.7kyr b2k by 10-20% (see figure 5.7a) . The application of the different production rate calculations from Masarik & Beer [2009] and Kovaltsov & Usoskin [2010] have minor influence on the normalized model results. The application of latter production rate calculations results in somewhat higher solar modulation. A quantification of this effect is difficult since the difference depends on the amplitude of the modulation. Basically, the difference is restricted to approx. 10% as an upper limit. Since some of the solar activity spikes are overestimated by the model, the model outcomes using the Masarik & Beer [2009] production rate are somewhat closer to the measurements in these cases.

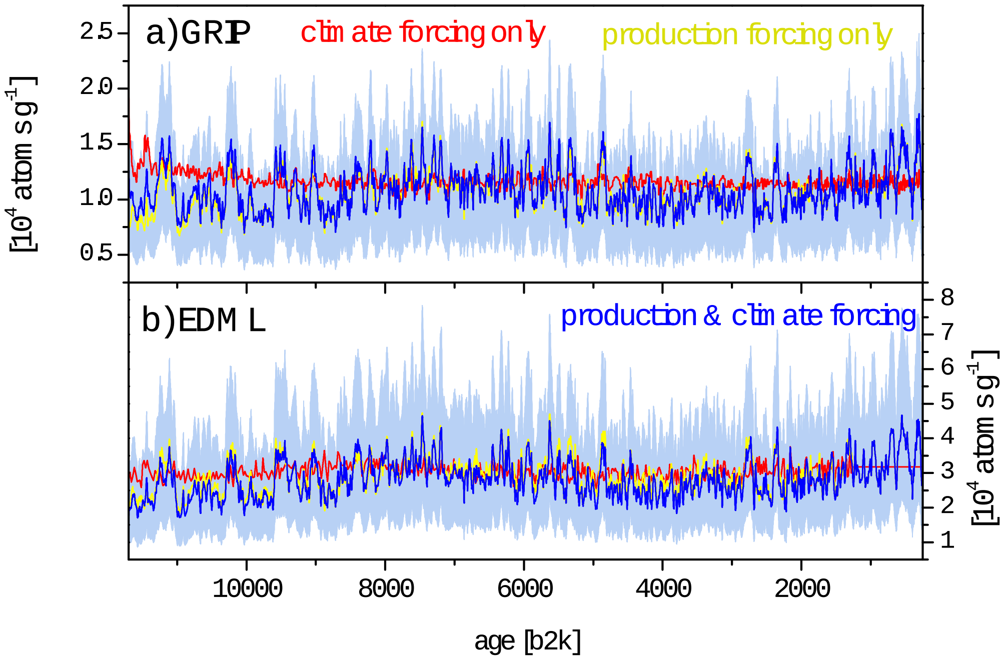

Figure 5.7.: Model results of ^{10}Be ice concentration in the two ice cores EDML and GRIP. Different colours denote different model input scenarios: In addition to the full forcing model results (blue), results from model runs with (i) constant production rate (red) and (ii) constant accumulation rate (yellow) are shown. Blue shaded band shows the full (sub-monthly) model resolution for the full forcing model results.

Early Holocene solar activity

The GISP ^{10}Be ice core measurements go back beyond 12 kyr and enable a comparison of the two ^{14}C-based solar activity reconstructions. Figure 5.8 shows that the production scenario 2 (pre-Holocene ^{14}C production from geomagnetic reconstruction) follows the measurements more closely. Indeed, the overall median of the model measurements difference is only 0.5% (mean: 2.4%, interquartile range: 18.8%) for the whole data set and -0.3% (mean 1.0%) for the period (9.4 - 11.7)kyr b2k in case of scenario 2 solar activity. Note that the normalization is based on the GRIP data during (0.35-9.36)kyr b2k and not on the here shown GISP measurements. This difference is significantly larger in case of the model results based on scenario 1 solar activity (no carbon cycle changes assumed, see section 5.3.3). In summary, the model results reveal a smaller early Holocene solar activity than given in Vonmoos *et al.* [2006] or Solanki *et al.* [2004]. These findings point to (i) a realistic estimation of the late glacial ^{14}C production rate estimated from the geomagnetic field reconstruction as well as (ii) an indirect hint on carbon cycle changes from late glacial to Holocene conditions which result in non-production ^{14}C variations.

Implications on ^{10}Be-based production rate reconstructions during the Holocene

In summary, the overall good matching of model results and measurements in the Holocene period indicates, that a great deal of multi-decadal to millennial ^{10}Be ice concentration variations can be explained by solar, geomagnetic and accumulation forcing. Regarding the latter, model results point to a small contribution of accumulation rate variability on the Holocene ^{10}Be variations making this cosmogenic radionuclide a suitable proxy for production rate variations. However, the quantitative amplitude of short-term production events requires further investigation.

These findings are in accordance to Steinhilber *et al.* [2012] who reconstructed solar activity of the last 9.4 kyr using a compilation of ^{10}Be ice core and ^{14}C tree ring measurements. The authors applied principal component analysis to derive a common production signal from the different time series and found "the first principal component [which] explains 69% of the total variance" representing the common production signal. Unpublished high-resolution (up to 2 years) ^{10}Be measurements exist from the EDML and GRIP core. These data as well as shorter time series from other ice cores (like Dye3, NGRIP or Dome F) may provide more detailes on model-measurement differences.

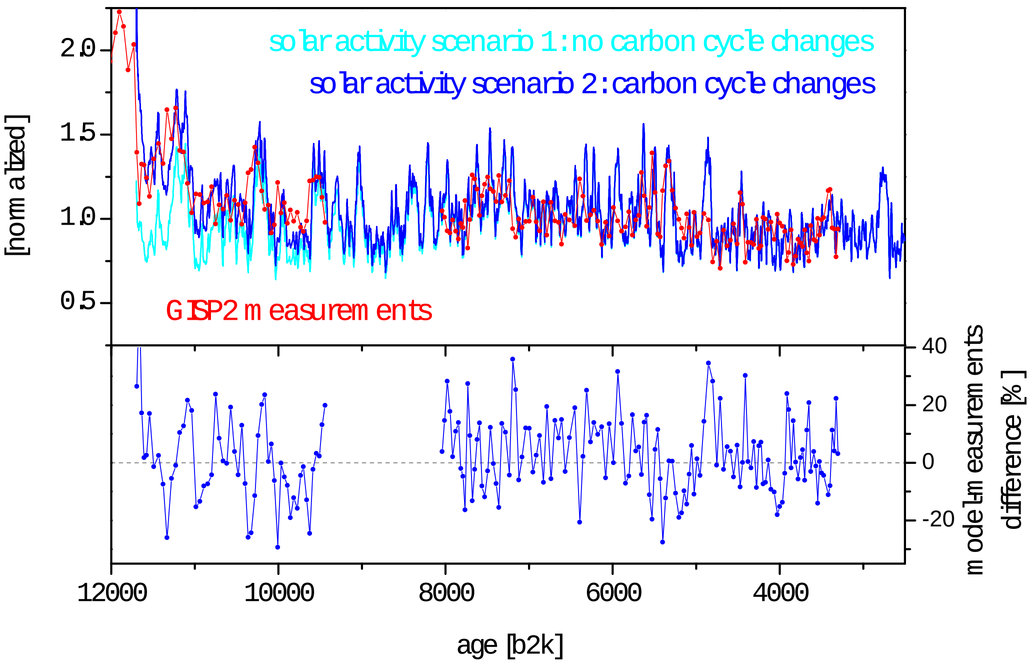

Figure 5.8.: Model-measurements comparison of the GISP2 ^{10}Be ice concentration. Model data comprises results based on the two different scenarios for ^{14}C-based solar activity reconstruction (see section 5.3.3). Note that measurements are not equidistant. Model results are smoothed using the median measurement resolution of 38 years for model (scenario 2) measurements comparison shown in the lower part. GISP2 measurements (as well as model results) are on the GICC05 timescale.

5.5. Model results: The Last Glacial Maximum

5.5.1. The Last Glacial Maximum

The most pronounced climate change which occurred in the last 100kyr was the transition from the Last Glacial Maximum (LGM) (about 27 kyr - 19 kyr b2k) to the Holocene. During the last glacial period (about 115 kyr - 11.7 kyr b2k), climate conditions were quite different from today: Climate modelling studies indicate that the global mean surface temperature difference between LGM and the pre-industrial period amounts -3.6°C to -5.7°C (range from different models applied) [Braconnot *et al.*, 2007] with larger changes in polar regions (maximum about -30°C over NH ice sheets [Braconnot *et al.*, 2007]). Indeed, besides being a main feature of temperature proxy time series, the glacial-interglacial transition is distinctively pronounced in reconstructions of greenhouse gas concentrations [Monnin *et al.*, 2001], polar aerosol fluxes [Fischer *et al.*, 2007], precipitation rates (see section 5.3) or the global sea level (see summary in the IPCC 2007 report [Jansen *et al.*, 2007]). In addition to this global climate transition, ice-core records indicate a variety of abrupt climate change events during the last glacial period with the Dansgaard-Oeschger events being the most pronounced ones (see e.g. Wolff *et al.* [2010] for a recent review). Similar to the glacial-interglacial periodicity, these events are detectable in a wide range of climate proxy records (especially from the northern hemisphere). However, they show quite different spatial characteristics with smaller amplitudes and different phasing in the southern hemisphere. These differences suggest changes in the climate system heat distribution rather than global mean temperature changes as being main driver for the Dansgaard-Oeschger events [Jansen *et al.*, 2007]. Compared to the Holocene period (see section 5.4), these characteristics of the last glacial in combination with changes in the cosmogenic production rate (see section 5.3.2) challenge the interpretation of ^{10}Be ice-core records which cover this period of time. As outlined in section 5.1, comparison of model results with respective measurements may reveal if variations in the accumulation rate and the geomagnetic field are able to quantitatively explain the ^{10}Be ice concentration variability.

Model runs for the last 75kyr are performed using the input data given in section 5.3. Different to the Holocene model runs, variations of solar activity are excluded and a constant long-term mean solar modulation potential of ϕ=550MV [Masarik & Beer, 1999] is assumed. For this long timescale, the data basis of ^{10}Be ice-core measurements is significantly dying. Basically, only four different ice-cores provide adequately resolved information on their ^{10}Be concentration which cover the last glacial: Vostok [Raisbeck *et al.*, 1987], GRIP/GISP [Yiou *et al.*, 1997; Finkel & Nishiizumi, 1997], Siple Dome A [Nishiizumi & Finkel, 2007] and Taylor Dome [Steig *et al.*, 1998, 2000]. Moreover, a long measurement time series of EDML core is currently in progress (J. Beer pers. communication). Given that the detection of longterm accumulation rate changes is challenging at small domes near the coast (E. Waddington, pers. communication), Antarctic Vostok and Greenland Summit cores remain the only candidates for a model-measurements comparison. Since long-term measurements from EDML core will be published shortly, the model evaluation will include Kohnen station, too.

5.5.2. Model measurements comparison

Greenland Summit

The measurements of the Greenland Summit ice cores compared to the respective model results are given in figure 5.9. The most obvious feature of both, measured and modelled ^{10}Be ice concentration is a distinct rise from Holocene to the Last Glacial Maximum by a factor of 2 - 3 on average. In addition, abrupt climate change events during the last glacial period are distinctively pronounced in the model and measurements data resembling the variations in the δ^{18}O measurements. As mentioned in section 5.4, the model underestimates the overall mean Holocene ice concentration by 28% and data normalized to the period (350-9360) yr b2k are therefore shown in figure 5.9 b. Given the large variability inherent to the measurements, the model reproduces the ^{10}Be ice core measurements surprisingly well: The overall median of the GRIP measurements-model difference (normalized to the Holocene period) shown in 5.9c is -2.1% (mean: -0.8%; interquartile range: 25.5%). Disregarding the Holocene period which was used for normalization, this value is slightly lower (median: -2.8%, mean: -1%), but biased by an obvious deviation previous to 65kyr b2k. Various reasons may account for this large difference, however, the loosely defined GICC05 timescale (and thus the derived accumulation rates) prior to 60kyr b2k hampers a detailed discussion. In the (11.7-65)kyr b2k period, model measurements difference is not randomly distributed around the median but shows some low frequency trends (see figure 5.9c). More precisely, the model overestimates the measurements within (20-30)kyr b2k by 11% (GRIP) and 4% (GISP), respectively. On the other hand, model results underestimate the ^{10}Be concentration in the (30-40)kyr b2k period (roughly 6-8% in case of both data sets). The interpretation of these findings is not straigthforward due to the two ice cores, three AMS laboratories (using different calibration standards) and different measurement procedures involved: All measurements comprised filtering of the melted ice to account for ^{10}Be related to micrometeorites. However, different groups accidentally applied two different filter pore sizes (and thus different filter efficiencies) in their measurement routine [Yiou *et al.*, 1997]. Baumgartner *et al.* [1997] investigated the effect of filtering by measuring the filtration residue of the small pore size filters. The authors found significant amounts of ^{10}Be stored in the small pore size filters and argue that recycled ^{10}Be related to aeolian dust could alter the ice concentration. They estimated in-significant contribution

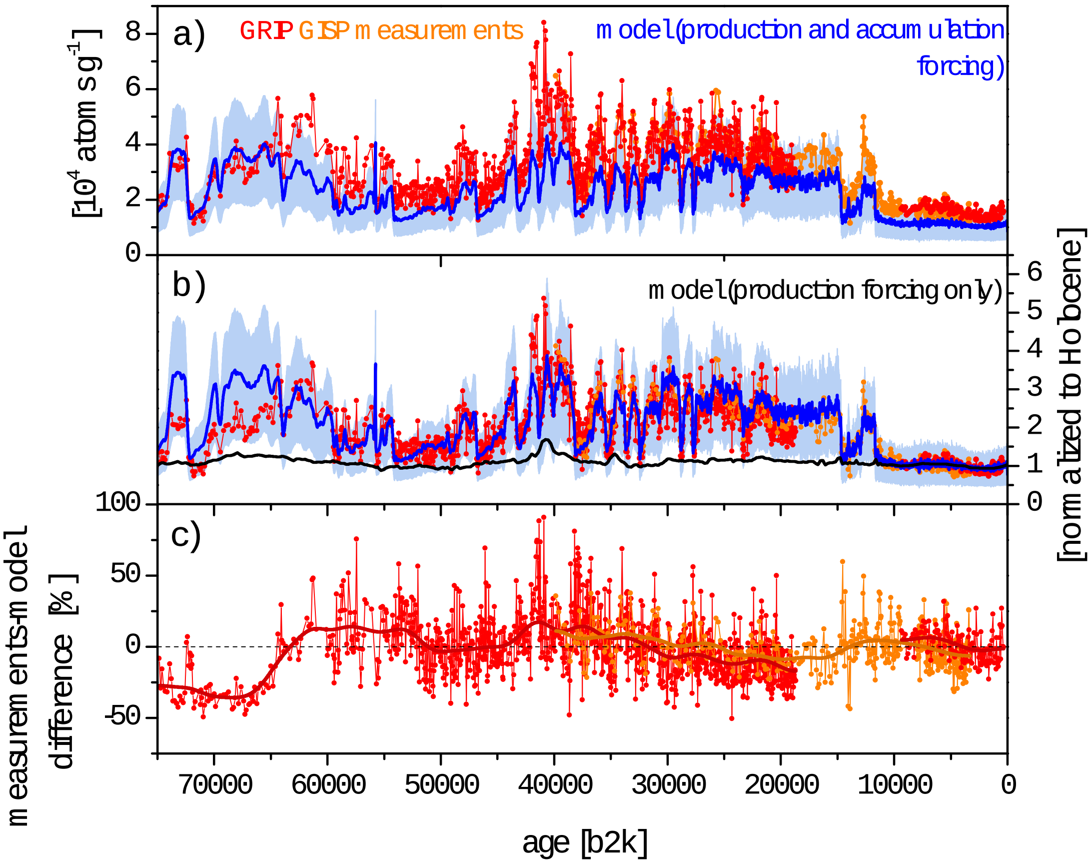

Figure 5.9.: Model-measurements comparison of ^{10}Be ice concentration of the GRIP (red dots) and GISP (orange dots) ice core: a) Comparison of absolute concentrations and b) data normalized to the respective overall mean Holocene concentration (350 yr b2k - 9360 yr b2k). In case of the GISP data, mean Holocene GRIP values are applied for normalization. Blue shaded bands show the full (monthly) model resolution while solid lines denote 10 year interpolations from yearly mean values. The black line shows a model result with constant accumulation rates (production variability based on geomagnetic activity, only). Note that geomagnetic activity imposes minor variations on the ^{10}Be ice core variations. Figure c) shows the relative measurements-model deviations (Gaussian smoothing dampens the amplitude of a 2 kyr oscillation to 0.1%). Note that no solar modulation is involved in the model runs. Data is on GICC05 timescale, some glacial measurements are scaled by a factor 1.25 to account for measurement flaws (see text for details), measurements are corrected for the ^{10}Be decay. Data: Finkel & Nishiizumi [1997],Yiou *et al.* [1997],Wagner *et al.* [2001a],Muscheler *et al.* [2004].

in Holocene samples but report on a share of recycled ^{10}Be during the glacial period of about 20%. Finally, different studys reported either (i) on the total ^{10}Be content of the (large pore size) filter plus filtrate (GISP - Finkel & Nishiizumi [1997]), (ii) on the ^{10}Be filtrate concentration only using large pore size filters (GRIP - Yiou *et al.* [1997]), or (iii) on the ^{10}Be filtrate concentration only using small pore size filters (GRIP - Yiou *et al.* [1997]). For the model comparison shown in figure 5.9 the common practice method was applied and measurements based on small pore size filtration were scaled by a factor 1.25 during the glacial period (R. Muscheler, pers. comm.). Unfortunately, the application of small pore size filters is not randomly distributed over the timeseries and the correction involves no shift of the measurements before 27.5kyr b2k and during several short periods afterwards (with the longest one spanning roughly 1000years). On the contrary, virtually all measurements between 37.8kyr b2k and 49.4kyr b2k are scaled by 25%. This scaling reduces the (absolute) overall model-measurements difference in the glacial GRIP values (GISP values disregarded since no correction involved) from -16.8% to -4.6%. Finally, a comparison with the GISP measurements which refer to both, ^{10}Be from filtration residue and filtrate, shows that the correction is reasonable since it significantly reduces the difference between the two data sets. However, the somewhat empirical (and time-dependent) correction introduces some additional uncertainty to the measurement data. Note that the overall measurements uncertainty is $\sim$ 7% [Yiou *et al.*, 1997].

It is important to recapitulate that the model does not account for any recycling of deposited ^{10}Be. Regarding a possible recycling effect Lal [2007] gives an estimation based on ice core-based assessments of aeolian dust fluxes (in combination with concentration of ^{10}Be in dust). In compliance with Baumgartner *et al.* [1997] his results point to significantly higher input of recycled ^{10}Be in Greenland ice during the more dusty last glacial period (contributions during the Holocene are below 10%, Lal [2007]). Indeed, while Baumgartner *et al.* [1997] find a share of 20%, Lal [2007] gives an estimation of 150%-200% for additional, dust-transported (recycled) ^{10}Be. Even if quantitative estimations are challenging due to various parameter estimations involved (e.g. the size distribution of aerosol which carries ^{10}Be), aeolian dust may contribute to the Greenland ^{10}Be ice concentration. However, the overall good agreement of model and measurement data points to less significance of recycling. Finally the measurements-model comparison rejects the dimension of this effect proposed by [Lal, 2007]. This is in line with ^{10}Be measurements in mid-latitudinal boundary layer air: Bremen [2011] measured ^{10}Be air concentrations in compiled high volume aerosol samples (more than 10 x 10^3m^3 of air per day; up to 200 x 10^3 m^3 of air per compilation) from Vienna which cover a large part of the time period October 2009 - September 2010. Due to the temporal coverage as well as the mid-latitudinal sampling site, the samples should comprise "old" ^{10}Be related to dust. However the resulting seasonal cycle closely resembles the respective model results which lack ^{10}Be recycling (see figure 4.17).

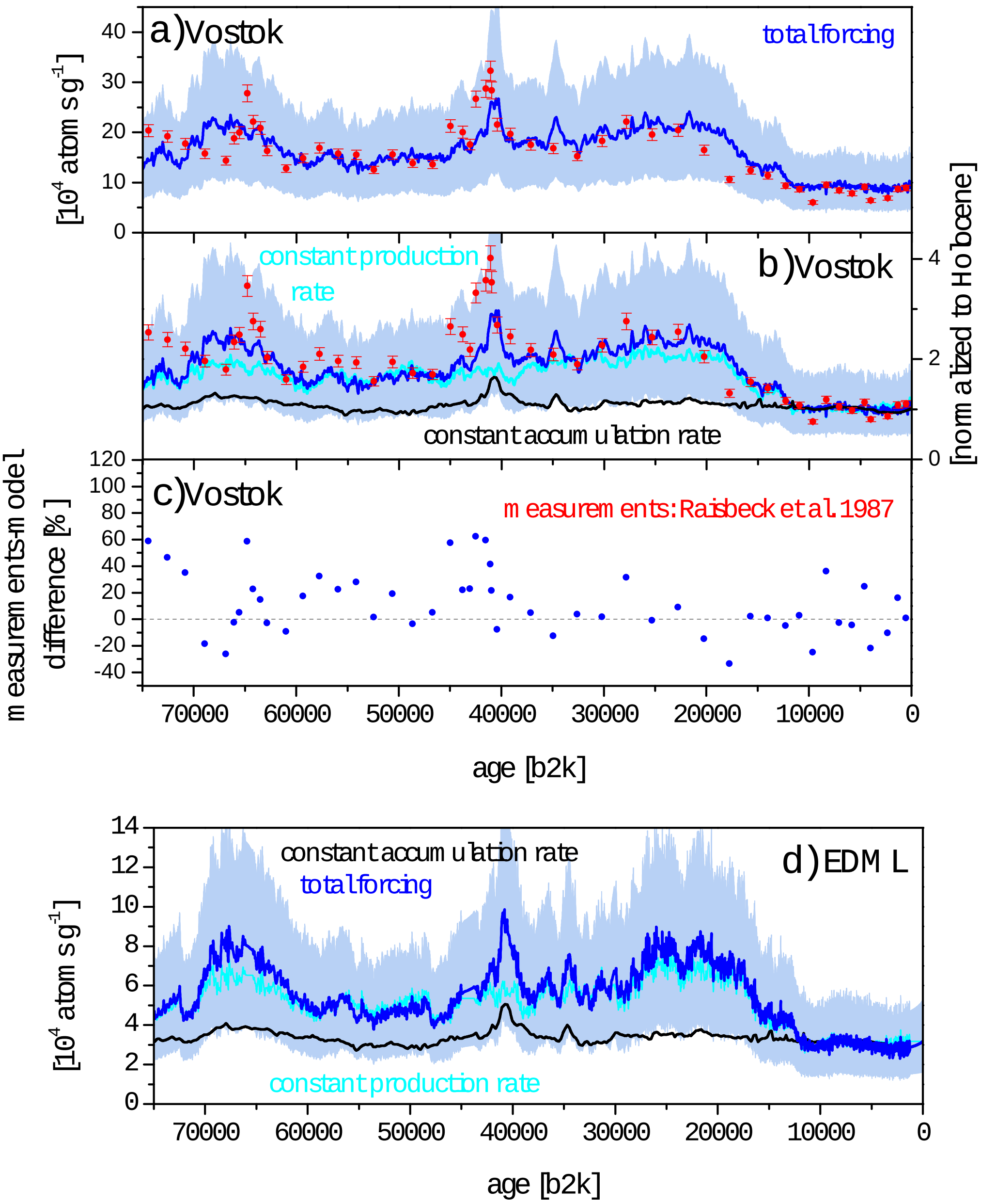

Figure 5.10.: Long-term model results of the Vostok and EDML ^{10}Be ice concentration. a) Absolute Vostok model results (shaded band: monthly resolution; blue line: 10 year interpolation) compared to measurements from Raisbeck *et al.* [1987]. Measurements are corrected for ^{10}Be decay. b) Same as a) but normalized to the respective Holocene mean value and compared with model results applying production forcing (black) and accumulation changes (light blue) only. c) Difference between measurements and (full forcing, blue line) model results. d) Respective model results for the EDML ice core (high-resolution measurements in process (J. Beer, pers. comm.))

Vostok and EDML

The model results of Antarctic Vostok and EDML ice cores are given in figure 5.10 and may support the interpretation of Greenland ^{10}Be records, even if the data basis is significantly smaller. The model overestimates the mean Holocene measurements from Vostok core by 11.9% which is partly on account of differences in the estimation of the current Vostok accumulation rate. As in case of Greenland, the difference between mean Holocene and glacial values is pronounced (factor of roughly 2-3 - similiar to Greenland). Common to the different δ^{18}O time series (or accumulation rate reconstructions) the shape of the glacial-interglacial transition differs between Greenland and Antarctic ^{10}Be concentrations: While the Greenland data significantly shows the characteristic variations of Younger Dryas and Bolling Allerod periods (see figure 5.9), the Vostok ^{10}Be concentration shows a constant rise interrupted by a plateau around 13-15kyr b2k. As expected, abrupt climate change events during the last glacial period are less pronounced than in case of the northern hemisphere measurements. Similar to the Greenland results, the model matches the (less resolved) Vostok rise from Holocene to the LGM quite well: The overall measurements-model difference (normalized to Holocene) during the pre-Holocene is 14% (mean; median: 11%; interquartile range: 30%) with the model tending to underestimate the ^{10}Be Holocene-LGM differenc (see model measurements differences in figure 5.10c). However, a significant share of this deviation may result from the two different ice core timescales applied: While the measurements as well as the local accumulation rate is based on the depth-age scale given in Parrenin *et al.* [2004], the global geomagnetic variability is tied to the GICC05 (Greenland) timescale. Indeed, figure 5.10 suggests that there is a time shift between the model and measurements related to the geomagnetic Laschamp event (around 42kyr b2k). Different to the GRIP data, the time period (20-40)kyr b2k shows no clear model deviation. However, the Vostok measurements data basis is significantly smaller and each sample only represents a few decades at most (G. Raisbeck, pers. comm.). Note that a significant contribution from recycled ^{10}Be in Antarctica is less likely compared to Greenland due to the overall low dust fluxes [Lal, 2007]. The EDML model results do not significantly deviate from Vostok results besides generally lower ice concentrations. However, the modelled EDML ^{10}Be concentration reveals a larger difference between Holocene and LGM values but overall lower concentrations (normalized to the Holocene) between 28kyr b2k and 39kyr b2k. High-resolution measurements of ^{10}Be which are currently in progress will greatly complement the Antarctic data basis.

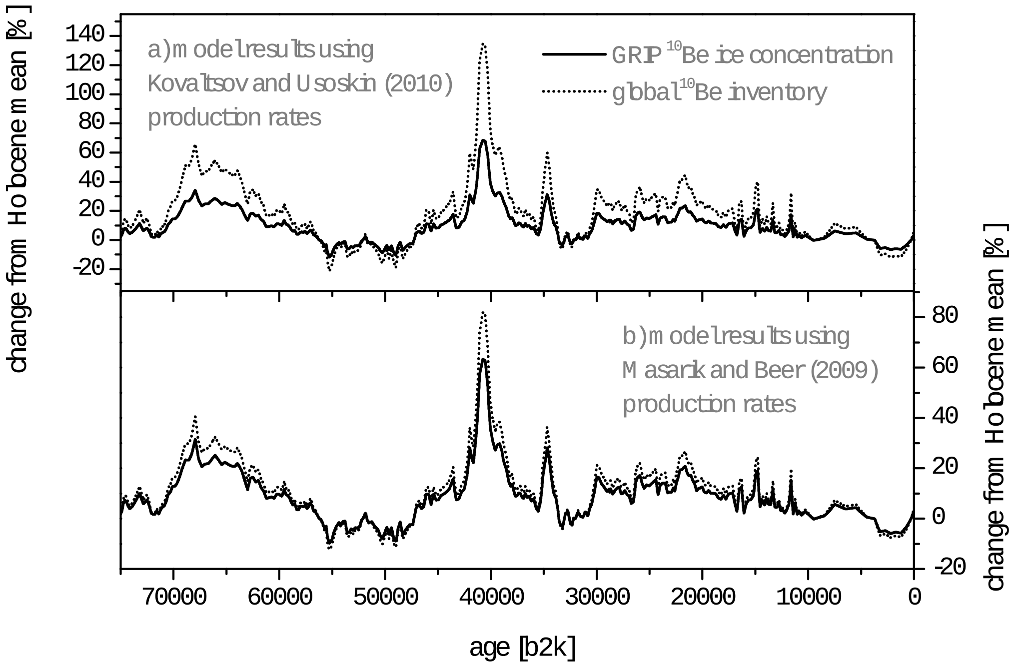

Figure 5.11.: Comparison between long-term model results using Masarik & Beer [2009] and Kovaltsov & Usoskin [2010] production rate calculations, respectively. All other time dependent input parameters except the geomagnetic field strength were kept constant. Note that the application of the different production rate calculations results in differences of the global ^{10}Be inventory by around 32-42% while the differences in Greenland ice concentration are generally lower (5-17%). Thus, the polar damping effect is much stronger in case of Kovaltsov & Usoskin [2010] (40-50%) than in case of Masarik & Beer [2009] (15-25%).

5.5.3. Interpretation of model results

The share of production and accumulation variability

Intending to assess the (long-term) share of production and accumulation variations on the variability of the model results, both parameters were kept constant alternately in different model runs shown in figures 5.9 and 5.10. It is obvious that the influence of the geomagnetic field variability is significantly lower than the impact of accumulation rate changes. The correlation between the GRIP model results using both accumulation and production forcing (reference) with an accumulation only run is 0.96 while the correlation with model results driven by (geomagnetic) production forcing only is 0.67. For the EDML site, the difference between respective values is somewhat lower (accumulation: 0.94; production: 0.74), but the accumulation rate remains being the dominating parameter. Basically, only strong geomagnetic excursions like the Laschamp event 42kyr b2k or a minimum around 65kyr b2k reveal distinct differences between the full forcing model run and results from accumulation forcing, only. Concerning this matter it is important to note that the here applied reconstruction of the geomagnetic field based on a compilation of sedimentary records [Laj *et al.*, 2004] shows the highest variations (and largest amplitude of the Laschamp event) among the different geomagnetic field reconstructions shown in figure 5.4. A main reason for the low share of production rate variability on the long timescale can be attributed to the damping of geomagnetic signals in high latitudes ("polar damping" - see also section 4.6.1). Figure 5.11 shows the amount of this effect for realistic variations in the geomagnetic field. The figure shows results from a model run with constant accumulation rates applied. In addition to the ^{10}Be GRIP ice concentration, the global atmospheric ^{10}Be inventory is shown. The variation of the global inventory is significantly larger in case of both production rate calculations applied in the model [Masarik & Beer, 2009; Kovaltsov & Usoskin, 2010]. Interestingly, the production rate variability in polar ice does insignificantly depend on the production rate calculations applied since the "polar damping" effect is significantly larger in case of the Kovaltsov & Usoskin [2010] production rates.

The share of wet and dry deposition

The share of ^{10}Be (and aerosol) wet and dry deposition representative for a specific sampling site is of particular importance regarding the reconstruction of the respective air concentration (and related production rates). In case of sampling sites with dominating wet deposition, the ice concentration resembles the concentration of fresh snow governed from air concentration in the scavenging process. On the contrary, additional dry deposition significantly increases the concentration of aged snow or firn compared to fresh snow. Thus, in case of dominating dry deposition, the deposition flux of ^{10}Be is commonly regarded as a proxy for air concentration (and related cosmogenic production). However, since the deposition process always involves both, dry and wet deposition, neither ice concentration nor the deposition flux are the perfect choice to reflect air concentration (e.g. Finkel & Nishiizumi [1997]). Eventually, the share of dry and wet deposition varies in time as a matter of accumulation variability. Thus, a model study which accounts for both deposition processes is the first-choice tool to reconstruct atmospheric variability from ice core records.

Figure 5.12 shows the share of wet deposition for the three sampling sites under investigation as resulting from the model runs. It is obvious that dry deposition dominates the Antarctic sites in case of both, Holocene and last glacial period and wet deposition is restricted below 15% (EDML) and 5% (Vostok), respectively. In case of Greenland summit, the here applied air-firn-transfer model predicts a dominance of wet deposition, following the work of Stanzick [2001]. Certainly, the decreasing accumulation rate during the LGM significantly enhances the share of dry deposition which results in alternating dominance

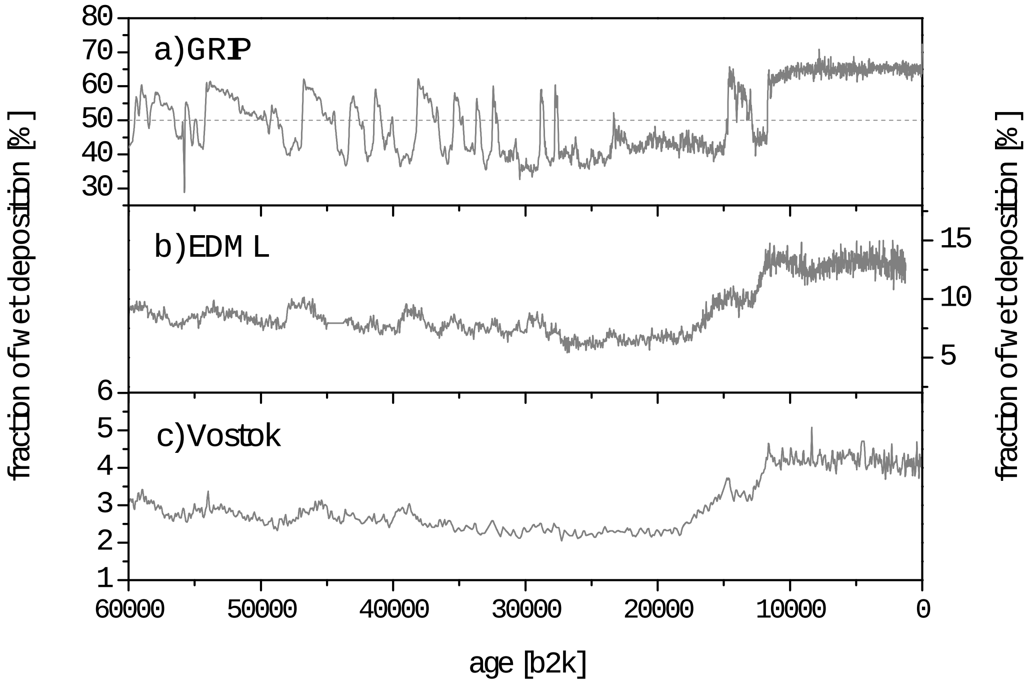

Figure 5.12.: Share of ^{10}Be wet deposition in case of the three sampling sites under investigation as resulting from model runs. Note that a prominent spike in the GRIP accumulation rate at 56 kyr b2k is an artefact of timescale extension.

of wet and dry deposition. Thus, with respect to reconstruction of cosmogenic production rate variability, neither ^{10}Be ice concentration nor the deposition flux at Greenland summit are suitable tools for reconstructing the production signal. More precisely, applying the GRIP/GISP ^{10}Be flux for the reconstruction of geomagnetic variability as done by Muscheler *et al.* [2005] results in an misinterpration of ^{10}Be air concentration (and related geomagnetic field strenght) during Dansgaard-Oeschger events (see 5.12).

Sensitivity of the model results to glacial-interglacial changes in the deposition process

The model results (shown in figures 5.9 and 5.10) are based on a time-independent parameterization which results from calibration with measurements representing the current observational period. More precisely, only geomagnetic and accumulation/precipitation changes contribute to the overall time variability. Since the state of the glacial (or early Holocene) atmosphere is not known, constant parameters of atmospheric transport and aerosol deposition (dry deposition velocity and scavenging efficiency) is a good first-order

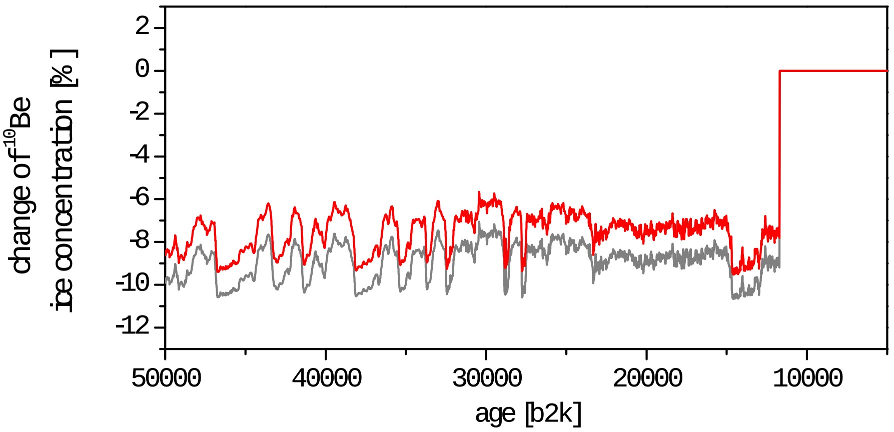

Figure 5.13.: Effect of a different Greenland aerosol scavenging efficiency during the last glacial on the GRIP ^{10}Be ice concentration. Both scenarios assume a factor 2 lower scavenging ratio as indicated from Antarctic parameterization. The scenarios differ in the spatial expansion of this effect: Including (i) all polar boxes (>60°N) (red) or (ii) the Greenland ice sheet only (grey).

approach. However, significant changes especially in terms of the glacial interglacial transition are likely. The here presented model approach represents a suitable tool to investigate the contribution of various (time-depending) processes on the ^{10}Be ice concentration. Certainly, investigations involve a detailed analysis of studies on the paleo-atmosphere which is beyond the scope of this work. Nevertheless, to demonstrate the uncertainty inherent to the model parameterization a scenario on Greenland scavenging is shortly presented.

The parameterization of the polar aerosol sinks (and related air-firn transfer) comprises a major difference between the Antarctic and Greenland Ice Sheet: Both, the boundary layer aerosol sink as well as the parameterization of the air-firn transfer model reveal a significantly lower scavenging efficiency for the Antarctic Ice Sheet (compared to Greenland, see section 3.4 and figure 4.11). Indeed, a colder Greenland climate could approximate the Antarctic parameterization with respect to aerosol wash-out. Therefore, a model run was performed with the Greenland scavenging efficiency reduced by a factor 2, which is roughly the difference between fresh snow ^{10}Be concentration in Greenland and Antarctica (see table 3.1). Figure 5.13 shows the difference of the results of this (reduced scavenging) model run compared to the results from observational period calibration. Two different scenarios are applied which either (i) assume changes in the scavenging ratio in the whole polar area (> 60°N) or (ii) restricted to the Greenland Ice Sheet box.

The effect of a reduced scavenging efficiency is twofold: On the one hand a reduced atmospheric aerosol sink increases the radionuclide concentration in the Greenland Ice Sheet boundary layer box. On the other hand, the air-firn transfer significantly reduces the ice concentration (lower aerosol sink). Obviously, these opposite effects do not cancel each other out which leads to the net effect of -6% to -11% reduction of the ^{10}Be ice concentration.

In summary, an unknown quantity of parameters could account for model-measurements deviations if they would vary in time. However, given the model results which show no systematic differences to the measurements in both cases, Greenland and Antarctica (figures 5.9 and 5.10), a systematic difference between Holocene and glacial conditions in atmospheric transport or deposition of ^{10}Be seems to be unlikely. However, it can not be excluded, that several effects cancel each other out. Additional information on glacial-interglacial differences in deposition (and aerosol transport) can be obtained from other ice core data: Ice-core records of aerosol ionic compounds may support the interpretation of glacial/interglacial changes of aerosol cycle parameters even if aerosol characteristics like the size distribution may differ. Fischer *et al.* [2007] give a review on "glacial/interglacial changes in mineral dust and sea-salt records in polar ice cores" and show results from Greenland GISP2 as well as Antarctic Vostok and Dome C station. Both aerosol components underly a distinct rise in ice concentration as well as deposition flux from Holocene to the LGM. However, different to ^{10}Be, the glacial/interglacial differences are much higher with factors up to 80 as in case of Greenland mineral dust concentration (compared to a factor 2-3 in case of ^{10}Be). Different to ^{10}Be, changes in the accumulation rate are not able to fully explain the increase from interglacial to glacial period, and respectively calculated deposition fluxes show a weaker but still pronounced increase. Taking into account the different source regions for both mineral dust and sea salt aerosol, the authors argue that "stronger sources, more efficient transport, and/or less deposition en route must be the main drivers of the observed increase". Interestingly an estimation of all contributing effects can not fully account for the whole glacial/interglacial difference mainly in case of mineral dust [Fischer *et al.*, 2007]. The unexplained "additional factor" is largest in case of Greenland records. If the missing process which enhances glacial dust fluxes is related to the deposition process, this would also apply to ^{10}Be. However, in this case the model should underestimate the glacial ^{10}Be ice concentration. Results of reduced scavenging model runs shown in figure 5.13 argue in the opposite direction. In addition to these assessments from Fischer *et al.* [2007], Kaufmann *et al.* [2010] report on ammonium and non-sea salt sulfate fluxes in Antarctic Dome C and EDML ice cores which are indicators of biological activity in the Southern Ocean and do not show a major variation over the glacial/interglacial transition, which is largely in line with constant deposition processes. In summary, different aerosol ionic compounds give no uniform picture with respect to the glacial deposition process but, if any, point to a stronger deposition flux in the last glacial period.

5.5.4. Outlook: Implications on ^{10}Be-based production rate reconstructions

The detection of the production signal inherent to the ^{10}Be ice concentration is much more difficult for the pre-Holocene period than in case of the Holocene. At first, the model results reveal that polar damping of geomagnetic variations challenges the reconstruction of the longterm production trends (see figure 5.11). Second, major shifts in the polar accumulation rate (related to climate variability) mask the production signal on different timescales. Finally, parameters of the aerosol transport and deposition may significantly depend on climate conditions and vary in time. Indeed, a first sensitivity test on aerosol scavenging (see figure 5.13) revealed, that different aerosol deposition parameters during the last glacial could result in significant changes of the ^{10}Be ice concentration. Those (climate-induced) shifts of the ^{10}Be ice concentration could significantly mask or simulate production rate variations. Given the difference of the δ^{18}O time series in Greenland and Antarctica, a combination of high-resolution records from both hemispheres could significantly enhance an attempt of ^{10}Be-based reconstruction of the geomagnetic field.
On the other hand, an overall good agreement of the model results with the measurements in both cases, Greenland and (low-resolution) Antarctic data indicates that there is no general shift from Holocene to glacial conditions in atmospheric transport and deposition. At least if not opposite effects cancel each other out. Assuming no major changes in the parameterization of the model (based on the current observational period), the model can be 'inverted' and differences between measurements and the respective model results can be attributed to changes in geomagnetic field. This attempt basically follows the work of Muscheler *et al.* [2005] but involves the following improvements:

- The application of the air-firn-transfer model allows for a straightforward reconstruction of the ^{10}Be air concentration (and thus the production signal).
- The model atmosphere accounts for transport effects (polar damping of geomagnetic variations).
- An update on the Greenland Summit accumulation rates is applied.
- The use of new production calculations of Kovaltsov & Usoskin [2010] predict somewhat higher dependence of polar ^{10}Be on the geomagnetic field strength.

The model is 'inverted' using a feedback control attempt (PID controller - see appendix D) and results are shown in Figure 5.14a, compared to other reconstructions of the geomagnetic dipole strength. Besides the compilation of GRIP and GISP ^{10}Be measurements, a constant solar activity of ϕ=550MV and the accumulation rates based on the GICC05 age-scale (restricted to polar latitudes $>$ 60°N) are input to the model. Figure 5.14b shows

the Greenland ^{10}Be measurements (compilation of GRIP and GISP measurements) which are the basis of the model inversion as well as the model results which illustrate quality control. As argued in appendix D2, the application of a PID-controller is not a real inversion and still model-measurements differences remain depending on the adjustment of the PID parameters. More precisely, the PID controlling results in an over- or undershoot prior to matching the new ^{10}Be concentration. A second source of uncertainty is the (online) elimination of the seasonal cycles inherent to the model results (see appendix D). Together, both effects amount up to 20% for a single measurement and an overall model-measurements offset around 1.5%. However, besides this small offset, these method-based errors result in 'high-frequency noise' and smoothed model-measurements differences (cutoff frequency $\approx$ 1/3000 yr) are generally lower than 1.3%. Admittedly, short-term oscillations might indeed depend on the parameterization of the method to some extent.
The resulting reconstruction of the geomagnetic dipole strength is basically compatible to the (ice-core ^{10}Be flux based) results of Muscheler *et al.* [2005]. Indeed, the dipole strength is higher during the period 14kyr b2k and 31kyr b2k and the amplitude of the Laschamp event (around 42kyr b2k) is larger. The results for this Laschamp excursion fall below the value of zero which points to a misinterpretation at least in case of very low geomagnetic field strength. A comparison of the new Antarctic ^{10}Be model results with respective Vostok measurements which are no input to the model inversion can hold for a validation of the different geomagnetic variations. Figure 5.14c shows the model results based on the new geomagnetic dipole field strength compared to previous results (based on the GLOPIS data of Laj *et al.* [2004]) and the measurements from Raisbeck *et al.* [1987]. Obviously, the model better reproduces the ^{10}Be measurements during the Laschamp event which supports the new reconstruction of the geomagnetic field. In case of the (14 - 31) kyr b2k period, a clear improvement of the model results is not detectable due to the scarce data basis. At least, the Vostok measurements do not reject a higher geomagnetic field strength during this period. Finally, the new Vostok model results reveal a much higher short-term variability based on the new high-resolution geomagnetic field strength reconstructed from the GRIP/GISP2 ^{10}Be time series. A great deal of this variability does likely not origin in geomagnetic field variations but in insufficient representation of the Greenland climate variability (as well as unknown (short-term) solar activity) in the model inversion.

5.6. Summary

Within this chapter, the atmospheric box-model presented in chapter 4 was coupled to the air-firn-transfer module (chapter 3.4) and applied on the ice core timescale up to 75kyr. In doing so, the ^{10}Be ice concentration could be quantitatively simulated for the first time. Accumulation rate as well as production changes (geomagnetic and solar forcing) drive the

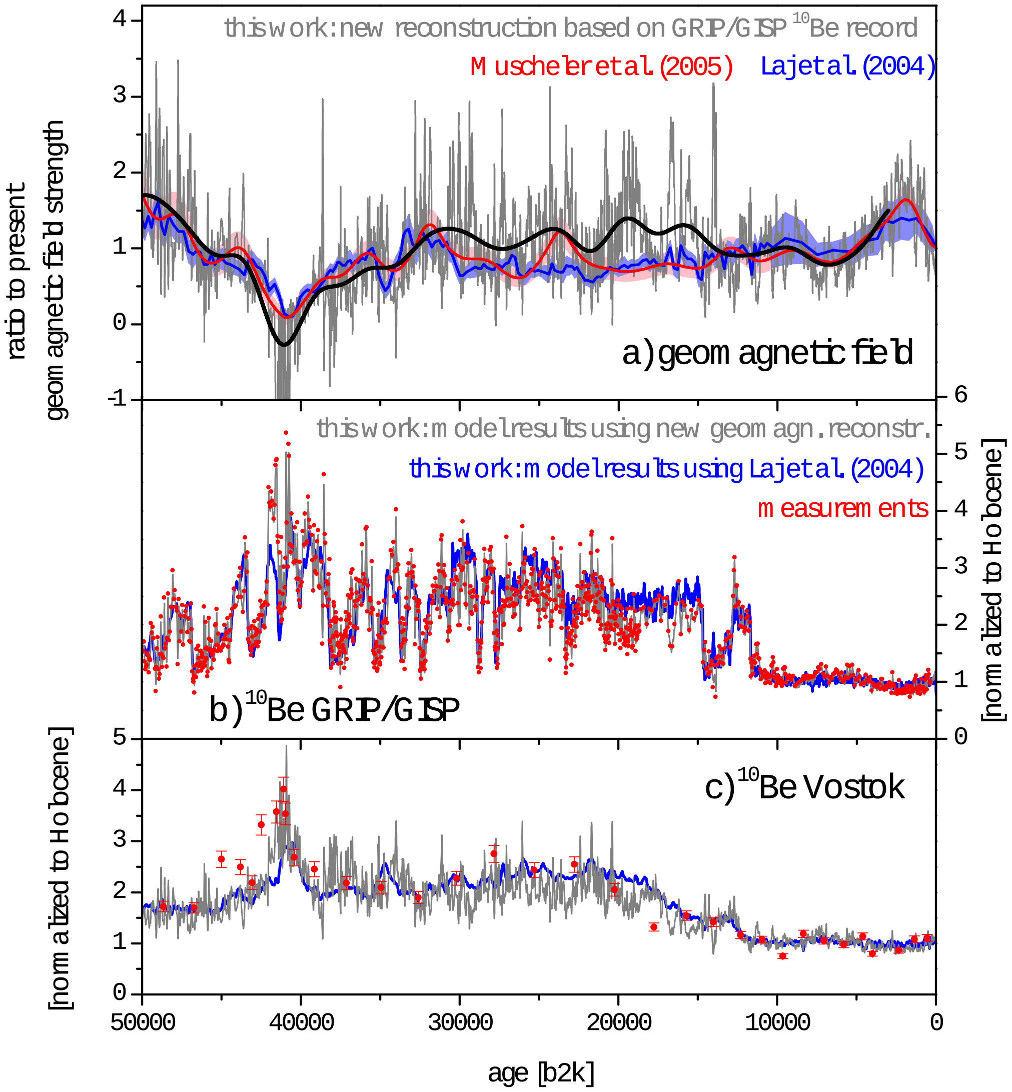

Figure 5.14.: Reconstruction of the geomagnetic field based on a compilation of GRIP and GISP ^{10}Be measurements within a model inversion (see text for details). a) New geomagnetic field strength (grey) and smoothed data (black line, cutoff frequency: 1/3000 years^{-1} similar to the smoothing applied in Muscheler *et al.* [2005]) compared to previous reconstructions [Laj *et al.*, 2004; Muscheler *et al.*, 2005]. b) Model inversion input data: GRIP and GISP measurements (red) [Yiou *et al.*, 1997; Finkel & Nishiizumi, 1997; Wagner *et al.*, 2001a; Muscheler *et al.*, 2004] compared to the model results using the new geomagnetic data (for quality control) (grey) and previous model results based on Laj *et al.* [2004] (blue). c) Validation of the new geomagnetic field strength with Vostok model-measurements comparison (grey) and previous model results using Laj *et al.* [2004] (blue). Measurements are corrected for ^{10}Be decay.

temporal variability of the model results.

In summary, the measurements-model differences were too large to avoid any normalization in the interpretation of the ice concentration. However, normalized data sets reveal that the model well reproduces a great deal of the variability of Greenland and Antarctic observations and offers the opportunity to investigate main contributions. For the Holocene period it could be shown that a large part of 22-year averages of the ^{10}Be concentration measured in the Antarctic EDML core can be explained by solar and geomagnetic activity changes. Indeed, accumulation rate changes contribute marginally to multi-decadal variability. This finding is in line with Steinhilber *et al.* [2012] who applied principal component analysis to both, two ^{10}Be ice core records and the ^{14}C INTCAL09 data and found the common production signal being the most dominant signal in the data. The application of two different scenarios in the reconstruction of solar activity from ^{14}C and subsequent ^{10}Be modelling showed, that previous studies (Solanki *et al.* [2004] and Vonmoos *et al.* [2006]) overestimated early Holocene solar activity. In terms of the large variations of the observed ^{10}Be ice concentration on the long timescale (i.e. the last 75kyr), the model results show an overall good agreement with measurements from GRIP/GISP and Vostok ice cores. This finding indicates that a major contribution of recycled ^{10}Be to the glacial Greenland ice concentration (as proposed by Lal [2007]) can be rejected. Regarding the share of production and accumulation (climate) forcing, the situation is different to the Holocene. Changes in the accumulation rate dominate the ^{10}Be ice concentration variability imposing variations of up to 300%. On the other hand, geomagnetic production effects are less decisive (<35% excluding the Laschamp geomagnetic excursion) partly due to a damping of the geomagnetic influence in polar latitudes. The application of new production rate calculations [Kovaltsov & Usoskin, 2010] in the model shows, that the geomagnetic modulation at polar sites is up to 50% lower compared to the global atmospheric inventory. However, the amount of damping depends on the production rate calculations applied and the use of Masarik & Beer [2009] data indicates significantly smaller damping. Regarding model measurements differences, various unconsidered processes like changes in the glacial atmospheric transport or deposition could account for the discrepancies. Imputing the differences to an incorrect representation of production variability, a new ^{10}Be-based reconstruction of the past geomagnetic dipole strength can be obtained from model 'inversion'. In doing so, past dipole moments reveal lower values during the Laschamp event as well as higher strength during the (14-31) kyr b2k period compared to previous reconstructions.

6. Overall summary and outlook

Up to now more than 20 polar ice cores provide data on ^{10}Be ice concentration variability on timescales ranging from centuries to more than 100kyr. The interpretation of these measurements is still challenging, although significant improvements regarding production rate calculations, ice core dating and the reconstruction of paleoclimate parameters were made in recent years. Intending to improve the understanding of ^{10}Be ice core variations, the overarching goal of this work was the establishment of a climatological model approach allowing for the simulation of the ^{10}Be ice concentration on long (ice core-related) timescales. Model-building was accomplished within three main stages comprising: (i) the investigation of polar radionuclide climatology, (ii) configuration of a global atmospheric multi-box model and (iii) applications on ice core time scales backed up by an air-firn transfer module.

The compilation and investigation of various (natural) radionuclide measurements in polar areas enabled a deeper insight into their polar climatology (summarized in section 3.5) which is a crucial precondition for every meaningful model attempt. Especially long-term high-quality air concentration measurements allowed for the investigation of radionuclide transport to ice core drilling sites and contributed to the understanding of ice core records. However, regarding the respective data basis, two main aspects need further investigation. At first, there is a clear disproportion between sampling sites at accessible coastal areas and remote ice sheet sites. Basically, only one ice sheet site each hemisphere provides data covering several years of observations. Second, measurements of the ^{10}Be air-concentration are virtually restricted to Neumayer Station. Hence, analysis of its atmospheric transport as well as model validation has to rely on (readily available) short-lived radionuclides. Summing up both aspects, there are hardly any measurements of the ^{10}Be boundary layer air concentration on the ice sheets which, on the contrary, provide the ^{10}Be ice core records of interest. Regarding the spatial variability of mean ^{10}Be ice concentration, the thesis could significantly increase the data basis around the low accumulation Kohnen Station (EDML drilling site). However, ^{10}Be measurements at very low accumulation sites (like Vostok or Dome F) are sparse and call for further ^{10}Be data. Since the transition from Holocene to glacial aerosol deposition is related to a major drop in the mean accumulation rates, observations at low accumulation sites are especially important to investigate the deposition process during the last glacial period.

On the global scale, an established box model of the global atmosphere was configurated to simulate aerosol-borne radionuclides using extensive observations of short-lived radionuclides. Calibration with bomb fission nuclides and validation with ^{7}Be revealed, that the comparably low-resolution model is capable to reproduce their climatological features in the atmosphere (see summary in section 4.7). Both, calibration as well as validation of the model may be still improved using appropriate data. Regarding the former task, the simulation of aerosol-bound nuclides required some significant modifications of the original model setup with e.g. recalibration of the boundary layer - free troposphere coupling. Here, an independent tracer in addition to bomb fission nuclides would significantly enhance the model performance. Global measurements of the short-lived radionuclide ^{24}Na [Matthews, 2011] as well as ^{222}Rn or ^{210}Pb could be appropriate tracers concerning this matter. However, in the latter cases the model resolution would have to be enhanced to 2.5 dimensions (at least) as to separate the boundary layer into maritime and continental boxes. Regarding model validation, tropical as well as high southern latitudes lack observations of radionuclide air concentration. The international monitoring system in the CTBTO framework provides additional, globally distributed and high-resolution measurements of natural radionuclide activity concentration in boundary layer air. Moreover, this growing data is backed-up by stored daily high-volume aerosol samples from currently 65 [CTBTO, 2012] stations worldwide. Additional measurements of ^{10}Be could greatly improve the understanding of atmospheric radionuclide transport and contribute to unsolved tasks like (i) recycling of ^{10}Be or (ii) ^{10}Be/^{7}Be (or ^{22}Na/^{7}Be, Bremen [2011]) applications as a tracer for intrusions of stratospheric air masses.

In the final analysis, the model was coupled to an air-firn module and, for the first time, long-term model results could be quantitatively confronted with ice core measurements of ^{10}Be. While the model closely reproduces the main features of Holocene and glacial ^{10}Be records, discrepancies remain on different time scales. Future investigations have to aim at two aspects. At first, the model is an appropriate tool to investigate transport and deposition effects relevant for ice core ^{10}Be (see first attempts in sections 4.6.2 and 5.3.3). Relevant processes which contribute to glacial/interglacial differences may comprise: (i) the Stratosphere-Troposphere Exchange (e.g. Land & Feichter [2003]), (ii) changes in the global Brewer-Dobson circulation or (iii) changes in the global sink distribution related to shifts in the hydrological cycle (e.g. Braconnot *et al.* [2007]). Different to the application of GCMs, these processes can be investigated independently using the present model approach. Second, model measurements comparison of ice core records can easily be made for other drilling sites which provide observations covering various periods of time (at different resolution). On the glacial/interglacial timescale, ongoing high-resolution measurements of ^{10}Be on the EDML ice core will greatly challenge the model‘s performance. Since Antarctic records are supposed to be less effected by millennial-scale variability, these measurements will contrast and complement the findings from high-resolution Greenland measurements.

All in all, this work contributed to the overall understanding of atmospheric ^{10}Be and its variation on ice core-related timescales. Having an established model setup at hand, it is possible to investigate detailed open questions in future studies.

Bibliography

Adler, R.F., G.J., Huffman, Chang, A., Ferraro, R., Xie, P.P., Janowiak, J., Rudolf, B., Schneider, U., Curtis, S., Bolvin, D., Gruber, A., Susskind, J., Arkin, P., & Nelkin, E. 2003. The version-2 global precipitation climatology project (GPCP) monthly precipitation analysis (1979-present). *Journal of Hydrometeorology*, **4**, 1147–1167.

Akata, N., Kawabata, H., Hasegawa, H., Sato, T., Chikuchi, Y., Kondo, K., Hisamatsu, S., & Inaba, J. 2008. Total deposition velocities and scavenging ratios of ^{7}Be and ^{210}Pb at Rokkasho, Japan. *Journal of Radioanalytical and Nuclear Chemistry*, **277**, 347–355.

Aldahan, A., Possnert, G., Johnsen, S.J., Clausen, H.B., Isaksson, E., Karlen, W., & Hansson, M. 1998. Sixty year ^{10}Be record from Greenland and Antarctica. *Proceedings of the Indian Academic Society (Earth Planetary Science)*, **107(2)**, 139–147.

Aldahan, A., Hedfors, J., Possnert, G., Kulan, A., Berggren, A.-M., & Söderström, C. 2008. Atmospheric impact on beryllium isotopes as solar activity proxy. *Geophysical Research Letters*, **35**, L21812.

Allen, M.D., & Raabe, O.G. 1985. Slip correction measurements of spherical solid aerosol particles in an improved Millikan apparatus. *Aerosol Science and Technology*, **4**, 269–286.

Allen, R.M., & Smith, L.A. 1996. Monte Carlo SSA: Detecting irregular oscillations in the presence of colored noise. *Journal of Climate*, **9**, 3373–3404.

Alley, R.B., Meese, D.A., Shuman, C.A., Gow, A.J., Taylor, K.C., Grootes, P.M., White, J.W.C., Ram, M., Waddington, E.D., Mayewski, P.A., & Zielinski, G.A. 1993. Abrupt increase in Greenland snow accumulation at the end of the Younger Dryas event. *Nature*, **362**, 527–529.

Alley, R.B., Finkel, R.C., Nishiizumi, K., Anandakrishnan, S., Shuman, C.S., Mershon, G., Zielinski, G.A., & Mayewski, P.A. 1995. Changes in continental and sea-salt atmospheric loadings in central Greenland during the most recent deglaciation: model-based estimates. *Journal of Glaciology*, **41(139)**, 503–514.

Andersen, K.K., Svensson, A., Johnsen, S.J., Rasmussen, S.O., Bigler, M., Röthlisberger, R., Ruth, U., Siggaard-Andersen, M.-L., Steffensen, J.P., Dahl-Jensen, D., Vinther, B.M., & Clausen, H.B. 2006. The Greenland Ice Core Chronology 2005 15-42 ka. Part 1: Constructing the time scale. *Quaternary Science Reviews*, **25**, 3246–3257.

Arnold, J.R. 1956. Beryllium-10 produced by cosmic rays. *Science*, **124**, 584–585.

Arthern, R.J., Winebrenner, D. P., & Vaughan, D.G. 2006. Antarctic snow accumulation mapped using polarization of 4.3-cm wavelength microwave emission. *Journal of Geophysical Research*, **111**, D06107.

Asgeirsson, B. U. 2012. *Modelling radiocarbon and carbon cycle changes from the Last Glacial Maximum to the Holocene.* Master thesis, Institut für Umweltphysik, University of Heidelberg.

Auer, R. M. 1997. *Saisonale und langzeitliche Variation von ^{10}Be, ^{7}Be und ^{210}Pb im Aerosol der Küstenantarktis.* Diploma thesis, Institut für Umweltphysik, University of Heidelberg.

Balkanski, Y.J., Jacob, D.J., Gardner, G.M., Graustein, W.C., & Turekian, K.K. 1993. Transport and residence times of tropospheric aerosols inferred from a global three-dimensional simulation of ^{210}Pb. *Journal of Geophysical Research*, **98(D11)**, 20,573–20,586.

Bard, E., Raisbeck, G.M., Yiou, F., & Jouzel, J. 1997. Solar modulation of cosmogenic nuclide production over the last millennium: comparison between ^{14}C and ^{10}Be records. *Earth and Planetary Science Letters*, **150**, 453–462.

Baroni, M., Bard, E., Petit, J.R., Magand, O., & Bourles, D. 2011. Volcanic and solar activity, and atmospheric circulation influences on cosmogenic ^{10}Be fallout at Vostok and Concordia (Antarctica) over the last 60 years. *Geochimica et Cosmochimica Acta*, **75**, 7132–7145.

Barry, R., & Gan, T.Y. 2011. *The global cryosphere.* Cambridge University Press.

Bartol-Research-Institute. 2010. http://neutronm.bartol.udel.edu/~pyle/bri_table.html.

Baskaran, M., C.H.Coleman, & Santschi, P.H. 1993. Atmospheric depositional fluxes of ^{7}Be and ^{210}Pb at Galveston and College Station, Texas. *Journal of Geophysical Research*, **98(D2)**, 20,555–20,571.

Baumgartner, S., Beer, J., Wagner, G., Kubik, P., Suter, M., Raisbeck, G.M., & Yiou, F. 1997. ^{10}Be and dust. *Nuclear Instruments and Methods in Physics Research B*, **123**, 296–301.

Beer, J., Oeschger, H., Finkel, R.C., Castagnoli, G.C., Bonino, G., Attolini, M.R., & Galli, M. 1985. Accelerator measurements of ^{10}Be: The 11 year solar cycle from 1180-1800 A.D. *Nuclear Instruments and Methods in Physics Research B*, **10/11**, 415–418.

Beer, J., Bonani, G., Hofmann, H.J., Suter, M., Synal, H.A., Wölfli, W., Oeschger, H., Siegenthaler, U., & Finkel, R.C. 1987. ^{10}Be measurements on polar ice: comparison of Arctic and Antarctic records. *Nuclear Instruments and Methods in Physics Research B*, **29**, 203–206.

Beer, J., Siegenthaler, U., Bonani, G., Finkel, R.C., Oeschger, H., Suter, M., & Wölfli, W. 1988. Information on past solar activity and geomagnetism from ^{10}Be in the Camp Century ice core. *Nature*, **331**, 675–679.

Beer, J., Blinov, A., Bonani, G., Finkel, R.C., Hofmann, H.J., Lehmann, B., Oeschger, H., Sigg, A., Schwander, J., Staffelbach, T., Stauffer, B., Suter, M., & Wölfli, W. 1990. Use of ^{10}Be in polar ice to trace the 11-year cycle of solar activity. *Nature*, **347**, 164–166.

Bennett, B.G. 2002. Worldwide dispersion and deposition of radionuclides produced in atmospheric tests. *Health Physics*, **82(5)**, 644–655.

Berggren, A.M., Beer, J., Possnert, G., Aldahan, A., Kubik, P., Christl, M., Johnsen, S.J., Abreu, J., & Vinther, B.M. 2009. A 600-year annual ^{10}Be record from the NGRIP ice core, Greenland. *Geophysical Research Letters*, **36**, L11801.

Braconnot, P., Otto-Bliesner, B., Harrison, S., Joussaume, S., Peterchmitt, J.-Y., Abe-Ouchi, A., Crucifix, M., Driesschaert, E., Fichefet, Th., Hewitt, C.D., Kageyama, M., Kitoh, A., Lainé, A., Loutre, M.-F., Marti, O., Merkel, U., Ramstein, G., Valdes, P., Weber, S.L., Yu, Y., & Zhao, Y. 2007. Results of PMIP2 coupled simulations of the Mid-Holocene and Last Glacial Maximum - Part 1: experiments and large-scale features. *Climate of the Past*, **3**, 261–277.

Bremen, R. 2011. *Pilotstudie zum Einsatz von kosmogenem ^{22}Na als stratosphärischen Luftmassentracer*. Diploma thesis, Institut für Umweltphysik, University of Heidelberg.

Bromwich, D.H. 1988. Snowfall in high southern latitudes. *Reviews of Geophysics*, **26(1)**, 149–168.

Bromwich, D.H., Robasky, F.M., Keen, R.A., & Bolzan, J.F. 1993. Model variations of precipitation over the Greenland ice sheet. *Journal of Climate*, **6**, 1253–1268.

Broomhead, D.S., & King, G.P. 1986. Extracting qualitative dynamics from experimental data. *Physica*, **20D**, 217–236.

Brost, R.A., Feichter, J., & Heimann, M. 1991. Three-dimensional simulation of ^{7}Be in a Global Climate Model. *Journal of Geophysical Research*, **96, D12**, 22,423–22,445.

Caballero-Lopez, R. A., & Moraal, H. 2004. Limitations of the force field equation to describe cosmic ray modulation. *Journal of Geophysical Research*, **109**, A01101.

Chae, J.-S., Byun, J.-I., Yim, S.A., Choi, H.-Y., & Yun, J.-Y. 2011. ^{7}Be in ground level air in Daejeon, Korea. *Radiation Protection Dosimetry*, 1–4.

Channell, J.E.T., Xuan, C., & Hodell, D.A. 2009. Stacking paleointensity and oxygen isotope data for the last 1.5 Myr (PISO-1500). *Earth and Planetary Science Letters*, **283**, 14–23.

Chmeleff, J., von Blanckenburg, F., Kossert, K., & Jakob, D. 2010. Determination of the ^{10}Be half-life by multicollector ICP-MS and liquid scintillation counting. *Nuclear Instruments and Methods in Physics Research B*, **268**, 192–199.

Conen, F., & Robertson, L.B. 2002. Latitudinal distribution of radon-222 flux from continents. *Tellus*, **54B**, 127–133.

Considine, D.B., Bergmann, D.J., & Liu, H. 2005. Sensitivity of Global Modeling Initiative chemistry and transport model simulations of radon-222 and lead-210 to input meteorological data. *Atmospheric Chemistry and Physics*, **5**, 3389–3406.

CTBTO. 2012. http://www.ctbto.org/map/.

Cuffey, K.M., & Clow, G.D. 1997. Temperature, accumulation, and ice sheet elevation in central Greenland through the last deglacial transition. *Journal of Geophysical Research*, **102(C2)**, 26,383–26,396.

Dahl-Jensen, D., Johnsen, S.J., Hammer, C.U., Clausen, H.B., & Jouzel, J. 1993. Past accumulation rates derived from observed annual layers in the GRIP ice core from Summit, Central Greenland. *Pages 517–532 of:* Peltier, W.R. (ed), *Ice in the climate system.* NATO ASI Series. Springer, Berlin, Heidelberg.

Davidson, C.I., Bergin, M.H., & Kuhns, H.D. 1996. The deposition of particles and gases to ice sheets. *In:* Wolff, E.W., & Bales, R.C. (eds), *Chemical exchange between the atmosphere and polar snow.* NATO ASI Series. Springer, Berlin, Heidelberg.

Delaygue, G., & Bard, E. 2011. An Antarctic view of Beryllium-10 and solar activity for the past millennium. *Climate Dynamics*, **36(11-12)**, 2201–2218.

Delmas, R.J. 1992. Free tropospheric reservoir of natural sulfate. *Journal of Atmospheric Chemistry*, **14**, 261–271.

Dibb, J.D., Meeker, L. D., Finkel, R. C., Southon, J. R., Caffee, M. W., & Barrie, L. A. 1994. Estimation of stratospheric input to the Arctic troposphere: ^{7}Be and ^{10}Be in aerosols at Alert, Canada. *Journal of Geophysical Research*, **99**, 12,855–12,864.

Dibb, J.E. 1990. Recent deposition of ^{210}Pb on the Greenland Ice Sheet: variations in space and time. *Annals of Glaciology*, **14**, 51–54.

Dibb, J.E. 1992. The accumulation of ^{210}Pb at Summit, Greenland since 1855. *Tellus*, **44B**, 72–79.

Dibb, J.E. 2007. Vertical mixing above Summit, Greenland: Insights into seasonal and high frequency variability from the radionuclide tracers ^{7}Be and ^{210}Pb. *Atmospheric Environment*, **41(24)**, 5020–5030.

Dibb, J.E. 2012. *Personal communication.* University of New Hampshire.

Dibb, J.E., & Jaffrezo, J.-L. 1993. Beryllium-7 and lead-210 in aerosol and snow in the Dye 3 Gas, Aerosol and Snow Sampling Program. *Atmospheric Environment*, **27A**, 2751–2760.

Doering, C. 2007. *Measurements of the distribution and behaviour of beryllium-7 in the natural environment.* PhD thesis, Queensland University of Technology, Brisbane, Australia.

Dorrian, M.-D. 1997. Particle size distributions of radioactive aerosols in the environment. *Radiation Protection Dosimetry*, **69**, 117–132.

Dörr, H., & Münnich, K.-O. 1990. ^{222}Rn flux and soil air concentration profiles in West-Germany. Soil ^{222}Rn as tracer for gas transport in the unsaturated soil zone. *Tellus*, **42B**, 20–28.

Durana, L., Chudy, M., & Masarik, J. 1996. Investigation of Be-7 in the Bratislava atmosphere. *Journal of Radioanalytical Nuclear Chemistry*, **207**, 345–356.

Elsig, J., Schmitt, J., Leuenberger, D., Schneider, R., Eyer, M., Leuenberger, M., Joos, F., Fischer, H., & Stocker, T.F. 2009. Stable isotope constraints on Holocene carbon cycle changes from an Antarctic ice core. *Nature*, **461**, 507–510.

Elsässer, C. 2008. *Untersuchung der Langzeit-Variabilität kosmogener und terrigener Radioisotope im antarktischen Aerosol.* State examination thesis. Institut für Umweltphysik, University of Heidelberg.

Elsässer, C., Wagenbach, D., Weller, R., Auer, M., Wallner, A., & Christl, M. 2011. Continuous 25-years aerosol records at coastal Antarctica: Part 2. Variability of the radionuclides ^{7}Be, ^{10}Be and ^{210}Pb. *Tellus*, **63B**.

EML-Fallout. 2010. *Fallout Programm.* Environmental Measurements Laboratory (EML): http://www.nbl.doe.gov/htm/EML_Legacy_Website/databases.htm.

EML-HASP. 2011. *High Altitude Sampling Program.* Environmental Measurements Laboratory (EML): http://www.nbl.doe.gov/htm/EML_Legacy_Website/databases.htm.

EML-SASP. 2010. *Surface Air Sampling Programm.* Environmental Measurements Laboratory (EML): http://www.nbl.doe.gov/htm/EML_Legacy_Website/databases.htm.

Enting, I. 1982. *Nuclear weapons data for use in carbon cycle modelling.* Tech. rept. 44. CSIRO Div. of Atmos. Res., Melbourne, Australia.

Feely, H.W., Seitz, H., Lagomarsino, J., & Biscaye, P.E. 1966. Transport and fallout of stratospheric radioactive debris. *Tellus*, **18**, 316–328.

Feely, H.W, Larsen, R.J., & Sanderson, C.G. 1989. Factors that cause seasonal variations in Beryllium-7 concentrations in surface air. *Journal of Environmental Radioactivity*, **9**, 223–249.

Field, C.V., & Schmidt, G.A. 2009. Model-based constraints on interpreting 20th century trends in ice core ^{10}Be. *Journal of Geophysical Research*, **114**, D12110.

Field, C.V., Schmidt, G.A., Koch, D., & Salyk, C. 2006. Modeling production and climate-related impacts on ^{10}Be concentration in ice cores. *Journal of Geophysical Research*, **111**, D15107.

Finkel, R.C., & Nishiizumi, K. 1997. Beryllium 10 concentrations in the Greenland Ice Sheet Project 2 ice core from 3-40 ka. *Journal of Geophysical Research*, **102(C12)**, 26,699–26,706.

Fischer, H. 1997. *Räumliche Variabilität in Eiskernzeitreihen Nordostgrönlands.* PhD thesis, Institut für Umweltphysik, University of Heidelberg.

Fischer, H., Siggaard-Andersen, M.-L., Ruth, U., Röthlisberger, R., & Wolff, E. 2007. Glacial/Interglacial changes in mineral dust and sea-salt records in polar ice cores: sources, transport, and deposition. *Reviews of Geophysics*, **45**, RG1002.

Garcia-Munoz, M., Mason, G.M., & Simpson, J.A. 1975. The anomalous ^{4}He component in the cosmic-ray spectrum at $\leq$50 MeV per nucleon during 1972-1974. *Astrophysical Journal*, **202**, 265–275.

Ghil, M., Allen, M.R., Dettinger, M.D., Ide, K., Kondrashov, D., Mann, M.E., Robertson, A.W., Saunders, A., Tian, Y., Varadi, F., & Yiou, P. 2002. Advanced spectral methods for climatic time series. *Review of Geophysics*, **40**, 1–41.

Gleeson, L.J., & Axford, W.I. 1968. Solar modulation of galactic cosmic rays. *The Astrophysical Journal*, **154**, 1011–1026.

Griffiths, A.D., Zahorowski, W., Element, A., & Werczynski, S. 2010. A map of radon flux at the Australian land surface. *Atmospheric Chemistry and Physics*, **10**, 8969–8982.

Grinsted, A., Moore, J.C., & Jevrejeva, S. 2004. Application of the cross wavelet transform and wavelet coherence to geophysical time series. *Nonlinear Processes in Geophysics*, **11**, 561–566.

Guelle, W., Balkanski, Y.J., Schulz, M., Dulac, F., & Monfray, P. 1998. Wet deposition in a global size-dependent aerosol transport model 1. Comparison of a 1 year ^{210}Pb simulation with ground measurements. *Journal of Geophysical Research*, **103(D10)**, 11,429–11,445.

Hammer, S. 2008. *Quantification of the regional H_2 sources and sinks inferred from atmospheric trace gas variability.* PhD thesis, University of Heidelberg.

Hammer, S., Wagenbach, D., Preunkert, S., Pio, C., Schlosser, C., & Meinhardt, F. 2007. Lead-210 observations within CARBOSOL: A diagnostic tool for assessing the spatiotemporal variability of related chemical aerosol species? *Journal of Geophysical Research*, **112**.

Heikkilä, U. 2007. *Modeling of the atmospheric transport of the cosmogenic radionuclides ^{10}Be and ^{7}Be using the ECHAM5-HAM General Circulation Model.* PhD thesis, ETH Zurich.

Heikkilä, U., & Smith, A. M. 2012. Influence of model resolution on the atmospheric transport of ^{10}Be. *Atmospheric Chemistry and Physics Discussions*, **12**, 18531–18564.

Heikkilä, U., Beer, J., & Alfimov, V. 2008a. Beryllium-10 and beryllium-7 in precipitation in Dübendorf (440 m) and at Jungfraujoch (3580 m), Switzerland (1998-2005). *Journal of Geophysical Research*, **113**, D11104.

Heikkilä, U., Beer, J., & Feichter, J. 2008b. Modeling cosmogenic radionuclides ^{10}Be and ^{7}Be during the Maunder Minimum usiong the ECHAM5-HAM General Circulation Model. *Atmospheric Chemistry and Physics*, **8**, 2797–2809.

Heikkilä, U., Beer, J., & Feichter, J. 2009. Meridional transport and deposition of atmospheric ^{10}Be. *Atmospheric Chemistry and Physics*, **9**, 515–527.

Heimann, M., Monfray, P., & Polian, G. 1990. Modeling the long-range transport of ^{222}Rn to subantactic and antarctic areas. *Tellus*, **42B**, 83–99.

Herbst, K., Kopp, A., Heber, B., Steinhilber, F., Fichtner, H., Scherer, K., & Matthiä, D. 2010. On the importance of the local interstellar spectrum for the solar modulation parameter. *Journal of Geophysical Research*, **115**, D00120.

Hesshaimer, V. 1997. *Tracing the global carbon cycle with bomb radiocarbon,*. PhD thesis, University of Heidelberg, Heidelberg, Germany.

Hirao, S. 2012. *Personal communication.*

Hirao, S., Yamazawa, H., & Moriizumi, J. 2010. Estimation of the global ^{222}Rn flux density from the earth‘s surface. *Japanese Journal of Health Physics*, **45(2)**, 161–171.

Horiuchi, K., Uchida, T., Sakamoto, Y., Ohta, A., Matsuzaki, H., Shibata, Y., & Motoyama, H. 2008. Ice core record of ^{10}Be over the past millennium from Dome Fuji, Antarctica: A new proxy record of past solar activity and a powerful tool for stratigraphic dating. *Quaternary Geochronology*, **3**, 245–261.

Indermühle, A., Stocker, T.F., Joos, F., Fischer, H., Smith, H.J., Wahlen, M., Deck, B., Mastroianni, D., Tschumi, J., Blunier, T., Meyer, R., & Stauffer, B. 1999. Holocene carbon-cycle dynamcis based on CO_2 trapped in ice at Taylor Dome, Antarctica. *Nature*, **398**, 121–126.

Ioannidou, A., Manolopoulou, M., & Papastefanou, C. 2005. Temporal changes of ^{7}Be and ^{210}Pb concentrations in surface air at temperate latitudes (40° N). *Applied Radiation and Isotopes*, **63**, 277–284.

Jacobs, G.A., & Mitchell, J.L. 1996. Ocean circulation variations associated with the Antarctic Circumpolar Wave. *Geophysical Research Letters*, **23(21)**.

Janowiak, J.E., Gruber, A., Kondragunta, C.R., Livezey, R.E., & Huffman, G.J. 1998. A comparison of the NCEP-NCAR reanalysis precipitation and the GPCP rain gauge-satellite combined dataset with observational error considerations. *Journal of Climate*, **11**, 2960–2979.

Jansen, E., Overpeck, J., Briffa, K.R., Duplessy, J.-C., Joos, F., Masson-Delmotte, V., Olago, D., Otto-Bliesner, B., Peltier, W.R., Rahmstorf, S., Ramesh, R., Raynaud, D., Rind, D., Solomina, O., Villalba, R., & Zhang, D. 2007. *Climate Change 2007: The Physical Science Basis. Contribution of Working Group I to the Fourth Assessment Report of the Intergovernmental Panel on Climate Change.* Cambridge University Press, Cambridge, United Kingdom and New York, NY, USA. Chap. Palaeoclimate, pages 433–497.

Johnsen, S.J., Dahl-Jensen, D., Dansgaard, W., & Gundestrup, N. 1995. Greenland paleotemperatures derived from GRIP bore hole temperature and ice core isotope profiles. *Tellus*, **47B**, 624–629.

Joos, F., Gerber, S., Prentice, I.C., Otto-Bliesner, B.L., & Valdes, P. 2004. Transient simulations of Holocene atmospheric carbon dioxide and terrestrial carbon since the Last Glacial Maximum. *Global Biogeochemical Cycles*, **18**, GB2002.

Junge, C.E. 1963. *Air Chemistry and Radioactivity.* International Geophysics Series, vol. 4. Academic Press New York and London.

Junge, C.E. 1975. Processes responsible for the trace content in precipitation. In: Isotopes and impurities in snow and ice. *In: Isotopes and impurities in snow and ice*, vol. 118. International Association of Hydrological Sciences.

Kapsner, W.R., Alley, R.B., Shuman, C.A., Anandakrishnan, S., & Gr, P.M. 1995. Dominant influence of atmospheric circulation on snow accumulation in Greenland over the past 18,000 years. *Nature*, **373**, 52–54.

Kaufmann, P., Fundel, F., Fischer, H., Bigler, M., Ruth, U., Udisti, R., Hansson, M., de Angelis, M., Barbante, C., Wolff, E., Hutterli, M., & Wagenbach, D. 2010. Ammonium and non-sea salt sulfate in the EPICA ice cores as indicator of biological activity in the Southern Ocean. *Quaternary Science Reviews*, **29**, 313–323.

Köhler, P., Muscheler, R., & Fischer, H. 2006. A model-based interpretation of low-frequency changes in the carbon cycle during the last 120000 years and its implications for the reconstruction of atmospheric $\Delta\ ^{14}$C. *Geochemistry Geophysics Geosystems*, **7**.

King, J. C., & Turner, J. 1997. *Antarctic meteorology and climatology.* Cambridge University Press.

Klose, S. 2010. *Der saisonale Zyklus des terrigenen Radionuklids ^{210}Pb in der Antarktis.* Bachelor thesis, Institut für Umweltphysik, University of Heidelberg.

König-Langlo, G., King, J.C., & Pettre, P. 1998. Climatology of the three coastal Antarctic stations Dumont d'Urville, Neumayer, and Halley. *Journal of Geophysical Research*, **103**, 10,935–10,946.

Knudsen, M.F., Riisager, P., Donadini, F., Snowball, I., Muscheler, R., Korhonen, K., & Pesonen, L.J. 2008. Variations in the geomagnetic dipole moment during the Holocene and the past 50 kyr. *Earth and Planetary Science Letters*, **272**, 319–329.

Koch, D. M., & Mann, M. E. 1996. Spatial and temporal variability of ^{7}Be surface concentrations. *Tellus*, **48B**, 387–396.

Koch, D.M., Jacob, D.J., & Graustein, W.C. 1996. Vertical transport of tropospheric aerosols as indicated by ^{7}Be and ^{210}Pb in a chemical tracer model. *Journal of Geophysical Research*, **101(D13)**, 18,651–18,666.

Kolb, W. 1992. *Aktivitätskonzentrationen von Radionukliden in der bodennahen Luft Norddeutschlands und Nordnorwegens im Zeitraum von 1963 bis 1990.* Report PTB-Ra-29. Physikalisch Technische Bundesanstalt, Braunschweig, Germany.

Kollár, D., Leya, I., Masarik, J., & Michel, R. 2000. Calculation of cosmogenic nuclide production rates in the Earth atmosphere and in terrestrial surface rocks using improved neutron cross sections. *Meteoritics and Planetary Science*, **35(suppl.)**, A90–A91.

Korschinek, G., Bergmaier, A., Faestermann, T., Gerstmann, U.C., Knie, K., Rugel, G., Wallner, A., Dillmann, I., Dollinger, G., von Gostomski, Ch. Lierse, Kossert, K., Maiti, M., Poutivtsev, M., & Remmert, A. 2010. A new value for the half-life of ^{10}Be by Heavy-Ion Elastic Recoil Detection and liquid scintillation counting. *Nuclear Instruments and Methods in Physics Research B*, **268**, 187–191.

Korte, M., Constable, C., Donadini, F., & Holme, R. 2011. Reconstructing the Holocene geomagnetic field. *Earth and Planetary Science Letters*, **312**, 497–505.

Kovaltsov, G.A., & Usoskin, I.G. 2010. A new 3D numerical model of cosmogenic nuclide ^{10}Be production in the atmosphere. *Earth and Planetary Science Letters*, **291**, 182–188.

Kubik, P.W., & Christl, M. 2010. ^{10}Be and ^{26}Al measurements at the Zurich 6 MV Tandem AMS facility. *Nuclear Instruments and Methods in Physics Research B*, **268**, 880–883.

Kulan, A. 2007. *Atmospheric production and transport of cosmogenic ^{7}Be and ^{10}Be.* PhD thesis, University of Uppsala, Uppsala, Sweden.

Kulan, A., Aldahan, A., Possnert, G., & Vintersved, I. 2006. Distribution of ^{7}Be in surface air of Europe. *Atmospheric Environment*, **40**, 3855–3868.

Laj, C., Kissel, C., Mazaud, A., J.E.T.Channell, & Beer, J. 2000. North Atlantic paleointensity stack since 75ka (NAPIS-75) and the duration of the Laschamp event. *Philosophical Transactions of the Royal Society of London*, **358**, 1009–1025.

Laj, C., Kissel, C., & Beer, J. 2004. High resolution global paleointensity stack since 75 kyr (GLOPIS-75) calibrated to absolute values. *Pages 255–265 of: Timescales of the Paleomagnetic Field.* AGU Monograph.

Lal, D. 1988. Theoretically expected variations in the terrestrial cosmic-ray production rates of isotopes. *Pages 216–233 of:* Castagnoli, C. (ed), *Solar-Terrestrial Relationships and the Earth Environment in the last Millennia.* Soc. Italiana di Fisica, Bologna.

Lal, D. 2007. Recycling of cosmogenic nuclides after their removal from the atmosphere; special case of appreciable transport of ^{10}Be to polar regions by aeolian dust. *Earth and Planetary Science Letters*, **264**, 177–187.

Lal, D., & Peters, B. 1967. Cosmic ray produced radioactivity on the Earth. *In: Handbuch der Physik Bd.46/2.* Springer, Berlin.

Lambert, G., Ardouin, B., & Sanak, J. 1990. Atmospheric transport of trace elements toward Antarctica. *Tellus*, **42B**, 76–82.

Land, C., & Feichter, J. 2003. Stratosphere-Troposphere exchange in a changing climate simulated with the general circulation model MAECHAM4. *Journal of Geophysical Research*, **108(D12)**, 8523.

Latuske, N. 2006. *Solare Variabilität und Klimaänderungen auf einer Zeitskala von einigen Dekaden bis Jahrhunderten im Holozän.* PhD thesis, Institut für Umweltphysik, University of Heidelberg.

Lazarev, V. 2003. *The cosmogenic and anthropogenic ^{36}Cl in the environment.* PhD thesis, Technical University of Munich, Munich, Germany.

Lee, H.N., & Feichter, J. 1995. An intercomparison of wet precipitation scavenging schemes and the emission rates of ^{222}Rn for the simulation of global transport and deposition of ^{210}Pb. *Journal of Geophysical Research*, **100**, 23,252–23,270.

Leppänen, A.-P., Usoskin, I.G., Kovaltsov, G.A., & Paatero, J. 2012. Cosmogenic ^{7}Be and ^{22}Na in Finland: Production, observed periodicities and the connection to climatic phenomena. *Journal of Atmospheric and Solar-Terrestrial Physics*, **74**, 164–180.

Levin, I., Glatzel-Mattheier, H., Marik, T., Cuntz, M., Schmidt, M., & Worthy, D.E. 1999. Verification of German methane emission inventories and their recent changes based on atmospheric observations. *Journal of Geophysical Research*, **104(D3)**, 3447–3456.

Levin, I., Naegler, T., Heinz, R., Osusko, D., Cuevas, E., Engel, A., Ilmberger, J., Langenfelds, R.L., Neininger, B., v.Rohden, C., Steele, L.P., Weller, R., & ., D.E. Worthy. 2010a. The global SF_6 source inferred from long-term high precision atmospheric measurements and its comparison with emission inventories. *Atmospheric Chemistry and Physics*, **10**, 2655–2662.

Levin, I., Naegler, T., Kromer, B., Diehl, M., Francey, R.J., Gomez-Pelaez, A.J., Schäfer, A., Steele, L.P., Wagenbach, D., Weller, R., & Worthy, D.E. 2010b. Observations and modelling of the global distribution and long-term trend of atmospheric $^{14}CO_2$. *Tellus*, **62B**, 26–46.

Lewis, Brent. 2007. *Matlab 1976 Standard Atmosphere Calculator.* http://www.mathworks.com/matlabcentral/fileexchange/13635-complete-1976-standard-atmosphere.

Liu, H., Jacob, D., Bey, I., & R.M. Yantosca, R.M. 2001. Constraints from ^{210}Pb and ^{7}Be on wet deposition and transport in a global three-dimensional chemical tracer model driven by assimilated meteorological fields. *Journal of Geophysical Research*, **106, D11**, 12,109–12,128.

Lockhart, L.B., Patterson, R.L., Saunders, A.W., & Black, R.W. 1963. *Fission product radioactivity in the air along the 80th meridian (west) during 1961.* NRL report 5869. U.S. NAVAL Research Laboratory,Washington, D.C.

Martell, E.A. 1966. The size distribution and interaction of radioactive and natural aerosols in the stratosphere. *Tellus*, **18(2)**, 486–498.

Masarik, J., & Beer, J. 1999. Simulation of particles fluxes and cosmogenic nuclide production in the earth´s atmosphere. *Journal of Geophysical Research*, **D104**, 12,099–13,012.

Masarik, J., & Beer, J. 2009. An updated simulation of particle fluxes and cosmogenic nuclide production in the Earth´s atmosphere. *Journal of Geophysical Research*, **114**, D11103.

Masarik, J., & Reedy, R.C. 1995. Terrestrial cosmogenic-nuclide production systematics calculated from numerical simulations. *Earth and Planetary Science Letters*, **136**, 381–395.

Matthews, M. 2011. Relating to model building, an independent tracer to calibrate the BL-FT coupling would enhance the model‘s performance. *In: Science and Technology 2011, held 2-10 June, 2011 in Vienna, Austria.*

Mayewski, P.A., Rohling, E.E., Stager, J.C., Karlén, W., Maasch, K.A., Meeker, L.D., Meyerson, E.A., Gasse, F., van Kreveld, S., Holmgren, K., Lee-Thorp, J., Rosqvist, G., Rack, F., Staubwasser, M., Schneider, R.R., & Steig, E.J. 2004. Holocene climate variability. *Quaternary Research*, **62**, 243–255.

Mazarik, J. 2010. *Environmental Radionuclides: Tracers and Timers for terrestrial processes.* Elsevier. Chap. Origin and distribution of radionuclides in the continental environment.

Mazaud, A., Laj, C., & Bender, M. 1994. A geomagnetic chronology for antarcticic ice accumulation. *Geophysical Research Letters*, **21(5)**, 337–340.

McCracken, K.G. 2004. Geomagnetic and atmospheric effects upon the cosmogenic ^{10}Be observed in polar ice. *Journal of Geophysical Research*, **109**, A04101.

Megumi, K., Matsunami, T., Ito, Kiiyoda, S., Mizohata, A., & Asano, T. 2000. Factors, especially sunspot number, causing variations in surface air concentrations and depositions of ^{7}Be in Osaka, Japan. *Geophysical Research Letters*, **27(3)**, 361–364.

Monnin, E., Indermühle, A., Dällenbach, A., Flückiger, J., Stauffer, B., Stocker, T.F., Raynaud, D., & Barnola, J.-M. 2001. Atmospheric CO_2 concentrations over the last glacial termination. *Science*, **291**, 112–114.

Moore, H.E., Poet, S.E., & Martell, E.A. 1973. ^{222}Rn, ^{210}Pb, ^{210}Bi and ^{210}Po profiles and aerosol residence times versus altitude. *Journal of Geophysical Research*, **78**, 7065–7075.

Muscheler, R. 2000. *Nachweis von Änderungen im Kohlenstoffkreislauf durch Vergleich der Radionuklide ^{10}Be, ^{36}Cl und ^{14}C.* PhD thesis, ETH Zurich, Switzerland.

Muscheler, R., Beer, J., Wagner, G., Laj, C., Kissel, C., Raisbeck, G.M., Yiou, F., & Kubik, P.W. 2004. Changes in the carbon cycle during the last deglaciation as indicated by the comparison of ^{10}Be and ^{14}C records. *Earth and Planetary Science Letters*, **219**, 325–340.

Muscheler, R., Beer, J., Kubik, P.W., & Synal, H.A. 2005. Geomagnetic field intensity during the last 60000 years based on ^{10}Be and ^{36}Cl from the Summit ice cores and ^{14}C. *Quaternary Science Reviews*, **24**, 1849–1860.

Muscheler, R., Snowball, I., Joos, F., Müller, S., Beer, J., & Vonmoos, M. 2007. Solar activity during the last 1000 yr inferred from radionuclide records. *Quanternary Science Reviews*, **27**, 82–97.

Myslek-Laurikainen, B., Matul, M., Mikolajewski, S., Trzaskowska, H., Preibisz, Z., Garanty, I., Kubicki, M., Rakowski, P., Krynicki, T., & Stefanski, M. 2006. Air aerosol sampling station AZA-1000 at Polish Polar Station in Hornsund, Spitsbergen. *Nukleonika*, **51(2)**, 137–140.

Naegler, T. 2005. *Simulating bomb radiocarbon: Consequences for the global carbon cycle.* PhD thesis, University of Heidelberg, Heidelberg, Germany.

Naegler, T., & Levin, I. 2006. Closing the global radiocarbon budget 1945-2005. *Journal of Geophysical Research*, **111**, D12311.

Nagai, H., Tada, W., & Kobayashi, T. 2000. Production rates of ^{7}Be and ^{10}Be in the atmosphere. *Nuclear Instruments and Methods in Physics Research B*, **172**, 796–801.

NGRIP. 2004. High-resolution record of Northern Hemisphere climate extending into the last interglacial period. *Nature*, **431**, 147–151.

Nishiizumi, K., & Finkel, R. 2007. *Cosmogenic radionuclides in the Siple Dome A ice core.* Digital media. http://nsidc.org/data/docs/agdc/nsidc0307_nishiizumi/index.html.

Nishiizumi, K., Imamura, M., Caffee, M.W., Southon, J.R., Findel, R.C., & J-McAninch. 2007. Absolute calibration of ^{10}Be AMS standards. *Nuclear Instruments and Methods in Physics Research B*, **258**, 403–413.

NOAA. 1976. *U.S. Standard Atmosphere.* Tech. rept. National Oceanic and Atmosphere Adminitration (NOAA).

OBrien, K. 1979. Secular variations in the production of cosmogenic isotopes in the Earth‘s atmosphere. *Journal of Geophysical Research*, **84**, 423–431.

OBrien, K., Lerner, A. De La Zerda, Shea, M.A., & Smart, D.F. 1991. The production of cosmogenic isotopes in the Earth‘s atmosphere and their inventories. *Pages 317–341 of: The sun in time.* Sonett M.P., Giampapa M.S. Matthews M.S.

Oerter, H., Fischer, H., & Sperlich, P. 2008. Spatial variability of δ^{18}O upstream and around the EDML drilling site. *In: Quaternary Climate: from Pole to Pole, EPICA Open Science Conference, Venice, Itly, November 10-13.*

Oerter, H., Wilhelms, F., Hansson, M., Holmlund, P., Ingwander, S., Karlin, T., & Fujita, S. 2011. Stable isotope content and snow accumulation between 1964 and 2007/08 along the ice divide from Kohnen-Station towards Dome Fuji, East Antarctica. *EGU General Assembly 2011, Vienna, Austria.-8. April 2011.*

Oeschger, H., Siegenthaler, U., Gugelmann, A., & Schotterer, U. 1975. A box-diffusion model to study the carbon dioxide exchange in nature. *Tellus*, **27**, 168–192.

Offermann, C. 2006. *Rezente Variabilität der kosmogenen Radionuklide ^{10}Be und ^{7}Be im Bereich der Küstenantarktis.* Diploma thesis, Institut für Umweltphysik, University of Heidelberg.

Paatero, J., Hatakka, J., Mattsson, R., & Viisanen, Y. 1998. Analysis of daily ^{210}Pb air concentrations in Finland, 1967-1996. *Radiation Protection Dosimetry*, **77(3)**, 191–198.

Paatero, J., Buyukay, M., Holmén, K., Hatakka, J., & Viisanen, Y. 2010. Seasonal variation and source areas of airborne lead-210 at Ny-Ålesund in the High Arctic. *Polar Research*, **29(3)**, 345–352.

Papastefanou, C. 2008. *Radioactive Aerosols.* Radioactivity in the environment, vol. 12. Elsevier.

Parrenin, F., Rémy, F., Ritz, C., Siegert, M. J., & Jouzel, J. 2004. New modeling of the Vostok ice flow line and implication for the glaciological chronology of the Vostok ice core. *Journal of Geophysical Research*, **D20102**.

Pedro, J. 2012. *Personal communication.* ACE CRC Tasmania.

Pedro, J., van Ommen, T.D., Curran, M.A., Morgan, V., Smith, A.M., & McMrrow, A. 2006. Evidence for climate modulation fo the ^{10}Be solar activity proxy. *Journal of Geophysical Research*, **111**, D21105.

Pedro, J., Smith, A.M., Simon, K.J., van Ommen, T.D., & Curran, M.A. 2011. High-resolution records of the beryllium-10 solar activity proxy in ice from Law Dome, East Antarctica: measurement, reproducibility and principal trends. *Climate of the Past*, **7**, 707–721.

Peng, T.H., Broecker, W.S., Mathieu, G.C, Li, Y.H., & Bainbridge, A.E. 1979. Radon evasion rates in the Atlantic and Pacific oceans as determined during the Geosecs program. *Journal of Geophysical Research*, **84**, 2471–2486.

Peterson, K.R. 1970. An empirical model for estimatiing world-wide deposition from atmospheric nuclear detonation. *Health Physics*, **18**, 357–378.

Phillpot, H. R., & Zillman, J. W. 1970. The surface temperature inversion over the Antarctic continent. *Journal of Geophysical Research*, **75**, 4161–4168.

Pourchet, M., Magand, O., Frezotti, M., Ekaykin, A., & Winther, J.-G. 2003. Radionuclides deposition over Antarctica. *Journal of Environmental Radioactivity*, **68**, 137–158.

Preiss, N., Melieres, M.-A., & Pourchet, M. 1996. A compilation of data on lead 210 concentration in surface air and fluxes at the air-surface and water-sediment interfaces. *Journal of Geophysical Research*, **101(D22)**, 28847–28862.

Rahn, K.A., & McCaffrey, R.J. 1979. Compositional differences between Arctic air and snow. *Nature*, **280**, 479–480.

Rahn, K.A., & McCaffrey, R.J. 1980. On the origin and transport of the winter arctic aerosol. *Annals of the New York Academy of Sciences*, **338**, 486–503.

Raisbeck, G.M., Yiou, F., Fruneau, M., Loiseaux, J.M., Lieuvin, M., Ravel, J.C., & Lorius, C. 1981a. Cosmogenic ^{10}Be concentrations in Antarctic ice during the past 30,000 years. *Nature*, **292**, 825–826.

Raisbeck, G.M., Yiou, F., Fruneau, M., Loiseaux, J.M., Lieuvin, M., & Ravel, J.C. 1981b. Cosmogenic ^{10}Be/ ^{7}Be as a probe of atmospheric transport processes. *Geophysical Research Letters*, **8(9)**, 1015–1018.

Raisbeck, G.M., Yiou, F., Bourles, D., Lorius, C., Jouzel, J., & Barkov, N.I. 1987. Evidence for two intervals of enhanced ^{10}Be deposition in Antarctic ice during the last glacial period. *Nature*, **326**, 273–277.

Raisbeck, G.M., Yiou, F., Jouzel, J., & Petit, J.R. 1990. ^{10}Be and δ^2H in polar ice cores as a probe of the solar variability‘s influence on climate. *Philosophical Transactions of the Royal Society of London.A*, **330**, 463–470.

Rasmussen, S.O., Andersen, K.K., Svensson, A.M., Steffensen, J.P., Vinther, B.M., Clausen, H.B., Siggaard-Andersen, M.-L., Johnsen, S.J., Larsen, L.B., Dahl-Jensen, D., Bigler, M., Röthlisberger, R., Fischer, H., Goto-Azuma, K., Hansson, M.E., & Ruth, U. 2006. A new Greenland ice core chronology for the last glacial termination. *Journal of Geophysical Research*, **111**, D06102.

Rasmussen, S.O., Seierstad, I.K., Andersen, K.K., Bigler, M., Dahl-Jensen, D., & Johnsen, S.J. 2008. Synchronization of the NGRIP, GRIP, and GISP2 ice cores across MIS 2 and palaeoclimatic implications. *Quaternary Science Reviews*, **27(1-2)**, 18–28.

Rath, H. 1988. *Simulation der globalen ^{85}Kr- und ^{14}CO$_2$-Verteilung mit Hilfe eines zeitabhängigen, zweidimensionalen Modells der Atmosphäre,*. PhD thesis, Universität Heidelberg, Germany.

Rehfeld, S., & Heimann, M. 1995. Three dimensional atmospheric transport simulation of the radioactive tracers ^{210}Pb, ^{7}Be, ^{10}Be and ^{90}Sr. *Journal of Geophysical Research*, **100(D12)**, 26.141–26,161.

Reimer, P.J., Baillie, M.G.L., Bard, E., Bayliss, A., Beck, J.W., Blackwell, P.G., Bronk-Ramsey, C., Buck, C.E., Burr, G.S., Edwards, R.L., Friedrich, M., Grootes, P.M., Guilderson, T.P., Hajdas, I., Heaton, T.J., Hogg, A.G., Hughen, K.A., Kromer, K.F. Kaiser B., McCormac, F.G., Manning, S.W., Reimer, R.W., Richards, D.A., Southon, J.R., Talamo, S., Turney, C.S.M., van der Plicht, J., & Weyhenmeyer, C.E. 2009. INTCAL09 and MARiNE09 radiocarbon age calibration curves, 0-50,000 years CAL BP. *Radiocarbon*, **51(4)**, 1111–1150.

Robertson, L.B., Stevenson, D.S., & Conen, F. 2005. Test of a northwards-decreasing ^{222}Rn source term by comparison of modelled and observed atmospheric ^{222}Rn concentrations. *Tellus*, **57B**, 116–123.

Roedel, W. 2000. *Physik unserer Umwelt: Die Atmosphäre.* Springer-Verlag Berlin Heidelberg New York.

Rohlfs, J. 2004. *Zeitliche Variationen von ^{10}Be in der Küstenantarktis - Eine Eiskernzeitreihe von Berkner Island.* Diploma thesis, Institut für Umweltphysik, University of Heidelberg.

Roos, P., Holm, R., Persson, R.B.R., Aarkrog, A., & Nielsen, S.P. 1994. Deposition of ^{210}Pb, ^{137}Cs, $^{239+240}$Pu, ^{238}Pu, and ^{241}Am in the Antarctic Peninsula Area. *Journal of Environmental Radioactivity*, **24**, 235–251.

Rotschky, G., Holmlund, P., Isaksson, E., Mulvaney, R., Oerter, H., van den Broeke, M.R., & Winther, J.-G. 2007. A new surface accumulation map for western Dronning Maud Land, Antarctica, from interpolation of point measurements. *Journal of Glaciology*, **53(182)**, 385–395.

Ruth, U., Barnola, J.-M., Beer, J., Bigler, M., Blunier, T., Castellano, E., Fischer, H., Fundel, F., Huybrechts, P., Kaufmann, P., Kipfstuhl, S., Lambrecht, A., Morganti, A., Oerter, H., Parrenin, F., Rybak, O., Severi, M., Udisti, R., Wilhelms, F., & Wolff, E. 2007. "EDML1": a chronology for the EPICA deep ice core from Dronning Maud Land, Antarctica, over the last 150000 years. *Climate of the Past*, **3**, 475–484.

Sanak, J., Lambert, G., & Ardouin, B. 1985. Measurement of stratosphere-to-troposphere exchange in Antarctica by using short-lived cosmonuclides. *Tellus*, **37B**, 109–115.

Schery, S. 2001. *Understanding radioactive aerosols and their measurement.* Kluwer Academic Publishers.

Schery, S., & Huang, S. 2004. An estimate of the global distribution of radon emissions from the ocean. *Geophysical Research Letters*, **31**, L19104.

Schery, S.D., & Wasiolek, M.A. 1998. *^{222}Rn and Thoron in the human environment.* World Scientific, Singapore. Chap. Modeling ^{222}Rn flux from the earth‘s surface, pages 207–217.

Schmidt, G.A., Shindell, D.T., Miller, R.L., Mann, M.E., & Rind, D. 2004. General circulation modelling of Holocene climate variability. *Quaternary Science Reviews*, **23**, 2167–2181.

Serreze, M.C., & Barry, R.C. 2005. *The arctic climate system.* Cambridge University Press.

Shaw, G. 1979. Considerations on the origin and properties of the Antarctic Aerosol. *Reviews of Geophysics and Space Physics*, **17**, 1983–1997.

Shaw, G.E. 1995. The Arctic Haze phenomenon. *Bulletin of the American Meteorological Society*, **76**, 2403–2413.

Siegenthaler, U. 1983. Uptake of excess CO_2 by an outcrop-diffusion model ocean. *Journal of Geophysical Research*, **88(C6)**, 3599–3608.

Siegenthaler, U., Heimann, M., & Oeschger, H. 1980. ^{14}C variations caused by changes in the global carbon cycle. *Radiocarbon*, **22(2)**, 177–191.

Simmonds, I. 2003. *Antarctic Peninsula Climate Variability: Historical and Paleoenvironmental Perspectives.* Antarctic Research Series, vol. 79. AGU, Washington, D. C. Chap. Regional and large-scale influences on Antarctic Peninsula climate, pages 31–42.

Simpson, J.A. 1983. Elemental and isotopic composition of the galactic cosmic rays. *Annual Review of Nuclear and Particle Science*, **33**, 323–381.

Slinn, W.G.N. 1977. Some approximations for the wet and dry removal of particles and gases from the atmosphere. *Water, Air, and Soil Pollution*, **7**, 513–543.

Smart, D.F., & Shea, M.A. 2008. World grid of calculates cosmic ray vertical cutoff rigidities for Epoch 1995.0. *Proceedings oft he 30th International Cosmic Ray Conference Mexico City*, **1(SH)**, 733–736.

Smith, A.M., Fink, D., Chid, D., Levchenko, V.A., Morgan, V.I., Curran, M., Etheridge, D.M., & Elliott, G. 2000. ^{7}Be and ^{10}Be concentrations in recent firn and ice at Law Dome, Antarctica. *Nuclear Instruments and Methods in Physics Research B*, **172**, 847–855.

Solanki, S.K., Usoskin, I.G., Kromer, B., Schüssler, M., & Beer, J. 2004. Unusual activity of the Sun during recent decades compared to the previous 11,000 years. *Nature*, **431**, 1084–1087.

Southon, J. 2004. A radiocarbon perspective on Greenland ice-core chronologies: Can we use ice cores for ^{14}C calibration? *Radiocarbon*, **46**, 1239–1259.

Sportisse, B. 2007. A review of parameterizations for modelling dry deposition and scavenging of radionuclides. *Atmospheric Environment*, **41**, 2683–2698.

Stanzick, A. 1996. *Räumliche und zeitliche Depositionsvariationen der Radioisotope ^{10}Be und ^{210}Pb in Eisbohrkernen Zentralgrönlands.* Diploma thesis, Institut für Umweltphysik, University of Heidelberg.

Stanzick, A. 2001. *Raum-Zeit-Variationen von Be-10, Pb-210 und Cl-36 in der grönländischen Firndecke: Luft-Firn-Transfer und rezente Trends.* PhD thesis, Institut für Umweltphysik, University of Heidelberg.

Steffen, K., & Box, J. 2001. Surface climatology of the Greenland ice sheet: Greenland Climate Network 1995-1999. *Journal of Geophysical Research*, **106(D24)**, 33,951–33,964.

Steig, E.J. 1996. *Beryllium-10 in the Taylor Dome ice core: Applications to Antarctic glaciology and paleoclimatology.* PhD thesis, University of Washington.

Steig, E.J., Polissar, P.J., Stuiver, M., Grootes, P.M., & Finkel, R.C. 1996. Large amplitude solar modulation cycles of ^{10}Be in Antarctica: implications for atmospheric mixing processes and interpretation of the ice core record. *Geophysical Research Letters*, **23**, 523–526.

Steig, E.J., Brook, E.J., White, J.W.C., Sucher, C.M., Bender, M.L., Lehman, S.J., Morse, D.L., Waddington, E.D., & Clow, G.D. 1998. Synchronous climate changes in Antarctica and the North Atlantic. *Science*, **282(5386)**, 92–95.

Steig, E.J., Morse, D.L., Waddington, E.D., Stuiver, M., Grootes, P.M., Mayewski, P.A., Twickler, M.S., & Whitlow, S.I. 2000. Wisconsinan and Holocene climate history from an ice core at Taylor Dome, Western Ross Embayment, Antarctica. *Geografiska Annaler*, **82A**, 213–235.

Steinhilber, F., Abreu, J. A., Beer, J., Brunner, I., Christl, M., Fischer, H., Heikkilä, U., Kubik, P.W., Mann, M., McCracken, K.G., Miller, H., Miyahara, H., Oerter, H., & Wilhelms, F. 2012. 9,400 years of cosmic radiation and solar activity from ice cores and tree rings. *Proceedings of the National Academy of Sciences*, **109(16)**, 5967–5971.

Stohl, A. 2006. Characteristics of atmospheric transport into the Arctic troposphere. *Journal of Geophysical Research*, **111**, D11306.

Stohl, A., Forster, C., Frank, A., Seibert, P., & Wotawa, G. 2005. Technical note: The Lagrangian particle dispersion model FLEXPART version 6.2. *Atmospheric Chemistry and Physics*, **5**, 2461–2474.

Stone, J., Fifield, K., Beer, J., Vonmoos, M., Obrist, C., Grajcar, M., Kubik, P., Muscheler, R., Finkel, R., & Caffee, M. 2004. Co-precipitated silver-metal oxide aggregates for accelerator mass spectrometry of ^{10}Be and ^{26}Al. *Nuclear Instruments and Methods in Physics Research B*, **223-224**, 272–277.

Svensson, A., Andersen, K.K., Bigler, M., Clausen, H.B., Dahl-Jensen, D., Davies, S.M., Johnsen, S.J., Muscheler, R., Rasmussen, S.O., Röthlisberger, R., Seierstad, I., Steffensen, J.P., & Vinther, B.M. 2008. A 60000 year Greenland stratigraphic ice core chronology. *Climate of the Past*, **4**, 47–57.

Sykora, I., & Fröhlich, K. 2010. *Environmental Radionuclides: Tracers and Timers for terrestrial processes.* Radioactivity in the environment, vol. 16. Elsevier. Chap. Radionuclides as tracers of atmospheric processes, pages 51–88.

Szegvary, T., Conen, F., & Ciais, P. 2009. European ^{222}Rn inventory for applied atmospheric studies. *Atmospheric Environment*, **43**, 1536–1539.

Taylor, K.C., White, J.W.C., Severinghaus, J.P., Brook, E.J., Mayewski, P.A., Alley, R.B., Steig, E.J., Spencer, M.K., Meyerson, E., Meese, D.A., Lamorey, G.W., Grachevc, A., Gowh, A.J., & Barnett, B.A. 2004. Abrupt climate change around 22 ka on the Siple Coast of Antarctica. *Quaternary Science Reviews*, **23**, 7–15.

Todd, J.F., Wong, G.T.F., Olsen, C.R., & Larsen, I.L. 1989. Atmospheric depositional characteristics of Beryllium 7 and Lead 210 along the southeastern Virginia coast. *Journal of Geophysical Research*, **94(D8)**, 11,106–11,116.

Torrence, C., & Compo, G.P. 1998. A practical guide to wavelet analysis. *Bulletin of the American Meteorological Society*, **79**, 61–78.

Turekian, K.K., Nozaki, Y., & Benninger, L.K. 1977. Geochemistry of atmospheric radon and radon products. *Annual Review of Earth and Planetary Sciences*, **5**, 227–255.

Turekian, K.K, Benninger, L.K., & Dion, E.P. 1983. ^{7}Be and ^{210}Pb total deposition fluxes at New Haven, Connecticut and at Bermuda. *Journal of Geophysical Research*, **88(C9)**, 5411–5415.

Udisti, R., Becagli, S., Castellano, E., Delmonte, B., Jouzel, J., Petit, J.R., Schwander, J., Stenni, B., & Wolff, E.W. 2004. Stratigraphic correlations between the European Project for Ice Coring in Antarctica (EPICA) Dome C and Vostok ice cores showing the relative variations of snow accumulation over the past 45 kyr. *Journal of Geophysical Research*, **109**, D08101.

UNSCEAR. 2000. *Sources and effects of ionizing radiation, UNSCEAR 2000 Report to the General Assembly.* Tech. rept. United Nations Scientific Committee on the Effects of Atomic Radiation, http://www.unscear.org/, Vienna, Austria, 2000.

Usoskin, I.G. 2008. A history of solar activity over millennia. *Living Reviews in Solar Physics*, **5(3)**.

Usoskin, I.G., & Kovaltsov, G.A. 2008. Production of cosmogenic ^{7}Be isotope in the atmosphere: Full 3-D modeling. *Journal of Geophysical Research*, **113**, D12107.

Usoskin, I.G., Solanki, S., Schüssler, M, Mursula, K., & Alanko, K. 2003. A Millennium-scale sunspot number reconstruction: Evidence for an unusually active sun since the 1940s. *Physical Review Letters*, **91**.

Usoskin, I.G., Alanko-Huotari, K., Kovaltsov, G.A., & Mursula, K. 2005. Heliospheric modulation of cosmic rays: Monthly reconstruction for 1951-2004. *Journal of Geophysical Research*, **110**, A12108.

Usoskin, I.G., Field, C.V., Schmidt, G.A., Leppänen, A.-P., Aldahan, A., Kovaltsov, G.A., Possnert, G., & Ungar, R.K. 2009. Short-term production and synoptic influences on atmospheric ^{7}Be concentrations. *Journal of Geophysical Research*, **113**, D06108.

Usoskin, I.G., Galina, A., Bazilevskaya, A., & Kovaltsov, G. A. 2011. Solar modulation parameter for cosmic rays since 1936 reconstructed from ground-based neutron monitors and ionization chambers. *Journal of Geophysical Research*, **116**, A02104.

Valet, J.-P. 2003. Time variations in geomagnetic intensity. *Reviews of Geophysics*, **41(1004)**.

Vautard, R., Yiou, P., & Ghil, M. 1992. Singular spectrum analysis: A toolkit for short, noisy chaotic signals. *Physica D*, **58**, 95–126.

Vedder, C. 2009. *Modeling climate and production-related impacts on ice-core Beryllium-10.* PhD thesis, Columbia University.

Vinther, B.M., Clausen, H.B., Johnsen, S.J., Rasmussen, S.O., Andersen, K.K., Buchardt, S.L., Dahl-Jensen, D., Seierstad, I.K., Siggaard-Andersen, M.-L., Steffensen, J.P., Svensson, A.M., Olsen, J., & Heinemeier, J. 2006. A synchronized dating of three Greenland ice cores throughout the Holocene. *Journal of Geophysical Research*, **111**, D13102.

Vonmoos, M., Beer, J., & Muscheler, R. 2006. Large variations in Holocene solar activity: Constraints from ^{10}Be in the Greenland Ice Core Project ice core. *Journal of Geophysical Research*, **111**, A10105.

Wagenbach, D. 1996. Coastal Antarctica: Atmospheric chemical composition and atmospheric transport. *Pages 173–199 of:* Wolff, E.W., & Bales, R.C. (eds), *Chemical exchange between the atmosphere and polar snow.* NATO ASI Series. Springer, Berlin, Heidelberg.

Wagenbach, D. 2012. *Personal cummunication.*

Wagenbach, D., Görlach, U., Moser, K., & K.O.Münnich. 1988. Coastal Antarctic aerosol: the seasonal pattern of its chemical composition and radionuclide content. *Tellus*, **40B**, 426–436.

Wagenbach, D., Legrand, M., Fischer, H., Pichlmayer, F., & Wolff, E.W. 1998. Atmospheric near-surface nitrate at coastal Antarctic sites. *Journal of Geophysical Research*, **103(D9)**, 11,007–11,020.

Wagenbach, D., Bohleber, P., & Preunkert, S. 2012. Cold, Alpine ice bodies revisted: What may we learn from their impurity and isotope content? *Geografiska Annaler: Series A, Physical Geography*, **94**, 245–263.

Wagner, G., Masarik, J., Beer, J., Baumgartner, S., Imboden, D., Kubik, P.W., Synal, H.A., & Su, M. 2000. Reconstruction of the geomagnetic field between 20 and 60 kyr BP from cosmogenic radionuclides in the GRIP ice core. *Nuclear Instruments and Methods in Physics Research B*, **172**, 597–604.

Wagner, G., Beer, J., Masarik, J., Muscheler, R., Kubik, P.W., Mende, W., Laj, C., Raisbeck, G.M., & Yiou, F. 2001a. Presence of the Solar de Vries Cycle (∼205 years) during the Last Ice Age. *Geophysical Research Letters*, **28(2)**, 303.

Wagner, G., Laj, C., Beer, J., Kissel, C., Muscheler, R., Masarik, J., & Synal, H.A. 2001b. Reconstruction of the paleoaccumulation rate of central Greenland during the last 75 kyr using the cosmogenic radionuclides ^{36}Cl and ^{10}Be and geomagnetic field intensity data. *Earth and Planetary Science Letters*, **193**, 515–521.

Warren, S. 2007. *World Weather / Climate Extremes Archive*. http://wmo.asu.edu/world-lowest-temperature. Access in July 2012.

Webber, W.R., & Higbie, P.R. 2003. Production of cosmogenic Be nuclei in the Earth´s atmosphere by cosmic rays: Its dependence on solar modulation and the interstellar cosmic ray spectrum. *Journal of Geophysical Research*, **1355,**, 1355.

Webber, W.R., Higbie, P.R., & McCracken, K.G. 2007. Production of the cosmogenic isotopes ^{3}H, ^{7}Be, ^{10}Be, and ^{36}Cl in the Earth's atmosphere by solar and galactic cosmic rays. *Journal of Geophysical Research*, **112**, A10106.

Wegner, A. 2003. *Die Geschichte der Sonnenaktivität im Antarktischen Eis Nachweis produktionsbedingter ^{10}Be-Schwankungen*. Diploma thesis, Institut für Umweltphysik, University of Heidelberg.

Weller, R., Wöltjen, J., Piel, C., Resenberg, R., Wagenbach, D., König-Langlo, G., & Kriews, M. 2008. Seasonal variability of crustal and marine trace elements in the aerosol at Neumayer Station, Antarctica. *Tellus B*, **60(5)**, 742–752.

Weller, R., Wagenbach, D., Legrand, M., Elsässer, C., Tian-Kunze, X., & G., König-Langlo. 2011. Continuous 25-years aerosol records at coastal Antarctica: Part 1. Inter-annual variability of ionic compounds and links to climate indices. *Tellus*, **63B**, 901–919.

Wershofen, H. 2011. *personal communication.* PTB Braunschweig.

Wershofen, H., & Arnold, D. 2005. *Radionuclides in ground-level air in Braunschweig - report of the PTB Trace Survey Station from 1998 to 2003.* PTB-Ra-45. PTB Braunschweig.

Wilkening, M.H., & Clements, W.E. 1975. Radon 222 from the ocean surface. *Journal of Geophysical Research*, **80**, 3828–3830.

Winkler, R., & Rosner, G. 2000. Seasonal and long-term variation of ^{210}Pb concentration in air, atmospheric deposition rate and total deposition velocity in south Germany. *The Science of the Total Environment*, **263**, 57–68.

Winkler, R., Dietl, F., Frank, G., & Tschiersch, J. 1998. Temporal variation of ^{7}Be and ^{210}Pb size distributions in ambient aerosol. *Atmospheric Environment*, **32**, 983–991.

Wolff, E.W., Chappellaz, J., Blunier, T., Rasmussen, S.O., & Svensson, A. 2010. Millennial-scale variability during the last glacial: The ice core record. *Quaternary Science Reviews*, **29**, 2828–2838.

Yang, S., Odah, H., & Shaw, J. 2000a. Variations in the geomagnetic dipole moment over the last 12000 years. *Geophysical Journal International*, **140**, 158–162.

Yang, X., North, R., & Romney, C. 2000b. *CMR Nuclear Explosion Database (Revision 3).* CMR Technical Report 00/16. Center for Monitoring Research, U.S. Army Space and Missile Defense Command, Alington VA, US.

Yiou, F., Raisbeck, G.M., Bourles, D., Lorius, C., & Barkov, N.I. 1985. ^{10}Be in ice at Vostok Antarctica during the last climatic cycle. *Nature*, **316**, 616ff.

Yiou, F., Raisbeck, G.M., Baumgartner, S., Beer, J., Hammer, C., Johnsen, S., Jouzel, J., Kubik, P.W., Lestringuez, J., Stievenard, M., Suter, M., & Yiou, P. 1997. Beryllium 10 in the Greenland Ice Core Project ice core at Summit, Greenland. *Journal of Geophysical Research*, **102 (C12)**, 26,783–26,794.

Young, J.A., & Silker, W.B. 1980. Aerosol deposition velocities on the pacific and atlantic oceans calculated from ^{7}Be measurements. *Earth and Planetary Science Letters*, **50**, 92–104.

Zhuo, W., Guo, Q., Chen, B., & Cheng, G. 2008. Estimating the amount and distribution of radon flux density from the soil surface in China. *Journal of Environmental Radioactivity*, **99(7)**, 1143–1148.

Ziegler, L.B., Constable, C.G., Johnson, C.L., & Tauxe, L. 2011. PADM2M: a penalized maximum likelihood model of the 0-2 Ma paleomagnetic axial dipole moment. *Geophysical Journal International*, **184**, 1069–1089.

List of Figures

A. Additional figures

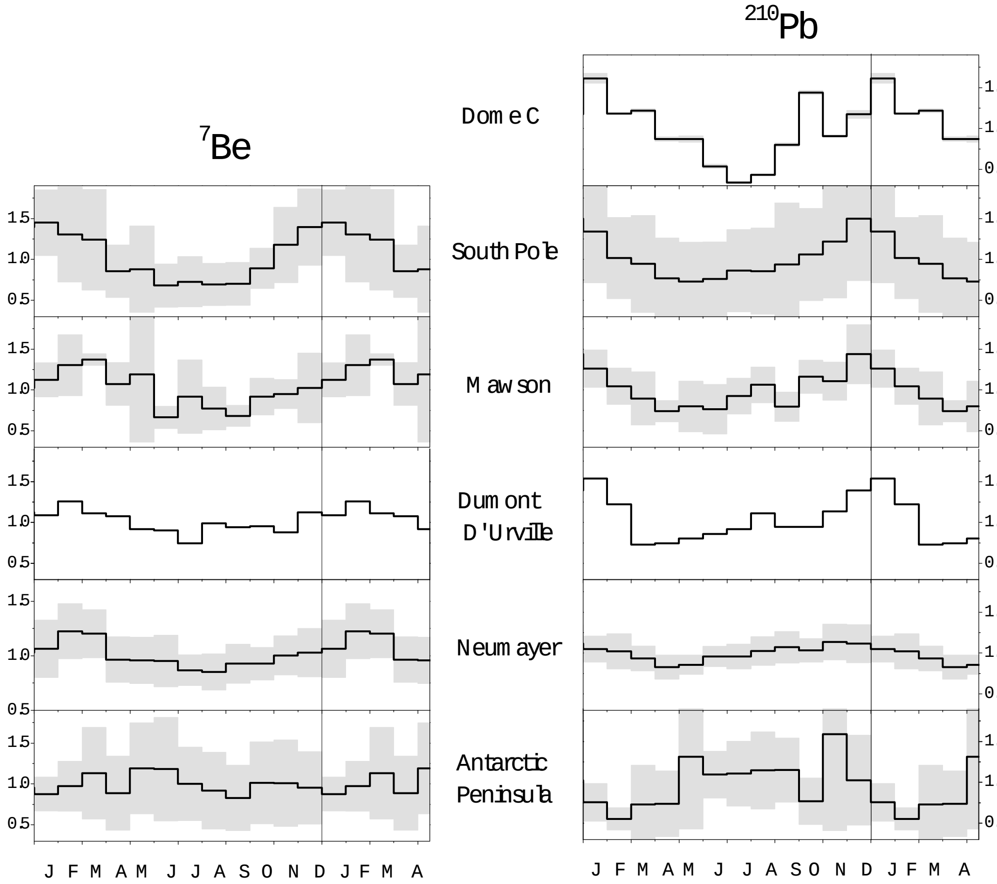

Figure A.1.: Seasonal cycles of ^{7}Be and ^{210}Pb at different Antarctic sampling stations. Grey shaded areas denote 1σ-standard deviation in case of multi-year measurements and error of volume determination in case of Dome C. Data: EML-SASP [2010], Sanak *et al.* [1985], Lambert *et al.* [1990], Klose [2010].

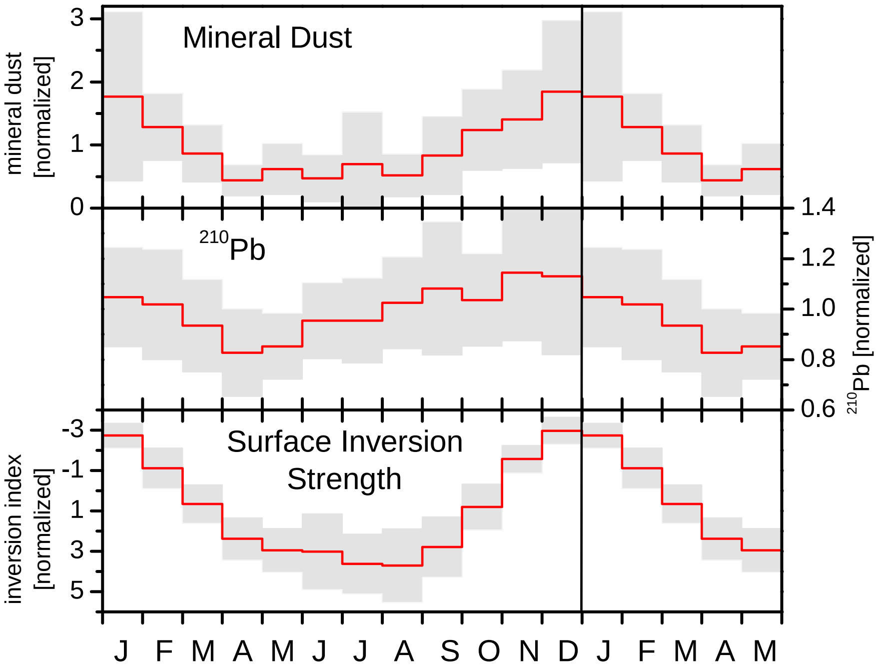

Figure A.2.: Coastal Antarctic boundary layer surface inversion strength seasonality: Mean seasonal cycles of mineral dust at Neumayer Station [Weller *et al.*, 2008], ^{210}Pb at Neumayer Station and the respective temperature inversion strength (calculated from upper air soundings, G. König-Langlo pers. comm., see supporting information of Elsässer *et al.* [2011] for details).

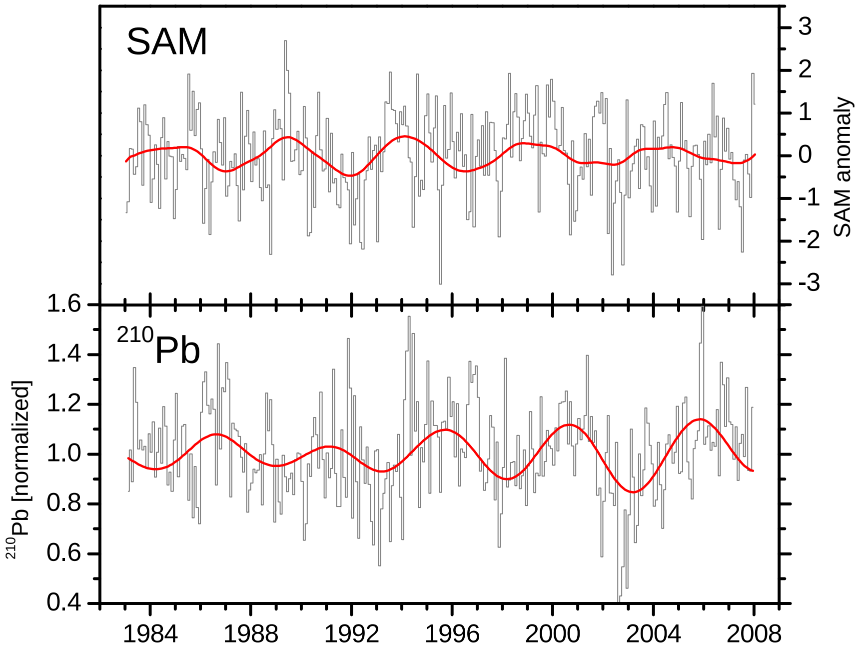

Figure A.3.: Comparison of the de-seasonalized and de-trended Neumayer ^{210}Pb time series with the Southern Annular Mode (SAM) index. Red curves denote SSA filtering (i.e. first plus second component) which correspond to variability in the 4-6yr range.

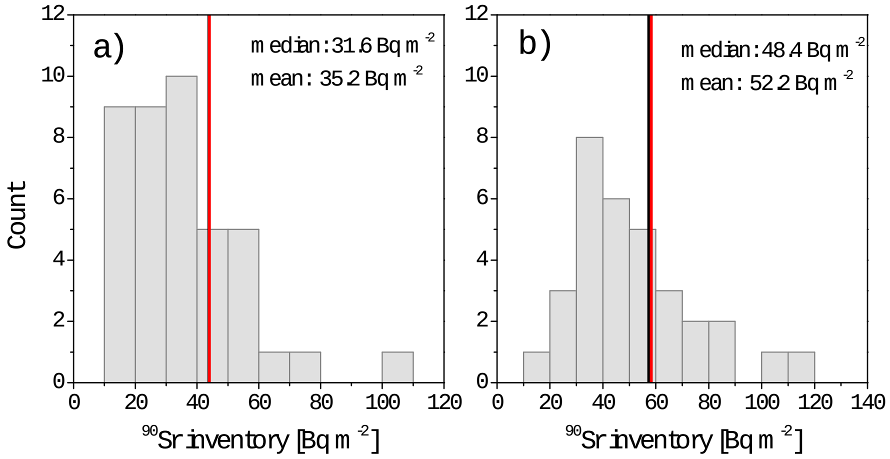

Figure A.4.: ^{90}Sr inventory in the Antarctic area reported from Pourchet *et al.* [2003]. The two histograms differ in mean accumulation of respective measurement sites: a) accumulation rates <10 cm yr^{-1} representative for the 80°S - 90°S model box and b) accumulation rates between 10 cm yr^{-1} and 60 cm yr^{-1} representative for the 70°S - 80°S model box. Vertical lines depict model results for the respective box before (black) and after (red) adjustment to ^{7}Be air concentration. Note that the extrapolated values given in UNSCEAR [2000] are significantly higher: 80 Bq m^{-2} for 80°S - 90°S and 220 80 Bq m^{-2} in case of 70°S - 80°S.

B. Measuring ^{10}Be, ^{7}Be and ^{210}Pb

The short-lived nuclides ^{7}Be and ^{210}Pb are measured by low-level gamma spectroscopy using DSG and Canberra detector systems. In short, a germanium semiconductor is combined with amplifier devices and a multi channel analyser to record the gamma spectrum of a specific sample. To allow for high detection efficiencies, the semiconductor is built as large as possible which requires high voltage as well as nitrogen cooling. Since shipping of Antarctic filters to the Heidelberg laboratory is once a year only, especially measurements of ^{7}Be (half life: 53.3 days) require a very low background to detect activities lower than 1Bq. Hence, detectors are shielded with lead and copper and measurements are conducted in an underground laboratory. After detector calibration the full energy gamma lines at 478keV and 48keV are used to evaluate ^{7}Be and ^{210}Pb activities, respectively. Air filters having mean sampling volumes of 20000m^{3} of air are folded and measured for 2-3 days on average. Double cellulose filters are used to estimate aerosol filtration efficiency which is commonly around 86%. Air volumes are corrected for standard conditions (see details in Elsässer [2008]).

Measurements of long-lived ^{10}Be require Accelerator Mass Spectrometry (AMS) and thus chemical extraction of ^{10}Be from the sample. To this end, samples are spiked with ^{9}Be carrier solution and Beryllium isotopes are extracted by using ion exchange resin columns. While ice samples are melted under acidic environment, air filters are leached using hydrochloric acid. Subsequently, $Be(OH)_2$ is precipitated from the sample together with silver-metal oxide as described in Stone *et al.* [2004]. After several iterations of dilution and centrifugation to separate isobaric boron, $Be(OH)_2$ is oxidized to BeO and pressed into targets for AMS analysis. For details on the chemical solutions and work flow applied see Elsässer [2008]. AMS measurements presented within this thesis have been performed at VERA laboratory in Vienna.

C. Time series analysis tools

Singular Spectrum Analysis

Singular Spectrum Analysis (SSA) allows for separating main signals and noise in short time series [Broomhead & King, 1986; Vautard *et al.*, 1992]. In brief, the (auto-) covariance matrix of a single time series is orthogonalized and so-called Empirical Orthogonal Functions (EOF) are calculated as associated eigenvectors. Projecting the time series onto the different EOFs results in principal components of the time series. In doing so, the EOFs correspond to data-adaptive filters [Vautard *et al.*, 1992] which produce uncorrelated components of the data. The single parameter of the method is the embedding dimension of the eigenvectors M, i.e. the window length to produce the covariance matrix and the proper choice is the key challenge of SSA. The selection of M depends on the signal under investigation as well as the setting of task. Basically, larger values result in higher spectral resolution while lower values enhance the statistical confidence. The SSA method applied in this work is backed up with a Monte Carlo approach following Allen & Smith [1996]. In doing so, the significance of a detected signal is estimated against red noise which is considered as a characteristic feature of geophysical time series [Ghil *et al.*, 2002].
For the investigation of the Neumayer radionuclide air concentration time series, a wide range of window length parameters (M=30-150 months) was tested taking into account that SSA generally achieves the analysis of periods in the range M/5 - M [Vautard *et al.*, 1992] and is restricted to <N/2 (with N being the length of the time series). The basic results of SSA were found to be basically independent from the choice of M. However, the detailed shape of single signals as well as the decomposition quality vary with M.

Wavelet Analysis

Geophysical time series are rarely stationary in time. Therefore, the Neumayer time series were further investigated using Wavelet Analysis which is a capable tool for the investigation of temporal varying periodicities. To this end, the code offered by Grinsted *et al.* [2004] (based on Torrence & Compo [1998]) was used. Several wavelet functions may be applied to investigate a time series within a wavelet transform. Since it was intended to qualitatively determine the time behaviour of the time series periodicities, a Morlet-6 wavelet was

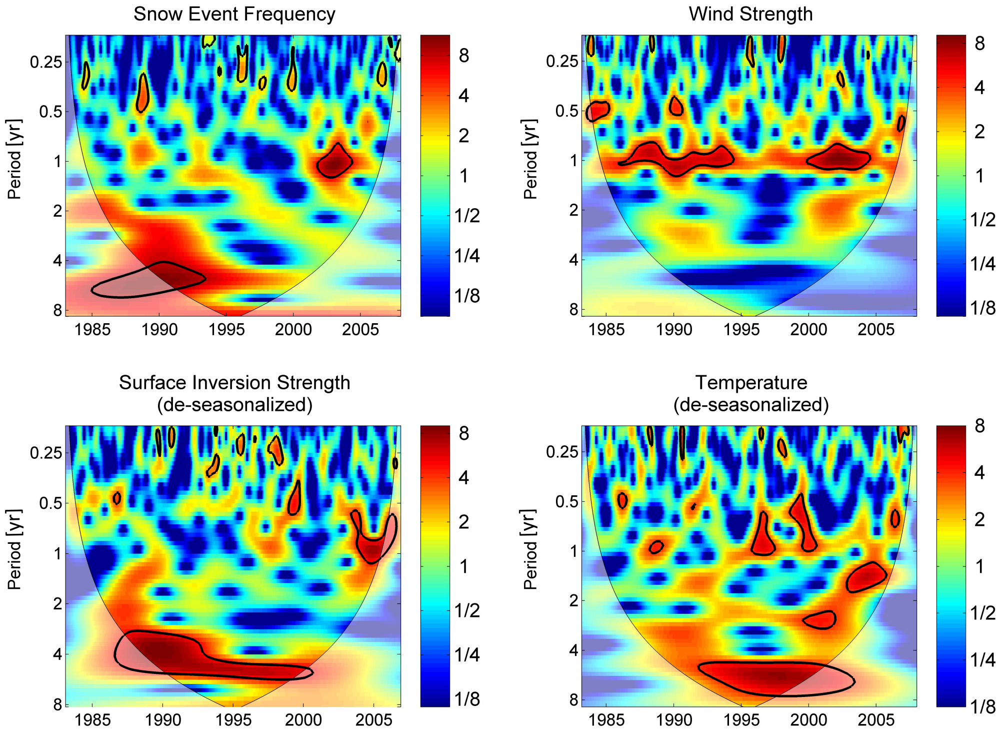

Figure C.1.: Wavelet analysis of meteorological parameters at the Neumayer Station, Antarctica using a Morlet-6 wavelet and the code offered by Grinsted *et al.* [2004]. Colour code denominates spectral power of the data under investigation. Black lines boarder areas which are formally significant (5% level) against red noise. Light coloured areas display regions out of the 'cone of influence' were edge effects might distort the analysis.

applied, only. Finally, this is in line with Torrence & Compo [1998] who state that "the choice of wavelet function is not critical" regarding qualitative results. Figure C.1 and C.2 show additional results of further time series investigated within time series analysis and reveal that variability in the 4-6 years period range is a common feature of meteorological parameters at Neumayer station. For the original time series see supplementary information of Elsässer *et al.* [2011].

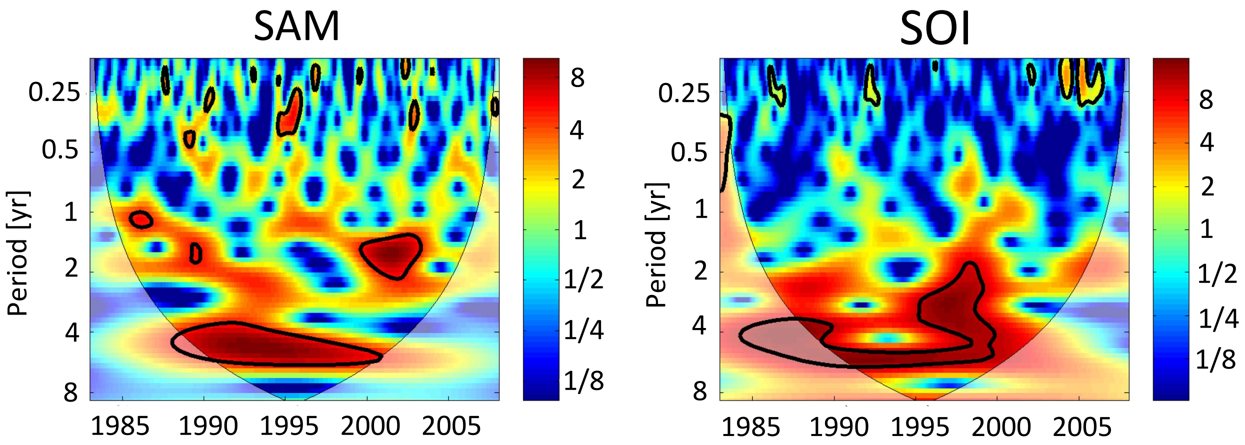

Figure C.2.: Wavelet analysis of the Southern Annular Model (SAM) index and the Southern Oscillation Index (SOI). See figure C.1 for details.

D. Model tools and numerical recipes

D.1. Model calibration based on bomb-fission radionuclides

As summarized in section 4.4, the model is adapted for the simulation of aerosol-borne radionuclides using global data sets of the bomb fission radionuclides ^{90}Sr and ^{137}Cs. To this end, the following calibration strategy was applied:

1. **Dry deposition:** The dry deposition velocity is assumed to be globally constant at 0.12 cm s^{-1} (see table 3.2). This value is estimated from spatial ^{10}Be trends (see section 3.4) and lies in the range of suggested dry deposition velocities for aerosol-bound radionuclides [Sportisse, 2007].
2. **Initial values for wet deposition:** Initial values of the scavenging ratio (ratio between radionuclide rain and air concentration) are obtained from contemporaneous measurements (long-term time series) of ^{90}Sr boundary layer air activity concentration and the deposition flux at 24 global monitoring stations [EML-SASP, 2010; EML-Fallout, 2010].
3. **Boundary layer - free troposphere coupling:** Model results of time-integrated ^{90}Sr deposition in the 18 boundary layer boxes are adapted to UNSCEAR [2000] data by varying the diffusive boundary layer - free troposphere exchange.
4. **Scavenging ratio:** Model results of the ^{90}Sr activity concentration in the 18 boundary layer boxes are adapted to EML-SASP [2010] data by varying the scavenging ratio. Since phase differences in seasonal cycles may distort the comparison of monthly data, a Gaussian smooth of model and measurements data is used to compare both time series.
5. Iteration of 3. and 4.
6. **Fine tuning** (see below)
7. Iteration of 3. and 4.

While first-order calibration explains much of the radionuclides' variability, several effects have to be accounted for within a fine tuning of the model.

- **Arctic haze phenomenon:** Comparison of ^{90}Sr atmospheric activity concentration and deposition flux measurements at Thule (Greenland coast, Arctic basin) revealed, that the respective deposition velocity is up to an order of magnitude higher during July and August compared to the rest of the year. This effect contributes to the 'Arctic haze phenomenon' (see section 3.2.2) and can not be accounted for by solely using accumulation rate variations. Hence, the scavenging ratio of the northern polar boxes (except the Greenland ice sheet) is modulated with a seasonal variation based on the deposition velocities derived from Thule station time series.

- **Polar boundary layer inversion seasonality:** Chapter 3 revealed that seasonal variations of the boundary layer inversion strength are a prominent feature of the vertical transport in the polar atmosphere. Hence, the diffusive boundary layer - free troposphere airmass transport (of the Antarctic (70°S - 90°S) and Greenland ice sheet boxes) is modulated with a seasonal cycle. For this purpose relative seasonal amplitudes of polar ^{210}Pb air concentration measurements (see figure A.1) were applied.

- **Tropical seasonality:** In case of tropical boundary layer boxes, the seasonal cycle of ^{90}Sr concentration model results are quite different from measurements. Indeed, heavy meteorological events like monsoon rain may significantly influence the aerosol sink. Certainly, precipitation regimes of the tropics (e.g. regional shift of the Inter-Tropical Convergence Zone) are not captured by the model's 10° resolution. To account for this effect, scavenging ratios of the tropical boxes are modulated with a seasonal cycle to fit the ^{90}Sr seasonality. However, this may be an unrealistic extrapolation of local conditions at single measurement sites to the total boundary layer box.

- **Extrapolation of missing information in polar areas:** Due to missing data in case of the Greenland Ice Sheet, the respective scavenging ratio is adapted from Antarctic coastal box as a first-order estimation. This is reasonable since mean accumulation rates broadly coincide. The turnover time of diffusive airmass exchange with the free polar troposphere is obtained from the northern mid polar box (70°to 80°) surrounding the Ice Sheet. Finally, the scavenging ratio of the most northern polar box (80°to 90°) is adapted from the mid northern polar box ((70°to 80°).

D.2. Long-term model runs

Although the model resolution is rather coarse, model applications on the multi-millennial timescale are challenging. Basically, short turnover times as well as seasonal variations of airmass fluxes and aerosol deposition significantly increase computing time. However, different to climate models which e.g. include a carbon cycle, the present atmospheric model reaches equilibrium conditions quite fast (i.e. within several simulated years). It was thus possible to apply a multi-processor model setup and separate the time period under investigation into several steps. At the end of each time step model results were overlain by 100 years to exclude possible edge effects. In doing so, 50kyr model runs could be accomplished within a day by using a customary (multi-processor) PC.

D.3. Model inversions

In order to reconstruct cosmogenic production using radionuclide measurements, both, the carbon cycle as well as the ^{10}Be model had to be inverted. Avoiding unfeasible numerics, a PID-controller was used in the Simulink model to online adjust the production rate to a given time series of measurements (basically following an idea of Muscheler [2000]). A PID-controller is a control engineering tool consisting of three parts which differently control the process of a feedback control system: a Proportional, an Integral and a Derivative term. In case of the application within the radionuclide model, the simulated radionuclide time series represents the process variable and the set point is the respective measurement time series. The model error (model measurement deviation) is input to the PID-controller. The basic parameters of the controller are the relative contributions of the different terms. Moreover, a reasonable scaling of the data involved (set point and process variable) is necessary. The inversion of the ^{10}Be model and carbon cycle model cannot be compared directly due to the very different geochemical cycles. On the one hand the strong damping of the carbon cycle produces a smooth atmospheric ^{14}C signal making the choice of the proper controller settings a less critical issue. On the other hand, ice core records show noisy variations in the concentration of ^{10}Be. In this case it is necessary to choose the proper PID parameters to reduce overshoot and limit the adjusting time. Several parameter settings were tested using a step function as set point, which is considered as a worst-case scenario. Equilibrium is reached after a few years.
In case of the ^{10}Be model, the seasonal cycle inherent to the ^{10}Be ice concentration hampers the online adaption of high-resolution model results to measurements which commonly represent multi-annual means. So far, a weighted moving average filter is applied to eliminate seasonal cycles online. Online filtered model results equal 'a posteriori' filtered data in case of absent multi-annual variability (difference $<10^{-4}\%$). However, short-term oscillations may give rise to differences.

E. Carbon cycle modelling and ^{14}C based reconstruction of solar activity

Cosmogenic ^{14}C and ^{10}Be basically coincide with respect to atmospheric production processes but differ concerning their atmospheric behaviour: While ^{10}Be attaches to submicron aerosol, ^{14}C oxidizes to ^{14}CO and finally ^{14}CO$_2$ and enters the global carbon cycle. To compare common production variability, carbon cycle dynamics have to be taken into account. To this end, both, the carbon cycle model of Oeschger and Siegenthaler [Oeschger *et al.*, 1975; Siegenthaler, 1983] (implemented version of Latuske [2006]) as well as the GRACE model [Hesshaimer, 1997; Naegler, 2005; Levin *et al.*, 2010b] are applied. The former model is rather basic in coupling a one box atmosphere with a simple biosphere and a one-dimensional box-diffusive ocean consisting of 43 vertical layers. The GRACE model is a more complex carbon cycle model developed for the interpretation of bomb radiocarbon. Originally built for the time scale of centuries, this model was configurated for the long time scale by Asgeirsson [2012] by e.g. reducing the atmosphere to one box only. In doing so, the long-term behaviour of both models do not considerably differ but model results somewhat deviate on shorter timescales (see Asgeirsson [2012] for details). Figure E.1 shows ^{14}C model results using geomagnetic dipole strength reconstructions given in section 5.2 in comparison to ^{14}C measurements (INTCAL09, Reimer *et al.* [2009]).

For the reconstruction of solar activity, the Siegenthaler-Oeschger model is applied. Global mean ^{14}C production rate calculations are obtained from Masarik & Beer [1999] which are not fundamentally different from updated results [Masarik & Beer, 2009] with respect to radiocarbon. The model is "inverted" by using a PID controller as explained in appendix D. Two different scenarios take unknown glacial carbon cycle / production conditions into account

1. Assuming that changes in the carbon cycle fluxes are marginal, the glacial INTCAL09 [Reimer *et al.*, 2009] data is used for the reconstruction of the entire time interval (50-0) kyr BP. Basically, this approach uses the atmospheric ^{14}C concentration to assess the glacial production rate.

2. Geomagnetic dipole strength reconstructed by Laj *et al.* [2004] as well as a mean solar activity of Φ=550MeV is used to assess the glacial production rate. The deviations between the amount of ^{14}C produced and the INTCAL09 data is assumed to result

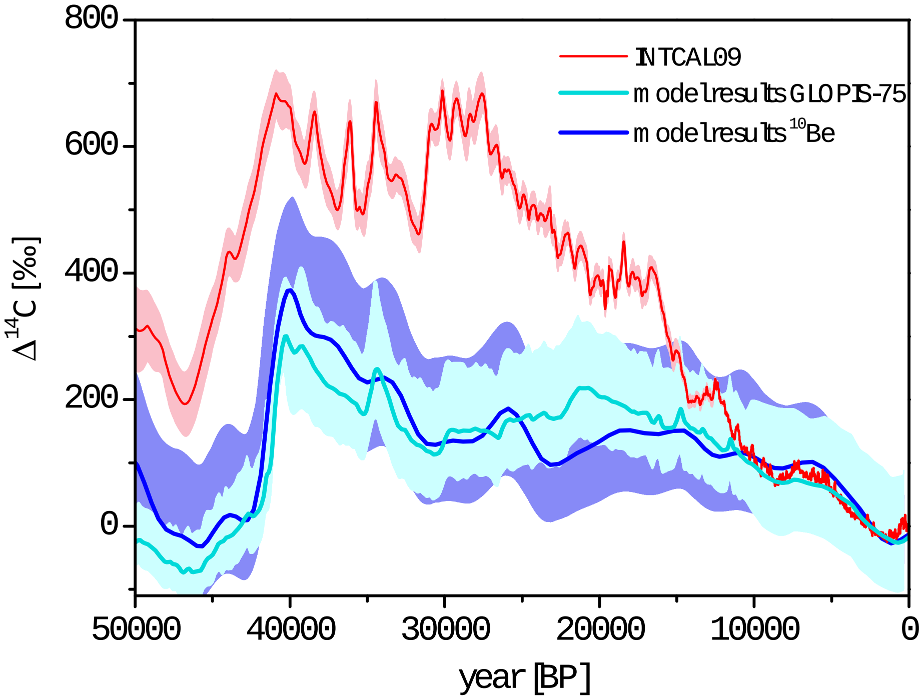

Figure E.1.: INTCAL09 ^{14}C measurements (red) [Reimer *et al.*, 2009] compared to carbon cycle model results. Model results differ in the geomagnetic reconstructions applied: (i) GLOPIS75 sediment data from Laj *et al.* [2004] (light blue) or (ii) reconstructions based on GRIP/GISP ^{10}Be data (deep blue) [Muscheler *et al.*, 2005]. Shaded areas denote uncertainty. In case of model results, errors are based on uncertainty of geomagnetic input data.

from carbon cycle changes which are not supposed to influence the longterm ^{14}C behaviour (see e.g. Muscheler [2000]).

The resulting solar modulation parameter variations of both scenarios are given in figure 5.5. Note that the two scenarios do not boarder a "real" ^{14}C production, since the geomagnetic activity used in scenario 2 may be erroneous. Eventually, the data of Laj *et al.* [2004] seems to be at the upper end of geomagnetic field reconstructions during 10-20kyr BP (see figure 5.4) making scenario 2 a lower boundary of solar activity reconstruction.

Publications related to this thesis

Elsässer, C., Wagenbach, D., Levin, I., Asgeirsson, B., Laj, C., Muscheler, R., (2012). Modelling atmospheric ^{10}Be on a 75 kyr timescale: Dependence on a varying geomagnetic field strength and climate change. Radiocarbon 2012, held 9-13 July, 2012 in Paris, France.

Elsässer C., Wagenbach D., Weller R., Auer M., Wallner A., Christl M. (2011). Continuous 25-yr aerosol records at coastal Antarctica. Part 2: variability of the radionuclides ^{7}Be, ^{10}Be and ^{210}Pb. Tellus B, Vol. 63. DOI: 10.1111/j.1600-0889.2011.00543.x.

Weller R., Wagenbach D., Legrand M., Elsässer C., Tian-Kunze X., König-Langlo G. (2011). Continuous 25-yr aerosol records at coastal Antarctica. Part 1: inter-annual variability of ionic compounds and links to climate indices. Tellus B, Vol. 63. DOI: 10.1111/j.1600-0889.2011.00542.x.

Elsässer C., Wagenbach D., Levin I., Bremen R., Weller R., Schlosser C., Auer M. (2011). Observations of atmospheric radionuclide cycles: The benefit for global paleoclimate studies. Science and Technology 2011, held 2-10 June, 2011 in Vienna, Austria.

Elsässer C., Wagenbach D., Oerter H., Wegner A., Wallner A., Preunkert S., Hansson M. (2011). ^{10}Be and ^{210}Pb in Antarctic air and firn: A tool for examining the air-firn transfer of sub-micron aerosol. EGU General Assembly 2011, held 3-8 April, 2011 in Vienna, Austria.

Elsässer C., Wagenbach D., Oerter H., Wegner A., Hansson M., Wallner A. (2010). What may be learned from cosmogenic Beryllium-10 measurements in near surface Antarctic firn? 24. Internationale Polartagung der Deutschen Gesellschaft für Polarforschung, held 6-10 September, 2010 in Obergurgl, Austria.

Elsässer C., Wagenbach D., Levin I., Weller R., Wallner A. (2010). Long-term variability of cosmogenic and terrigenous radionuclides observed in the coastal Antarctic troposphere. EGU General Assembly 2010, held 2-7 May, 2010 in Vienna, Austria.

Acknowledgements

First and foremost, I am deeply grateful to Dietmar Wagenbach and Ingeborg Levin for the opportunity to work in an exciting field of research. It was a great pleasure to be part of their delightful working groups and I enjoyed the motivating ensemble of continuous interest together with confidence in my work. Above all, I am indebted for the many lessons on the mindset of environmental physics.

I want to thank Norbert Frank who kindly accepted the review of my thesis although being busy with moving his research group from Paris to Heidelberg.

This work would not have been possible without the preliminary work of both, members of the IUP ice and climate and carbon cycle group. The current GRACE model is based on Tobias Naegler and it was inspiring to contribute his work especially due to Tobias' helpful teaching. Many students of Dietmar's ice and climate group contributed to large amounts of radionuclide measurements which could be summarized to draw a picture of their polar climatology.

The Alfred Wegener Institute provided firn and ice samples from various polar surveys. Especially Rolf Weller and Hans Oerter were helpful contact persons for the Neumayer station and Antarctic traverses. In addition, thanks to M. Hansson (Stockholm University) for the JASE snow pit samples.

The Vera Laboratory at the University of Vienna accomplished measurements of ^{10}Be and I want to thank especially Anton Wallner for his kind support.

I am grateful for the many peoples steady efforts in geoscience measurement and monitoring studies which allow for modelling attempts. While relying on plenty of data sets, I want to emphasize some essential contributions: I am indebted to Raimund Muscheler (Lund University) for ^{10}Be and ^{14}C data as well as for helpful discussions. Ilya Usoskin (University of Oulu) kindly provided (at that time unpublished) results of cosmogenic production rate calculations. Jürg Beer (EAWAG Duebendorf) offered production rates as well as ^{10}Be measurements from the EDML ice core. Grant Raisbeck (CSNSM, Orsay) sent his results of ^{10}Be measurements at Vostok ice core. Carlo Laj (LSCE Gif-sur-Yvette) kindly provided reconstructions of the geomagnetic dipole strength. Herbert Wershofen (PTB Braunschweig) and Jack Dibb (University of New Hampshire) shared longterm radionuclide monitoring data, Clemens Schlosser (BFS Freiburg) and Matthias Auer (CTBTO Vienna) were helpful contact persons for all kind of atmospheric radionuclide issues, Hans Oerter (AWI Bremerhaven) provided Antarctic accumulation rates, Anders Svensson (University of Copenhagen) offered data and hints on the GRIP accumulation rates, Shigekazu Hirao (Nagoya University) provided (updated) ^{222}Rn fluxes, M. Christl (ETH Zurich) offered his geomagnetic reconstructions and Gert König-Langlo (AWI, Bremerhaven) meteorological data from upper air soundings at Neumayer station. Moreover, thanks to Joel Pedro (ACE CRC, Tasmania) and Ulla Heikkilä (ANSTO) for inspiring discussions on the interpretation of polar ^{10}Be. Eventually, I want to thank all scientist who did not hesitate to extensively answer a lot of questions on various topics (representative for many others: E. Waddington, F. Parrenin and J.R. Petit).

Special thanks go to all current (or former) ice and climate and carbon cycle group members. Especially Rebecca Bremen, Stefanie Klose and Birgir Asgeirsson for radionuclide measurements and backup in ^{14}C modelling, respectively. Thanks to Pascal Bohleber who was a helpful colleague for getting started with mystery time series analysis and did a lot of proof reading. Thanks to Mario, Michael, Clemens, Paul and Lars for maintaining the performance of our gamma-laboratory and Helga Baus for ^{10}Be chemistry. All other members - especially the longterm fellows Barbara, Pascal, Helene, Sam, Felix, Cora and Michael and of course Dietmar and Ingeborg - thank you for making the IUP more than a place to work and trips to Kühtai, Schauinsland, Pitztal, Dresden, Vinschgau and various conferences in Vienna, Obergurgl, Paris and Geilenkirchen.

Finally, a big "thank you" to my family and especially to Sarah. Without their encouragement and understanding this work would not have been possible!